Stratified Flow Over Topography: Steady Nonlinear Waves, Boundary Layer Instabilities, and Crater Topography

by

Nancy Soontiens

A thesis
presented to the University of Waterloo
in fulfillment of the
thesis requirement for the degree of
Doctor of Philosophy
in
Applied Mathematics

Waterloo, Ontario, Canada, 2013

I hereby declare that I am the sole author of this thesis. This is a true copy of the thesis, including any required final revisions, as accepted by my examiners.

I understand that my thesis may be made electronically available to the public.

Abstract

This thesis investigates several aspects of stratified flow over isolated topography in ocean, lake, and atmospheric settings. Three major sub-topics are addressed: steady, inviscid internal waves trapped over topography in a pycnocline stratification, topographically generated internal waves and their interaction with the viscous bottom boundary layer, and flow over large-scale crater topography in the atmosphere.

The first topic examines the conditions that lead to very large internal waves trapped over topography in a fluid with a pycnocline stratification. This type of stratification is connected to ocean or lake settings. The steady-state Euler equations of motion are used to derive a single partial differential equation for the isopycnal displacement in supercritical flows under two conditions: a vertically varying background current under the Boussinesq approximation and a constant background current under non-Boussinesq conditions. A numerical method is developed to solve these equations for an efficient exploration of parameter space. Very large waves are found over depression topography when the background flow speed is close to a limiting value. Variations in the background current are examined, as well as comparisons between Boussinesq and non-Boussinesq results.

The second topic aims to extend the above subject by considering unsteady, viscous flows. Once again, supercritical flow over topography in a pycnocline stratification generates internal waves. These internal waves interact with the viscous bottom boundary layer to produce bottom boundary instabilities. The three-dimensional aspects of these instabilities are studied under changes in viscosity. The boundary layer instabilities have important implications for sediment transport in the coastal oceans or lakes.

Lastly, the final topic is motivated by the connection between dust streaks on the Martian surface and crater topography. Flow over a large 100-km diameter crater is examined with numerical simulations conducted using the Weather Research and Forecasting model. Modifications to the stratification and topography are applied. It is found that a large hydraulic structure of amplitude comparable to the crater depth forms in many cases. This structure may have important implications for dust transport in the atmosphere. In addition, Martian atmospheric parameters are used to study the flow properties under Mars-like conditions.

Acknowledgements

There are many people to whom I owe thanks for making this thesis possible. First and foremost, I would like to thank my supervisors Dr. Marek Stastna and Dr. Michael Waite for the opportunity to make mistakes and learn from them. Your guidance and careful encouragement will always be remembered. Many thanks to my committee members Dr. Paul Kushner, Dr. Kevin Lamb, Dr. Francis Poulin, and Dr. Andrea Scott for your detailed review.

The administration and staff within the Applied Mathematics department helped to make the graduate school experience as seamless and smooth as possible. Thank you to Helen Warren for help with scholarship applications and to Stephanie Martin for taking up the much needed role of filling Helen's shoes when she retired. In addition, thank you to the members of the Women in Mathematics Committee, especially Dr. Barbara Csima and Dr. Sue Ann Campbell, for the opportunity to connect with senior female faculty members and for being a role model to a female mathematics student encased in an office full of men.

My family is owed many thanks for understanding and supporting my desire for an extended period in education. Thank you to my mother Joanne, her partner Earl, to my siblings Bill, Marie, and Wendy, and to my siblings at heart Kari, Eddie, Dan, Hana, and Ryan. A special thanks to Bill and Betty Ann for the many visits to the farmhouse.

The experience of graduate school wouldn't be the same without friends and office mates. Acknowledgement goes out to all of my office mates, especially to Timothy Rees for the puzzles I am still trying to solve, to Kristopher Rowe for organizing the afternoon soccer games, and to Wentao Liu for being the best boss. Thank you to Michael Dunphy for being forgiving whenever I swamped belize and to Christopher Subich for the many insights into the world of numerics. For reminding me that there is a world beyond the campus I owe thanks to my friend Wendi Zou. And for providing me with just enough distraction to keep me sane, thank you to all of the members of the Karate Club and the Warriors Band.

Finally, thank you to Will, my love and life partner. Thank you for your patience and encouragement during the undertaking of this degree and for your flexibility as we begin the next steps of our lives together. Your support and love has carried me through a degree that, 10 years ago, I would have never imagined pursuing.

Dedication

To my mother, Joanne and to my life partner, Will.

Table of Contents

List of Tables

List of Figures

Chapter 1

Introduction

Stratified flow over topography is an important topic in the study of environmental and geophysical fluid dynamics. The movement of water and air in the oceans, lakes, and atmospheres over bottom features such as mountains, canyons, and depressions can generate internal waves as a response to buoyancy forces when density stratification is present. At large amplitudes these internal waves can overturn and break, leading to irreversible mixing which has important implications for the momentum and energy budgets in environmental and geophysical flows. As a result, there is a wide variety of literature on this topic, ranging from theoretical studies to laboratory experiments to field observations. A useful background overview on the topic of stratified flow over topography is provided in the monograph by Baines (1995).

The study of stratified flow over topography has a rich mathematical history encompassing problems in partial differential equations, linear and nonlinear theories, and asymptotic and perturbation analysis. In recent years, the general topic of stratified flow over topography has been advanced through numerical simulations of the equations of motion for a fluid. These numerical techniques have granted access to problems that are excessively difficult or impossible to study analytically. With increasing computational power this field now considers realistic and physical flow conditions that in some cases lead to encouraging matches with observations. The numerical techniques allow for analysis of important flow variables that cannot always be captured by observations. Recently, both observational and numerical procedures have advanced significantly allowing for a more complete understanding of the topic. This thesis examines stratified flow over topography using a combination of analytical techniques and numerical methods.

This thesis will contribute to the study of stratified flow over topography by consid-

ering three related topics: 1) steady waves trapped over topography, 2) topographically generated internal waves and their interaction with a viscous bottom boundary layer, and 3) large-scale atmospheric flow over crater topography. These subjects are applicable to lakes and the coastal oceans with pycnocline stratifications (topics 1 and 2) and atmospheric conditions on Earth and Mars (topic 3). This chapter gives a general overview of environmental and geophysical fluid dynamics. A more detailed background and literature review is given in each of the following three chapters.

Fluid dynamics is described by the conservation equations for momentum, mass, and energy. The equations of motion for an atmosphere under the effects of rotation are given by (e.g. Gill, 1982):

$$\rho\left(\frac{D\mathbf{u}}{Dt} + 2\boldsymbol{\Omega}\times\mathbf{u}\right) = -\nabla p + \rho\mathbf{g} + \mu\nabla^2\mathbf{u}, \tag{1.1a}$$

$$\frac{D\rho}{Dt} + \rho\nabla\cdot\mathbf{u} = 0, \tag{1.1b}$$

$$\rho T c_p \theta^{-1}\frac{D\theta}{Dt} = \nabla\cdot(k\nabla T - \mathbf{F}_{rad}) + Q_H, \tag{1.1c}$$

$$p = R\rho T, \tag{1.1d}$$

$$\theta = T\left(\frac{p_0}{p}\right)^{(R/c_p)}. \tag{1.1e}$$

Equation (1.1a) is the Navier-Stokes equation and expresses the conservation of momentum where $\mathbf{u}$ is the velocity vector, p is the pressure, ρ is the density, $\mathbf{g}$ is the gravity vector, μ is the dynamic viscosity, and $\boldsymbol{\Omega}$ is the angular velocity of the reference frame. The term $2\boldsymbol{\Omega}\times\mathbf{u}$ represents the Coriolis force due to the planet's rotation. This term is removed if the effects of rotation are not to be considered, or if they are insignificant compared to other mechanisms (e.g. inertia, buoyancy, and so on). Finally,

$$\frac{D}{Dt} = \frac{\partial}{\partial t} + \mathbf{u}\cdot\nabla$$

is the material derivative which is the total rate of change following the flow. In the atmosphere, on the scales for which viscosity is important the effects of compressibility are usually negligible (Gill, 1982), hence, the form of the last term in (1.1a).

Equation (1.1b) is the continuity equation and describes the conservation of mass. Equation (1.1c) is the energy equation where T is the temperature, c_p is the specific heat, R is the ideal gas constant, p_0 is a reference pressure, and θ is the potential temperature

given by (1.1e). The first term on the right hand side of (1.1c) represents the diffusion of heat, where k is the thermal conductivity. This term is often neglected because it is small when considering large-scale motions (Gill, 1982). The second term $\mathbf{F}_{rad}$ is the radiative heating term and can be calculated from the absorbing, emitting, and reflecting components of the atmosphere system. The final term Q_H represents other heating components such as latent heat transfer due to phase changes of the fluid. A relationship between the pressure, density, and temperature is provided in (1.1d), the ideal gas law.

These equations are in general impossible to solve analytically due to their strong nonlinearity, but under certain assumptions they can be simplified, and this can in turn give insights into the types of motions present in the atmosphere. One key assumption is to neglect the effects of viscosity by removing the viscous term in (1.1a) since viscous effects in the free atmosphere are unimportant compared to other aspects of the flow. This approximation is used by the Weather Research and Forecasting (WRF) model, a numerical tool employed in this research. The equations solved by this model are written in a slightly different form than those presented above and the details can be found in Skamarock et al. (2008).

Under conditions of incompressible flow, such as an in the ocean or lakes, where rotational effects are excluded, the equations of motion are (Kundu and Cohen, 2008):

$$\frac{D\mathbf{u}}{Dt} = -\frac{1}{\rho_0}\nabla p + \frac{\rho}{\rho_0}\mathbf{g} + \nu\nabla^2\mathbf{u}, \tag{1.2a}$$

$$\nabla \cdot \mathbf{u} = 0, \tag{1.2b}$$

$$\frac{D\rho}{Dt} = \kappa\nabla^2\rho. \tag{1.2c}$$

Once again, these equations are derived from the conservation of momentum (1.2a), mass (1.2b), and energy (1.2c). In this set of equations ρ_0 is a constant reference density and the Boussinesq approximation has been applied so that changes in density are included only in the buoyancy term. Under this approximation the full continuity equation takes the incompressible form expressed in (1.2b). The Boussinesq equations can also be applied to atmospheric flow under conditions of low Mach number and small flow depth scale compared to the scale height (Kundu and Cohen, 2008). Effects of making the Boussinesq approximation will be discussed in the context of steady flows over topography for an incompressible fluid with a small ratio of vertical to horizontal length scales. The assumption of incompressibility is appropriate for the lake and ocean applications considered Chapters 2 and 3. The Boussinesq approximation is not applied to the atmospheric flows considered in Chapter 4.

Often, the conservation of energy (1.2c) is framed in terms of the temperature T, and an equation of state is used to relate the temperature and density. Instead, we have stated the conservation of energy in terms of ρ by assuming a linear equation of state. The constant κ is the molecular diffusivity. The parameter ν is the kinematic viscosity and is an important part of studying boundary layer instabilities Chapter 3. When viscous effects and diffusion are not considered the last term in (1.2a) and the term on the right hand side of (1.2c) are removed and the equations are often referred to as the Euler equations of motion.

These sets of equations provide the basis for studying topographic flows in this thesis. One final consideration that should be discussed is the appropriate treatment of the lower boundary condition at $z = h(x)$, the bottom topography. For inviscid dynamics, the no normal flow boundary condition is applied so that $\mathbf{u} \cdot \mathbf{n} = 0$ where $\mathbf{n}$ is the normal vector of the lower boundary. When viscous effects are important the no slip boundary condition is also applied so that $\mathbf{u} = 0$ along the lower boundary. The upper and side boundary conditions differ among the subjects discussed and will be presented on a case by case basis.

These equations will primarily be examined in a numerical framework. Several different domains are considered and will be discussed in each chapter. However, the first subject presented in this thesis takes a different approach by deriving a steady form of (1.2) under inviscid conditions. In Chapters 2 and 3, pycnocline stratifications are considered in environments motivated by ocean and lake settings. Several modifications to the stratification profile, such as the location of the pycnocline and density difference across the pycnocline are examined. In Chapter 4, atmospheric flow is considered with several variations in the stratification, such as an atmosphere with a constant buoyancy frequency, two-layer atmospheres, and an atmosphere with a near-surface temperature inversion. These stratifications will be discussed in detail in each chapter.

1.0.1 Plan of Thesis

This thesis is divided into three major sub-topics in stratified flow over topography. The research goals of each of these topics is provided next. While these topics span a variety of scales and flow environments, they share the common theme of stratified flow over topography and are studied using similar methods and techniques. The overall intent is to contribute to the general picture of stratified flow over topography by connecting studies on inviscid flows in a pycnocline stratification, the interaction between internal waves and the boundary layer, and mesoscale topographic flows in the atmosphere.

Although the three major subjects share a common set of fundamental tools and back-

ground material, each has its own relevant set of literature, with some cross over. As such, each chapter will consist of a self-contained introduction and conclusion in order that connections to previous work may be highlighted to their fullest. The final chapter of the thesis provides some concluding comments and general reflections.

Steady Internal Waves over Topography

Chapter 2 focuses on the long time state of inviscid flow over topography with the goal of further understanding the very large-amplitude waves trapped over topography that have been computed in previous studies (Stastna and Peltier, 2005). Several variations of the Dubreil-Jacotin-Long (DHL) equation are used to study features such as shear background currents, trapped cores, non-Boussinesq solutions, and adjustments in the polarity of the topography in a fully nonlinear framework. Comparisons with time-dependent numerical solutions from a code called the Internal Gravity Wave solver (Lamb, 1994) are included in a few key cases. Conditions which lead to the development of very large trapped internal waves of depression are discussed. Multiple solutions to the DJL equation for flows with a shear background current are discovered and compare well with numerical simulations. These results have been published in two papers (Soontiens et al., 2010, 2013b) and these are expanded upon here. Many thanks to Christopher Subich for helping to develop the numerical techniques used for solving the DJL equation.

Topographically Generated Internal Waves and Boundary Layer Instabilities

Chapter 3 adds to the recent discussion on boundary layer instabilities induced by propagating internal solitary waves. Waves generated by supercritical flow over topography are considered. The primary goal of this study is to examine the three-dimensionalization of boundary layer instabilities. This is a natural extension to the inviscid studies from the previous chapter. It is found that small changes in the viscosity can drastically affect the three-dimensionalization process. This study also proved to be an experimental testing ground for a pseudo-spectral code developed by a former PhD student (Subich, 2011; Subich et al., 2013). Christopher's help in learning how to use the code and in setting up some of the problems is appreciated. The work described in this chapter remains unpublished but will be considered for publication in the future.

Flow Over Large-Scale Crater Topography

Chapter 4 is motivated by the connection between dust streaks on the Martian surface and crater topography. Since flow over crater topography is not a widely studied topic (being inherently three-dimensional), a preliminary investigation on the effects of stratification, rotation, and topographic modifications is provided first. It is found that a retreating gravity current within the crater act as a modified topography, forcing addiional gravity waves. These results have been published by Soontiens et al. (2013a) and are expanded upon here. This is followed by studies which consider Mars-like atmospheric conditions and implications for dust lifting are discussed.

Chapter 2

Steady Internal Waves over Topography

2.1 Introduction

Internal waves are ubiquitous in the coastal oceans and lakes where tidal or wind forcing, combined with interactions with the bottom topography, drive the generation of these waves. The discovery that these waves, which can reach very large amplitudes, has led to the realization that they may play an important role in the energy and momentum budgets of the oceans (Garrett and Munk, 1979), and could influence the transport of sediments and nutrients in lakes, and thereby affect ecosystem dynamics (Imberger and Patterson, 1989; Hodges et al., 2000). Hence, internal waves have become an important area of research in physical oceanography and limnology, with a desire to understand their generation and evolution, and a goal of determining how their presence can affect processes on both small and large scales.

As with many physical phenomena in nature this problem is by no means an easy one to solve, yet, a considerable amount of research has examined internal waves from many perspectives, including analytical, numerical, observational, and experimental view points (e.g. see Helfrich and Melville, 2006; Guo and Chen, 2013, for an overview). It is the combination of these view points that has advanced our understanding of this topic, and a cross-disciplinary approach to internal waves, which spans oceanography, limnology, biology, applied mathematics, scientific computation as well as other disciplines, continues to fuel this topic as an active area of research.

This chapter contributes to research on internal waves in the oceans and lakes by considering steady flows over topography or, more specifically, long-time states produced by a consistent forcing in the form of a background current. While the oceans and lakes are generally dynamic bodies with time-varying forcing, this idealized problem can provide insights into the size and shape of internal waves without complicated, and often intractable, representations of more realistic flow conditions. As well, this type of process study can act as a numerical laboratory for exploring the effects of variations in topography and other flow features. An overview of the literature pertaining to internal waves and steady flows is presented first, with derivations and computations following.

Mathematically, internal waves are described by the equations of motion for an inviscid, density stratified fluid, most often referred to as the Euler equations of motion. These exact equations are nonlinear and, hence, are very difficult to solve analytically. Several strategies exist to overcome this barrier, including deriving approximate theories such as the Korteweg deVries (KdV) equation (see e.g. Benney, 1966; Grimshaw and Smyth, 1986) which assumes only weak nonlinearity and dispersion, or using numerical models to simulate the fully nonlinear equations of motion. Each of these strategies has its strengths and weaknesses. For one, KdV theory is an approximate theory that assumes that wave amplitudes are small, and as such, has had difficulty in describing the very large internal wave features of some observations (Helfrich and Melville, 2006). However, with the addition of an extra cubic nonlinear term, the extended KdV equation (or Gardner equation) predicts the broadening behaviour observed in large internal waves, yet only gives a qualitatively correct model (Stastna and Peltier, 2005). The KdV equation has been widely used to study nonlinear internal waves, and its theory now includes extensions for flow over topography (Djordjevic and Redekopp, 1978; Grimshaw and Smyth, 1986) and for broadening behaviour in the extended KdV or Gardner equation (Kakutani and Yamasaki, 1978; Melville and Helfrich, 1987).

Alternatively, numerical simulations of the fully nonlinear Euler equations pose their own benefits and challenges. Mainly, these simulations can be computationally expensive, since often a large range of length scales must be resolved in order to properly represent the motion. As such, a thorough investigation of parameter space is often unattainable. However, with the advent of increased computational power, these types of studies are becoming more practical and have been used to compare the weakly nonlinear KdV theory to fully nonlinear results (Lamb and Yan, 1996; Stastna and Peltier, 2005). These types of comparisons are helpful in determining where approximate theories such as the KdV equation break down.

An alternative approach is the use of steady-state theory, leading to the so-called Dubriel-Jacotin-Long (DJL) equation (Dubreil-Jacotin, 1932; Long, 1953), which is a sin-

gle nonlinear partial differential equation for the isopycnal displacement. An isopycnal is a curve of constant density and the isopycnal displacement is the distance an isopycnal is displaced from its far upstream location. This theory does not make any approximations with respect to nonlinearity, and is equivalent to the steady form of the fully nonlinear Euler equations. However, it does not give any information about transient states and cannot represent dynamical situations such as wave overturning. Numerical simulations are the best tool to use in these scenarios. Nevertheless, several studies have confirmed that DJL solutions can match the results of long-time numerical simulations of the Euler equations almost exactly (Lamb, 1999; Stastna and Peltier, 2005), rendering DJL theory a very useful tool. Hence, this chapter presents results using both the DJL theory and numerical simulations, with a focus on large-amplitude waves trapped over topography. The use of DJL theory allows for an efficient exploration of parameter space in order to determine when large trapped states may occur, while the numerical simulations reveal the details of transient processes in a few key cases.

The DJL equation has been used in several studies with idealized density profiles in the atmosphere (Laprise and Peltier, 1989; Smith, 1985) and oceans and lakes (Brown and Christie, 1998; Tung et al., 1982; Stastna and Lamb, 2002a). With a pycnocline stratification representative of oceans and lakes, DJL theory has had success at describing steady large-amplitude waves, for both waves trapped over topography and freely propagating waves. Further, fully nonlinear theory has been used to determine limiting amplitudes for freely propagating internal solitary waves, which arise under three conditions (Lamb, 2002; Stastna and Lamb, 2002a): (1) the breaking limit, which describes the onset of isopycnal overturning; (2) the shear-instability limit, for which waves become unstable (Lamb and Farmer, 2011); and (3) the conjugate flow limit, for which waves broaden and flatten out (Lamb and Wan, 1998; Rusås and Grue, 2002). Similar limiting amplitudes for breaking waves have been discovered in laboratory experiments and theoretical computations of layered fluids (Fructus et al., 2009). There is some evidence that these limiting amplitudes do not apply to resonantly generated waves trapped over topography (Stastna and Peltier, 2005), explaining the very large laminar disturbances and the wave amplitude-inflow speed hysteresis captured by the DJL equation (Soontiens et al., 2010).

The conjugate flow limit led Stastna and Peltier (2005) to consider waves generated over topography for inflow speeds close to the conjugate flow speed, c_j. Their numerical simulations yielded very large trapped laminar disturbances over the topography which were confirmed to satisfy the DJL equation. The term conjugate flow is due to Benjamin (1966) and describes two horizontally uniform states connected by a wave front of permanent form. The concept of conjugate flows has been used to understand the broadening and flattening of internal solitary waves in some oceanic observations (Duda et al., 2004;

Helfrich and Melville, 2006). Lamb and Wan (1998) have presented the conjugate flow theory for continuously stratified fluids with and without the Boussinesq approximation. They provide a detailed method for calculating conjugate flow speeds for a general density stratification. A similar method is used to calculate conjugate flow speeds in this chapter.

The conjugate flow speed is an important parameter that is used to define supercritical flow conditions for which no upstream propagating modes exist. The definition of criticality is somewhat ambiguous in the literature, often framed in terms of a linear long wave speed (e.g. see Baines, 1995) which is not appropriate in the context of large-amplitude nonlinear waves (Stastna and Peltier, 2005), because nonlinear waves have larger propagation speed than the linear long wave speed. In this work, a flow is said to be supercritical if the background speed U_0 is greater than the conjugate flow speed. Several studies have examined the steady states of subcritical and supercritical flows over topography using shallow water theories (Lawrence, 1987; Esler et al., 2005, 2007, 2009) or using weakly nonlinear theory (Grimshaw and Smyth, 1986). This chapter will examine similar flow conditions, however, for a continuously stratified fluid using a fully nonlinear framework. Interesting results from shallow water theory, such as hysteresis and downstream recovery jumps, can now be examined with an exact theory for a continuously stratified fluid, and distinctions between the results for the two cases can be made. Since the DJL equation is nonlinear multiple states, or hysteresis, are possible. This is also reflected in the time-dependent simulations by flow history, an important point that is not captured by steady theory.

This chapter is organized as follows: First, Section 2.2 provides a description of the fully nonlinear DJL theory used to study the trapped internal waves. As well, an outline of the numerical methods and description of experiments is provided in this section. The results are presented in Section 2.3. This section includes an analysis of the multiple states found for sheared background currents, a description of trapped waves with vortex cores, a discussion of symmetry breaking between elevation and depression waves, a comparison of Boussinesq and non-Boussinesq results, and an examination of transcritical flows. Most of these results have been published in two papers (Soontiens et al., 2010, 2013b), which are expanded upon in this chapter. Finally, the chapter concludes with a discussion of how these results connect with the current literature and directions for future work in Section 2.4.

2.2 Methodology

This section provides an overview of the most important tools that have been used in this chapter. First, a description of the theory describing fully nonlinear, steady flows is provided, with an overview of the relevant equations and the conditions of their applicability. Second, an overview of several numerical methods explains the techniques used to solve these equations. Finally, a description of experimental parameters and flow conditions is included at the end of the section.

2.2.1 Nonlinear Theory

This section outlines the equations used in this study in order to examine steady waves over topography in a continuously stratified fluid using a fully nonlinear framework. The discussion begins with a presentation of the Dubreil-Jacotin-Long (DJL) equation in a simple case, i.e. a continuously stratified fluid under the Boussinesq approximation with a constant background velocity. This presentation is followed by derivations of two extensions to the DJL equation: first, a Boussinesq fluid with a sheared background current, and second, a non-Boussinesq fluid with constant background velocity. Finally, a discussion of conjugate flows, an important concept in the definition of super- and sub-criticality in flows for which nonlinear effects are important, is provided.

The Dubreil-Jacotin-Long Equation

The equations governing fluid dynamics are nonlinear and, in general, are very difficult to solve analytically. Nonetheless, useful insights can be gained by considering special cases which lead to simplifications to the governing equations of motion. One such simplification involves considering the steady-state form of the equations of motion which, under certain circumstances, leads to a single equation for the isopycnal displacement η. This equation is often referred to as the Dubreil-Jacotin-Long (DJL) equation (Dubreil-Jacotin, 1932; Long, 1953) and has contributed to considerable understanding of steady flow over topography.

We consider a variable density fluid over an infinite domain with horizontal coordinate x, $-\infty < x < \infty$, and vertical coordinate z, $-|h_0| < z < H$ (or $0 < z < H$ for elevated topography), and wish to solve for the density ρ and velocity (u, w). We consider a class of problems where the upstream vertical velocity is zero, the upstream horizontal velocity is specified to be constant or a function of z, and the upstream density profile is given by

$\bar{\rho}(z)$. These problems will be solved on a numerical domain that spans $[-L, L] \times [-|h_0|, H]$ ($[-L, L] \times [0, H]$ for elevated topography).

For a Boussinesq fluid with constant background current U_0, the DJL equation with boundary conditions is given by

$$\nabla^2 \eta + \frac{N_B^2(z-\eta)}{U_0^2}\eta = 0, \tag{2.1a}$$

$$\eta = 0 \text{ at } z = H, \tag{2.1b}$$

$$\eta = h(x) \text{ at } z = h(x), \tag{2.1c}$$

$$\eta \to 0 \text{ as } x \to \pm\infty, \tag{2.1d}$$

where

$$N_B^2(z) = -\frac{g}{\rho_0}\frac{d\bar{\rho}}{dz}(z), \tag{2.2}$$

g is the acceleration due to gravity, ρ_0 is a constant reference density, $\bar{\rho}(z)$ is the density profile in the far upstream, and $h(x)$ is the lower boundary. The upper and lower boundary conditions are derived from requiring that the upper and lower boundaries are streamlines. The horizontal boundary conditions state that the isopycnal displacement is zero far away from the topography. Numerically, this boundary condition is implemented at $x = \pm L$, the horizontal extent of the numerical domain. An additional restriction is posed on the topography so that $h(x) \to 0$ as $x \to \pm\infty$. The definition of η and a visualization of the numerical domain is illustrated in Figure 2.1.

Note that for the special case of $N(z) = N_0$, a linear stratification, the DJL equation reduces to a linear partial differential equation given by

$$\nabla^2 \eta + \frac{N_0^2}{U_0^2}\eta = 0. \tag{2.3}$$

This equation has been applied to the study of atmospheric flows over topography in a variety of situations (Laprise and Peltier, 1989; Smith, 1985; Magalhães and Young, 1995) and has been reformulated as an integral equation as an alternate means of deriving solutions (Muraki, 2011). It is intriguing that a set of nonlinear equations can be reduced to a single linear partial differential equation in this special case.

In the following, two other forms of the DJL equation are derived. The method used to derive the equations is similar to that used by Stastna (2001) for the DJL equation which describes freely propagating internal solitary waves. The first case represents a Boussinesq fluid with vertically varying background current $U(z)$. The second case represents a non-Boussinesq fluid with constant background current U_0. In both cases the buoyancy frequency is allowed to vary with height.

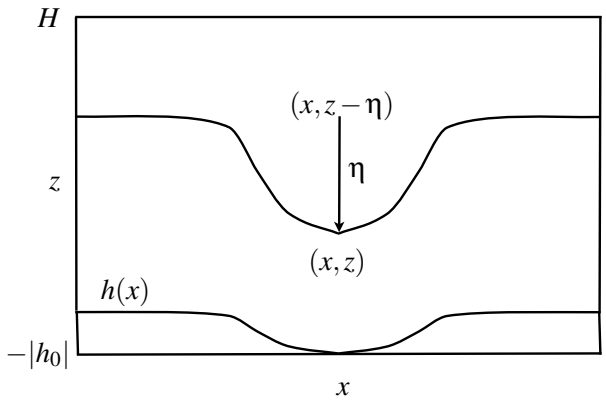

Figure 2.1: A single isopycnal contour over topography $h(x)$. The isopycnal displacement $\eta(x,z)$ is defined as the distance the isopycnal is displaced from its far upstream value. The left and right boundaries are given by $x = \pm L$ Reprinted with permission from Soontiens, N., M. Stastna, M. L. Waite (2013). Trapped internal waves over topography: Non-Boussinesq effects, symmetry breaking and downstream recovery jumps. *Phys. Fluids 25*, 066602. Copyright 2013, American Institute of Physics.

Boussinesq with Vertically Varying Background Current

This section outlines the derivation of the DJL equation for a Boussinesq fluid with a vertically varying background velocity $U(z)$. Part of this derivation has been presented by Soontiens et al. (2010), but the details are expanded upon here.

The equations governing an inviscid, incompressible, stratified fluid under the Boussinesq approximation in two dimensions are

$$u_t + uu_x + wu_z = -\frac{p_x}{\rho_0}, \tag{2.4a}$$

$$w_t + uw_x + ww_z = -\frac{p_z}{\rho_0} - \frac{\rho g}{\rho_0}, \tag{2.4b}$$

$$\rho_t + u\rho_x + w\rho_z = 0, \tag{2.4c}$$

$$u_x + w_z = 0, \tag{2.4d}$$

where u and w are the horizontal and vertical velocities respectively, p is the pressure, ρ is the density, ρ_0 is a constant reference density, g is the acceleration due to gravity, and

subscripts denote partial derivatives. Equations (2.4a) and (2.4b) describe the conservation of momentum in the horizontal and vertical directions respectively. Equation (2.4c) is called the energy equation since it describes the conservation of internal energy with a linear equation of state applied (Kundu and Cohen, 2008). Finally, (2.4d) is called the continuity equation which describes the conservation of mass. The fluid extends over an infinite domain in x.

Since the fluid is subject to a background current $U(z)$, the velocity fields can be decomposed as

$$u(x,z,t) = U(z) + \tilde{u}(x,z,t),$$
$$w(x,z,t) = \tilde{w}(x,z,t),$$

where $\tilde{u}(x,z,t)$, $\tilde{w}(x,z,t)$ are the perturbed parts of the flow. This substitution results in the following set of equations:

$$\tilde{u}_t + (\tilde{u} + U(z))\,\tilde{u}_x + \tilde{w}\,(U'(z) + \tilde{u}_z) = -\frac{p_x}{\rho_0}, \tag{2.5a}$$
$$\tilde{w}_t + (\tilde{u} + U(z))\,\tilde{w}_x + \tilde{w}\tilde{w}_z = -\frac{p_z}{\rho_0} - \frac{\rho g}{\rho_0}, \tag{2.5b}$$
$$\rho_t + (\tilde{u} + U(z))\,\rho_x + \tilde{w}\rho_z = 0, \tag{2.5c}$$
$$\tilde{u}_x + \tilde{w}_z = 0. \tag{2.5d}$$

From (2.5d), one can define a streamfuction $(\tilde{u}, \tilde{w}) = (\psi_z, -\psi_x)$. In addition, we will introduce a background streamfunction $\psi^b(z) = \int U(s)\mathrm{d}s$ so that $\psi^{b\prime}(z) = U(z)$ where the prime denotes differentiation with respect to z. This formulation leads to a total streamfunction given by

$$\psi^T(x,z) = \psi^b(z) + \psi(x,z).$$

Now, the steady-state version of (2.5c) is

$$J\left(\rho, \psi^T\right) = 0,$$

where $J(a,b) = a_x b_z - a_z b_x$ is the Jacobian operator. A few interesting properties of the Jacobian operator will be used in the following derivations. Note that for a general f, g, and u

$$\begin{aligned} J(f(u)g,u) &= \left[f_u(u)u_x g + f(u)g_x\right]u_z - \left[f_u(u)u_z g + f(u)g_z\right]u_x \\ &= f(u)\left[g_x u_z - g_z u_x\right] \\ &= f(u)J(g,u). \end{aligned} \tag{2.6}$$

Additionally,

$$\begin{aligned} J(g, f(u)) &= g_x f_u(u) u_z - g_z f_u(u) u_x \\ &= f_u(u) J(g, u) \\ &= J(g f_u(u), u). \end{aligned} \tag{2.7}$$

These results will be applied several times in these derivations.

Assuming that all streamlines connect to a known upstream state, the density takes the form $\rho(x, z) = \bar{\rho}(z - \eta)$, where $\bar{\rho}(z)$ is the upstream density profile and $\eta(x, z)$ is the isopycnal displacement (a valid assumption when the upstream state remains unchanged and there are no instances of wave overturning), one can show that

$$J\left(\rho, \psi^T\right) = \bar{\rho}'(z - \eta) J\left(z - \eta, \psi^T\right) = 0.$$

The upstream density profile $\bar{\rho}(z)$ is stable and so $\bar{\rho}'(z) \geq 0$. Since the fluid is stratified $\bar{\rho}'(z - \eta) \neq 0$ everywhere so $J\left(z - \eta, \psi^T\right) = 0$ and thus

$$\psi^T(x, z) = F(z - \eta).$$

Also, considering the behaviour as $x \to -\infty$, we have $\eta \to 0, (u, w) \to (U(z), 0)$ and $\psi^T \to \psi^b(z)$. Hence

$$F(z) = \psi^b(z),$$

and

$$\psi^T(x, z) = \psi^b(z - \eta).$$

Now, assuming a steady state, one can take the curl of the momentum equations (2.5a) and (2.5b) and substitute the streamfunction to obtain

$$\begin{aligned} &\psi^T_{zz}\psi_{zx} + \psi^T_z \psi_{zzx} - \psi_{xz}\psi^T_{zz} - \psi_x \psi^T_{zzz} \\ &- \left(-\psi^T_{zx}\psi_{xx} - \psi^T_z \psi_{xxx} + \psi_{xx}\psi_{xz} + \psi_x \psi_{xxz}\right) = \frac{\rho_x g}{\rho_0}, \end{aligned}$$

which, after simplification, leads to

$$J\left(\nabla^2 \psi^T, \psi^T\right) + J\left(\frac{gz}{\rho_0}, \rho\right) = 0. \tag{2.8}$$

Let $\sigma^T = \nabla^2 \psi^T$, which expands to

$$\sigma^T = U'(z - \eta)\left(\eta_x^2 + (1 - \eta_z)^2\right) - U(z - \eta)\nabla^2 \eta. \tag{2.9}$$

Thus, (2.8) can be written as a vorticity equation:

$$J\left(\sigma^T, \psi^T\right) + J\left(\frac{gz}{\rho_0}, \rho\right) = 0. \tag{2.10}$$

Next, each term in (2.10) can be simplified. First, working with the $J\left(\frac{gz}{\rho_0}, \rho\right)$ term gives

$$\begin{aligned} J\left(\frac{gz}{\rho_0}, \rho\right) &= J\left(\frac{gz}{\rho_0}, \bar{\rho}(z-\eta)\right) \\ &= J\left(\bar{\rho}'(z-\eta)\frac{gz}{\rho_0}, z-\eta\right) \\ &= J\left(\frac{\bar{\rho}'(z-\eta)g}{\rho_0}\left(z-\eta\right), z-\eta\right) + J\left(\frac{\bar{\rho}'(z-\eta)g}{\rho_0}\eta, z-\eta\right) \\ &= J\left(\bar{\rho}'(z-\eta)\frac{g\eta}{\rho_0}, z-\eta\right). \end{aligned}$$

Next, working with $J\left(\sigma^T, \psi^T\right)$ and noting that $\psi^{b'}(z-\eta) = U(z-\eta)$ we have

$$\begin{aligned} J\left(\sigma^T, \psi^T\right) &= J\left(\sigma^T, \psi^b\left(z-\eta\right)\right) \\ &= J\left(U(z-\eta)\sigma^T, z-\eta\right) \end{aligned}$$

After the appropriate substitutions (2.10) becomes

$$J\left(U(z-\eta)\sigma^T + \frac{g}{\rho_0}\bar{\rho}'\left(z-\eta\right)\eta, z-\eta\right) = 0,$$

or

$$U(z-\eta)\sigma^T + \frac{g}{\rho_0}\bar{\rho}'(z-\eta)\eta = G(z-\eta)$$

where $G(\cdot)$ is a function with continuous partial derivatives.

Considering the upstream behaviour, as $x \to -\infty$, it follows that $\eta \to 0, \eta_x \to 0, \eta_z \to 0, \sigma^T \to U'(z)$. So $G\left(z\right) = U'(z)U(z)$ and so

$$U(z-\eta)\sigma^T + \frac{g}{\rho_0}\bar{\rho}'(z-\eta)\eta = U'(z-\eta)U(z-\eta).$$

After substituting (2.9) for σ^T the result is

$$U(z-\eta)\left[U'(z-\eta)\left(\eta_x^2+(1-\eta_z)^2\right)-U(z-\eta)\nabla^2\eta\right]+\frac{g}{\rho_0}\bar{\rho}'(z-\eta)\eta=U'(z-\eta)U(z-\eta).$$

Rearranging yields

$$\nabla^2\eta+\frac{U'(z-\eta)}{U(z-\eta)}\left[1-\left(\eta_x^2+(1-\eta_z)^2\right)\right]-\frac{g\bar{\rho}'(z-\eta)}{\rho_0U^2(z-\eta)}\eta=0.$$

Finally, after substituting the squared buoyancy frequency from (2.2)

$$\nabla^2\eta+\frac{U'(z-\eta)}{U(z-\eta)}\left[1-\left(\eta_x^2+(1-\eta_z)^2\right)\right]+\frac{N_B^2(z-\eta)}{U^2(z-\eta)}\eta=0. \tag{2.11}$$

Equation (2.11) is the DJL equation for a Boussinesq fluid with a non-constant background current. The appropriate boundary conditions are the same as those given in (2.1).

Non-Boussinesq with Constant Background Current

This section outlines the derivation of the DJL equation for a non-Boussinesq fluid with constant background velocity U_0. The derivation follows closely with that presented above, with a considerable amount of simplification due to the constant background current. Nonetheless, care must be taken when dealing with the non-Boussinesq description of the momentum equations. Part of this derivation has been presented by Soontiens et al. (2013b), but more details are included here.

The derivation begins with a presentation of the steady-state equations for a two-dimensional, inviscid, incompressible fluid:

$$\rho(uu_x+wu_z)=-p_x, \tag{2.12a}$$
$$\rho(uw_x+ww_z)=-p_z-\rho g, \tag{2.12b}$$
$$u\rho_x+w\rho_z=0, \tag{2.12c}$$
$$u_x+w_z=0, \tag{2.12d}$$

where u is the horizontal velocity, w is the vertical velocity, ρ is the density, p is the pressure and g is the acceleration due to gravity. In this set of equations the effects of compressibility are neglected to arrive at the momentum equations (2.12a) and (2.12b) , the energy equation (2.12c), and the continuity equation (2.12d). As discussed in Kundu and Cohen (2008), the effects of compressibility can be neglected in flows with a low Mach

number (flow speeds are much smaller than the speed of sound) and in flows with a small ratio of vertical to horizontal length scales. This is a standard technique used in studies of internal waves applied to ocean or lake stratifications and has been used in previous theoretical investigations of non-Boussinesq internal waves (see e.g. Lamb and Wan, 1998). Since effects of compressibility are neglected, the main non-Boussinesq effect is manifested in the momentum equations. This is appropriate for the types of flows applicable to ocean or lake settings considered here.

From the continuity equation (2.12d), one can define a streamfunction ψ so that $u = \psi_z$ and $w = -\psi_x$ which allows (2.12c) to be written as

$$J(\rho, \psi) = 0.$$

The density takes the form $\rho(x, z) = \bar{\rho}(z-\eta)$, where $\eta(x, z)$ is the isopycnal displacement and $\bar{\rho}(z)$ is the upstream density profile, which leads to

$$\begin{aligned} 0 &= J(\rho, \psi) \\ &= J(\ \bar{\rho}(z-\eta), \psi) \\ &= \bar{\rho}'(z-\eta) J(z-\eta, \psi). \end{aligned}$$

In the same manner as the previous derivation, this implies that $J(z-\eta, \psi) = 0$, which in turn gives ψ can as

$$\psi = F(z-\eta),$$

where $F(\cdot)$ is an arbitrary function. Considering far upstream behaviour, $\psi \to U_0 z$ and $\eta \to 0$ as $x \to -\infty$ gives $F(z) = U_0 z$. This implies

$$\psi = U_0(z-\eta).$$

Next, the momentum equations (2.12a) and (2.12b) can be rewritten in terms of ψ:

$$\begin{aligned} \rho(\psi_z \psi_{xz} - \psi_x \psi_{zz}) &= -p_x, \\ \rho(-\psi_z \psi_{xx} + \psi_x \psi_{xz}) &= -p_z - \rho g. \end{aligned}$$

Taking the curl of these equations eliminates the pressure terms which results in

$$\rho J(\nabla^2 \psi, \psi) + \rho_x J(\psi_x, \psi) + \rho_z J(\psi_z, \psi) + J(gz, \rho) = 0. \tag{2.13}$$

Each term in (2.13) can be rewritten in the form $J(\cdot, z-\eta)$. Beginning with the first term $\rho J(\nabla^2 \psi, \psi)$, notice that

$$\begin{aligned} J(U_0 \rho \nabla^2 \psi, z-\eta) &= J(U_0 \bar{\rho}(z-\eta) \nabla^2 \psi, z-\eta) \\ &= \bar{\rho}(z-\eta) J(\nabla^2 \psi, \psi). \end{aligned}$$

Thus, it has been shown that the first term can be written as

$$\rho J(\nabla^2\psi,\psi) = J(U_0\bar{\rho}(z-\eta)\nabla^2\psi, z-\eta). \tag{2.14}$$

In a similar manner to the previous derivation the term $J(gz,\rho)$ can be written as

$$J(gz,\rho) = J(g\bar{\rho}'(z-\eta)\eta, z-\eta). \tag{2.15}$$

Next, working with the term $\rho_x J(\psi_x,\psi)$ gives

$$\begin{aligned}\rho_x J(\psi_x,\psi) &= \bar{\rho}'(z-\eta)(-\eta_x)J(-U_0\eta_x, U_0(z-\eta)) \\ &= U_0^2\bar{\rho}'(z-\eta)\eta_x J(\eta_x, z-\eta).\end{aligned}$$

Consider that

$$\begin{aligned}J(\eta_x^2, z-\eta) &= 2\eta_x\eta_{xx}(1-\eta_z) - 2\eta_x\eta_{xz}(-\eta_x) \\ &= 2\eta_x J(\eta_x, z-\eta),\end{aligned}$$

which gives

$$\rho_x J(\psi_x,\psi) = \frac{U_0^2\bar{\rho}'(z-\eta)}{2} J(\eta_x^2, z-\eta).$$

Similar to previous steps, the $\bar{\rho}'(z-\eta)$ can be brought inside the Jacobian operator to arrive at

$$\rho_x J(\psi_x,\psi) = J\left(\frac{U_0^2\bar{\rho}'(z-\eta)}{2}\eta_x^2, z-\eta\right). \tag{2.16}$$

Finally, the last term is treated in a similar fashion:

$$\rho_z J(\psi_z,\psi) = U_0^2\bar{\rho}'(z-\eta)(1-\eta_z)J(1-\eta_z, z-\eta).$$

Considering

$$\begin{aligned}J(\eta_z(\eta_z-2), z-\eta) &= \left[\eta_{zx}(\eta_z-2) + \eta_z(\eta_{zx})\right](1-\eta_z) \\ &\quad - \left[\eta_{zz}(\eta_z-2) + \eta_z(\eta_{zz})\right](-\eta_x) \\ &= \left[2\eta_{zx}\eta_z - 2\eta_{zx}\right](1-\eta_z) - \left[2\eta_{zz}\eta_z - 2\eta_{zz}\right](-\eta_x) \\ &= 2\eta_{xz}(\eta_z-1)(1-\eta_z) - 2\eta_{zz}(\eta_z-1)(-\eta_x) \\ &= -2(1-\eta_z)J(\eta_z, z-\eta) \\ &= 2(1-\eta_z)J(1-\eta_z, z-\eta),\end{aligned}$$

it follows that

$$\rho_z J(\psi_z, \psi) = \frac{U_0^2 \bar{\rho}'(z-\eta)}{2} J(\eta_z(\eta_z - 2), z - \eta),$$

which leads to

$$\rho_z J(\psi_z, \psi) = J\left(\frac{U_0^2 \bar{\rho}'(z-\eta)}{2} \eta_z(\eta_z - 2), z - \eta\right), \tag{2.17}$$

in a similar manner to the previous steps.

Now, equations (2.14), (2.15), (2.16), and (2.17) can be substituted into (2.13) to obtain

$$J\left(U_0 \bar{\rho}(z-\eta)\nabla^2\psi + \frac{U_0^2 \bar{\rho}'(z-\eta)}{2}\eta_x^2 + \frac{U_0^2 \bar{\rho}'(z-\eta)}{2}\eta_z(\eta_z - 2) + g\bar{\rho}'(z-\eta)\eta, z - \eta\right) = 0.$$

Substituting $\nabla^2\psi = -U_0\nabla^2\eta$ and applying Jacobian properties gives

$$-U_0^2 \bar{\rho}(z-\eta)\nabla^2\eta + \frac{U_0^2 \bar{\rho}'(z-\eta)}{2}\eta_x^2 + \frac{U_0^2 \bar{\rho}'(z-\eta)}{2}\eta_z(\eta_z - 2) + g\bar{\rho}'(z-\eta)\eta = G(z-\eta), \tag{2.18}$$

where $G(\cdot)$ is an arbitrary function with continuous partial derivatives. Considering the far upstream behaviour, $\eta \to 0$ as $x \to -\infty$ gives $G(z) = 0$. Finally rearranging (2.18) produces

$$\nabla^2\eta + \frac{N_{NB}^2(z-\eta)}{U_0^2}\eta + \frac{N_{NB}^2(z-\eta)}{2g}\left[\eta_x^2 + \eta_z(\eta_z - 2)\right] = 0, \tag{2.19}$$

where

$$N_{NB}^2(z) = -\frac{g}{\bar{\rho}(z)}\frac{d}{dz}\bar{\rho}(z). \tag{2.20}$$

Equation (2.19) is the non-Boussinesq form of the DJL equation for a fluid with a constant background current U_0. The appropriate boundary conditions are the same as those given in (2.1).

Conjugate Flows

The derivations of the DJL equations presented above require that the upstream state is not affected by the wave disturbance or, in other words, there are no upstream propagating modes. Flows of this nature are called supercritical, although there has been some ambiguity in the literature on how to define this condition mathematically, especially in a nonlinear framework for a continuously stratified fluid. Traditionally, a supercritical flow

has been defined in terms of the Froude number, the ratio of the background speed to a linear wave speed defined as

$$F_r = \frac{U_0}{c_{lw}}.$$

In continuously stratified flows there are many wave modes and speeds, so c_{lw} is usually taken to represent the speed of the first linear mode (the fastest travelling mode). A flow is said to be supercritical when $F_r > 1$ and subcritical when $F_r < 1$.

This definition of criticality does not always exclude the formation of upstream propagating modes when applied to large-amplitude waves for which nonlinear effects are important. Results from Stastna and Peltier (2005) showed that a more appropriate definition is framed in terms of the conjugate flow speed, c_j, which is derived from a theory that treats nonlinearity exactly but neglects dispersion. From this perspective, the flow is subcritical when $U_0 < c_j$ and supercritical when $U_0 > c_j$, a necessary condition for flows with no upstream propagating modes.

For continuously stratified flows Lamb and Wan (1998) have presented the conjugate flow theory for both Boussinesq and non-Boussinesq fluids with a general density stratification. The equations which represent the conjugate flows in these cases are described by an eigenvalue problem, with eigenfunction $\eta_c(z)$ and eigenvalue c. For the Boussinesq case, the problem is described by

$$\eta_c'' + \frac{N_B^2(z-\eta_c)}{c^2}\eta_c = 0, \tag{2.21a}$$

$$\eta_c(0) = \eta_c(H) = 0. \tag{2.21b}$$

This problem is solved using a shooting method seeded with the linear long wave speed c_{lw} as an initial guess, and an auxiliary condition that describes the conservation of momentum flux:

$$T(\eta_c'(0)) = \int_0^H \eta_c'^3(z)dz = 0.$$

The auxiliary condition narrows the solution set to determine the appropriate conjugate flow speed c (the equation is nonlinear so there may be multiple solutions). The details of the shooting method are described by Lamb and Wan (1998).

A similar technique is used to solve for the non-Boussinesq conjugate flow speed, which is described by the following equation with auxiliary condition (Lamb and Wan, 1998):

$$\eta_c'' + \frac{N_{NB}^2(z-\eta_c)}{c^2}\eta_c + \frac{N_{NB}^2(z-\eta_c)}{2g}\eta_c'(\eta_c' - 2) = 0, \tag{2.22a}$$

$$\eta_c(0) = \eta_c(H) = 0, \tag{2.22b}$$

with auxiliary condition

$$T(\eta_c'(0)) = \int_0^H \bar{\rho}\,(z - \eta_c(z))\,\eta_c'^3(z)dz = 0.$$

Note that both of the conjugate flow equations have a similar form to their DJL counterparts, except with the x dependency removed. This is in accord with the use of conjugate flow theory to describe two horizontally uniform (flat) states separated by a wave of permanent form. The conjugate flow speed is the propagation speed of the disturbance connecting these two horizontally uniform states. Theoretically, this state is produced in the limit as the wave energy extends to infinity for a flat solitary wave (Lamb and Wan, 1998).

2.2.2 Numerical Methods

This section outlines several important numerical tools that have been fundamental in deriving the results presented in this chapter. First, an overview of the techniques used to solve the DJL equation is provided, followed by a detailed description of two ways to treat the lower boundary condition for this problem. Next, a brief outline of a solver for the Euler equations of motion under the Boussinesq approximation (IGW) is provided. This model is used to compare simulation results with the DJL solutions.

DJL Solver

Even the simplest form of the DJL equation can be difficult to solve analytically (indeed for non-constant buoyancy frequency we are not aware of any analytical solutions), hence there is a need for numerical methods in deriving solutions. The difficulties arise from the strongly nonlinear terms of equations (2.1), (2.11), (2.19), which make the problem of finding analytical solutions intractable. Furthermore, boundary conditions can pose an additional complication, as is the case with using the DJL equation to study flow over topography. For simplicity, the numerics will be discussed in terms of equation (2.1), although both of the numerical methods can be modified to handle equations (2.11) and (2.19) in a straightforward manner.

Both of the numerical methods outlined below use a pseudo-time stepping algorithm for finding solutions of (2.1). The problem is treated as the forced heat equation:

$$\frac{\partial \phi}{\partial s} = \nabla^2 \phi + \frac{N^2(z-\phi)}{U_0^2}\phi, \tag{2.23}$$

where ϕ represents the numerical solution of η. This equation is integrated forward in pseudo-time s until a steady state is achieved.

The pseudo-time stepping algorithm treats the Laplacian term implicitly and the nonlinear terms explicitly as follows:

$$\left(I - \Delta s \nabla^2\right) \phi^{n+1} = \phi^n + \Delta s R(\phi^n), \tag{2.24}$$

where ϕ^n represents the numerical solution of ϕ at the n^{th} pseudo-time step, and

$$R(\phi^n) = \frac{N^2(z - \phi^n)}{U_0^2}\phi^n.$$

In practice, $R(\cdot)$ can be modified to include the other nonlinear terms in (2.11) and (2.19). The integration is initialized with

$$\phi^0(x, z) = h(x)\frac{z - H}{h(x) - H},$$

and is terminated when successive iterations achieve a point-wise difference of less than 10^{-6} m (other criteria are possible, but we found this choice to be effective).

One of the difficulties in solving (2.1) is in the proper representation of the lower boundary condition. The details of the spatial discretization and implementation of the lower boundary condition for both methods is provided below. The first method maps the physical domain to a rectangular computational domain so that the lower boundary can be implemented in an exact manner. The second method solves the problem on a rectangular domain with embedded topography.

Another important aspect of the DJL solver is solution continuation, that is, using waves computed from a different set of parameters as an initial guess. This method allows for increased rates of convergence, since the initial guess is expected to be relatively close to the desired solution for moderate changes in parameter values. However, it should be noted that the nonlinearity inherent in the DJL equations can, at times, produce very different solutions, even for similar parameter values. In fact, with the solution continuation technique, multiple states for the same set of parameter values have been discovered, and this is described in detail below (Soontiens et al., 2010).

Additionally, the continuation technique is used to find solutions on larger grid sizes. A solution is first iterated to convergence on a coarse grid and then interpolated to a finer grid. The interpolant is used as an initial condition for iteration on the fine grid. This process contributes to increased convergence rates for large grids. The solution continuation technique is mainly used in conjunction with the mapped computations, which was the dominant method used in the experiments with shear background currents and hysteresis loops.

Mapped Method

The mapped method is based on an article by Soontiens et al. (2010) which examines DJL solutions for shear background currents. This method maps the physical domain $[-L, L] \times [h(x), H]$ to a rectangular computational domain $[-1, 1] \times [-1, 1]$. The mapping is given by

$$\xi = \frac{x}{L}, \quad \zeta = 2\frac{z - h(x)}{H - h(x)} - 1. \tag{2.25}$$

In this definition, ξ, ζ are in the computational domain and x, z are in the physical domain.

While this mapping produces a complicated expression for the Laplacian operator, the use of derivative matrices yields a relatively straightforward calculation. Computationally, the derivative matrices D_x and D_z are constructed by

$$D_x = \frac{1}{L}D_\xi + \frac{\partial \zeta}{\partial x}D_\zeta, \quad D_z = \frac{\partial \zeta}{\partial z}D_\zeta,$$

where D_ξ and D_ζ are the derivative matrices from the computational domain. A Chebyshev discretization is used in both directions, so D_ξ and D_ζ are easily constructed with Chebyshev differentiation matrices and Kronecker delta products as described by Trefethen (2000). The Laplacian operator is then easily constructed as

$$\nabla^2 \to L = D_x^2 + D_z^2.$$

Unfortunately, the Chebyshev representation of the Laplacian operator with mapping is full, which makes inversion of the $I - \Delta s \nabla^2$ matrix in (2.24) very expensive. A more efficient numerical method is desired and one such method is presented below. More details on the efficiency of the mapped method are provided by Soontiens et al. (2010). A detailed comparison of the mapping and embedded methods will be carried out in Subsection 2.3.1.

Embedded Boundary Method

For moderate grid sizes the mapped method is relatively inexpensive, however, large grid sizes quickly run up against memory requirements on typical workstations. A more efficient method that scales well with grid size is desired. This is accomplished by adapting a method used by Laprise and Peltier (1989) to model steady atmospheric flows over bell-shaped topography. Several modifications to their method need to be implemented since the authors considered a fluid with constant buoyancy frequency and a radiation upper boundary condition. The method and modifications are discussed briefly below.

The problem is solved on a rectangular domain $[-L, L] \times [h_b, H]$ with the topography, $z = h(x)$, embedded into the domain as depicted in Figure 2.1. In this context, h_b represents the bottom of the domain, which is $h_b = 0$ in the case of elevation topography and $h_b = -|h_0|$ in the case of depression topography, where h_0 is the amplitude of the topography.

The desired topographic boundary condition, $\eta(x, z = h(x)) = h(x)$ is achieved by iteratively setting an appropriate condition on $\eta(x, z = h_b)$ using the following algorithm,

$$\eta^{N+1}(x, z = h_b) = \eta^N(x, z = h_b) - \mathrm{err}^N,$$

$$\mathrm{err}^N = \eta^N(x, z = h(x)) - h(x),$$

where η^N represents $\eta(x, z)$ at the N^{th} iteration. The term err^N represents the error between $\eta^N(x, z = h(x))$ and the actual boundary condition. Additionally, $\eta^N(x, z = h(x))$ is calculated with a cubic spline interpolation. The algorithm is initialized with

$$\eta^0(x, z = h_b) = h(x),$$

and is terminated when a suitable error on the lower boundary condition is achieved (typically up to $10^{-7}H$).

This iterative algorithm for the lower boundary condition is combined with a Chebyshev decomposition in z and a Fourier decomposition in x, implying periodic boundary conditions in x. Note that the results produce $\eta \approx 0$ at $x = \pm L$ so that the horizontal boundary conditions in (2.1) are satisfied. This is the pseudo-time stepping algorithm is initialized with a wave that has zero isopycnal displacement at the horizontal boundaries. The Fourier decomposition yields the following equation, which is solved for each wave number k:

$$\left(\left(1 + \Delta s k^2\right) I - \Delta s D_{zz}\right) \widehat{\phi}^{n+1} = \widehat{\phi}^n + \Delta s \widehat{R(\phi^n)}, \tag{2.26}$$

where the hat symbol denotes a horizontal Fourier transform and D_{zz} represents the second derivative matrix in the vertical direction. With the Chebyshev discretization, D_{zz} can be built in a similar fashion as the mapped method. Computationally, this method is more efficient than the mapped method because the derivative matrices are one dimensional, and hence much smaller and more easily inverted.

Internal Gravity Wave Solver (IGW)

It is important to check the validity of the results produced with the DJL theory. This is accomplished through comparisons with results from numerical simulations of the time-dependent Euler equations of motion (2.4) using a model called the Internal Gravity Wave

solver (IGW) by Lamb (1994). The simulations are carried out from rest, with adaptive time-stepping until a steady state is achieved, at which point the output is compared to the results of the DJL theory.

The IGW model employs a second-order projection technique with variable time-stepping in order to integrate the fully nonlinear, non-hydrostatic, time-dependent Euler equations of motion (see Bell and Marcus (1992) and Lamb (1994) for details). The model uses a terrain-following vertical coordinate system with no normal flow conditions at the upper and lower boundaries, and inflow/outflow conditions at the left/right boundaries. The flow is accelerated from rest up to a desired background current $U(z)$. Experiments with different acceleration rates are conducted in order to reproduce the multiple states observed in the DJL results for a specified $U(z)$.

2.2.3 Description of Experiments

This section outlines the types of experiments that have been conducted using steady-state theory and, in some cases, time-dependent numerical simulations. A description of the types of problems that will be examined using this theory is provided, with details on the fluid properties and parameters.

Fluid Properties and Parameters

Most of the experiments presented consider steady flow of a density stratified fluid over topography in the supercritical regime (some subcritical cases are also considered). Several cases with various bottom topographies and density stratifications are examined. The general form of the bottom topography and density stratification are given by

$$h(x) = h_0 \mathrm{sech}^2\left(\frac{x}{w_D}\right),$$

$$\bar{\rho}(z) = \rho_0\left(1 - \Delta\rho \tanh\left(\frac{z - z_0}{d_0}\right)\right).$$

In these definitions, h_0 is the amplitude of the topography and w_D is a measure of the topographic width. The density profile represents a pycnocline stratification, where ρ_0 is the constant background density, $\Delta\rho$ describes the strength of the stratification, z_0 is the pycnocline height, and d_0 is a measure of the pycnocline thickness. Several variations on the parameters defining the density stratification and bottom topography are examined.

Some of these changes include topographic polarity (elevation and depression, or hill and valley), location of the centre of the upstream pycnocline, and stratification strength. The thickness of the pycnocline and the constant reference density are the same in each case with $d_0 = 0.1H$ and $\rho_0 = 1$.

In each case, the physical domain spans $x = [-L, L]$ and $z = [h(x), H]$. Some common parameters between cases are $\rho_0 = 1$, $d_0 = 0.1H$, and $w_D = 4.5H$. In addition, the amplitude of the topography is generally taken as $|h_0| = 0.1H$, with $h_0 > 0$ for elevation topography and $h_0 < 0$ for depression topography. Other parameters are varied and will be stated on a case by case basis. Note that the results from Soontiens et al. (2010) used depression topography defined as

$$h(x) = h_0 \text{sech}\left(\frac{x}{w_D}\right),$$

where $w_D = 1.25H$, which is similar to the topography profile stated earlier.

The results are presented in terms of scaled quantities. Quantities that measure distances will be scaled by the water column depth H. The velocities will be scaled by the conjugate flow speed c_j. In addition, the conjugate flow speed is usually presented in terms the linear long wave speed c_{lw}. The conjugate flow speed is affected by the water column depth and the properties of the density stratification and is calculated using a shooting method as outlined by Lamb and Wan (1998). This method treats the eigenvalue problem (2.21) similar to an initial value problem with $\eta_c(0) = 0$, and $\eta_c'(0) = d$. The conjugate flow equation is solved using several values of c and d to find profiles of $\eta_c(z)$. Only mode-one solutions and profiles with $\eta(H) = 0$ are considered. The auxiliary condition narrows the solution set. The shooting method is seeded with the linear long wave speed c_{lw}. This necessitates first finding the linear long wave speed, which is a relatively straightforward calculation.

Shear Background Currents and Multiple States

Multiple states and hysteresis loops have been discovered in cases with vertically varying background currents. Recall, the DJL equation under the Boussinesq approximation with vertically varying background current $U(z)$ is given by equation (2.11). Consider a shear background prescribed by

$$U(z) = U_0 + \frac{\Delta U}{2} \tanh\left(\frac{z - z_s}{d_s}\right), \tag{2.27}$$

where ΔU describes the strength of the shear, z_s indicates the shear level, and d_s describes the shear level thickness. With this form of velocity, a change in the location of the shear layer, z_s, will modify the average background current, unless U_0 is chosen appropriately. To keep the depth-averaged velocity, U_{avg}, the same between simulations U_0 is chosen as

$$U_0 = U_{avg} - \frac{\Delta U d_s}{2H}\left(\ln\left(\cosh\left(\frac{H - z_s}{d_s}\right)\right) - \ln\left(\cosh\left(\frac{-z_s}{d_s}\right)\right)\right).$$

Notice that if $z_s = \frac{H}{2}$ then $U_0 = U_{avg}$. This choice of z_s is used for most simulations, with the exception of a simulation with the shear current centered at $z_s = H$. The shear level thickness is set to $d_s = 0.1H$ in all simulations.

With the use of the solution continuation technique, multiple solutions to the DJL equation with non-constant background current can be discovered for a given density stratification and velocity profile. The average background speed U_0 is fixed, while the strength of the shear ΔU is modified in the solver. For certain parameter regimes, waves with very different properties are generated depending on whether ΔU was increased or decreased in the solver.

A similar technique is used to find multiple states with constant background currents and narrow topography.

Boussinesq and Non-Boussinesq

In addition to examining changes in the density stratification and topography, this chapter also considers the effect of making the Boussinesq approximation. To review, the DJL equation takes on a different form when the Boussinesq approximation is made. For reference, equations (2.1) and (2.2) describe the Boussinesq form of the DJL equation, whereas (2.19) and (2.20) describe the non-Boussinesq form, both with constant background speed U_0.

Generalizing the problem from a Boussinesq fluid to a non-Boussinesq fluid results in two changes in the mathematical description: 1) a change in the definition of the buoyancy frequency and 2) additional terms in the DJL equation due to the non-Boussinesq effects. To determine the effect of each of these changes, the DJL equation is solved in three circumstances for a given density profile and topographic shape: a) solve the non-Boussinesq equation with buoyancy frequency $N_{NB}(z)$, b) solve the Boussinesq equation with buoyancy frequency $N_{NB}(z)$, and c) solve the Boussinesq equation with buoyancy frequency $N_B(z)$. Each of these problems is solved for several background speeds U_0. Comparisons

between the first two problems indicate the effect of the non-Boussinesq terms, while comparisons between the last two problems determine the effect of the revised definition of buoyancy frequency. Comparisons between the first and last problems reveal the overall effects of the non-Boussinesq condition. Several density stratifications and density jumps, $\Delta\rho$ are considered.

2.3 Results

The following results have been published in part in two separate journal articles by Soontiens et al. (2010) and Soontiens et al. (2013b). The results on hysteresis, shear currents, and vortex cores have been presented in Soontiens et al. (2010). The results on comparisons between the numerical methods, elevation and depression topography, Boussinesq and non-Boussinesq comparisons, and subcritical flows are presented in Soontiens et al. (2013b) and are expanded upon here. Some extra details are included here for completeness. Copyright permission letters have been included at the end of this thesis.

Several situations have been investigated, beginning with a comparison of the two numerical methods for DJL solutions. This is followed by an investigation of multiple solutions to the DJL equation for the same flow parameters (this is discussed for cases with shear background currents, as well as varying topographic widths). Next, a study of the conditions which may lead to vortex cores over the waves with depression topography is provided, followed by a discussion of waves generated over elevation and depression topography. The effect of making the Boussinesq approximation is examined by varying the strength of the density stratification. Finally, several time-dependent simulations examine steady states which develop under subcritical flow conditions for which the flow is supercritical somewhere over hill topography.

2.3.1 Comparison of Numerical Methods

In the previous section, two numerical methods for solving the DJL equation were presented: a method involving a mapped domain and a method with an embedded boundary. It was suggested that the embedded boundary method is more computationally efficient, which is discussed further in this section.

Both methods are implemented using a pseudo-time stepping scheme which resembles the forced heat equation (2.23). The biggest expense in both methods is the inversion of the operator acting on ϕ^{n+1} on the left hand side of (2.24).

One of the main differences between the two methods is the numerical representation of the Laplacian operator, ∇^2. The embedded method employs a Fourier transform in x, which leads to an efficient computational form of the Laplacian. In contrast, the mapped method employs a Chebyshev decomposition in both x and z, which when combined with the mapping, leads to a full matrix in the numerical representation of the Laplacian making it difficult to invert. Meanwhile, the embedded method requires an extra iteration over the lower boundary condition which may lead to increased computation times. Nonetheless,

the convergence of the lower boundary condition is relatively quick and the embedded boundary method is generally more efficient.

Several cases are presented with a description of how the computation times scale with grid size. Two types of waves are used: 1) a small-amplitude trapped wave of depression with $U_0 = 1.25c_j$ and 2) a large-amplitude trapped wave of depression with $U_0 = 1.11c_j$. For simplicity, the Boussinesq with constant background speed form of the DJL equation is used. Typically, longer convergence times are observed for the large-amplitude waves. The results from several grid sizes are summarized Figure 2.2.

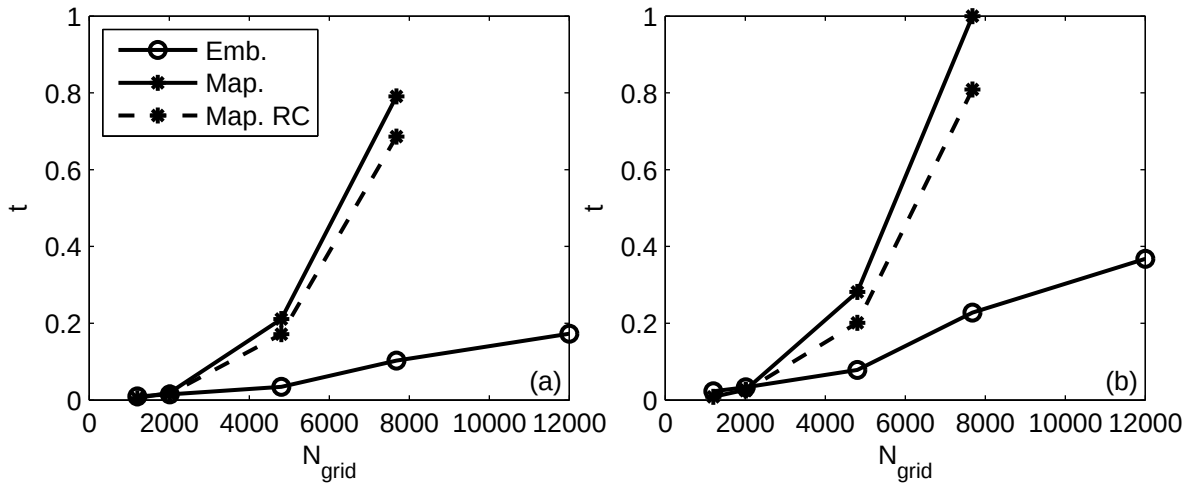

Figure 2.2: A comparison of computation times from the embedded and mapped methods for several grid sizes (N_{grid}) and waves. (a) Results for a small wave with $U_0 = 1.25c_j$ and (b) results for a large wave with $U_0 = 1.11c_j$ are shown. The embedded method is indicated with circles (o) and the mapped method with stars (*). The dashed lines utilized three iterations of resolution continuation (RC) and the solid lines do not. The results are normalized by longest computation time. $N_{grid} = m \times n$ where m and n are the number of grid points in x and z respectively.

For large grid sizes the embedded boundary method clearly outperforms the mapped method. Indeed, the memory requirements of the largest grid made it unfeasible to utilize the mapped method at this resolution on a typical workstation. This plot also highlights the efficiency of resolution continuation for the mapped method, however, resolution continuation acts to hinder the embedded method (not shown in the plot). The use of resolution continuation in the embedded method was inefficient, likely because it is more difficult to find a balance between efficient convergence of the pseudo-time stepping algorithm and the

bottom boundary iterations. Solving the problem over multiple grids makes the balance more difficult to attain. While neither of these methods are fully optimized, it is clear that the embedded method is superior for large grids. Additionally, the current implementation of the mapped method uses a Chebyshev discretization in both directions, leaving the centre of the domain less resolved since Chebyshev points are clustered near the boundaries. This can be overcome through an alternate discretization, as has been explored by Soontiens et al. (2010) for DJL solutions that are symmetric across the topography.

One of the disadvantages of the embedded boundary method is that it enforces periodic boundary conditions in x. Fortunately, for the problems considered here, this requirement coincides with the stated boundary conditions $\eta = 0$ at $x = \pm L$ to reasonable accuracy. However, this implies that asymmetric steady states cannot be discovered using this method, at least in its current framework. This perhaps could be addressed by using a cosine expansion in x. The mapped method can easily be adapted to find asymmetric states by changing the horizontal boundary conditions. This is applied to produce asymmetric steady states using the DJL theory.

2.3.2 Multiple States and Hysteresis

The results of this section have been outlined by Soontiens et al. (2010) and will be reproduced here. First, an overview of the types of trapped waves possible with shear background currents is provided, followed by a discussion of multiple states and hysteresis loops. Comparisons of the steady states are made with numerical simulations of the time-dependent Euler equations. In addition, multiple states are found for constant background currents with varying topography widths. Adapted with permission from Soontiens, N., C. Subich, M. Stastna (2010). Numerical simulation of supercritical trapped internal waves over topography. *Phys. Fluids 22*(11), 116605. Copyright 2010, American Institute of Physics.

The DJL equation is known to yield large-amplitude solutions for certain density stratifications and topographic profiles. An example of such a large wave is displayed in Figure 2.3 (b) where the density contours and velocity field are plotted. This wave was generated with a weak upstream shear current whose profile is displayed in the solid line of Figure 2.3 (a). In contrast, a small wave (Figure 2.3 (c)) is generated by a strong upstream shear current whose profile is given by the dashed line in Figure 2.3 (a). The vertical profiles of the horizontal, upstream velocity shown in Figure 2.3 (a) have the mean current U_0 removed. U_0 is the same value for both waves. Additionally, these waves have been computed with topographic width $w_D = 1.25H$ and the conjugate flow speed is $c_j = 1.17c_{lw}$. An important part of the discussion in this section is the transition between large- and

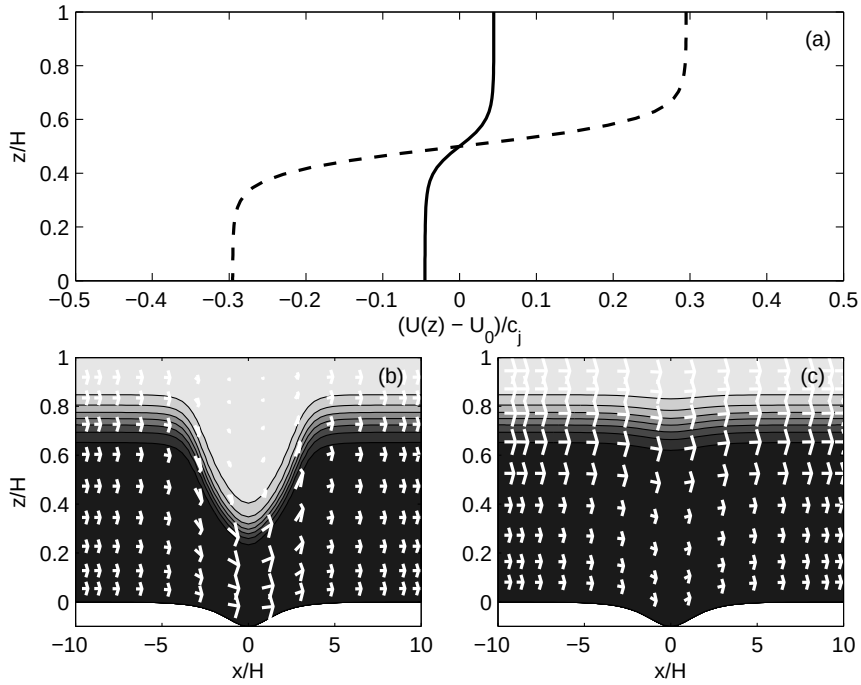

Figure 2.3: Trapped waves for two different shear currents. (a) Upstream velocity profiles; solid (dashed) line corresponds to panel (b) (panel (c)) respectively. (b) Shaded density contours with superimposed velocity field. (c) As in (b) but for a stronger shear. In each case, $U_0 = 1.06c_j$. Reprinted with permission from Soontiens, N., C. Subich, M. Stastna (2010). Numerical simulation of supercritical trapped internal waves over topography. *Phys. Fluids 22*(11), 116605. Copyright 2010, American Institute of Physics.

small-amplitude waves as the shear ΔU changes. Large-amplitude states are expected for small shear values since the bottom currents are stronger for small shears.

In Figure 2.4 (a) the wave amplitude versus mean inflow velocity for four different pycnocline centre heights is shown. In this plot and all plots to follow, the wave amplitude is defined as the maximum value of $|\eta(x, z)|$. For this case the upstream velocity profile is constant and the upstream velocity current is scaled by the conjugate flow speed from the density stratification in Figure 2.3 for ease of comparison. Since the stratification height is different in each case, this also causes a change in the conjugate flow speed between cases. In agreement with the findings of Stastna and Peltier (2005), it can be seen that there is a range of inflow speeds for which large-amplitude waves are obtained. Moreover, at their largest these disturbances displace the pycnocline well below the mid-depth, the

theoretical limit of freely propagating internal solitary waves for the stratification employed when the upstream current has no shear. Even more interestingly, when the pycnocline is centred at the mid-depth (solid line), and no free propagating ISWs would result, we still obtain trapped waves that attain an amplitude that can reach a quarter of the upstream water column depth. As the centre of the pycnocline moves up, both the linear longwave and conjugate flow speeds decrease. This is demonstrated through the linear longwave speed for a two-layer fluid $c = \left(g' \frac{h_1 h_2}{h_1+h_2}\right)^{1/2}$, where $g' = 2g\frac{\rho_2-\rho_1}{\rho_1+\rho_2}$ and h_1, ρ_1, h_2, ρ_2 are the layer depth and density of the upper and lower layers respectively (Helfrich and Melville, 2006). Since Figure 2.4 (a) shows a fixed range of inflow speeds this means that at some point no large trapped waves will be obtained. This is confirmed by the dot-dashed curve, corresponding to $z_0 = 0.8H$. For this curve the trapped waves look much like Figure 2.3 (c), with the largest isopycnal displacement occurring at the topography.

In Figure 2.4 (b) an example of the existence of multiple states, or a hysteresis loop, is displayed for upstream velocity profiles with shear and a stratification with $z_0 = 0.75H$ and $\Delta\rho = 0.02$. The mean upstream current is fixed at $U_0 = 1.06c_j$ but the strength of the shear layer ΔU is varied. It can be seen that as the shear layer strengthens, on the upper branch of solutions, the amplitude slowly decreases until $\Delta U \approx 0.55c_j$. For larger ΔU the wave amplitude decreases much more quickly, and above $\Delta U \approx 0.61c_j$ no large waves can be computed and the maximum isopycnal displacement occurs at the bottom boundary. As ΔU is decreased from $0.8c_j$, along the dashed curve, the waves remain small, with a maximum isopycnal displacement occurring at the bottom boundary, until $\Delta U \approx 0.31c_j$. At this point solutions rapidly jump to the upper branch, with wave amplitudes approaching $0.45H$. The case selected for subsequent comparison with time-dependent simulations is indicated with a vertical dotted line.

It is useful to confirm that the solutions to the steady problem, including both steady states in the case of hysteresis, may be attained in time-dependent simulations. In Figure 2.5 plots of the wave-induced horizontal velocities versus depth at the wave crest are shown. The mean upstream velocity has been subtracted. The DJL (simulation) profiles are shown as solid (dashed) lines, along with the upstream shear currents (dot-dashed line). Figure 2.5 (a) shows the profiles for the small wave in Figure 2.3 (c), while Figure 2.5 (b) shows the profiles for the large wave (also shown in Figure 2.3 (b)). In addition, the multiple states from Figure 2.4 (b) are also shown in the lower panels. The profiles for the small and large wave along the vertical line in Figure 2.4 (b) are shown in Figure 2.5 (c) and (d) respectively. In all cases, the simulation and DJL curves are nearly identical. In IGW simulations, multiple states were produced by varying the rate of acceleration.

In Figure 2.6 we demonstrate the manner in which the flow attains the final steady state

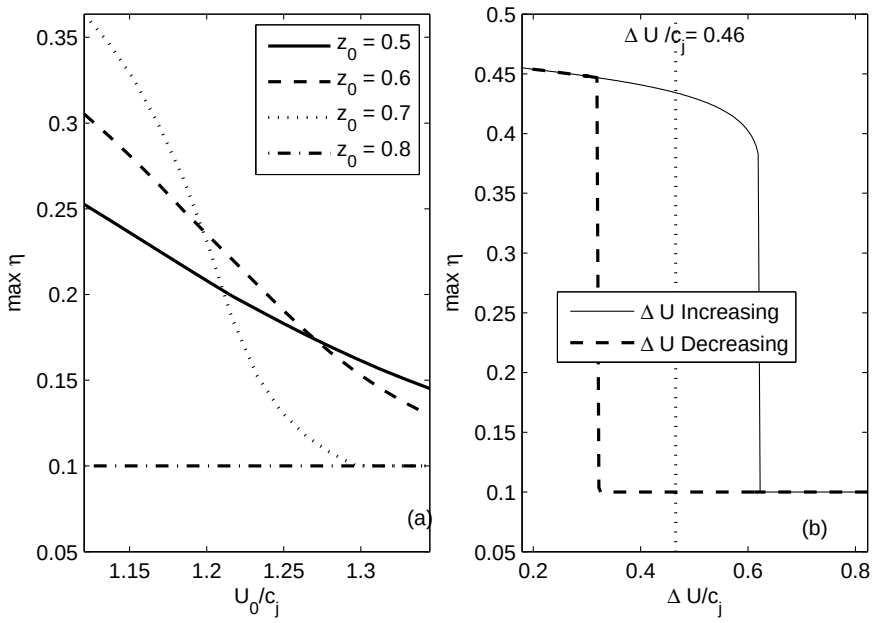

Figure 2.4: (a) Trapped wave amplitude vs U_0 for single pycnocline stratifications with variable pycnocline centre (z_0). (b) Example of multiple steady states, or hysteresis, for upstream shear current $U(z)$ with a fixed mean but varying shear layer strength. For easy comparison, the velocities are scaled by the conjugate flow speed (c_j) from the density stratification in Figure 2.3. The case selected for subsequent comparison with time-dependent simulations is indicated with a vertical dotted line. Adapted with permission from Soontiens, N., C. Subich, M. Stastna (2010). Numerical simulation of supercritical trapped internal waves over topography. *Phys. Fluids 22*(11), 116605. Copyright 2010, American Institute of Physics.

for the large wave in Figure 2.4 (b). The fluid is accelerated over the period $0 < t < 10$ so that the acceleration is not evident in the figure. Figure 2.6 shows a space-time, or Hovmöller plot, of the wave-induced horizontal velocity at the surface. Upstream (leftward) propagating waves of depression induce strong negative currents near the surface, and hence are indicated by dark streaks, while downstream propagating waves of depression are indicated by light streaks.

For early times $25 < t < 150$ both upstream and downstream propagating waves are generated. The upstream propagating disturbance begins to broaden and strengthen by $t = 80$, and its upstream propagation is completely arrested (by the background current) by $t = 120$. The trapped wave is fully formed by $t = 225$ with little change thereafter. The

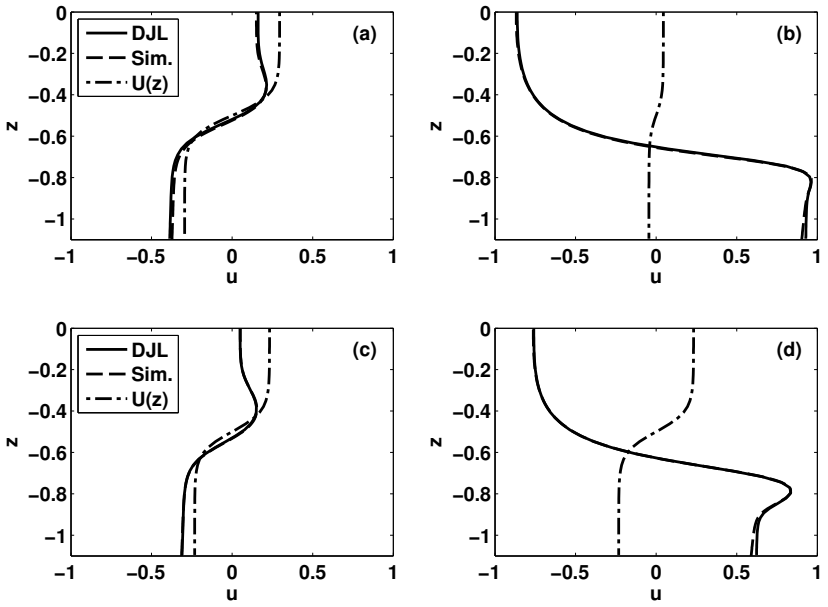

Figure 2.5: Comparison of the DJL theory with results of time-dependent simulations. Wave-induced velocities at the wave crest with the mean upstream velocity subtracted off are shown as functions of z. DJL (simulation) shown as solid (dashed) lines, along with the upstream shear currents (dot-dashed line). (a) Small wave in Figure 2.3 (c). (b) Large wave in Figure 2.3 (b). (c) Small wave in Figure 2.4 (b). (d) Large wave (same $U(z)$ as panel (c)) from Figure 2.4 (b). Note that the simulation and DJL curves are nearly identical. The stratification parameters are $\Delta\rho = 0.02$ and $z_j = 0.75H$. Note that the vertical coordinate has been shifted to $z - H$ in this figure. Reprinted with permission from Soontiens, N., C. Subich, M. Stastna (2010). Numerical simulation of supercritical trapped internal waves over topography. *Phys. Fluids 22*(11), 116605. Copyright 2010, American Institute of Physics.

downstream response is more complex, with a broad wave of depression forming for $t < 150$. This wave is connected to the trapped disturbance by a sharp transition region, which is especially evident between $90 < t < 140$ and $0 < x < 5$. This wave of depression is formed because of the conservation of mass, to balance the mass displaced over the topography. For sharper pycnoclines (not shown) simulations indicate that shear instability of this region is possible (Stastna et al., 2012). During the final adjustment to steady state, $150 < t < 250$, a smaller upstream oriented wave of depression fissions from the trapped wave. This wave has a propagation speed that is less than the mean upstream current, and

hence moves downstream. The steady state is achieved when the downstream disturbances have propagated out of the domain.

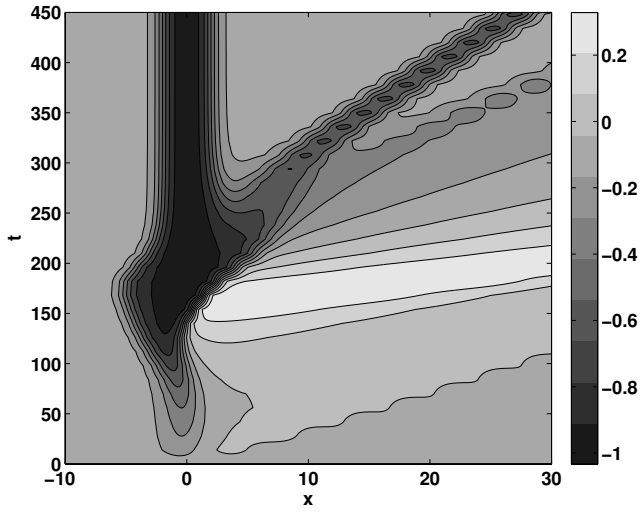

Figure 2.6: Space-time, or Hovmöller, plot of the wave-induced surface velocity during adjustment to the large trapped wave in Figure 2.4 (b). Reprinted with permission from Soontiens, N., C. Subich, M. Stastna (2010). Numerical simulation of supercritical trapped internal waves over topography. *Phys. Fluids 22*(11), 116605. Copyright 2010, American Institute of Physics.

A further examination of multiple states is presented in Figure 2.7 where hysteresis loops in $U_0 - \Delta U$ parameter space are plotted. Using single pycnocline stratifications, no instances of multiple steady states when the upstream velocity profile was constant were discovered, unless the topography was narrowed significantly. From Figure 2.7 it can be seen that the largest hysteresis loops occur when U_0 is near the conjugate flow speed, or in other words in cases for which a broad region of large trapped waves occurs. Furthermore, the lower branch of the hysteresis loop changes little from case to case, with only a slight broadening visible for the largest two U_0 cases shown. The upper branch becomes steeper as U_0 increases, indicating that equivalent increases in ΔU lead to larger decreases in trapped wave amplitude. Overall the results suggest that hysteresis is possible over a fairly large region of parameter space, though there are also instances (the largest U_0 case shown) for which large trapped disturbances are possible, yet the hysteresis loop is quite small.

Further, multiple states have been discovered for narrow topography and constant background currents. Figure 2.8 (a) shows a single isopycnal passing through the centre of the

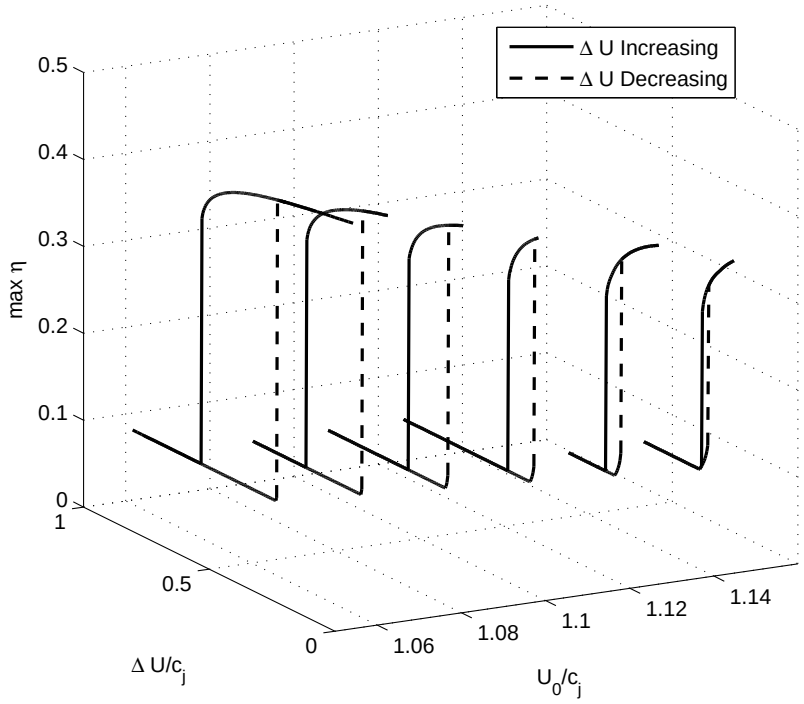

Figure 2.7: Three dimensional plot of hysteresis loops as U_0 and ΔU varies. The stratification parameters are $\Delta\rho = 0.02$ and $z_0 = 0.75H$. Adapted with permission from Soontiens, N., C. Subich, M. Stastna (2010). Numerical simulation of supercritical trapped internal waves over topography. *Phys. Fluids 22*(11), 116605. Copyright 2010, American Institute of Physics.

pycnocline far upstream for two waves produced from the same upstream background speed and topography width ($U_0 = 1.04c_j$ and $w_D = 0.21H$) and stratification. The bottom topography is indicated with a dashed line. It is clear from this figure that multiple steady states can indeed be obtained with a constant background current for narrow enough topography. Figure 2.8 (b) plots the hysteresis loop of wave amplitudes for $U_0 = 1.04c_j$ as w_D is varied. The results suggest that in order to consistently obtain large trapped waves in time-dependent simulations the bottom topography should have a half-width greater than $0.3H$ (for a background current of $U_0 = 1.04c_j$). In fact, it has been found that long before the upper branch begins to bend downward ($w_D \approx 0.3H$), the algorithm begins to systematically converge to the lower branch. By varying the topography width w_D we can determine when large trapped waves may be expected to form over narrow topography.

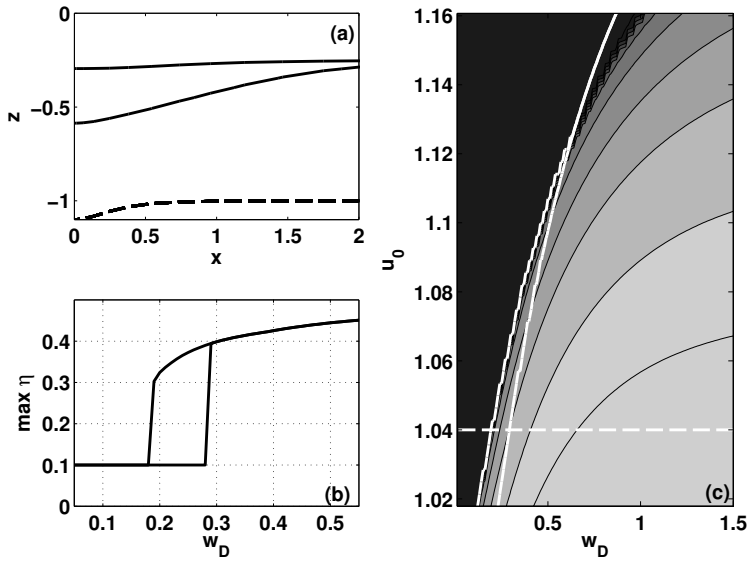

Figure 2.8: (a) Hysteresis with constant background flow as the width of the topography w_D changes. Solid - the isopycnal passing through the pycnocline middle for two waves with $w_D = 0.21H$ and $U_0 = 1.04c_j$, dashed - bottom topography. (b) Hysteresis loop as w_D varies, U_0 as in (a). (c) Shaded contours of the maximum isopycnal displacement in w_D - U_0 space for the simulations with decreasing w_D. Solid white - $\eta_{max} = 0.11H$ for both the w_D decreasing and increasing cases. Dashed white - U_0 as in (a) and (b). Note that the vertical coordinate has been shifted to $z - H$ in this figure. Reprinted with permission from Soontiens, N., C. Subich, M. Stastna (2010). Numerical simulation of supercritical trapped internal waves over topography. *Phys. Fluids 22*(11), 116605. Copyright 2010, American Institute of Physics.

In order to identify the region in which time-dependent simulations would be expected to yield only the large trapped waves, Figure 2.8 (c) shows a plot of shaded contours of the wave amplitude as w_D is decreased (corresponding to the upper branch in Figure 2.8 (b)) and background speed varies. The black shaded region represents those parts of parameter space in which the maximum isopycnal displacement occurs along the bottom boundary (and hence trapped waves are very small). The solid white lines are contours of $\eta_{max} = 0.11H$ for both the upper and lower branches of hysteresis. It can be seen that the hysteresis loop closes where the two contour lines meet at $U_0 \approx 1.125c_j$ and $w_D \approx 0.6H$. The region well to the right of the rightmost solid white line is thus the part of parameter space in which large trapped waves would be generated in time-dependent simulations. The dashed white line corresponds to the background speed used in Figure 2.8 (b). Based on

these results it is reasonable to conclude that as a conservative rule of thumb, large trapped waves can be expected in time-dependent simulations provided that the topography half-width is greater than about $1.0H$.

2.3.3 Vortex Cores

The results of this section have been outlined by Soontiens et al. (2010) and will be reproduced here. Adapted with permission from Soontiens, N., C. Subich, M. Stastna (2010). Numerical simulation of supercritical trapped internal waves over topography. *Phys. Fluids* *22*(11), 116605. Copyright 2010, American Institute of Physics.

It is well known that freely propagating internal solitary waves may form vortex cores, or regions of closed streamlines (Lamb, 2003). When no background shear current is present and under the Boussinesq approximation, vortex cores only form if significant stratification is present near the surface (bottom) for waves of depression (elevation). We have investigated the possibility of trapped waves forming vortex cores. In Figure 2.9 we show an example of a trapped wave with a vortex core when an upstream shear current is present ($U_0 = 0.95c_j$, $\Delta U = -0.38c_j$, $z_s = H$, $d_s = 0.1H$). It can be seen that in the stratified region streamlines follow isopycnals. Moreover, for this case the vortex core region is unstratified. For trapped waves with vortex cores, the computation of this steady wave employs the formal, mathematical continuation of the stratification and upstream velocity profiles outside of the water column (e.g. for $z > H$ since $z - \eta$ is outside of $[0, H]$). For the particular wave shown in Figure 2.9 the upstream density is very nearly constant at the upper boundary and hence the formal continuation for $z > H$ is not believed to be important. However, the upstream velocity profile does vary slightly near the upper boundary. An important question is whether a time-dependent simulation would yield a similar vortex core.

The results of such a simulation are shown in Figure 2.10. In panel (a) we show the wave-induced horizontal velocity profiles at the surface for two times in the simulation ($t = 336$, and 672). It can be seen that for early times the simulation yields a wave that is somewhat sharper than the DJL theory.. Of course, the horizontal profile is only a weak test of the match between simulation and theory. In panel (b) we thus consider the vertical profile of the wave-induced horizontal current at the wave crest. The background shear current is also shown as a dotted line. It can be seen that the match between the late time simulation and theory is excellent. In panel (c) we show the core region in detail. Here, small differences between the simulation and the theory become evident. Nevertheless, the theory yields a remarkably good prediction. The near-surface vorticity caused by the background current is the same sign as the vorticity caused by the wave-induced currents which leads to the formation of the trapped core (Lamb, 2003). This process is well represented by the steady theory, hence, the excellent match between theory and time-dependent results.

We performed the same comparison for the case of a vortex core when no shear current

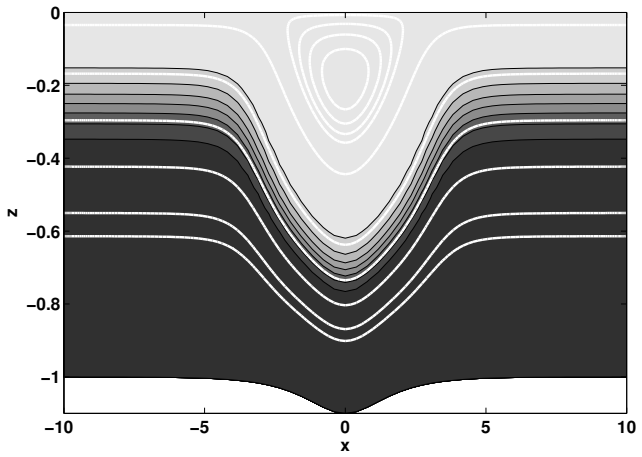

Figure 2.9: Vortex core for case with upstream shear current. Eight shaded density contours shown, overlaid by white contours of the streamfunction $\psi^T = [20, 40, 80, 120, 160, 200, 210, 212, 214, 216]$. Note that the vertical coordinate has been shifted to $z - H$ in this figure. Reprinted with permission from Soontiens, N., C. Subich, M. Stastna (2010). Numerical simulation of supercritical trapped internal waves over topography. *Phys. Fluids 22*(11), 116605. Copyright 2010, American Institute of Physics.

is present. The constant background velocity is $U_0 = 1.04c_j$ and the density profile is

$$\rho(z) = 1 - \Delta\rho \left(0.9 \tanh\left(\frac{z - z_0}{d_0} \right) + 0.2 \tanh\left(\frac{z - H}{d_0} \right) \right)$$

with $\Delta\rho = 0.02$, $z_0 = 0.75H$, and $d_0 = 0.1H$ as before. The results of this comparison are shown in Figure 2.11. The time-dependent simulations yielded a very active overturning region in the core region, as evidenced by panel (a) at $t = 336$. The active overturning and billow formation persisted for approximately 200 time units, however eventually the breaking region was washed out from the wave yielding a nearly constant density, weakly unsteady region with density matching the upstream surface density, as shown in panel (b) ($t = 672$). In panel (c) we show the comparison of vertical profiles of wave-induced horizontal velocities at the wave crest. It can be seen that the match is essentially exact over the wave body, with a more blunt profile yielded by the simulation in the core region. This is confirmed in the detailed plot shown in panel (d). The oscillations in the dot-dashed curve are due to the presence of active overturns and billows, though these are clearly significantly diminished for late times (dashed curve). That the core continues to be active even for late times is revealed in the contours of wave-induced horizontal velocity at

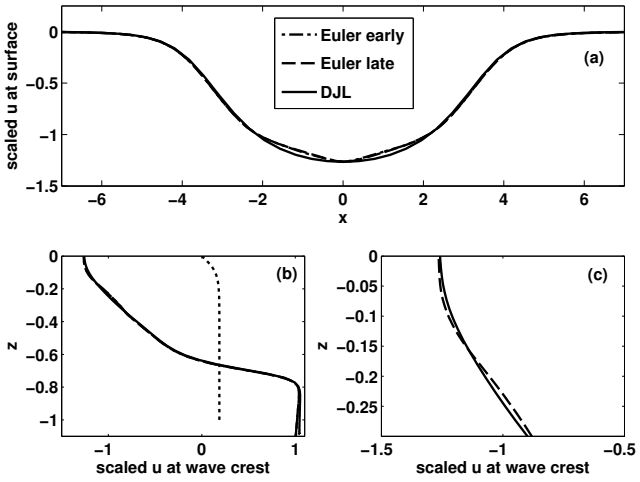

Figure 2.10: (a) Wave-induced surface velocities. (b) Vertical profile of horizontal velocity at the wave crest. (c) Detail of (b) in the core region. The DJL theory is the solid line, early, $t = 336$ (late $t = 672$) time-dependent simulation indicated by dot-dashed (dashed) line. In panel (b) $U(z)$ is denoted by a dotted line. Note that the vertical coordinate has been shifted to $z - H$ in this figure. Reprinted with permission from Soontiens, N., C. Subich, M. Stastna (2010). Numerical simulation of supercritical trapped internal waves over topography. *Phys. Fluids 22*(11), 116605. Copyright 2010, American Institute of Physics.

$t = 672$, shown in Figure 2.12. The currents, though small in magnitude, exhibit a clear upstream-downstream asymmetry, consistent with the fact that billows and vortices are produced on the downstream face of the core and are slowly advected out of the wave by the background current.

There have been a variety of more complicated theories proposed for the computation of the wave properties inside the vortex core, see Helfrich and White (2010) for the most complete theory presently available. However, time dependent simulations suggest that the vortex cores remain unsteady for a significant amount of time and exhibit asymmetry across the wave crest. In particular, for cases in which significant density stratification exists near the boundary it is unlikely any steady theory will be accurate. However, away from the core region the steady theory exhibits a remarkably good match with the time-dependent results. The above results suggest that breaking waves with a background shear current, for which little or no density stratification exists in the core region, may yield nearly steady trapped cores (perhaps in agreement with Figure 3 of Helfrich and

White (2010)). Vortex cores with a density stratification near the surface exhibit an active region of overturning for long simulation times, a feature that is not represented by the steady theory. Whether the late-time states found in these cases are truly physical can only be answered by performing three-dimensional simulations.

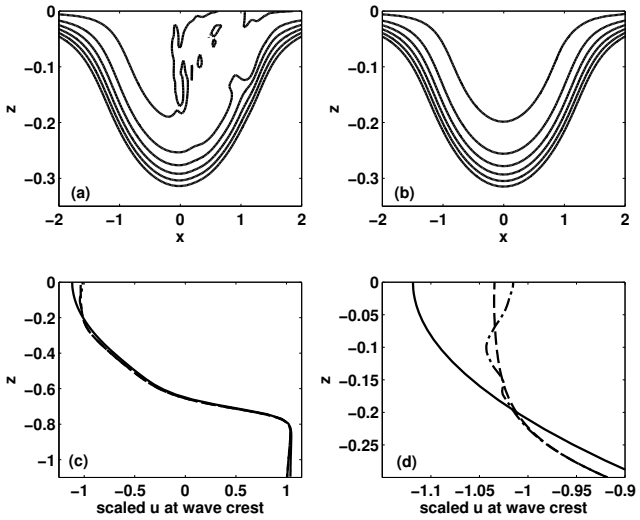

Figure 2.11: (a) Six isopycnals in the breaking, stratified near-surface region for an overturning trapped disturbance at $t = 336$. (b) As in (a) but at a later time ($t = 672$). (c) Vertical profile of horizontal velocity at the wave crest. (d) As in (c) but only the core region shown. DJL theory (solid line), time-dependent simulation corresponding to panel (a) (panel (b)) indicated by dashed (dot-dashed) line. Note that the vertical coordinate has been shifted to $z - H$ in this figure. Reprinted with permission from Soontiens, N., C. Subich, M. Stastna (2010). Numerical simulation of supercritical trapped internal waves over topography. *Phys. Fluids 22*(11), 116605. Copyright 2010, American Institute of Physics.

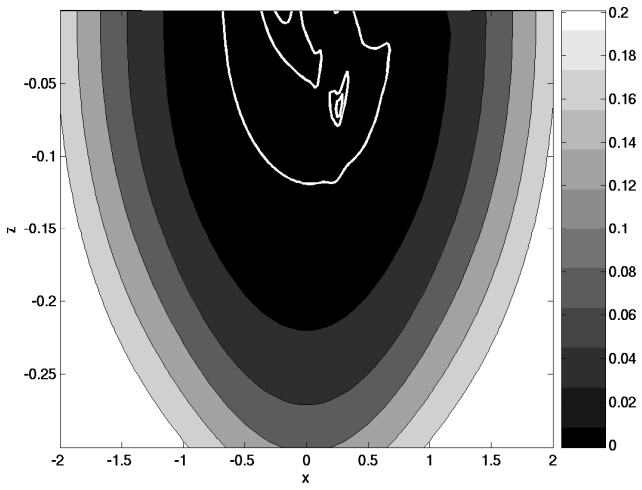

Figure 2.12: Details of the late time core region for the case from Figure 2.11. Six equally spaced shaded contour of total horizontal velocity at late times ($t = 672$) from 0.01 to 0.21. Superimposed in white are contours of $U = 0.0005, 0.001, 005$. Note that the vertical coordinate has been shifted to $z - H$ in this figure. Reprinted with permission from Soontiens, N., C. Subich, M. Stastna (2010). Numerical simulation of supercritical trapped internal waves over topography. *Phys. Fluids 22*(11), 116605. Copyright 2010, American Institute of Physics.

2.3.4 Elevation and Depression Topography

The investigation of elevation and depression waves trapped over topography is motivated by a symmetry property for freely travelling waves of elevation and depression (Lamb and Wan, 1998). The symmetry property is examined here, followed by efforts to determine if a similar property exists for trapped waves over topography. Parts of this discussion is presented in Soontiens et al. (2013b) and is expanded here.

Freely travelling steady waves in an inviscid fluid under the Boussinesq approximation are also described by a DJL equation, written in a reference frame following the wave. For a freely travelling wave with propagation speed c, this equation is given by

$$\nabla^2\eta + \frac{N^2(z-\eta)}{c^2}\eta = 0. \tag{2.28}$$

Such a wave, when reflected about the mid-depth, will also satisfy an equivalent form of the DJL equation. To see this, one can construct a wave reflected about $z = H/2$, defined as $e(x, y) = -\eta(x, z)$ where $y = H - z$, and show that it satisfies the DJL equation. Since $\eta(x, z)$ is a solution to (2.28), this equation can be written in terms of $e(x, y)$ and one can rewrite the Laplacian operator in the (x, y) coordinate system. A simple calculation shows that $\nabla^2 = \tilde{\nabla}^2$, where $\tilde{\nabla}^2 = \partial_{xx} + \partial_{yy}$. Hence, the equivalent DJL equation is

$$\tilde{\nabla}^2 e(x, y) + \frac{N^2(H-(y-e))}{c^2}e = 0.$$

This equation reveals that a travelling wave reflected about the mid-depth also satisfies the DJL equation with the requirement that the buoyancy frequency profile is also reflected about the mid-depth. This result does not necessarily carry over to the topographic extension of the DJL equation because the change in coordinates would also result in different set of boundary conditions, and hence modify the problem.

With this motivation, we set out to determine if there is a corresponding symmetry for trapped waves over topography. In order to accomplish this goal, a comparison is drawn between trapped waves of elevation and depression for a pycnocline centred above and below the mid-depth in Figure 2.13. In these examples, the pycnocline is centred at $z_0 = 0.75H$ or $z_0 = 0.25H$. For both of these stratifications the conjugate flow speed is $c_j = 1.17c_{lw}$ and we have chosen the background speed to be $U_0 = 1.07c_j$.

Solutions with depression topography are shown in Figure 2.13 (a-b). One of the most interesting features is the very large trapped wave of depression in Figure 2.13 (a). Very large disturbances in cases that considered non-constant background currents were

presented in the previous sections. With the pycnocline centred above the mid-depth, trapped waves of depression can have very large amplitude for U_0 close to c_j. This does not carry over to freely propagating waves of depression, which have a limiting amplitude as the propagation speed approaches the conjugate flow speed (Lamb and Wan, 1998). In contrast, when the pycnocline of a wave of depression is centred below the mid-depth (Figure 2.13 (b)), the wave amplitude is not very large since the pycnocline is too close to the bottom boundary to allow large trapped disturbances to form.

The elevation waves do not exhibit such a large contrast between the above mid-depth and below mid-depth pycnocline stratifications (see Figure 2.13 (c-d)). In Figure 2.13 (c), the above mid-depth solution showcases a small-amplitude wave since the pycnocline is too close to the top boundary for large amplitudes. The below mid-depth solution exhibits a larger wave, but it is not nearly as large as the corresponding large wave of depression. There is clearly a fundamental difference between trapped waves of depression and elevation with regards to large-amplitude solutions.

This observation can be explained by considering the effect of the topography on the depth of the water column. For elevation (depression) topography, the depth of the domain is decreased (increased) directly over the topography. This local change in depth motivates us to consider a local conjugate flow speed (c_{jloc}) over the centre of the topography. Since the depth of the water column changes over the topography there will also be a change in the local conjugate flow speed. In Table 2.1, we provide several calculations of the conjugate flow speed in a domain whose depth is given by the water column depth over the centre of the topography. We consider each of the stratifications and topography profiles presented in Figure 2.13.

The effects of the topography on the local conjugate flow speed are clear. An increase in the water column depth (depression topography) causes an increase in the local conjugate flow speed. By contrast, the elevation topography demonstrates a decrease in the local conjugate flow speed. This change in local conjugate flow speed can explain the very large disturbance over the depression topography seen in Figure 2.13 (a). Away from the topography the background flow is $U_0 = 1.07c_j$ and the flow is in a supercritical state. However, over the topography c_{jloc} has increased, which implies that locally the flow is less supercritical and, in some cases, may even transition into the subcritical regime. As the flow becomes less supercritical, there is a greater propensity for waves to travel upstream which leads to the very large disturbance in Figure 2.13 (a). The large waves form as a balance between the upstream directed parts of the flow and the background current. For elevation topography, the local conjugate flow speed decreases so that the flow becomes more supercritical and the trapped waves do not become as large. A more detailed explanation for the formation of the large waves by analysing the pressure field

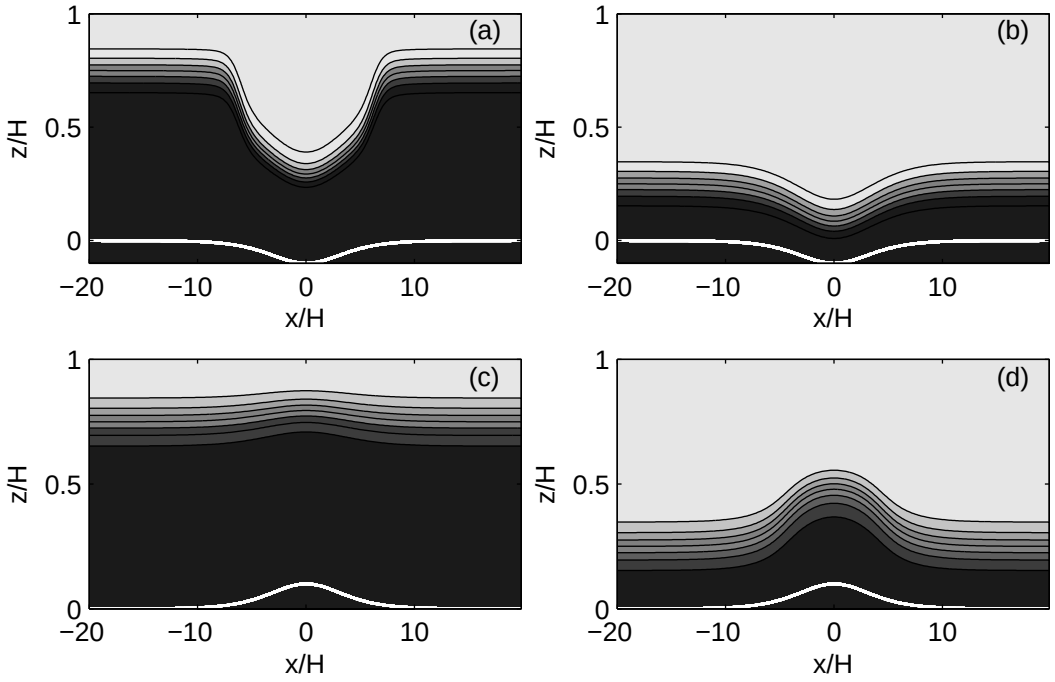

Figure 2.13: Plots of the density field for trapped depression waves (top) and elevation waves (bottom). On the left (a,c), the pycnocline is centred at $z_0 = 0.75H$ and on the right (b,d) it is centred at $z_0 = 0.25H$. In these cases, $U_0 = 1.07c_j$. The thick white line represents the bottom topography. Reprinted with permission from Soontiens, N., M. Stastna, M. L. Waite (2013). Trapped internal waves over topography: Non-Boussinesq effects, symmetry breaking and downstream recovery jumps. *Phys. Fluids 25*, 066602.Copyright 2013, American Institute of Physics.

and the balance of forces will be carried out in a future study.

Next, we examine the large-amplitude cases for both elevation and depression waves in more detail in order to determine when large trapped solutions may occur. As suggested by Figure 2.13, large-amplitude trapped waves of depression can occur when the pycnocline is centred above the mid-depth and large-amplitude waves of elevation can occur when the pycnocline is centred below the mid-depth. This has been confirmed through a series of experiments with several background speeds U_0 and pycnocline stratifications.

A closer examination of the properties of these large waves is presented in Figure 2.14. Here, we plot the maximum value of $|\eta|$ as a function of the background speed U_0 for both elevation and depression waves. The elevation waves are generated over hill topography

Table 2.1: Local conjugate flow speeds using water column depth above the centre of the topography H_{loc}. Upstream of the topography the conjugate flow speed is $c_j = 1.17c_{lw}$. Reprinted with permission from Soontiens, N., M. Stastna, M. L. Waite (2013). Trapped internal waves over topography: Non-Boussinesq effects, symmetry breaking and downstream recovery jumps. *Phys. Fluids 25*, 066602. Copyright 2013, American Institute of Physics.

Topography	z_0	H_{loc}	c_{jloc}/c_{lw}
Depression	$0.75H$	$1.1H$	1.24
Depression	$0.25H$	$1.1H$	1.25
Elevation	$0.75H$	$0.9H$	1.1
Elevation	$0.25H$	$0.9H$	1.09

with pycnocline centred at $z_0 = 0.4H$ and the depression waves are generated over hole topography with pycnocline centred at $z_0 = 0.6H$. In both cases the conjugate flow speed is $c_j = 1.02c_{lw}$. The depression waves reach larger amplitudes than the elevation waves for the background speeds and stratification considered here. In addition, both elevation and depression waves experience a growth in amplitude as U_0 approaches the conjugate flow speed. This observation can be explained by the form of equation (2.1). Notice that the nonlinear term, $N^2(z-\eta)\eta/U_0^2$, becomes smaller as U_0 becomes larger. Hence, nonlinear effects are less important for large U_0, explaining the reduction in amplitude for large U_0/c_j. For large enough U_0, ($U_0/c_j > 1.5$), the extreme value of η is $0.1H$ and occurs along the bottom boundary.

In addition to wave growth, we also observe a broadening of waves as U_0 approaches c_j. The depression waves tend to be broader than the elevation waves for U_0 close to c_j. However, for $U_0 \geq 1.2c_j$, the elevation waves are broader. Both elevation waves and depression waves tend to approach a minimum width for large U_0/c_j, and this width is set by the topography. In these cases we observe wavelengths that are approximately $1.9w_D$ for elevation waves and $1.8w_D$ for depression waves.

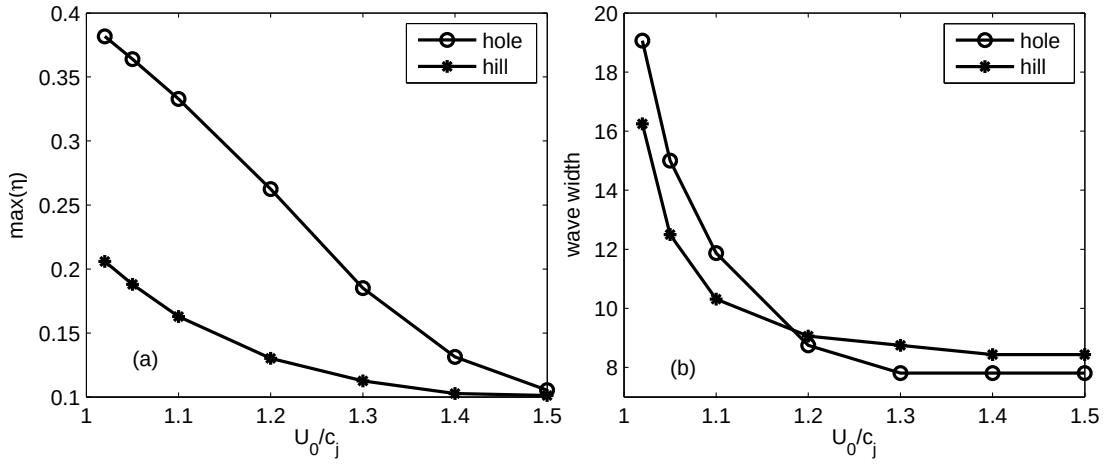

Figure 2.14: Diagram of wave properties as a function of the background velocity U_0. (a) Maximum value of $|\eta|$ (scaled by $1/H$) for waves over hole topography with $z_0 = 0.6H$ and hill topography with $z_0 = 0.4H$. (b) A measure of the wave width for the corresponding cases in panel (a). The wave width (scaled by $1/H$) is measured as twice the distance between the wave centre and the location where the surface wave-induced velocities reach half of their extreme value. In both cases the conjugate flow speed is $c_j = 1.02c_{lw}$. Reprinted with permission from Soontiens, N., M. Stastna, M. L. Waite (2013). Trapped internal waves over topography: Non-Boussinesq effects, symmetry breaking and downstream recovery jumps. *Phys. Fluids 25*, 066602. Copyright 2013, American Institute of Physics.

2.3.5 Boussinesq and Non-Boussinesq Waves

Next, we examine non-Boussinesq effects by comparing solutions of the non-Boussinesq DJL equation (2.19) to solutions of the Boussinesq DJL equation (2.1). These solutions were generated using a density profile with $z_0 = 0.75H$, $\Delta\rho = 0.05$, and depression topography. Typically, ocean or lakes stratification observe a density difference of less than 5% across the pycnocline. One might expect non-Boussinesq effects to become important at this value of $\Delta\rho$. For this stratification, the non-Boussinesq conjugate flow speed is $c_j = 1.17c_{lw}$ where c_{lw} is the linear long wave speed. The conjugate flow speed derived from the Boussinesq equation is very similar for this density stratification. The goal is to determine the effects of the additional non-Boussinesq terms in equation (2.19) and the effect of the non-Boussinesq definition of the buoyancy frequency $N_{NB}(z)$. These results are compared in Figure 2.15 where we plot the maximum value of $|\eta|$ as a function of background speed U_0. We consider three cases: a) the non-Boussinesq equation with $N_{NB}(z)$, b) the Boussinesq equation with $N_{NB}(z)$, and c) the Boussinesq equation with $N_B(z)$.

The effects of the additional non-Boussinesq terms are determined by comparing cases a) and b). Examining Figure 2.15, it is observed that these two cases are in close agreement for $U_0/c_j > 1.28$ and for $U_0/c_j < 1.18$. For $U_0/c_j > 1.28$, the wave amplitude is only slightly larger in the non-Boussinesq case. One of the more interesting features is the existence of a region of transition from small-amplitude waves to large-amplitude waves where the two cases deviate more significantly. As U_0 decreases, the transition from small waves to large waves occurs more gradually in the non-Boussinesq case. By contrast, the Boussinesq case exhibits relatively small waves above $U_0/c_j \approx 1.23$, below which there is an abrupt jump to larger waves. Thus, the main effect of the non-Boussinesq terms is in the transition from small waves to large waves, which occurs more gradually in the non-Boussinesq case.

Comparisons between case b) and c) indicate the effect of the non-Boussinesq definition of the buoyancy frequency. Figure 2.15 reveals that these two cases deviate only slightly and they both follow the same trend as U_0 decreases. Hence, the main effect of not making the Boussinesq approximation comes from the additional terms in equation (2.19). In this example, making the Boussinesq approximation where inappropriate can lead to an underestimate of wave amplitudes, particularly in the transition from small-amplitude to large-amplitude waves.

In addition, the shapes of the width curves (width is measured as twice the distance between the wave centre and the location where the wave-induced surface velocities reach half of their extreme value) for each of the cases are similar, although there are some differences mainly around the transition velocities from large to small waves (Figure 2.15 (b)). The overall trend is that large amplitudes are associated with broad waves. However,

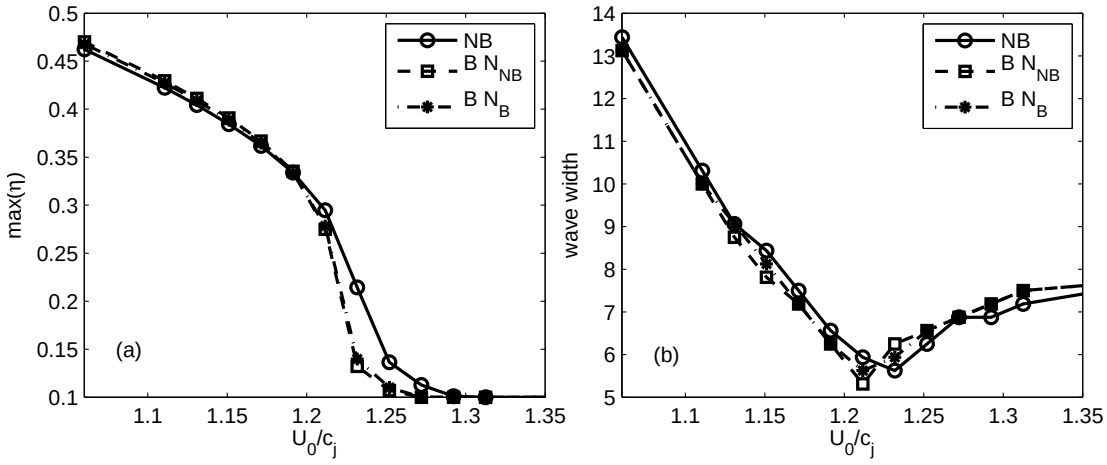

Figure 2.15: (a) Extreme value of $|\eta|$ (scaled by $1/H$) with varying background speeds U_0 for comparison between non-Boussinesq and Boussinesq results with $\Delta\rho = 0.05$, $z_0 = 0.75H$ and depression topography. (b) A measurement of wave width (scaled by $1/H$) is also included. Each curve represents a different set of simulations: non-Boussinesq solutions with $N_{NB}(z)$ (solid), Boussinesq solutions with $N_{NB}(z)$ (dashed), Boussinesq solutions with $N_B(z)$ (dot-dashed). In this plot, the background speed is scaled by the conjugate flow speed, c_j, as calculated for the non-Boussinesq case. The wave width is measured as in Figure 2.14.

around the transition to smaller amplitude the waves exhibit a narrowing trend followed by an abrupt broadening in a cusp-like behaviour. For small waves (large U_0), the limiting width approaches the width of the topography. This is observed in all three cases, although the location of the cusp occurs at a slightly higher velocity in the non-Boussinesq case. This sharp transition and cusp-like behaviour was not noted in the depression waves of Figure 2.14 with $z_0 = 0.6H$ and $\Delta\rho = 0.02$.

Next, we examine the wave-induced velocities for waves generated with $U_0 = 1.23c_j$ for each of these cases. This choice of U_0 represents one of the velocities in the range of transition between large- and small-amplitude waves. In Figure 2.16 (a), normalized wave-induced surface velocities reveal the horizontal structure of the waves. At this value of U_0, the waves in the Boussinesq case are slightly broader than the waves in the non-Boussinesq case, however, the horizontal structure of the waves is almost indistinguishable between the two Boussinesq cases. Panel (b) displays the vertical structure of the waves through the centre of the domain, scaled by the conjugate flow speed, which allows for comparison of velocity magnitudes. This plot reveals that the non-Boussinesq case yields larger wave-

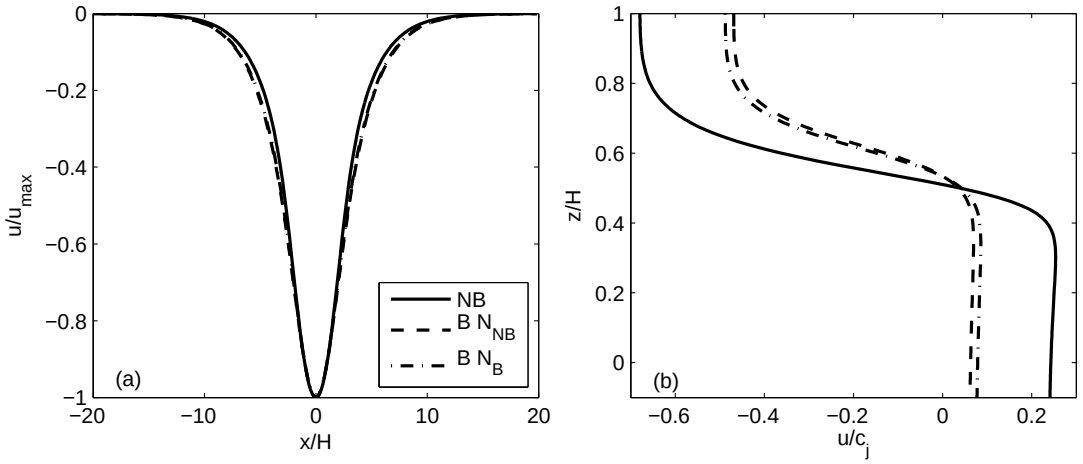

Figure 2.16: An example of the spatial structure of waves from the Boussinesq and non-Boussinesq waves in Figure 2.15 for $U_0 = 1.23c_j$. (a) Normalized wave-induced velocities at the surface. (b) Wave-induced velocities through $x = 0$ scaled by the non-Boussinesq conjugate flow speed.

induced velocities than both of the Boussinesq cases. For $U_0 \gtrsim 1.28c_j$ the wave-induced velocities between the Boussinesq and non-Boussinesq waves exhibit a close match.

We further highlight the effects of making the Boussinesq approximation by comparing wave amplitudes of Boussinesq and non-Boussinesq waves for several density stratifications and background velocities in Figure 2.17. The goal is to determine where the Boussinesq approximation breaks down, in terms of the density stratification and the background speed. All of the stratifications use $z_0 = 0.75H$ but the density change is modified between cases, taking $\Delta\rho = [0.05, 0.1, 0.15, 0.2]$. Interestingly, very large waves (small U_0) do not vary significantly between the Boussinesq and non-Boussinesq solutions. For example, even for a large density change, $\Delta\rho = 0.2$, the amplitude of the non-Boussinesq wave has decreased by only 3.1% when compared to the Boussinesq wave for $U_0 = 1.15c_j$. Additionally, the very small waves (large U_0) also do not vary significantly between non-Boussinesq and Boussinesq results. Rather, the biggest deviations between the Boussinesq and non-Boussinesq solutions occur during the transition from large- to small-amplitude waves as U_0 increases. The transition occurs more gradually in the non-Boussinesq cases and becomes even more gradual for higher $\Delta\rho$. This behaviour can be explained by additional nonlinear terms in the non-Boussinesq DJL equation (2.19). As U_0 increases the $N^2(z-\eta)\eta/U_0^2$ term becomes less important, and in the Boussinesq limit the problem becomes close to solving Laplace's equation for large enough U_0. However, the non-Boussinesq equation includes

additional nonlinear terms that do not depend on U_0. For large $\Delta\rho$, and hence larger $N^2_{NB}(z)$, these nonlinear terms are more pronounced, explaining the more gradual transition to small-amplitude states as U_0 increases. Hence, the non-Boussinesq effects are most important for large density differences, particularly in the region of transition from large- to small-amplitude waves. For the largest density jump, $\Delta\rho = 0.2$, the non-Boussinesq wave amplitude increases by 120% when $U_0 = 1.25c_j$. Even for a moderate density jump, $\Delta\rho = 0.1$, the non-Boussinesq wave is 68% larger. Hence, for $\Delta\rho \geq 0.1$ the Boussinesq approximation is not trustworthy for moderate values of U_0.

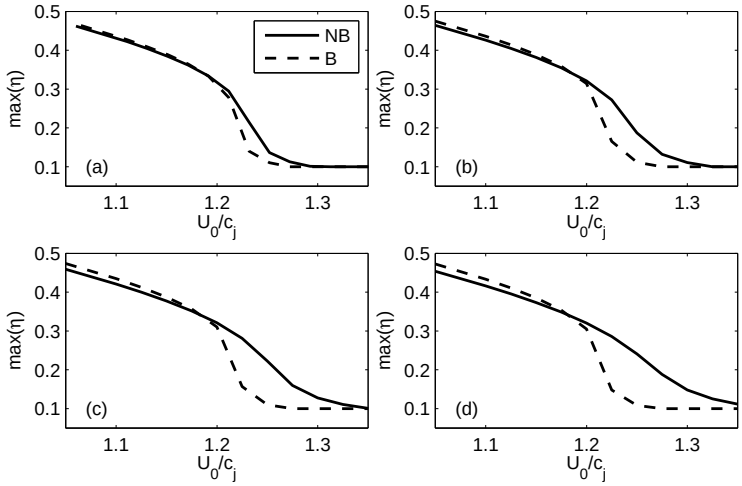

Figure 2.17: Comparison of non-Boussinesq (solid) and Boussinesq (dashed) maximum $|\eta|$ (scaled by $1/H$) for several background speeds and stratifications. (a) $\Delta\rho = 0.05$, (b) $\Delta\rho = 0.1$, (c) $\Delta\rho = 0.15$, (d) $\Delta\rho = 0.2$. The non-Boussinesq conjugate flow speed has been used for scaling. Reprinted with permission from Soontiens, N., M. Stastna, M. L. Waite (2013). Trapped internal waves over topography: Non-Boussinesq effects, symmetry breaking and downstream recovery jumps. *Phys. Fluids 25*, 066602. Copyright 2013, American Institute of Physics.

We continue to investigate the non-Boussinesq effects by considering a stratification with a very large density jump $\Delta\rho = 0.45$ and $z_0 = 0.75H$. It is a worthwhile exercise to examine the non-Boussinesq effects at this magnitude. The goal is to further classify how the Boussinesq approximation breaks down, and which terms are responsible for this breakdown. For this stratification the non-Boussinesq conjugate flow speed is $c_{jNB} = 1.1c_{lw}$ and the Boussinesq conjugate flow speed is $c_{jB} = 1.17c_{lw}$.

Once again, the transition from large waves to small waves with increasing U_0 is much

more gradual in the non-Boussinesq case (Figure 2.18). Both of the Boussinesq solutions exhibit a very sharp transition from large-amplitude to small-amplitude waves. In addition, the cusp-like behaviour in the wave width is no longer present in the fully non-Boussinesq case but does appear in the other cases presented. Notably, the two Boussinesq cases also deviate significantly at this stratification, particularly in the amplitudes of the largest waves, since using the $N_{NB}(z)$ definition of the buoyancy frequency is the same as defining an alternate density stratification in terms of an integral equation. However, the general trend and cusp-like behaviour are similar in both Boussinesq cases, which greatly contrast the fully non-Boussinesq case. These results indicate that the sudden transition from large- to small-amplitude waves is mathematically manifested in the additional nonlinear terms of the non-Boussinesq equation while the differences in amplitudes of the largest waves may be due to the alternative definition of the buoyancy frequency, at least for the stratifications considered here.

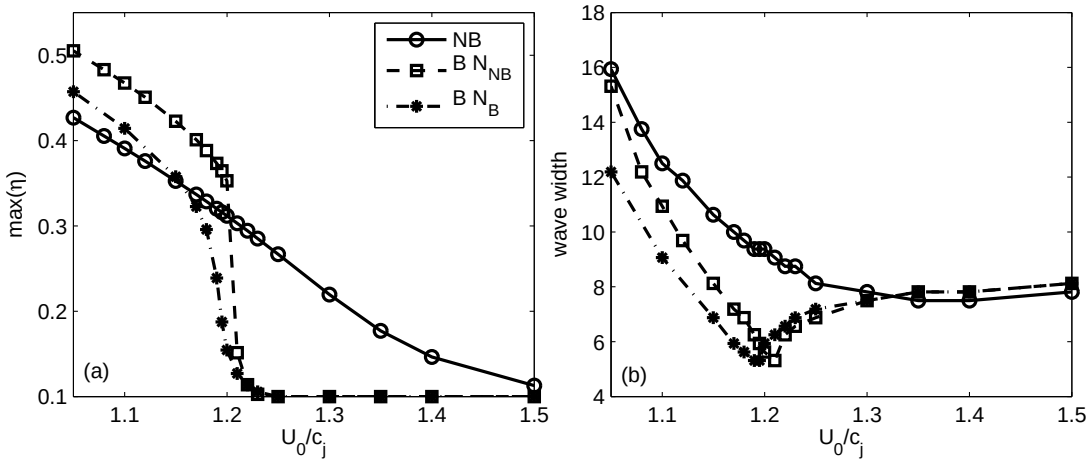

Figure 2.18: (a) Extreme value of η (scaled by $1/H$) and (b) measurement of wave width (scaled by $1/H$) for a stratification with $\Delta\rho = 0.45$ and $z_0 = 0.75H$. Results for the non-Boussinesq equation with $N_{NB}(z)$ (solid), the Boussinesq equation with $N_{NB}(z)$ (dashed), and the Boussinesq equation with $N_B(z)$ (dot-dashed) are shown. The wave width is measured as in Figure 2.14. The velocity is scaled by the non-Boussinesq conjugate flow speed, $c_{jNB} = 1.1c_{lw}$.

2.3.6 Subcritical Flows

In the above discussion we have considered inflows that were larger than the conjugate flow speed. Such flows preclude the upstream propagation of both linear and nonlinear waves. However, there has been some suggestion in the literature (Esler et al., 2005, 2007; Stastna et al., 2012) that it is possible for a finite amplitude, steady wave train to form in the lee of topography for flows over a hill that, while subcritical away from the hill, are supercritical somewhere over the hill. This subcritical to supercritical transition can lead to a downstream recovery jump and a steady state that is horizontally asymmetric across the topography. The results that follow are adapted with permission from Soontiens, N., M. Stastna, M. L. Waite (2013). Trapped internal waves over topography: Non-Boussinesq effects, symmetry breaking and downstream recovery jumps. *Phys. Fluids 25*, 066602. Copyright 2013, American Institute of Physics.

In Figure 2.19 we show the density fields from time-dependent, nearly impulsively started simulations. These simulations are performed with a pycnocline stratification centred at $z_0 = 0.75H$ and density jump $\Delta\rho = 0.02$ and the Boussinesq approximation is used for all simulations. We have taken $\Delta\rho = 0.02$ since non-Boussinesq effects are unimportant for this density jump. It can be seen that for all U_0 values shown, a large-amplitude wave forms downstream of the hill, and that the crest of this wave overshoots the mid-depth. For early times it can be seen that this wave is terminated on its downstream end by a so-called "downstream recovery jump" (DRJ). The DRJ does not restore the pycnocline to its far upstream location, instead leading to a long dispersive wave train (not visible in the figure) and it is this wave train that eventually returns the pycnocline to its upstream state. This occurs far downstream of the topography. Indeed, the location of the DRJ gradually shifts downstream, and in all nonbreaking cases we found that the DRJ continues to move downstream. Thus the DRJ is not a part of the steady state reached by the fluid. Instead the steady state consists of the wave visible between $x = -20$ and $x = 20$ in panels (b, d, f). In the most subcritical case shown, spatially growing shear instability sets in (visible for $x > 36$ in panel g) and leads to a rapid breakdown of the DRJ. We hypothesize that a DRJ that undergoes a turbulent breakdown will reach a quasi-steady state, in analogy with solutions of the shallow water equations studied by Esler et al. (2005). However, two-dimensional simulations cannot confirm or deny this hypothesis. Moreover, the final location of the turbulent DRJ would likely be sensitive to the manner in which the flow was accelerated, since a slower acceleration would mean more time spent in the subcritical regime.

Similar types of disturbances generated by flow over topography have been discovered using weakly nonlinear theories such as the KdV equation (Grimshaw and Smyth, 1986;

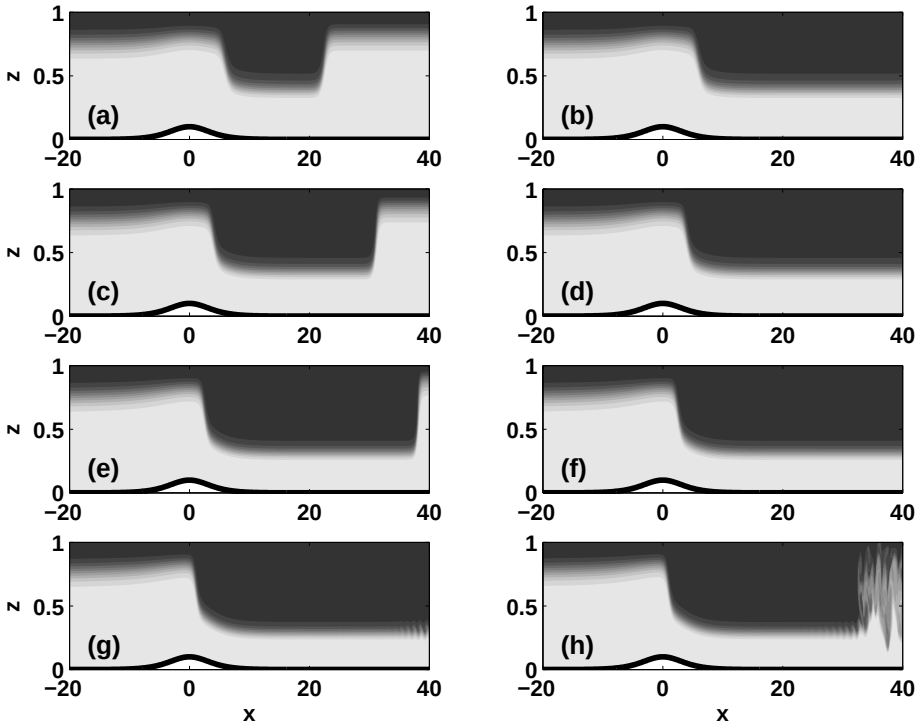

Figure 2.19: Density fields after 5 (10) hours on the left (right) column, where $U_0 = [0.96, 0.91, 0.85, 0.80]c_j$ from top to bottom. Reprinted with permission from Soontiens, N., M. Stastna, M. L. Waite (2013). Trapped internal waves over topography: Non-Boussinesq effects, symmetry breaking and downstream recovery jumps. *Phys. Fluids 25*, 066602. Copyright 2013, American Institute of Physics.

Baines, 1995). The solutions presented here are derived from simulations of the fully nonlinear equations of motion for a continuously stratified fluid, and hence, represent situations that are not fully described by weakly nonlinear theory. Indeed, the amplitude of the downstream depression is quite large, up to three times the topographic amplitude, and hence simply does not fit the small amplitude assumption of the KdV equation.

When more than one topographic hill is present, the downstream hill can be expected to generate different waves during the adjustment process. This is demonstrated in Figure 2.20, which shows the shaded horizontal velocity as well as three isopycnals in white at various times $t = [745, 993.3, 1987, 2483]t_d$, where $t_d = H/c_j$. It can be seen that for early times (Figure 2.20 (a-b)) a much smaller-amplitude wave forms downstream of the second hill, in comparison with wave generated between the two hills. This is because the DRJ

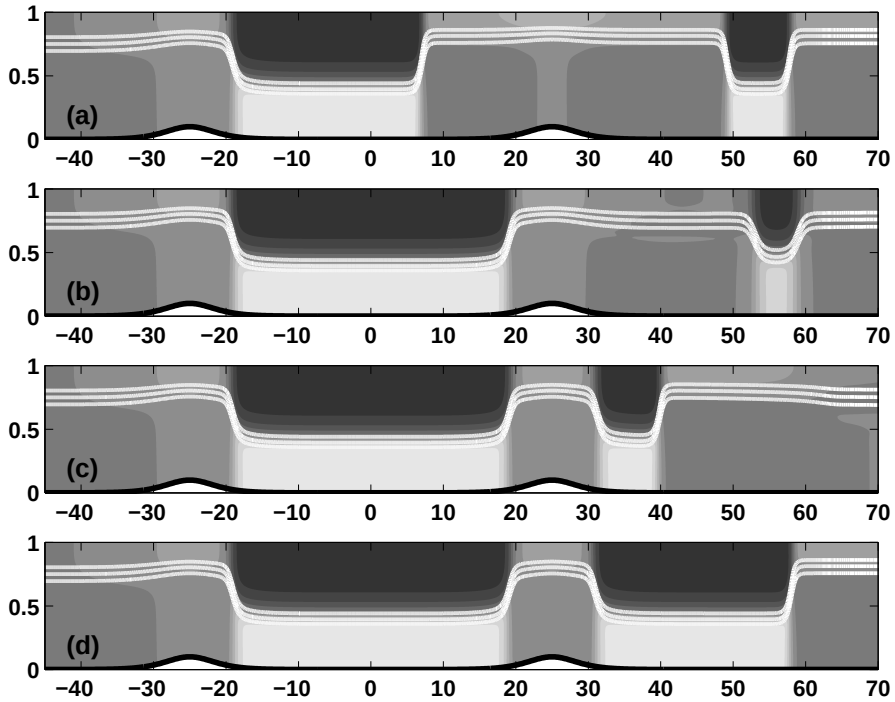

Figure 2.20: Horizontal velocity fields with three white isopycnals superimposed for the double hill case. The background speed is $U_0 = 0.96c_j$ The results are presented at non-dimensional times (a) $t^* = 745$, (b) $t^* = 993.3$, (c) $t^* = 1987$, (d) $t^* = 2483$. The scaling time is taken to be $t_d = H/c_j$. Reprinted with permission from Soontiens, N., M. Stastna, M. L. Waite (2013). Trapped internal waves over topography: Non-Boussinesq effects, symmetry breaking and downstream recovery jumps. *Phys. Fluids 25*, 066602. Copyright 2013, American Institute of Physics.

from the first hill leads to a pycnocline that overshoots its far upstream height. When the wave generated behind the upstream hill extends far enough in the downstream direction so that the flow over the second hill is modified, the second downstream wave is "freed" and propagates upstream, decreasing in amplitude as it goes (in panel (b) the wave is near the limiting wave amplitude given by the conjugate flow to the far upstream state). When this wave reaches the second hill it cannot propagate further upstream and it grows (panel c) and begins to broaden. The long time state is thus an asymmetric state with the wave amplitude unchanged (apart from the region in the immediate vicinity of the second hill).

These results suggest that the symmetric, trapped waves computed theoretically from the DJL equation above are not the only possible steady states. Indeed, for inflows that are

formally subcritical with respect to the conjugate flow speed an asymmetric steady state is possible. This possibility has been examined through a reformulation of the DJL boundary value problem. Considering a Boussinesq fluid with constant background velocity U_0, a boundary value problem for asymmetric DJL solutions could be stated as

$$\nabla^2\eta + \frac{N^2(z-\eta)}{U_0^2}\eta = 0, \tag{2.29a}$$

$$\eta = 0 \text{ at } z = H, \tag{2.29b}$$

$$\eta = h(x) \text{ at } z = h(x), \tag{2.29c}$$

$$\eta(-L, z) = 0, \quad \eta_x(L, z) = 0. \tag{2.29d}$$

The horizontal boundary conditions are motivated by requiring zero isopycnal displacement at the upstream boundary and flat isopycnals at the downstream boundary. If a steady state is attainable then the isopycnals should be flat far way from the topography. Although the flow is formally subcritical, no upstream propagating modes existed for the inflow speeds tested. In order to produce the asymmetric states, the mapped numerical solver was initialized with an asymmetric initial guess and the iterations were continued until a suitably low error norm was achieved. This technique may prove useful in finding other steady states for transcritical flows in a fully nonlinear framework.

An example of asymmetric DJL solutions is displayed in Figure 2.21 (a). This solution corresponds to the wave in Figure 2.19 (b), the long time solution to the numerical simulation with $U_0 = 0.96c_j$. Both of these plots show similar features, including a slight elevation of the pycnocline above the topography, followed by a large depression feature in the lee. Additional wave properties for several background velocities are displayed in panel (b). This plot shows that the amplitude of the depression increases as the flow becomes more subcritical (U_0 decreases), which matches the trend observed in the numerical simulations of Figure 2.19. Additionally, the displacement over the topography crest does not vary significantly between cases. Although not shown here, the waves undergo a steepening trend as U_0 decreases, similar to what is observed in Figure 2.19.

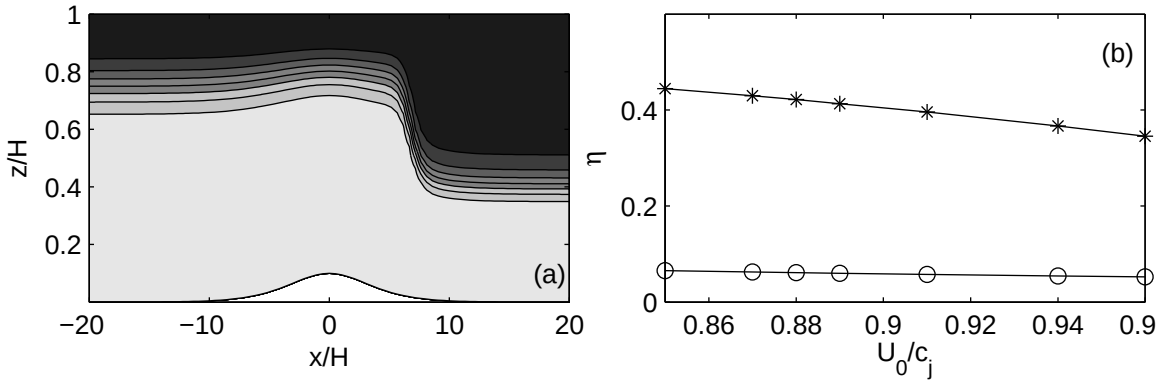

Figure 2.21: (a) An example of an asymmetric solution of the DJL equation, with $U_0 = 0.96c_j$. (b) Wave characteristics for asymmetric DJL solutions over several background speeds. The absolute value of the displacement of the $\rho = 1$ contour (scaled by $1/H$) at $x/H = 20$ (*) and at $x/H = 0$ (o) are shown. Reprinted with permission from Soontiens, N., M. Stastna, M. L. Waite (2013). Trapped internal waves over topography: Non-Boussinesq effects, symmetry breaking and downstream recovery jumps. *Phys. Fluids 25*, 066602. Copyright 2013, American Institute of Physics.

2.4 Discussion and Future Work

This chapter has presented examples of very large internal waves trapped over topography in a variety of situations, primarily focusing on results from the DJL equation, an exact theory which is equivalent to the steady Euler equations of motion. Although these trapped waves can reach amplitudes much larger than the limiting amplitude of freely propagating internal waves, they are found to be stable through reproduction in numerical time-dependent simulations that begin from a state of rest. Several different scenarios have been examined, including flows with a shear background current, flows over elevation and depression topography, flows with the Boussinesq approximation relaxed, and flows that are subcritical with respect to the conjugate flow speed away from hill topography but supercritical over it. This section summarizes these results and provides a discussion on connections to the relevant literature.

First, this work has presented derivations of the DJL equation in two cases for flow over topography: a Boussinesq fluid with a non-constant background current and a non-Boussinesq fluid with constant background current. These derivations correspond closely with that presented by Stastna (2001) for a freely propagating wave with shear background current. Other derivations for the DJL equation exist (e.g. Long, 1953; Brown and Christie, 1998), however, the derivations presented here provide some clarity in the form of the DJL equation for these specific cases. Abridged versions of these derivations were presented in Soontiens et al. (2010) and Soontiens et al. (2013b). Additionally, two numerical methods have been presented for the efficient computation of DJL solutions. An embedded boundary method, adapted from concepts by Laprise and Peltier (1989) but altered to examine a general density stratification and rigid lid upper boundary condition, offers the most efficient computations with increase in grid size.

For flows with shear background currents under the Boussinesq approximation multiple states were discovered for a given background current and density stratification. Sheared background currents were not considered for non-Boussinesq flows. These were computed from both the DJL theory and the numerical simulations. Indeed, the DJL results matched well with numerical simulations, except in some special cases of vortex cores when the stratification is close to the surface (see the discussion two paragraphs below). The DJL theory allows for an efficient exploration of parameter space, from which hysteresis loop graphs for several values of U_0 and shear ΔU were produced. Generally, multiple states existed only for U_0 close to the conjugate flows speed, while the large U_0 values produced a narrowing of the hysteresis loops. The occurrence of multiple states is not a phenomenon that is unique to continuously stratified flows over topography. Indeed, Lawrence (1987) found multiple states in steady flow over topography in a single layer fluid. The results

indicate that flow history is an important component in the outcome of steady flows. For instance the rate of acceleration in the numerical simulations determined whether a large- or small-amplitude wave developed. In the cases of constant background current no instances of hysteresis were discovered except for very narrow topographies.

The symmetry about the mid-depth between freely propagating waves of elevation and depression motivated the question of whether a similar symmetry condition exists for elevation and depression waves trapped over topography. The results indicated that large waves over depression topography are generally much larger than the largest waves of elevation. This discrepancy between elevation and depression waves was explained in terms of the local conjugate flow speed, which decreases (increases) for deeper (shallower) domains, hence changing the criticality of the flow near the topography. The local conjugate flow speed generalizes the notion of the local Froude number by Baines (1995) for single layer flows. Future work will consider an in-depth analysis of the balance of forces responsible for the large-amplitude waves.

Regions of closed streamlines, or vortex cores, were examined in two scenarios: for a flow with a negative shear current but constant density stratification near the surface and for a flow with density stratification close to the surface but constant background speed. In each of these cases, both DJL solutions and numerical simulations were presented, although the DJL technique is somewhat arbitrary since $z - \eta$ extends outside of the physical domain in the core region. Other theories have attempted to describe vortex cores in a steady framework using the DJL equation (Helfrich and White, 2010; King et al., 2011). The results from this chapter indicate that these structures are likely not steady especially when the density stratification changes near the surface, in which case, active regions of overturning persisted for long times. As such, the wave-induced velocity profiles throughout the core region from the DJL theory did not match well with the time-dependent results. However, the case with a background shear current agreed reasonably well with numerical simulations throughout the entire water column. Nevertheless, three-dimensional simulations are necessary to confirm the stability and quasi-steady nature of these structures.

Comparisons between Boussinesq and non-Boussinesq solutions outline the details of how the Boussinesq approximation breaks down for large density differences, a topic that has not been thoroughly investigated for trapped waves over topography. Relaxation of the Boussinesq approximation causes a more gradual transition from large- to small-amplitude waves as U_0 increases and the transition becomes even more gradual as the density jump, $\Delta\rho$ increases. A careful comparison between variations on the DJL equations reveals that the extra nonlinear terms in the non-Boussinesq DJL equation are responsible for the more gradual transition, at least for the stratifications considered here. Additionally, the revised

definition of the buoyancy frequency appears to be responsible for the slight variations in amplitude for the largest waves. Interestingly, the non-Boussinesq and Boussinesq waves do not deviate largely for the smallest values of U_0 even for large $\Delta\rho$. Rather it is for moderate values of U_0 where the Boussinesq waves have significant error, particularly for $\Delta\rho \gtrsim 0.1$. For the cases considered here, the differences between the Boussinesq and non-Boussinesq definitions of buoyancy frequency were noticeable only for large density jumps. Future work will examine pycnocline density profiles that include a linearly stratified layer.

Finally, this work presents a tool for studying subcritical flows with asymmetric states across the topography. Similar flow conditions have been studied using weakly nonlinear theory or for layered flows (Grimshaw and Smyth, 1986; Baines, 1995), however, not much has been presented for a continuously stratified fluid in a fully nonlinear framework. Since these asymmetric states have large amplitudes, they break the small-amplitude assumption of weakly nonlinear theory, and should be studied from a fully nonlinear perspective. Future work will compare weakly nonlinear and fully nonlinear results for these types of flow conditions.

The adaptation of the DJL theory to produce asymmetric states in subcritical flows is novel, and has connections with the work of Smith (1985), who used the DJL equation as a theory for downslope wind storms in mountain wave applications. These results also consisted of asymmetric states with flat isopycnals away from the topography, but was applied only to the constant N stratification of the atmosphere, yielding a linear equation for the streamline displacement. Although this approach is not entirely consistent with the physics it attempts to explain (for example, it uses a linear equation to represent a phenomenon which is associated with nonlinear events such wave breaking and it considers constant background wind when observations suggest a critical level is associated with these events), this theory has gained considerable traction in the literature. Often times, simple theories can lead to useful insights. The adaptation of the DJL theory to study subcritical asymmetric states in continuously stratified flows offers a considerable amount of simplicity when compared to weakly nonlinear and time-dependent strategies. Moreover, it could serve as a useful, fully nonlinear test for numerical models since the solution is laminar. However, it does not provide any information about the transient states, which, in some cases, are some of the most interesting features found in this flow environment. Additionally, it offers only a limited range of validity since DJL theory assumes no upstream propagating disturbances. Although the cases presented here are subcritical with respect to the conjugate flow speed, no significant upstream modes developed for the cases tested, hence the DJL theory can be applied.

Overall, the use of the DJL equation to examine trapped internal waves over topography in a steady framework has led to many useful insights. First, it provides an efficient

exploration of parameter space and predictions of the size and shapes of trapped waves. For example, changes in the density stratification, background current, and topographic profile are easily and efficiently studied using the DJL theory. From these results, interesting cases may be selected for further examination in time-dependent simulations. Second, the steady studies have provided insights into when and how the Boussinesq approximation breaks down under these flow conditions, which is considerably more difficult to study using time-dependent simulations for the number of cases considered here. This work has provided a thorough investigation of steady trapped waves over topography and provides opportunities for extensions to subcritical flows and asymmetric states.

Chapter 3

Topographically Generated Internal Waves and Boundary Layer Instabilities

3.1 Introduction

The previous chapter considered inviscid steady flow over topography, in which certain parameter regimes led to very large internal waves trapped over topography. One may wonder whether these internal waves could interact with the bottom boundary layer when viscous effects are taken into account. Several studies have pointed to an important link between propagating internal solitary waves and boundary layer instabilities. Bogucki et al. (1997) have observed increased concentrations of particulate matter spread high into the water column following the passage of an internal solitary wave packet on the California shelf (in this situation the stratification is concentrated near the bottom). These waves were hypothesized to be resonantly generated by flow over topography and have been suggested to interact with the viscous bottom boundary layer to cause sediment resuspension through vortex shedding and high bottom shear stress.

Later, Bogucki and Redekopp (1999) proposed a mechanism to explain the sediment resuspension behaviour and the effects of propagating internal solitary waves of elevation on the bottom (though note these authors erroneously supposed the necessity of closed streamlines or a trapped core). They observed that the wave-induced velocities beneath an internal solitary wave of elevation led to an adverse pressure gradient which, in turn, initiated a separation bubble within the boundary layer at the front of the wave. Under

certain conditions related to the wave amplitude and Reynolds number, this separation bubble could evolve into a global instability with large variations in both space and time and vortex shedding high into the water column. Larger amplitude waves induce a stronger adverse pressure gradient and, as such, are more susceptible to vortex shedding. The vortex shedding and global instability produce strong bottom shear stresses which enhance sediment resuspension. Stastna and Lamb (2002b) examined this behaviour numerically and found vortex shedding could occur when internal solitary waves of elevation travelled in the presence a background current and that a trapped core was not necessary prior to the onset of vortex shedding.

Various other studies have worked to evaluate a critical wave amplitude and Reynolds number required for vortex shedding (Diamessis and Redekopp, 2006; Carr et al., 2008). In particular, the laboratory experiments of Carr et al. (2008), which involved internal solitary waves of depression, found qualitative agreement in the behaviour of vortex shedding with the numerical results of Diamessis and Redekopp (2006). However, several quantitative discrepancies were found. For example, the critical wave amplitude required for the onset of global instability found by Carr et al. (2008) was roughly half that found by Diamessis and Redekopp (2006). This is perhaps due to the three-dimensional effects that are present in the laboratory experiments but not in the numerical studies. Stastna and Lamb (2008) suggest that the weakly nonlinear representation of large waves used by Diamessis and Redekopp (2006) may lead to an overestimate in the prevalence of vortex shedding. Under certain stratification conditions, KdV or first order weakly nonlinear theory is known to overestimate wave speeds and underestimate wave widths for very large waves which extend beyond the validity of the theory. In fact, the absence of vortex shedding in the laboratory experiments of internal solitary waves of elevation by Carr and Davies (2010) under parameter regimes where shedding was observed by Diamessis and Redekopp (2006) indicates that care should be taken when studying this phenomenon numerically. Particularly, the use of either fully nonlinear waves that are solutions to the DJL equation or the generation of the relevant internal waves as part of the simulation is most appropriate.

Bogucki and Redekopp (1999) suggest that the resonant generation of internal waves over topography could produce waves large enough to lead to global instability. Stastna and Lamb (2008) considered transcritical flow over topography and found instabilities in the lee of the topography, as well as instabilities under an upstream propagating wave upstream of the topography. Other studies on the interaction of waves over topography and vortex shedding have added to the overall picture by considering corrugated topography (Carr et al., 2010) and sloping topography (Aghsaee et al., 2012). Recently, Aghsaee et al. (2012) have proposed an alternate Reynolds number based on the momentum thickness for diagnosing and predicting vortex shedding behaviour. This alternate formulation has

the advantage that it does not depend on the stratification profile.

The present study focuses on the interaction between internal waves generated by flow over topography and the viscous boundary layer. In accord with the current literature on internal waves and boundary layer interactions, we consider lab-scale flows of 1 m depth. It is computationally expensive to model these flows at field scales since both the internal waves and boundary layer must be well-resolved. This investigation serves as a testing ground for a numerical model developed by a former graduate student (Subich, 2011). Only supercritical flows are considered so that no upstream propagating modes exist. As in the studies listed above, it is found that the internal waves generated can induce vigorous instabilities in the boundary layer. This study aims to understand the three-dimensional aspects of these instabilities and the role that viscosity plays in their evolution (with the understanding that on the field scale the physical viscosity is often too small to be of practical use in numerical simulations). The simulations discussed here are laboratory scale, with depths of 1 m, although some work in scaling up to 10 m depths has been considered. Primarily, elevated topography with a pycnocline stratification relatively close to the bottom boundary is considered. One case regarding instabilities formed due to flow over depression topography is also presented.

The chapter is organized as follows. First, a description of the methods used in this study is provided in Section 3.2. This includes an overview of the numerical model employed, the relevant non-dimensional parameters, some calculations for useful diagnostics, and a description of the domain and flow fields. Next, Section 3.3 introduces the results which examine boundary layer instabilities both upstream and downstream of flow over elevated topography, as well as a simple depression topography case. Finally, a discussion which links this work to the relevant literature and outlines avenues for future research is provided in Section 3.4.

3.2 Methodology

This section outlines the tools used to study boundary layer instabilities generated by stratified flow over topography. First, a description of the numerical model is provided, followed by the definition of the Reynolds number, an important non-dimensional parameter used in the study of viscous flows. Next, calculations for the derivation of the bottom shear stress for flow over topography are detailed. Finally, a description of the experiments, including the fluid properties and topographic shape, concludes this section.

3.2.1 Numerical Model

The DJL results presented in the previous chapter focused on steady states of inviscid flows. However, some very interesting and important features relevant to coastal oceanography and limnology, such as the interaction between internal waves and the boundary layer, require the inclusion of viscous forces. In order to study these features, a numerical model called the Spectral and Pseudo-spectral Incompressible Navier-Stokes solver (SPINS) (Subich et al., 2013) is employed. This model is used to examine boundary layer instabilities that form as a result of flow over topography and their interactions with propagating internal waves along a pycnocline stratification.

The code was developed as a PhD project by Christopher Subich; the details are outlined in his thesis and a companion paper (Subich, 2011; Subich et al., 2013). In brief, the model uses pseudospectral techniques to integrate the Navier-Stokes equations of motion for an incompressible fluid. It includes several useful features such as grid mapping for topography, free slip or no slip boundary conditions in the vertical, the ability to model three-dimensional flows, and adaptive time-stepping, all in a scalable, parallelized framework. The configuration employed in the simulations discussed below consists of periodic horizontal boundary conditions and a Chebyshev discretization in the vertical with no slip boundary conditions. The spectral methods allow for high accuracy with only moderate grid sizes, and the Chebyshev grid naturally clusters points in the boundary layer where instabilities develop. In the three-dimensional results presented here, a flow environment is first simulated in two dimensions, and the two-dimensional flow fields are used to initialize a three-dimensional simulation with a small amount of noise to perturb the flow and trip any instabilities that develop. This process allows for three-dimensional runs in a more time efficient manner, since three-dimensional simulations are very expensive computationally.

3.2.2 The Reynolds Number

Non-dimensional parameters are important tools in the study of differential equations and fluid dynamics. These parameters help to classify types of solutions and can be useful in scaling analysis as well as asymptotic and perturbation theory. In this section, a non-dimensional parameter called the Reynolds number, which is important for viscous flows, is presented and its significance is discussed.

Viscosity plays an important role in the formation of boundary layer instabilities. The effects of viscosity are characterized by the Reynolds number,

$$Re = \frac{UL}{\nu},$$

where U is a characteristic velocity scale, L is a characteristic length scale, and ν is the kinematic viscosity of the fluid. The Reynolds number is the ratio of the inertial forces to the vicious forces. Turbulent flows are often associated with large Reynolds numbers.

Typically, the choice of L is flexible and often depends on the context of the problem (e.g. flow around a cylinder, flow through a pipe, etc.). There are several variations of the Reynolds number in the literature pertaining to boundary layer instabilities and internal waves. Diamessis and Redekopp (2006) and Carr et al. (2008) use a Reynolds number based on the stratification and domain characteristics, defined as

$$Re_w = \frac{c_0 H}{\nu}, \tag{3.1}$$

where c_0 is the linear wave speed, H is the depth of the domain, and ν is the kinematic viscosity. Other variations include the momentum thickness Reynolds number employed by Aghsaee et al. (2012) defined as

$$Re_{\theta_{sep}} = \frac{U\theta_{sep}}{\nu}, \tag{3.2}$$

where θ_{sep} is the momentum thickness and U is the inviscid horizontal velocity. The momentum thickness θ_{sep} is defined so that $\rho U_0^2 \theta_{sep}$ is the amount of momentum lost due to the boundary layer at the separation point (Kundu and Cohen, 2008). This variation of the Reynolds number is more useful than Re_w since it does not depend on stratification. Additionally, Re_w does not vary with the wave amplitude, so an additional parameter is needed when classifying vortex shedding when Re_w is employed. These Reynolds numbers have been used to classify threshold values for the onset of boundary layer instability and

vortex shedding due to the effects of a propagating internal solitary wave (Diamessis and Redekopp, 2006; Carr et al., 2008; Aghsaee et al., 2012).

In the cases presented here, the main parameter of interest is the viscosity ν, hence we define the Reynolds number as

$$Re = \frac{U_0 H}{\nu},$$

where H is the depth of the domain and U_0 is the speed of the background flow. We will not be using the Reynolds number to determine a critical threshold of the onset of instability. Rather, the Reynolds number is used to classify flow conditions, mainly, changes in viscosity.

3.2.3 Bottom Shear Stress

This section outlines the derivation of bottom shear stress, a useful diagnostic in the analysis of boundary layer instabilities. First, a discussion of the shear stress in the case of a flat bottom is provided. The shear stress calculation over bottom topography is slightly more complicated and is also presented.

For a flat bottom surface at $z = 0$, the shear stress is given by,

$$\tau = \mu \frac{du}{dz}\bigg|_{z=0} \tag{3.3}$$

where μ is the dynamic viscosity, and u is the along-wall flow speed (Kundu and Cohen, 2008). The bottom shear stress is an important factor in the suspension and transport of sediment. Empirical evidence suggests that a critical shear stress is required for the onset of sediment transport. As such, parametrizations for sediment pickup and transport have been developed and used in numerical simulation (García, 1999). These pickup parametrizations are often framed in terms of the critical shear stress, which depends on particle size and other properties of the sediment.

Shear Stress with Bottom Topography

The derivation is based on Cauchy's stress theorem which relates the stress vector to the Cauchy stress tensor, τ_{ij}. Cauchy's stress theorem (Kundu and Cohen, 2008) states

$$t_i = \tau_{ij} n_j, \tag{3.4}$$

where $\mathbf{t}$ is the stress vector in a plane with unit normal vector $\mathbf{n}$. For an incompressible fluid, the stress tensor is given by

$$\tau_{ij} = -p\delta_{ij} + 2\mu e_{ij} \tag{3.5}$$

where p is the fluid pressure, μ is the dynamic viscosity, and δ_{ij} is the Kronecker delta. The strain rate tensor, e_{ij}, is given by

$$e_{ij} = \frac{1}{2}\left(\frac{\partial u_i}{\partial x_j} + \frac{\partial u_j}{\partial x_i}\right). \tag{3.6}$$

Consider a topography given by $z = h(x)$. The unit normal vector is

$$\mathbf{n} = \frac{1}{\sqrt{1 + h'(x)^2}} \left(-h'(x), 0, 1\right)^T, \tag{3.7}$$

where the $'$ indicates differentiation with respect to x. Substituting this expression into Cauchy's stress theorem (3.4) gives the stress vector

$$\mathbf{t} = \begin{pmatrix} \tau_{11} & \tau_{12} & \tau_{13} \\ \tau_{21} & \tau_{22} & \tau_{23} \\ \tau_{31} & \tau_{32} & \tau_{33} \end{pmatrix} \begin{pmatrix} -h'(x) \\ 0 \\ 1 \end{pmatrix} \frac{1}{\sqrt{1 + h'(x)^2}}. \tag{3.8}$$

Further simplifying to

$$\mathbf{t} = \begin{pmatrix} -\tau_{11}h'(x) + \tau_{13} \\ -\tau_{21}h'(x) + \tau_{23} \\ -\tau_{31}h'(x) + \tau_{33} \end{pmatrix} \frac{1}{\sqrt{1 + h'(x)^2}}.$$

Using the expression for the Cauchy stress tensor, τ_{ij} from (3.5) and (3.6) we have

$$\mathbf{t} = \begin{pmatrix} -h'(x)\left(-p + 2\mu u_x\right) + \mu\left(u_z + w_x\right) \\ -h'(x)\mu\left(v_x + u_y\right) + \mu\left(v_z + w_y\right) \\ -h'(x)\mu\left(w_x + u_z\right) - p + 2\mu w_z \end{pmatrix} \frac{1}{\sqrt{1 + h'(x)^2}}.$$

We are interested in the bottom shear stress so we will consider the tangential component of the stress vector,

$$\begin{aligned} t_t &= \mathbf{t} \cdot \left(1, 0, h'(x)\right)^T \frac{1}{\sqrt{1 + h'(x)^2}} \\ &= \frac{2\mu h'(x)\left(w_z - u_x\right) + \mu\left(1 - h'(x)^2\right)\left(u_z + w_x\right)}{1 + h'(x)^2}, \end{aligned}$$

after simplification. The normal component is

$$\begin{aligned} t_n &= \mathbf{t} \cdot (-h'(x), 0, 1))^T \frac{1}{\sqrt{1+h'(x)^2}} \\ &= \frac{-p\left(1+h'(x)^2\right) - 2\mu h'(x)\left(w_x + u_z\right) + 2h'(x)^2 \mu u_x + 2\mu w_z}{1+h'(x)^2}. \end{aligned}$$

The bottom shear stress is given by the tangential component and thus

$$\tau = \frac{2\mu h'(x)\left(w_z - u_x\right) + \mu\left(1 - h'(x)^2\right)\left(u_z + w_x\right)}{1+h'(x)^2}. \tag{3.9}$$

For a flat surface, we should recover the bottom shear stress from (3.3). Indeed, a flat surface implies $h'(x) = 0$ so (3.9) reduces to

$$\tau = \mu\left(u_z + w_x\right).$$

Considering the boundary conditions at the surface, in particular, no normal flow requires that $w = 0$ along the surface. Hence, the stress reduces to

$$\tau = \mu \frac{du}{dz}$$

and the expected bottom stress is recovered.

3.2.4 Description of Experiments

The main point of interest in this chapter involves internal waves that are generated by a constant background current U_0 (outside the boundary layer) in a stratified fluid flowing over a bottom topography $h(x)$ and the interaction of these waves with the bottom boundary layer. A description of the topography, domain, and fluid properties is provided next, followed by a summary of simulation parameters.

Domain and Topography

In the x and z directions, the physical domain is bounded by $[-L_x/2, L_x/2] \times [h(x), H]$, where L_x is the streamwise length of the domain, $h(x)$ is the bottom topography, and H is the vertical extent of the domain. Some simulations are extended to a third, spanwise dimension (y), where the length in this dimension is typically $L_y = 0.1H$. In these

cases the grid spacing in the spanwise direction is set to closely match the grid spacing in the streamwise direction (x). The three-dimensional simulations are initialized with perturbed data from a two-dimensional run. The initialization data was chosen from a time when the flow is believed to be primarily two-dimensional but is close to the onset of three-dimensionalization. This is done in order to reduce computational cost. Several initialization times are chosen in these cases in order to determine the optimal time for beginning the three-dimensional simulation. Restart times are selected for outputs where the instabilities are beginning to form as observed by irregularities in the boundary layer but no small-scale motion within the instabilities is present. The onset of three-dimensionality occurs following many time steps after the commencement of the three-dimensional simulation.

The general form of the topography is given by

$$h(x) = \frac{h_0}{2}\left(\tanh\left(\frac{x + x_L/2}{\delta_x}\right) - \tanh\left(\frac{x - x_L/2}{\delta_x}\right)\right),$$

where h_0 is the topographic amplitude, x_L defines the width of the topography, and δ_x is a parameter that affects the slope. In most cases, elevation topography is considered with $h_0 = 0.1H$, but a depression case with $h_0 = -0.1H$ is also included. The parameters x_L and δ_x are varied between a few different values and the simulation parameters are summarized in Table 3.1. An example of a typical topography is displayed in Figure 3.1. This figure corresponds to the topography used in the simulations that examine downstream instabilities. This topography includes an extended flat region at its centre to contrast the $\text{sech}^2()$ profiles from the previous chapter.

Fluid Properties

A single pycnocline stratification is used, with the undisturbed density profile given by

$$\rho(z) = 1 - \Delta\rho \tanh\left(\frac{z - z_0}{d_0}\right).$$

In this definition, z_0 is the pycnocline location, d_0 determines the thickness of the pycnocline, and $\Delta\rho$ is half of the density difference across the pycnocline. This density profile has been normalized by a constant reference value ρ_0 (Subich et al., 2013). For the purposes of calculating stress values, a reference density typical of water, $\rho_0 = 1000$ kg m^{-3}, is used. Other density parameters are set as $z_0 = 0.3H$, $d_0 = 0.1H$, and $\Delta\rho = 0.02$. One simulation with depression topography uses $z_0 = 0.7H$.

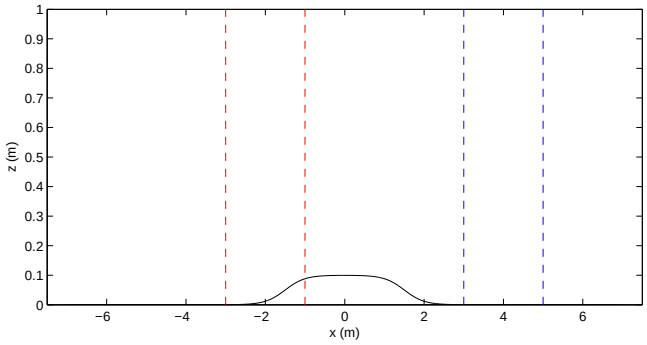

Figure 3.1: A visualization of the domain and topography for the simulations corresponding to the downstream instabilities summarized in Table 3.1. The red dashed lines indicate the region where upstream instabilities form and the blue dashed lines indicate the region where downstream instabilities form.

A constant background velocity of $U_0 = 0.35$ m s^{-1} in the x direction is used in each simulation. This velocity was chosen so that the flow would be supercritical with respect to upstream propagating internal waves. Numerically, this background current is implemented by accelerating the fluid from rest over a period of 10 seconds to allow the boundary layer to develop.

Simulation Parameters

Two types of instabilities will be examined in this chapter: instabilities that form on the upstream side of the topography and instabilities that form in the lee of the topography. The results will primarily focus on elevated topography, but one case with depression topography is considered. The role of topographic slope is investigated for the upstream instabilities, which are examined in a two-dimensional framework. Additionally, the downstream instabilities are examined in three-dimensional simulations with the objective of understanding the effect of viscosity on the three-dimensionalization process. The simulation parameters for these sets of experiments are outlined in Table 3.1.

The domain size and number of grid points changes between a few of the simulations, and as such, we have experimented with several different resolutions. The "Upstream instabilities" simulation employs the finest vertical resolution with Δz as small as 1×10^{-4} m in the boundary layer up to $\Delta z = 0.004$ m in the middle of the domain. There were many grid points throughout the boundary layer, however, note that the boundary layer does grow with time. At an intermediate time, $t = 40$ s, the boundary layer is approximately

Table 3.1: Summary of parameters for simulations with SPINS. L_x (m) and H (m) are the length of the domain in the x and z directions, respectively. N_x and N_z are the number of grid points in x and z.

Description	Domain size	Grid size	x_L (m)	δ_x (m)	ν (m^2 s^{-1})
Upstream instabilities	50×1	5000×400	3	0.5	10^{-6}
Upstream, slope	60×1	9000×200	4	0.8	10^{-6}
Downstream, $Re = 350000$	$14 \times 0.1 \times 1$	$2944 \times 48 \times 192$	3	0.5	10^{-6}
Downstream, $Re = 175000$	$14 \times 0.1 \times 1$	$2944 \times 48 \times 192$	3	0.5	2×10^{-6}
Downstream, $Re = 87500$	$14 \times 0.1 \times 1$	$2944 \times 48 \times 192$	3	0.5	4×10^{-6}
Hole, $Re = 350000$	$14 \times 0.1 \times 1$	$2944 \times 48 \times 192$	3	0.5	1×10^{-6}

0.025 m thick, divided over many grid points (more than 50). At a later time, $t = 72$s, the boundary layer expands to approximately 0.04 m thick. The horizontal resolution in this case is $\Delta x = 0.01$ m. Hence, the high resolution simulations are very well resolved. When the number of vertical grid points is reduced to 200 the grid spacing in the boundary layer is still quite small with approximately 30 points across the boundary layer 0.04 m thick boundary layer at $t = 72$ s and $\Delta z = 0.008$ m in the middle of the domain. The three-dimensional simulations used a similar vertical resolution and had approximately equal grid spacing in the streamwise and spanwise directions.

3.3 Results

The results are organized as follows: First, a general overview of the flow environment is provided, focusing on the generation of internal waves by supercritical flow over topography and the interaction of these internal waves with the bottom boundary. Next, instabilities that form on the upstream side of the topography are examined more closely. The downstream instabilities are then examined in three-dimensional simulations, focusing on the role of viscosity. Finally, three-dimensional instabilities that from in the separation region by flow over depression topography are considered.

3.3.1 General Results

A general overview of the flow environment is provided in Figure 3.2 where we have plotted the streamwise velocity in the lowest 50% of the domain and vorticity in the lowest 20% of the domain at several output times in the case of flow over elevated topography. The parameters used in this case are from the "Upstream instabilities" simulation in Table 3.1. The result is similar to a situation described by Stastna and Lamb (2008) where resonantly generated internal waves by transcritical flow over topography were produced. In Stastna and Lamb (2008), the authors observed an acceleration of flow on the downstream slope of the topography, which in turn induces a convergence zone in the topographic lee. Boundary layer instabilities formed in the convergence zone, and led to vigorous motions within the boundary layer. These instabilities subsequently interacted with the topographically generated internal waves. They also observed an instability and separation bubble forming on the upstream side of the topography. This bubble was induced by an upstream travelling internal solitary wave. In the results of Stastna and Lamb (2008) the flow was described as transcritical because the Froude number $F_r = U_0/c_{lw}$ was close to one, where c_{lw} is the linear long wave speed. In these results, we consider a supercritical flow for which $U_0 > c_j$, where c_j is the conjugate flow speed as described in the previous chapter. For the stratification presented here the linear long wave speed is $c_{lw} = 0.25$ m s^{-1}, the conjugate flow speed is $c_j = 0.28$ m s^{-1} and the background flow speed is $U_0 = 0.35$ m s^{-1}.

Figure 3.2 showcases a similar scenario to that described by Stastna and Lamb (2008). Over the topography a trapped wave of elevation is formed and directly in the topographic lee the isopycnals are displaced below their far upstream value for early times (e.g. Figure 3.2 (a)). Immediately following the location of downward displaced isopycnals, a wave train of slightly elevated isopycnals forms and travels downstream as time progresses (Figure 3.2 (a), (c)). The downstream flow can thus be understood as a lee wave of depression

terminated by an undular bore. Eventually, the undular bore region is strongly affected by the boundary layer instabilities underlying it, as demonstrated in Figure 3.2 (e) and (g) where short scale oscillations throughout the pycnocline are apparent. The boundary layer instabilities form as a result of the convergence induced by the accelerated flow in the footprint of the topographic lee wave. At the earliest times in Figure 3.2 (a), the accelerated flow terminates at $x \approx 4$ m but this region moves downstream at later times. In Figure 3.2 (b) instabilities are beginning to form in the boundary layer between $x = 3$ m and $x = 4$ m, just upstream of the termination point of the accelerated flow region.

By $t = 30$ s in Figure 3.2 (c), (d) the boundary layer instabilities are well developed. At later times in Figure 3.2 (e-h), the instabilities become more vigorous and travel downstream along with the elevated isopycnals, interacting with the pycnocline along the way. As a rough estimate, the region that contains the instabilities is advected downstream at a rate of approximately 0.1 m s $^{-1}$, which is slower than the background speed due to the frictional effects of the boundary. Additionally, as suggested by Stastna and Lamb (2008), the downstream depression wave in the topographic lee is upstream oriented so that it would travel upstream if it were not being advected downstream by the background current. The three-dimensional nature of these instabilities will be studied more closely in Subsection 3.3.3. An interesting feature at $t = 50$ s in Figure 3.2 (g), (h) is the beginning of an instability on the upstream slope of the topography around $x = -2.5$ m. In the work by Stastna and Lamb (2008) an upstream instability also forms as the result of a separation bubble induced by an upstream travelling internal solitary wave. In their results, this instability remains in the footprint of the internal wave of elevation as it travels upstream. Since the flow is supercritical in this case no upstream travelling wave is possible, yet an instability still forms. This instability will be investigated more closely in Subsection 3.3.2.

A closer examination of the boundary layer environment is provided in Figure 3.3 where we plot the scaled bottom shear stress over time. The bottom shear stress is defined in Equation 3.9. The value of the upstream stress has been subtracted in these plots. For the times plotted here the maximum stress observed was on the order of 0.4 kg m^{-1} s^{-2}. This plot demonstrates that the instabilities can induce large stresses compared to upstream values, and hence, may be important for sediment resuspension as discussed in many other studies (Bogucki et al., 1997; Bogucki and Redekopp, 1999). At the latest times, $t = 44$ s and $t = 48$ s, the onset of the upstream instability is apparent.

Although not shown here, a third region of instability was observed in these simulations. These instabilities formed along the upper boundary $z = 1$ m in the right half of the domain, downstream of the topography. Unlike the downstream bottom boundary instabilities, the generation point of these instabilities remained stationary. These features will not be discussed in this chapter since the no slip condition along the upper bound-

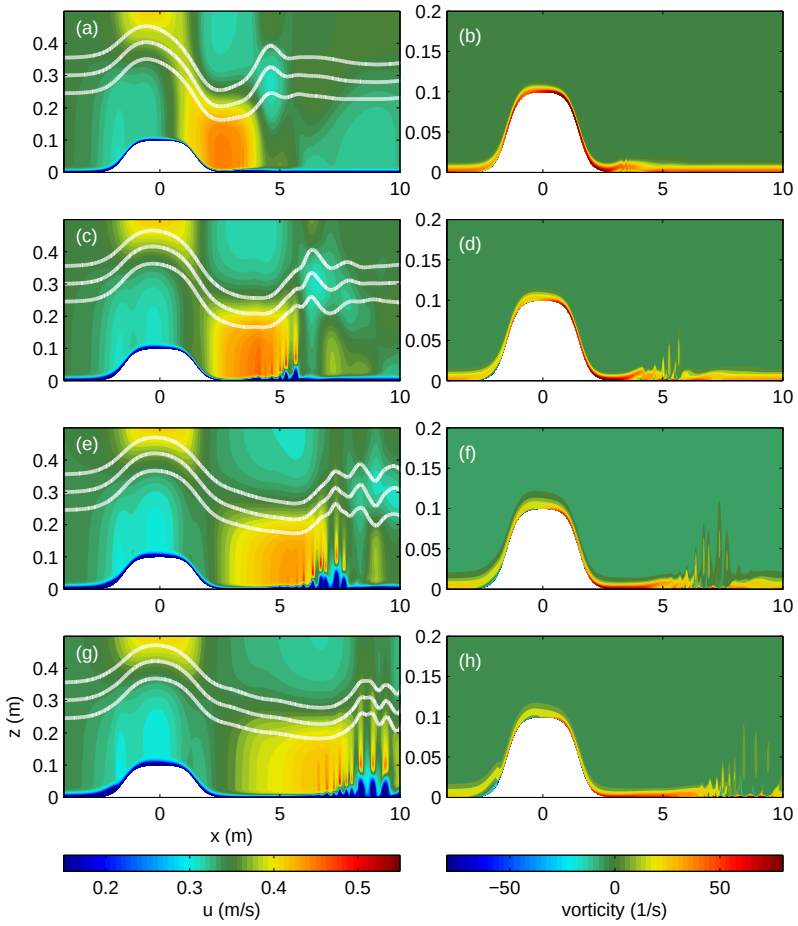

Figure 3.2: A general overview of the flow environment in the case of elevated topography. Shaded contours of the streamwise velocity overlaid with three white density contours through the pycnocline on the left and shaded contours of vorticity on the right. The results are displayed for four times: (a-b) $t = 20$ s, (c-d) $t = 30$ s, (e-f) $t = 40$ s, and (g-h) $t = 50$ s. These results are from early times of the "Upstream instabilities" experiment described in Table 3.1

ary is not physical for coastal ocean and lake applications though it could be relevant for an experimental flume. The instabilities are not expected to affect the results here since they are rather isolated from the stratification and do not interact with the pycnocline or propagating internal waves.

One last issue that remains to be discussed in this general overview is the adequacy

of the resolution employed in these simulations. The results presented here used a grid of size 5000×400 in the horizontal and vertical respectively. The numerical model uses a Chebyshev discretization in the vertical, hence, grid points are clustered near the upper and lower boundary and the vertical grid spacing is not uniform. Hence, the 0.04 m thick boundary layer at $t = 72$ s is very well resolved with on the order of 50 grid points across the boundary layer vertically. Horizontally, the grid spacing is uniform with $\Delta x = 0.01$ m and the instabilities are believed to be very well resolved. It was found that inadequate vertical resolution resulted in velocity overshoots at the top of the boundary layer upon acceleration of the fluid from rest. No such overshoots were observed in the results presented here under high vertical resolution. The formation of the boundary layer instabilities, both upstream and downstream, did not change in the presence of the overshoots, hence three-dimensional simulations use a lower vertical resolution in order to achieve practical computation timelines.

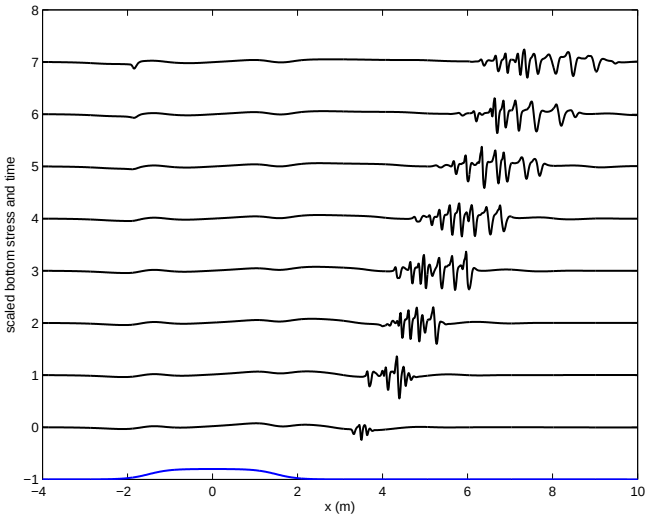

Figure 3.3: The departure of bottom shear stress from its upstream values at several times for the simulation presented in Figure 3.2. The vertical axis indicates the times in seconds at which the stress is calculated. The blue curve indicates the bottom topography.

3.3.2 Upstream Instabilities

The upstream instabilities are an interesting phenomenon that require further investigation. In Figure 3.4, the deviation in the bottom shear stress from its upstream value is plotted for several times. This plot demonstrates that the instability grows over time and may have the potential to shed vortices that travel downstream with the background current. Indeed, at the latest time displayed in Figure 3.4, $t = 84$ s, the onset of this behaviour is observed, where oscillations in the bottom shear stresses appear as far downstream of the generation site as $x = -1$ m. This is the latest time in the simulation output. The upward slope of the hill topography, as well as the supercritical flow, will naturally lift these vortices and send them over the topographic crest. Vortex shedding induced by boundary layer instabilities has been examined in a number of studies including numerical simulations and laboratory experiments (Stastna and Lamb, 2002b; Diamessis and Redekopp, 2006; Carr et al., 2008; Aghsaee et al., 2012). These studies have determined that there is a critical wave amplitude and Reynolds number for vortex shedding induced by propagating internal solitary waves of depression and elevation over a flat bottom. In some cases, the vortices could ascend high into the water column, interacting with the propagating wave or pycnocline. Aghsaee et al. (2012) concluded that their threshold criterion could not be carried over to higher Reynolds number flows because the three-dimensional effects of the turbulent boundary layer would likely be important and not accounted for in their two-dimensional simulations. The simulations we have considered use Re_w on the same order of magnitude as Aghsaee et al. (2012) ($Re_w \sim O(10^5)$) in a three-dimensional framework, although we do not consider a wide enough range of parameters in order to add to the threshold condition for vortex shedding.

While streamwise periodicity is convenient numerically, it is important to ensure that the observed vortex shedding behaviour is not affected by "wrap-around", since potentially, the propagating disturbances downstream of the topography could have wrapped around to modify upstream flow conditions in this plot. The Hovmöller diagram in Figure 3.5 (a) demonstrates the propagation of these disturbances throughout the domain. Due to the periodicity, the disturbances begin to interact with the upstream side of the topography at approximately $t = 74$ s, hence, the vortex shedding behaviour seen at $t = 84$ s in Figure 3.4 is likely influenced by this interaction. Nevertheless, the potential for a vortex to form on the upstream side of a hill in a geophysical framework has interesting implications for sediment transport across a topographic crest. A constant background current has the potential to initiate the formation of upstream instabilities, which could then shed vortices after an interaction with a disturbance in the flow field that has a source far upstream (perhaps due to an upstream wave disturbance). Since geophysical flows are rarely entirely

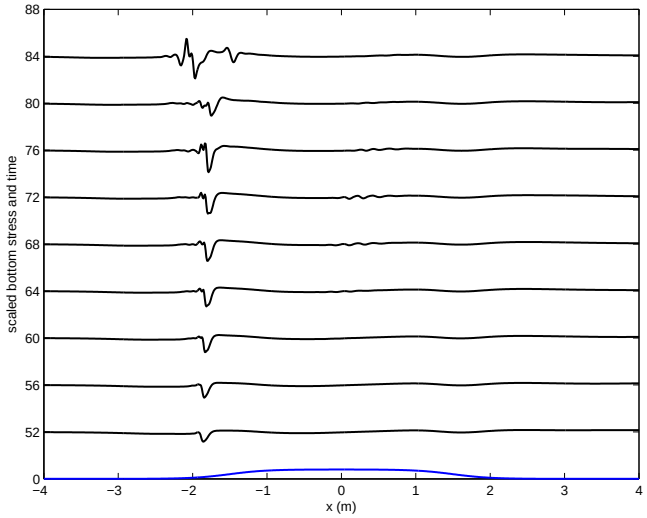

Figure 3.4: As in Figure 3.3 but at later times and focusing on the region with upstream instabilities.

steady this scenario has the potential to be realized in the field, and is perhaps more likely to be realized than a more idealized instability argument based on mathematical stability analysis of a simple flow.

The vortex shedding behaviour is visualized further in Figure 3.5 (b) and (c) where we have plotted the vorticity at two times: $t = 72$ s and $t = 84$ s. In Figure 3.5 (b) there is a clear difference in the thickness of the boundary layer upstream of the topography ($x < -3$ m) and along the topographic slope. The vorticity is unscaled but the colour bar in the figure has been adjusted to emphasize vorticity in the boundary layer. The result is a roll up behaviour in the vorticity on the upstream slope around $x = -1.7$ m indicating that a vortex shedding event is imminent. This is prior to the interaction with the periodic flow. Note that there is a region of negative vorticity very close to the boundary approximately between $x = -3$ m and $x = -2$ m. This region is topped by a layer of positive vorticity that is predominant throughout the boundary layer. At a later time $t = 84$ s in Figure 3.5 (c), a vortex has shed and is separated from the boundary layer at $x \approx -1.5$ m. As mentioned previously, this shedding behaviour may be modulated by interaction with a propagating disturbance.

In order to determine if the vortex formation could occur without the interaction with a propagating disturbance, we have conducted an additional experiment with an extended domain, $L_x = 60$ m, but with lower vertical resolution ($N_x \times N_z = 9000 \times 200$). The

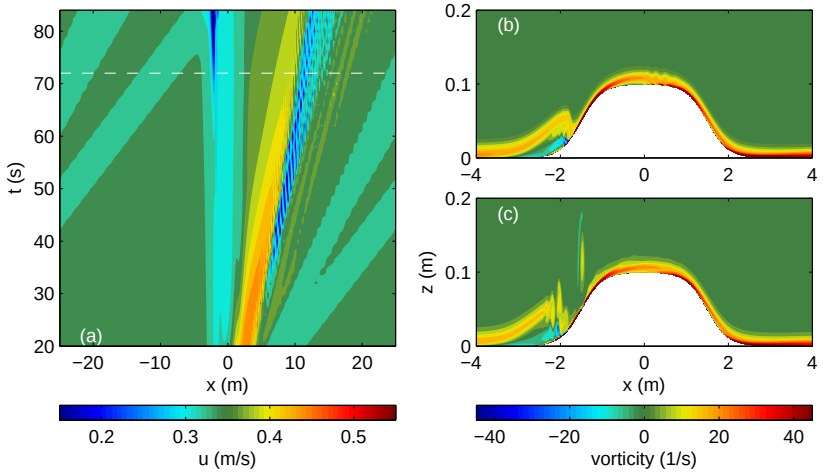

Figure 3.5: (a) A Hovmöller diagram showcasing the horizontal velocity at $z = 0.05$ m above the bottom surface throughout time. (b) The vorticity at $t = 72$ s and (c) at $t = 84$ s. The white dashed line in panel (a) corresponds to the time plotted in panel (b).

results are presented in Figure 3.6 which corresponds to Figure 3.5, but for a slightly longer simulation time up to $t = 90$ s. Here, the downstream propagating disturbances wrap around but do not reach the topography for the times displayed. In Figure 3.6 (b) at time $t = 72$ s, the roll up behaviour that was observed in Figure 3.5 is also present. Indeed, the vorticity profiles look very similar between these two plots at this time. At $t = 84$ s in Figure 3.6 (c) we start to see some deviation from the previous case. This is not expected to be caused by the lower resolution since the earlier time states are closely matched. Still, a vortex is released from the instability which travels downstream and approaches the crest of the topography around $x = -1$ m. This vortex is still quite close to the bottom boundary and its vertical scale is smaller than the one produced previously. This result indicates that vortices may be released from the upstream instability under a constant background current forcing after a significant length of time has passed. This also provides some confidence in simulations with a lower vertical resolution, since the early time features of the upstream instabilities are almost identical.

Another consideration in the formation of these upstream instabilities is the role of the shape of the topography. We have conducted an additional simulation with a reduced topographic slope as described in Table 3.1. As a result of reducing the topographic slope, we have also increased the horizontal length scale of the topography. The deviation in the bottom shear stress for this experiment is presented in Figure 3.7. The development of the

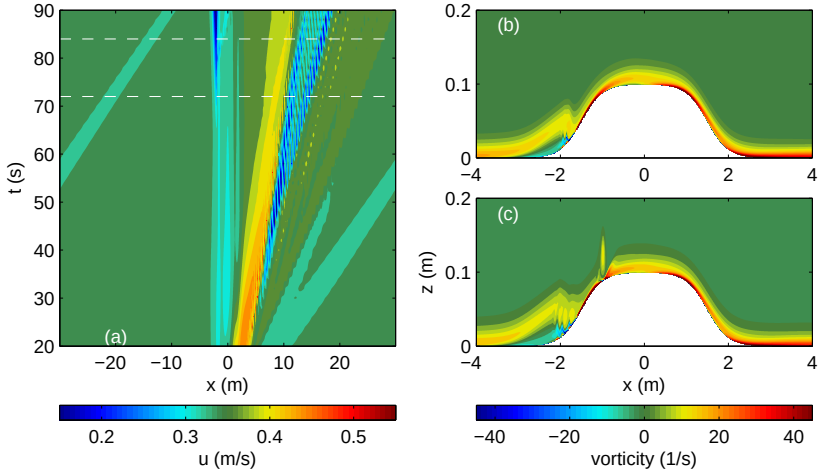

Figure 3.6: As in Figure 3.5 but for a simulation with a longer domain $L_x = 60$ m and lower resolution.

instability in this case begins at a much later time than previously ($t = 84$ s as opposed to $t = 52$ s). Perhaps this is due to the increased horizontal scale of the overlying trapped wave of elevation. As suggested by Stastna and Lamb (2008), narrower waves of elevation induce more vigorous boundary layer instabilities and vortex shedding due to the shorter horizontal length scale of the region of convergence, and hence, stronger adverse pressure gradient caused by the propagating internal solitary wave. An adverse pressure gradient acts against the flow direction to cause a deceleration. A shorter length scale over which the adverse pressure gradient develops implies a stronger gradient. Although the trapped wave is not propagating, its increased horizontal scale also leads to increased time scales in the formation of the instability.

This final case leads to some insights as to why the instability on the upstream slope of the topography forms and provides a connection to previous literature on the topic. As described by Stastna and Lamb (2008), instabilities in the footprint of an internal solitary wave of elevation form due to a convergence zone from the interaction of wave-induced velocities and the background flow. The adverse pressure gradient induced by the solitary wave is responsible for the formation of the boundary layer instabilities (Bogucki et al., 1997; Diamessis and Redekopp, 2006). In boundary layer theory, an adverse pressure gradient acts against the background flow to cause deceleration and a thickening of the boundary layer (Kundu and Cohen, 2008). This behaviour is observed along the upstream slope of the topography in Figure 3.5 (b) in the area prior to the vorticity roll-up. Downstream of this region the boundary layer is much thinner. In this region, the wave-induced

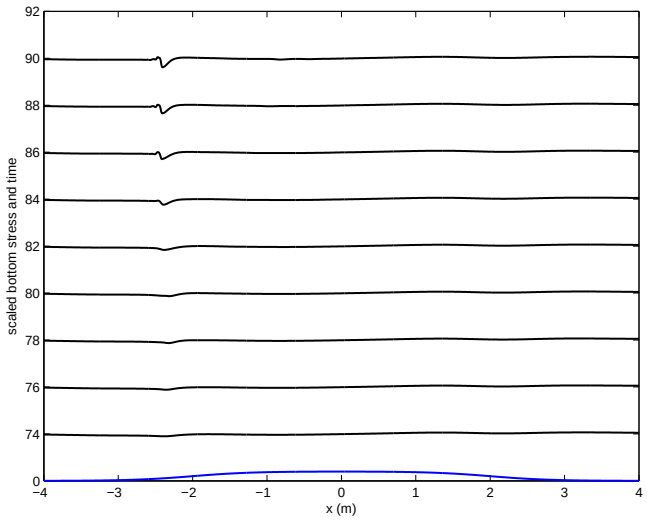

Figure 3.7: As in Figure 3.4 but for a simulation with a modified topographic slope, as described in Table 3.1.

velocities act against the background current, causing a convergence zone and the onset of an instability. For the case with a decreased topographic slope, the convergence region is stretched out horizontally due to the increased topographic length scale, hence, there is a longer timescale for the onset of instability.

Finally, the background current $U_0 = 0.35$ m s^{-1} is quite strong and is in the supercritical flow regime. This is perhaps the topographic analogue to the "strong background current" case considered by Stastna and Lamb (2008) in Figure 4 (a). The strong background current washes out disturbances downstream and no upstream propagating waves are present. As a result, a strong separation bubble forms in the footprint of the internal wave leading to instability and eventual vortex shedding. In the presence of a very weak background current no such instabilities would be expected to form, though the waves generated by the flow over the topography would be different as well. These lee waves are in a sense similar to the weakly nonlinear waves studied by Diamessis and Redekopp (2006), with higher wave-induced velocities than exact internal solitary waves.

3.3.3 Three-Dimensionalization of Downstream Instabilities

One of the major advantages of the SPINS code relative to other numerical models appropriate for studying internal gravity waves, such as IGW, is its ability to model three-dimensional flow environments with high accuracy. Many of the numerical investigations on the types of boundary layer instabilities discussed in this chapter have been two-dimensional (Diamessis and Redekopp, 2006; Stastna and Lamb, 2008). However, the often vigorous motions associated with the destabilization of a separation bubble in the viscous boundary layer is undoubtedly subject to three-dimensionalization in a physical flow environment (Alam and Sandham, 2000). As such, this next section will address the three-dimensionalization of these instabilities, focusing on the instabilities found in the lee of the topography. Here, we investigate the effect of viscosity on the three-dimensionalization process.

A description of the method employed to initialize the three-dimensional simulation is warranted. Since well-resolved three-dimensional simulations starting from a state of rest are excessively expensive, we have saved computational resources by initializing the three-dimensional simulation with two-dimensional results. A two-dimensional simulation is integrated up until the time of the onset of the downstream instabilities. These flow fields are then extended into three dimensions and perturbed slightly. The resulting fields are used as the three-dimensional initial conditions. Admittedly, the outcome of the three-dimensional simulation may be dependent on the choice of restart time and perturbation scale. As such, we have been modest in the selection of these two values. The three-dimensional simulations are started at time $t = 18$ s. As seen in Figure 3.2 (a),(b), this time is prior to the onset of the downstream instabilities. Additionally the velocity fields are perturbed multiplicatively by 0.35×10^{-4}, a few orders of magnitude smaller than the background current speed. With these choices, three-dimensional effects become apparent around $t = 23$ s, and will be discussed in detail in the following discussion. After this time, significant filtering due to unresolved turbulence is applied by the numerical model. At later times, as the instabilities begin to break down, small-scale motions are unresolved in the numerics and the spectral model applies a filter to remove aliasing error in the highest frequencies (Subich et al., 2013). As a result, spurious jumps in the density field occur due to numerical error and the simulation is terminated when this occurs.

A few comments on the computational resources is provided before the discussion of the results. Each of the three-dimensional simulations were performed on the gpc machines of the SciNet Computer Consortium (Loken et al., 2010) over a period of four days with 256 processors. The grid size was $2944 \times 48 \times 192$ in a physical domain spanning $14 \times 0.1 \times 1$ m.

First, an overview of the three-dimensional aspects of the wave and instabilities is presented in Figure 3.8 where we have plotted several flow characteristics at time $t = 23$ s for a simulation with $Re = 350000$. The wave and pycnocline are visualized through the gray $\rho = 1.005$ surface. At this time, the motion in the pycnocline is primarily two-dimensional, although the pycnocline is clearly affected by the presence of the instabilities. Three-dimensional fluctuations are observed in the red and blue contours that display the surfaces where $v = \pm 0.01$ m s^{-1}. These isosurfaces indicate that three-dimensional motions exist primarily in the region of the boundary layer instabilities. Additionally, spanwise velocities can reach a significant fraction of the background current speed which is $U_0 = 0.35$ m s^{-1}. In the spanwise direction, two wavelengths of the instability are apparent in this plot, particularly in the region where the spanwise motions are visible higher into the water column around $x = 4$ m and $z = 0.05$ m. The background surface displays the streamwise velocity through $y = 0.09$ m.

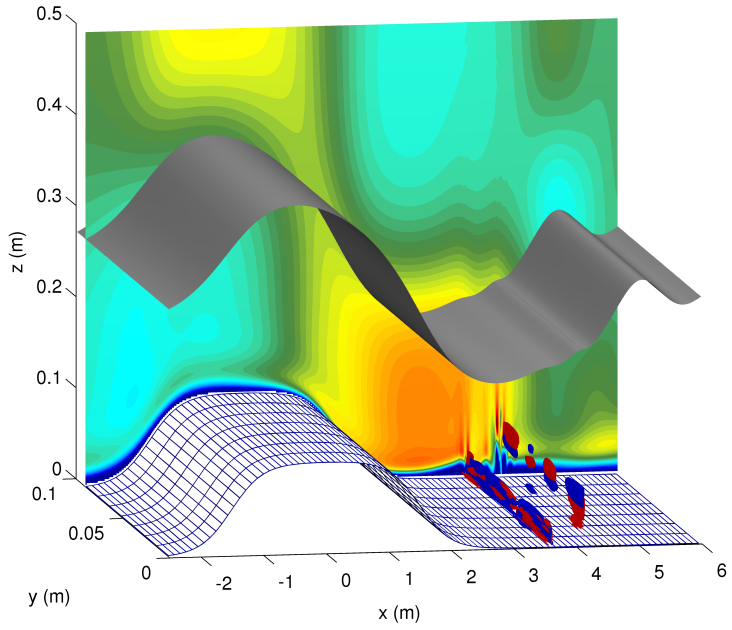

Figure 3.8: A three-dimensional image of the downstream instabilities at $t = 23$ s. The gray surface displays the $\rho = 1.005$ contour, a visualization of the wave. The red and blue colours indicate the $v = \pm 0.01$ m s^{-1} surfaces respectively. The background surface displays the streamwise velocity u with the same colour bar as that shown in Figure 3.2.

This plot provides a good overview of the three-dimensional aspects of the flow but only

from a qualitative perspective. It does not reveal how three-dimensional the instabilities are, nor where the most three-dimensional motions occur. Clearly, there is a great deal of three-dimensionality in the boundary layer instabilities and we have quantified this behaviour by examining the kinetic energy per unit mass defined as

$$KE = \frac{1}{2}\left(u^2 + v^2 + w^2\right).$$

We have developed several diagnostics that make use of the kinetic energy and provide information about the strength and location of the three-dimensionalization. First, we will present the mean kinetic energy in the spanwise direction scaled by the maximum kinetic energy. This diagnostic allows us to determine which parts of the flow have the highest spanwise mean kinetic energies, and how the mean kinetic energy profile relates to the pointwise maximum. Second, we will calculate the standard deviation of the kinetic energy in the spanwise direction and again scale it by the maximum kinetic energy. This quantity indicates spanwise departures of the kinetic energy from the mean and so, reveals how three-dimensional the flow is. Higher departures from the mean (or higher standard deviations) indicate that the flow is more three-dimensional.

These diagnostics are displayed in Figure 3.9 where we have plotted the results for the $Re = 350000$ case at time $t = 23$ s. First, in Figure 3.9 (a) the mean kinetic energy displays the signature of the internal wave overlying the topography as well as the downstream instabilities in the topographic lee. It is clear that the maximum kinetic energies occur in the instabilities, outlined by the dashed white rectangle. These instabilities induce large fluctuations in the velocity fields, resulting in the high values of kinetic energy. The standard deviation of the kinetic energy in this region is displayed in Figure 3.9 (b). As expected, the instabilities induce significant three-dimensional structure with departures greater than 10% of the maximum kinetic energy. Two vortical structures are observed in this plot at $x = 3.6$ m and $x = 4.1$ m. The first instance contains the largest departures from the mean and the three-dimensional structure is concentrated at the center of the vortex. The second instance extends higher into the water column and the largest departures from the mean occur along a longer vertical filament. This plot indicates that significant three-dimensional motions can occur close to the boundary layer and higher into the water column as the instabilities separate from the boundary.

Viscosity

Next, we will examine the role of viscosity on the three-dimensionalization process. Two additional cases are considered with $Re = 175000$ and $Re = 87500$, i.e. the viscosity has

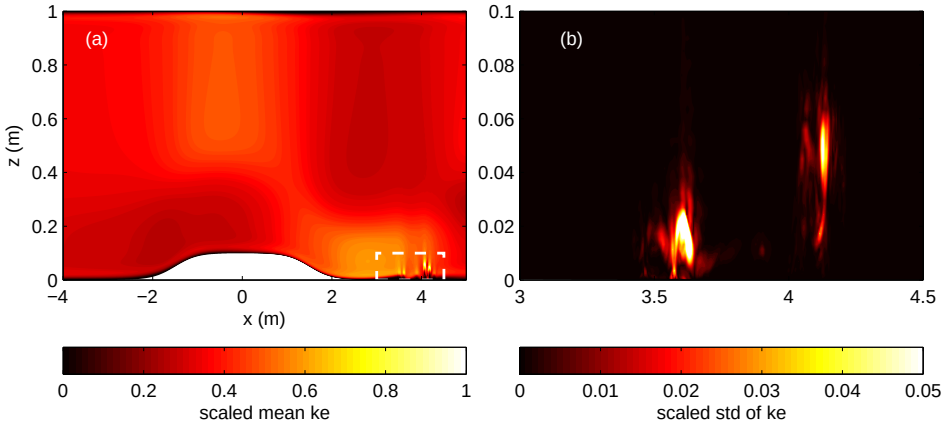

Figure 3.9: Results from the $Re = 350000$ three-dimensional simulation at time $t = 23$ s. (a) The mean kinetic energy across the spanwise direction scaled by the maximum of the kinetic energy. (b) The spanwise standard deviation of the kinetic energy scaled by the maximum kinetic energy. The white-dashed rectangle indicates the viewing area of panel (b). The maximum kinetic energy in this case was 0.17 m^2 s^{-2}.

been increased by a factor of two in each subsequent case. The same density stratification, initial state, and background speed are applied among all of the cases. Each state is first evolved in two dimensions and then extended to three dimensions at $t = 18$ s. The results of the $Re = 175000$ case are displayed in Figure 3.10. A similar scenario to that was observed in the $Re = 350000$ case is followed here. The largest values of the mean kinetic energy occur in the downstream boundary layer instabilities observed in Figure 3.10 (a). Additionally, the two vortices in Figure 3.10 (b) display a similar structure to that seen previously, however the departures from the mean are smaller than the higher Reynolds number case (the maximum kinetic energies are very similar in both cases). The increased viscosity is likely to dampen the three-dimensional motions which results is less three-dimensional structure.

Next, the Reynolds number is reduced even further to $Re = 87500$ and the results are displayed Figure 3.11. Here, we begin to see changes in the three-dimensional structure from the previous two cases. First, the distribution of high kinetic energy in Figure 3.11 (a) has changed. While high kinetic energy still occurs in the area of the instabilities, the scale is roughly the same as the kinetic energy induced by the topographic flow in the downstream accelerated region. This is qualitatively different from the previous cases where the kinetic energy induced by the instabilities is much stronger than in the other regions of the flow environment. Additionally, the three-dimensional structure has been

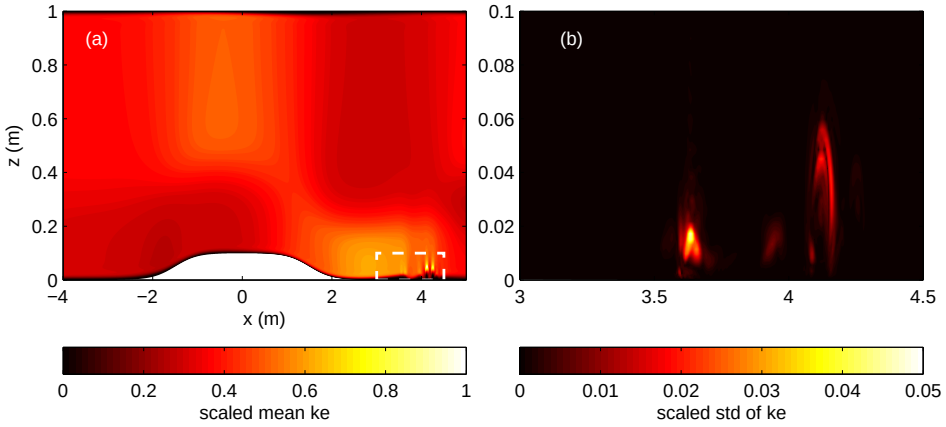

Figure 3.10: As in Figure 3.9 but for the case with $Re = 175000$. The maximum kinetic energy in this case was 0.16 $m^2\ s^{-2}$.

very much reduced, as indicated in Figure 3.11 (b). Note that the colour bar has been rescaled so that the maximum departures in this plot are less than 0.2% of the maximum kinetic energy, more than an order of magnitude less than that observed in the $Re = 350000$ case in Figure 3.9. Additionally, the maximum departures occur in the second instability, i.e. the instability that is higher up into the water column. It is not surprising that the decrease in Reynolds number reduces the propensity for three-dimensional motions since the higher viscosity tends to damp all motion. However, the fact that the Reynolds number has only been decreased by a factor of four, or indeed a factor of two between the latest two cases, and still such different results are observed is interesting. It is important to use an accurate value of the viscosity if such instabilities are to be studied in great detail. Increased computing power allows for more accurate representations of high Reynolds number flow, yet we are still on the edge of studying well-resolved, high Reynolds number flows in three dimensions.

An important question that remains to be addressed is whether the onset of three-dimensionalization would affect the likelihood that these instabilities can resuspend sediment. It is likely that the breakdown of the instabilities and transition to turbulence occurs more rapidly in three dimensions (Aghsaee et al., 2012). The results we have presented do not consider the fully three-dimensional transition to turbulence, as we are not yet equipped to fully resolve this process in a direct numerical simulation as the computation times are impractical. The three-dimensional simulations presented here each finished in four days with 256 processor utilized on the SciNet computer network. For the purpose of studying early three-dimensionalization, we found that these computations

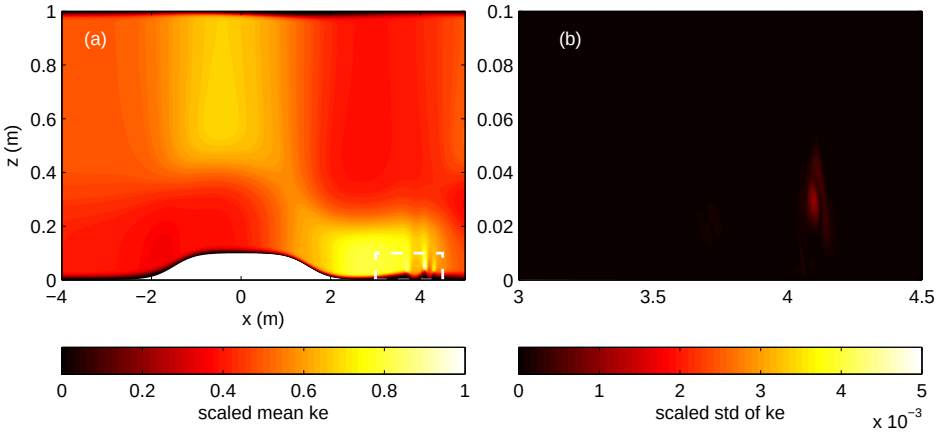

Figure 3.11: As in Figure 3.9 but for the case with $Re = 87500$. The maximum kinetic energy in this case was 0.12 m^2 s^{-2}.

were fairly expensive and we will leave a high resolution direct numerical simulation of the turbulent breakdown to other work. Yet, our results do indicate some potential for sediment transport outside of the boundary layer as the instabilities enter higher into the water column (up to $z = 0.06$ m in Figure 3.9 (b)) prior to breakdown. We conclude that these types of instabilities are likely to have an impact on sediment resuspension, prior to any turbulent, three-dimensional breakdown. This finding is supported by a discussion by Aghsaee et al. (2012) which compares the secondary, spanwise instability found in instances of wave breaking and aerofoil dynamics to the boundary layer instabilities induced by internal waves. In those circumstances, the instabilities initially retained a primarily two-dimensional structure, as was observed here. Aghsaee et al. (2012) did not examine the boundary layer instabilities in three dimensions, but rather used other three-dimensional studies to make an inference about these instabilities.

3.3.4 Depression Topography

As a final simulation, we will consider the development of boundary layer instabilities in flow over depression topography. Here, we consider the same equation for $h(x)$, but set $h_0 = -0.1$ m in order to obtain a depression rather than a hill. In addition, we have relocated the pycnocline to be centred at $z_0 = 0.7H$. As seen in the previous chapter, large waves of depression trapped over the topography may occur for a pycnocline centered above the mid-depth. This case also uses the same background current speed and velocity, $U_0 = 0.35$ m s^{-1}, giving $Re = 350000$.

An overview of the flow environment at time $t = 34$ s is provided in Figure 3.12. Similar to Figure 3.8 we have plotted a gray density surface ($\rho = 0.995$), the spanwise velocity at $v = \pm 0.02$ m s^{-1}, and the streamwise velocity in the background. In this case, the instabilities form along the leading slope of the topography, in a separation region formed by flow over this slope. This is different from the separation caused by the convergence downstream of the topography in the elevation case. Notice that no instabilities form on the downward slope of the elevated topography, even though this slope is a similar shape to the case presented here. At early times the flow on the downslope side of the elevation topography is strongly accelerated because of the large wave and there is no possibility of a separation region or reversed flow to form within the boundary layer. In the depression topography case, flows along the downslope side are relatively weak so that the adverse pressure gradient can induce flow reversal in the boundary layer.

We have also investigated the kinetic energy at this time in Figure 3.13. First, the maximum kinetic energy in this plot is much smaller than the elevation case. The instabilities in this case are less vigorous than those seen previously and remain confined to the boundary layer. The maximum energy values in this case occur close to the upper boundary where the flow is accelerated due to the formation of a propagating internal wave. Additionally, this case yields greater deviations in the kinetic energy (greater than 10% in some areas) as seen in Figure 3.13 (b) (notice that the colour bar has been adjusted). However, the instabilities are significantly less energetic than those produced in the elevation case. It is likely that the instabilities produced in the convergence zone of the elevation topography case would have a greater impact on sediment transport than the ones reported here.

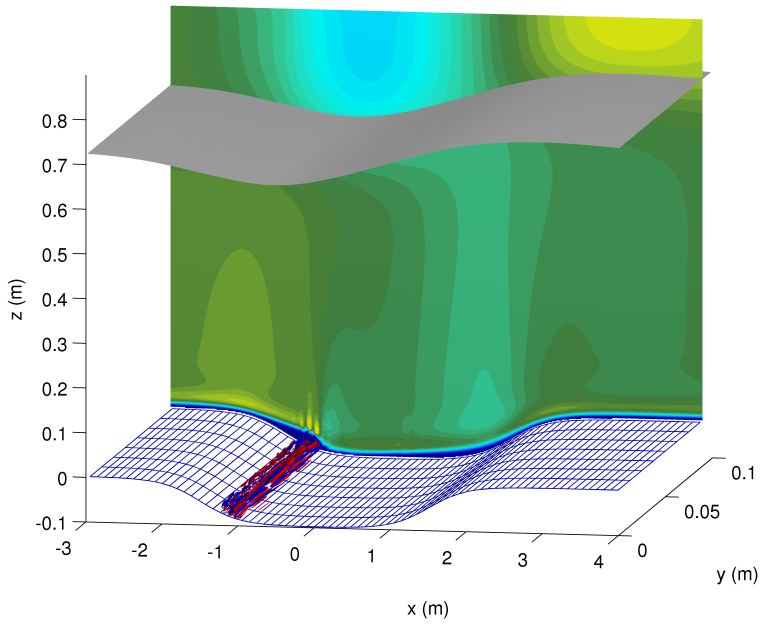

Figure 3.12: A three-dimensional image of the downstream instabilities over depression topography at $t = 34$ s. The gray surface displays the $\rho = 0.995$ contour, a visualization of the wave. The red and blue colours indicate the $v = \pm 0.02$ m s^{-1} surfaces respectively. The background surface displays the streamwise velocity u.

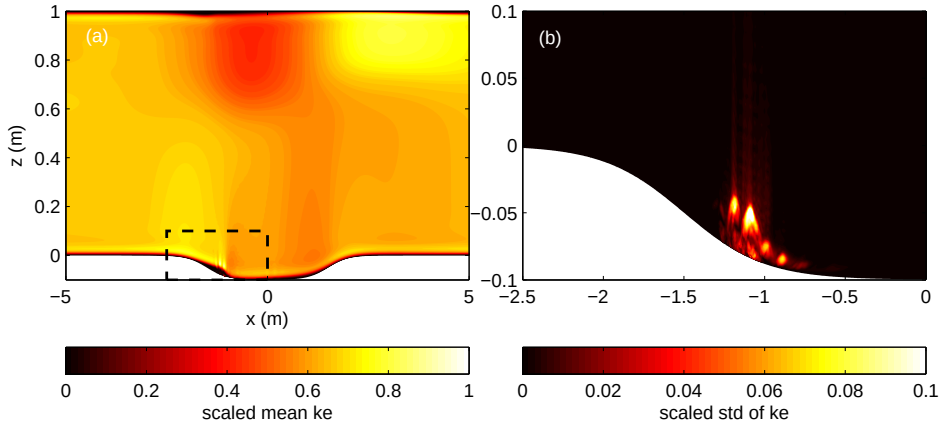

Figure 3.13: As in Figure 3.9 but for the case with a depression topography and $Re = 350000$. The maximum kinetic energy in this case was 0.09 m^2 s^{-2}.

3.4 Discussion and Future Work

In this chapter, internal waves generated by a constant background current flowing over topography were found to induce boundary layer instabilities. The interaction of internal solitary waves with the boundary layer has been investigated previously from a number of perspectives: observational, experimental, and numerical (e.g. Bogucki et al., 1997; Carr et al., 2008; Carr and Davies, 2010; Diamessis and Redekopp, 2006). The conditions that lead to boundary layer separation induced by the propagating internal solitary wave and the subsequent onset of vortex shedding have been examined in these studies. Diamessis and Redekopp (2006) and Carr et al. (2008) have both prescribed vortex shedding behaviour based on a critical wave amplitude and critical wave Reynolds number, Re_w, defined in (3.1). However, the findings of Aghsaee et al. (2012) have pointed to a more appropriate threshold condition based on the momentum thickness Reynolds number, $Re_{\theta_{sep}}$, defined in (3.2). These Reynolds number have been established in the literature, but we have applied a simpler Reynolds number based on the background flow speed in the current investigation. Carr and Davies (2010) found no separation bubble or vortex shedding in the case of waves of elevation in a parameter range similar to that used by Diamessis and Redekopp (2006). The representation of the internal solitary wave by Diamessis and Redekopp (2006) was derived from first order weakly nonlinear theory (KdV theory) which may not be applicable in the large-amplitude cases required to induce vortex shedding (Stastna and Lamb, 2008). An accurate prescription of the internal solitary wave as well as a highly accurate numerical model are required to study boundary layer instabilities numerically (Stastna and Lamb, 2002b; Diamessis and Redekopp, 2006; Stastna and Lamb, 2008). As such, we have used an approach where the solitary waves are not prescribed ahead of time, but rather, they are generated by a constant flow over topography using a spectrally accurate numerical model. We have also investigated instabilities downstream of the topography from a three-dimensional perspective, whereas most of the numerical studies to date have been restricted to two dimensions.

The cases presented in this chapter have primarily examined instabilities developed by supercritical flow over elevated topography at laboratory scales (1 m depth). Laboratory scales were examined due to the excessive computational resources required to model field-scale flows in three-dimensions with a well-resolved boundary layer. Scaled up simulations will be considered in future work. In these results, a trapped wave of elevation forms directly over the topography and, at early times, the isopycnals directly in the topographic lee are depressed below their upstream levels. In this region, the flow is strongly accelerated resulting in a convergence zone where the accelerated flow meets with the slower moving background current. The accelerated region moves downstream over time. The result is

the formation of boundary layer instabilities due to a separation bubble that forms in the convergence region. The three-dimensional characteristics of these instabilities have been investigated, primarily focusing on the effects of changes in viscosity.

The strongly accelerated flow on the lee slope of the topography is responsible for the formation of these instabilities. This is perhaps similar to the results of Diamessis and Redekopp (2006) where instabilities had formed in the rear half of an internal solitary wave of depression due to an adverse pressure gradient created by the wave-induced velocities. However, they used weakly nonlinear theory to define these waves which is known to overestimate wave speeds for certain stratifications and wave amplitudes. Hence, the strongly accelerated flow in these results may induce large velocities similar to the large velocities used in the results of Diamessis and Redekopp (2006). In both cases, instabilities were formed in the region where the flow begins to decelerate. A similar scenario was examined by Stastna and Lamb (2008) for transcritcal flow over topography.

The three-dimensionality of these instabilities was examined up until a point where the numerical model could not accurately represent the break down of the instabilities due to limits in the resolution. The formation of the instabilities in both two and three dimensions were similar. Three-dimensional effects became important around $t = 23$ s where significant deviations in the kinetic energy (greater than 10% of the maximum kinetic energy) along the spanwise direction were observed. By this time, the three-dimensional instabilities extended away from the boundary layer, hence, it is believed that three-dimensional effects would not affect the likelihood that these types of instabilities could suspend sediment at early times. However, since the instabilities would break down more rapidly in three dimensions the time scale of their effect on sediment may be altered. Reducing the Reynolds number by a factor of four through an increase in the viscosity drastically changed the three-dimensional nature of the flow due to the dampening effects of viscous flows. Only a few Reynolds number cases were discussed here so future work will consider a more thorough investigation of the effects of viscosity. Additionally, measurements of the $Re_{\theta_{sep}}$ will be evaluated for a more insightful comparison to other work. It would be useful to study these three-dimensional effects under higher resolution and further into the development of the instabilities.

Another type of instability was discovered on the upstream side of the topography after a long period of integration. This instability is perhaps akin to the one discovered by Stastna and Lamb (2008) beneath an upstream propagating internal solitary wave of elevation generated by transcritical flow over topography. Since the flow in this study is strictly supercritical, no upstream propagating disturbances are possible. Other types of topographic flows, such as flows over mountains in the atmosphere, have been known to produce upstream propagating disturbances (Epifanio and Durran, 2001) and this is

discussed in the next chapter in the context of crater topography. This instability has the potential to shed downstream propagating vortices if a constant background flow persists for long enough or if a separate disturbance interacts with the topography. Therefore, there is potential for sediment to be transported across a topographic crest through this instability mechanism. In the future, this instability could be investigated more closely by considering the effects of background speed, the topography shape, and perhaps in three dimensions. There is a clear trade off between the increased likelihood for an instability to form over a topography with a higher slope and the ability for that instability to ascend over the topographic crest. This could be investigated in a future study.

One final case considered flow over depression topography, which saw an instability form in the region of separation on the downward slope of the depression. This separation region formed due to an adverse pressure gradient along the downward facing slope. This separation region did not form in the case of elevation topography because the strongly accelerated flow overcame the adverse pressure gradient effects. Additionally, these instabilities were significantly less energetic than the instabilities observed in the elevation case (even though the spanwise variation of kinetic energy was actually a larger fraction of the maximum kinetic energy). However, this is only one scenario examining depression topography and a more thorough investigation of parameter space is necessary. For example, the parameters leading to the very large trapped waves of depression in the previous chapter may be interesting to examine here.

Of the instabilities discussed in this chapter the most significant, in terms of sediment resuspension, are those found in the lee of elevated topography. These instabilities were energetic and often extended outside of the boundary layer indicating a possibility for sediment resuspension and transport higher into the water column. This result provides an important clue as to where to expect internal wave induced sediment resusupension in the field. Field scientists interested in examining this process could place measurement devices in the downstream regions of elevated topography where lee waves are likely to form. Stratifications close to the bottom boundary may be expected to produce such resuspension mechanisms.

Chapter 4

Flow Over Large-Scale Crater Topography

4.1 Introduction

Atmospheric flow over large-scale topography such as mountains and valleys is an important part of the dynamics of the atmosphere. On large scales, the internal waves generated by flow over topography, often called mountain waves or lee waves, are known to impose a drag due to wave breaking that must be parametrized in general circulation models where their scales are not explicitly resolved (e.g. McLandress, 1998; Kim et al., 2003). On smaller scales, flow over mountain topography can have a significant impact on meteorological events such as pulsating downslope wind storms (Scinocca and Peltier, 1989), which can be hazardous to aircraft and real estate developments on the lee side of mountains. A thorough overview of the literature on mountain waves is provided in reviews such as Smith (1989), Baines (1995), and Wurtele et al. (1996).

The study of flow over crater topography has been examined to some extent in the past and has important implications for flow environments on Earth (Fritts et al., 2010; Soontiens et al., 2013a) and on other planets such as Mars (Pirraglia, 1976; Pickersgill and Hunt, 1979) where large-scale crater topography is abundant (Read and Lewis, 2004). On Mars, observations of bright depositional and dark erosional streaks of dust near craters, as well as dune-like features within crater interiors, indicate that flow over crater topography may have an influence on dust lifting and deposition (Veverka et al., 1978, 1981; Lee, 1984; Fenton et al., 2003). This chapter examines flow over large-scale crater topography using time-dependent numerical simulations with the goal of providing insights into the

dynamical processes that may be associated with dust lifting. First, an overview of the relevant literature regarding topographic flows in the atmosphere is provided.

Historically, mountain waves and topographic flows have been examined from a two-dimensional perspective, however, with the advent of increased computing power three-dimensional numerical studies have become attainable. From an analytical perspective, three-dimensional results are very difficult to obtain due to the complicated nonlinear nature of the flow, however, some theoretical techniques have been applied to small-amplitude disturbances (Wurtele, 1957; Smith, 1979). One of the fundamental differences between two- and three-dimensional flows is the manner in which wave energy propagates away from the disturbance (Smith, 1979). In the hydrostatic limit, wave energy is found directly over the topography in two dimensions but not necessarily in three dimensions, where wedge-like wave patterns may occur (Smith, 1980). As a result, wave breaking in three dimensions often requires increased topographic amplitudes when compared to their two-dimensional counterparts, since wave energy aloft may be dispersed laterally (Smith, 2003). Furthermore, with access to the third dimension, the motion at the surface level could be deflected laterally rather than over the topography, a phenomenon known as flow splitting. Lateral deflections are especially applicable to high-amplitude topography and strongly stratified fluids, and may lead to a reduction in wave amplitudes aloft, and hence may have a significant impact on wave breaking in three dimensions (Epifanio and Durran, 2001; Olafsson and Bougeault, 1996). Three-dimensional effects associated with flow over crater topography are considered in this chapter.

Another important aspect of topographic flows is the occurrence of extreme wind events in the lee of the topography called downslope wind storms. Such events can pose a hazard to aviation traffic near mountain ranges and can cause millions of dollars in property damage to settlements in the topographic lee as was the case in the Boulder, Colorado 1972 wind storm (Doyle et al., 2000). Several theories, ranging from fully nonlinear frameworks to steady-state analytical models, have been proposed to explain these wind events (see e.g. Peltier and Clark, 1979; Smith, 1985; Durran, 1986). A commonality between each of these theories is the presence of a wind-reversal or critical level. However, the function or role of this critical level is often debated. For example, Peltier and Clark (1979) suggest that the critical level acts as a reflective layer causing a resonance that amplifies velocities. By contrast, the theory proposed by Smith (1985) suggests that the critical level acts like the free surface in single layer hydraulic flows. The theory of Smith (1985) is steady and requires an *a priori* assumption of a critical level or stagnant region, and so, is not predictive. The increase in surface wind speeds caused by downslope wind storms has been suggested to have an impact on dust lifting in the Martian atmosphere under conditions associated with night-time temperature inversions (Magalhães and Young, 1995).

As such, the combination of Martian temperature inversions and crater topography will be considered in this work.

A feature often associated with downslope wind storm is the hydraulic jump, which is characterized by steepening of streamlines when fast moving fluid abruptly meets with relatively slow moving fluid (Smith, 2003; Armi and Mayr, 2011). In addition, there is often a change in potential temperature across the hydraulic jump. Traditionally, the hydraulic jump is associated with topographic flow in a single layer fluid; however, similar structures have been noted in continuously stratified flows (Smyth and Holloway, 1988; Armi and Mayr, 2011). The hydraulic jump is a feature that will be examined throughout this chapter.

The literature on orographic flows in the atmosphere is primarily focused on elevated topography such as mountains; however, crater topography has been examined to some extent in the past. Preliminary work by Pirraglia (1976) and Pickersgill and Hunt (1979) applied a steady-state linear theory to a Martian crater of 100-km diameter in order to examine lee wave characteristics. However, the authors only considered the elevated rims of the topography and neglected to include the depression of the crater bowl. On Earth, Fritts et al. (2010) used numerical simulations to study a 1.2-km diameter crater from the Arizona desert and observed a flow separation, Kelvin-Helmholtz billows, sloshing, and seiche behaviour that could be responsible for the break up of cold-pool air. Additionally, laboratory experiments have examined rotating flow over crater topography (Davies et al., 1975). Further research into topographic crater flows could provide insights into the mechanisms that are responsible for the dust streaks observed near craters on the Martian surface.

This chapter examines many of the features listed above in the context of flow over crater topography. Crater topography offers a different perspective on orographic flows when compared to traditional mountain wave studies due to the inherently three-dimensional nature of the crater shape, as well as the combination of both elevation and depression topography. The literature on mountain wave studies provides a strong foundation for pursuing more complicated topographic profiles such as craters.

This chapter is organized as follows: First, an overview of the methodology, including an explanation of the design of the topography and domain, an overview of the numerical methods employed in this chapter, an explanation of the non-dimensional parameters used to classify flow regimes, and a description of the experiments is provided in Section 4.2. Second, simulation results are provided in Section 4.3. Some of the results are reproduced from a study by Soontiens et al. (2013a) and have been expanded upon in this chapter. Finally, a summary and discussion is included in the final Section 4.4.

4.2 Methodology

An overview of the methodology is presented in this section. This includes a visualisation of the crater topography and domain, a description of the numerical model employed in the simulations, an overview of important non-dimensional parameters applicable to flow over topography, and a description of the numerical simulation sets.

4.2.1 Topography and Background State

Large crater topography of diameter 100 km and depth 2 km is used in the present numerical simulations and mathematical analysis. The crater also includes elevated topography at the crater edges to represent the rim-like structure noted in many impact craters (Jankowski and Squyres, 1992). The rim height is 100 m and the rim width is about 10 km. A visualization of the crater topography through $y = 0$ km is depicted in Figure 4.1. Other variations on the topography are considered which include a crater without rims and a crater with reduced diameter, but the main results centre on the topography depicted in Figure 4.1. The topography is centred at the origin in a domain 400 km by 400 km horizontally and 30 km vertically (unless otherwise noted below).

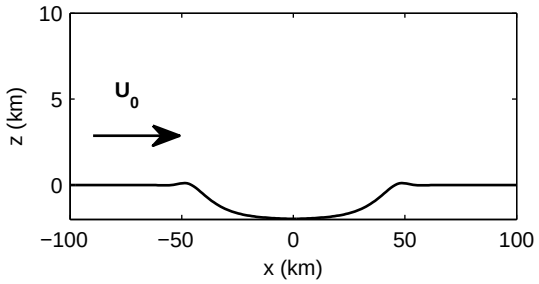

Figure 4.1: Visualization of the crater topography through $y = 0$ km. This figure has been reprinted from Soontiens, N., M. Stastna, M. L. Waite (2013). Numerical simulations of waves over large crater topography in the atmosphere. *J. Atmos. Sci. 70*, 1216. ©American Meteorological Society. Used with permission.

The equations used to define the crater topography are given by

$$h(x,y) = \frac{h_0}{2}\left(1 - (1+h_r)\,\mathrm{sech}\left(\frac{r-r_c}{2x_a}\right)\right)\left(-1 + \tanh\left(\frac{r-r_c}{x_a}\right)\right), \tag{4.1}$$

where

$$r = \sqrt{x^2 + y^2}.$$

The parameters h_0, r_c, h_r, and x_a control the crater depth, crater radius, rim height, and crater wall slope, respectively. In the base case, these parameters are set to $h_0 = 2$ km, $r_c = 50$ km, $h_r = 0.1$, and $x_a = 5$ km. The result is the crater shape depicted in Figure 4.1. The crater dimensions were chosen to be in line with previous work on flow over crater topography (Pirraglia, 1976; Pickersgill and Hunt, 1979) and to approximately match with survey data of Martian crater profiles (Burt et al., 1976; Jankowski and Squyres, 1992).

Previous studies on flow over crater topography have been considered in the context of the Martin atmosphere (Pirraglia, 1976; Pickersgill and Hunt, 1979) and Earth's atmosphere (Fritts et al., 2010). Pirraglia (1976) and Pickersgill and Hunt (1979) both examine a crater topography of diameter 100 km in a model Martian atmosphere with discontinuous wind profiles using linear theory. Their results displayed a ship-wake pattern of waves in the lee of the crater. An important difference between their work and the results presented here pertains to the profile of the crater topography used in the analysis. The crater used by Pirraglia (1976)and Pickersgill and Hunt (1979) only represented the rim structure and neglected the depression topography of many impact craters. On Earth, craters are typically much smaller and one such crater from the Arizona desert is considered in work by Fritts et al. (2010). These authors modelled a crater of diameter 1.2 km and examined the sloshing and mixing of the cool air within the crater depression. These previous studies provide a foundation that can be expanded upon in the study of flow over crater topography by representing larger craters and the inclusion of depression topography.

The background atmospheric profile is stratified with constant buoyancy frequency N, given by

$$N^2 = \frac{g}{\bar{\theta}} \frac{d\bar{\theta}}{dz}, \tag{4.2}$$

where $\bar{\theta}(z)$ is the background potential temperature and g is the acceleration due to gravity. This stratification defines a background potential temperature profile given by

$$\bar{\theta}(z) = \theta_0 \exp\left(\frac{N^2}{g} z\right), \tag{4.3}$$

where θ_0 is the potential temperature at $z = 0$. The surface potential temperature is set as $\theta_0 = 288$ K for Earth-like atmospheres and $\theta_0 = 203$ K for Mars-like atmospheres.

The background wind is constant in the streamwise (x) direction, with $U_0 = 10$ m s^{-1}. In addition, the standard base case considered in these results sets the buoyancy frequency as $N = 0.01$ s^{-1}. Several variations on the background atmospheric conditions are considered and will be discussed in later sections.

4.2.2 Numerical Model and Domain

Simulations in this chapter were performed with the Advanced Research dynamical core of the Weather Research and Forecasting model (WRF) in its idealized configuration (Skamarock et al., 2008). This model integrates the fully compressible, non-hydrostatic Euler equations of motion using a terrain-following vertical coordinate system and an Arakawa C-grid. The time stepping scheme employs a splitting method in order to treat the acoustic modes without using an excessively small time step. The WRF model has many adaptable features, such as the inclusion of planetary boundary layer parametrizations and options for running simulations with the hydrostatic approximation. Most of the simulations presented here employ the basic configuration, however some experiment with planetary boundary layer schemes and hydrostatic dynamics are discussed.

The WRF model is a powerful tool used by many atmospheric scientists on projects from numerical weather prediction to idealized simulations. The simulations presented here use the idealized approach in order to gain understanding of the dynamical processes without the influence of complicated chemistry and cloud physics which can occur in the real atmosphere. The goal is not to reproduce all aspects of the atmosphere perfectly, but rather to study one aspect of a dynamical process that can occur in a stratified fluid. In this case, the focus is on the internal waves generated over crater shaped topography.

In addition to WRF, another tool for modelling atmospheric flows is the planetWRF model (Richardson et al., 2007). This work has modified the WRF architecture to consider large-scale atmospheric flows on other planets such as Mars, Venus, and Titan. While the planetWRF model was not used extensively in this research since we were focused on mesoscale dynamics and idealized flows rather than planetary scales, the model was helpful in choosing potential temperature and wind profiles that are more representative of a Martian atmosphere. Several simulations with Martian atmospheric parameters are presented in this thesis.

The WRF simulations use a numerical grid that is uniform horizontally with equal grid spacing in the streamwise (x) and spanwise (y) directions. The grid is stretched vertically to produce finer grid-spacing ($\Delta z \approx 120$ m) near the surface up to $\Delta z \approx 500$ m in the upper atmosphere. The vertical grid spacing does not exceed $\Delta z = 150$ m below $z = 15$ km. Several variations on the resolutions are discussed in these results, however, a typical simulation uses horizontal resolution $\Delta x = \Delta y = 500$ m and 200 vertical grid points. The boundary conditions are open in the x direction and symmetric in the y direction. At the lower boundary, free-slip boundary conditions are employed. This lower boundary condition is in line with other studies of inviscid topographic flows (e.g. Bell and Thompson, 1980; Lee et al., 2006); however, several simulations with a parametrized boundary layer

and surface friction are also considered. A Rayleigh damping layer begins at $z = 15$ km in order to prevent wave reflections from the upper boundary. The initial velocity profiles are

$$(u_0, v_0) = (U_0, V_0),$$

and the initial vertical velocity, w_0, is set by the WRF preprocessing system (Skamarock et al., 2008). In most cases $V_0 = 0$ m s^{-1}, however one case considers a shear wind in the spanwise direction as described below. Most of the numerical simulations were performed on the GPC supercomputer at the SciNet HPC Consortium (Loken et al., 2010).

4.2.3 Non-Dimensional Parameters

Several parameters have been used to classify characteristics of flow over topography in a stratified fluid with constant background speed and constant buoyancy frequency (Afanasyev and Peltier, 1998). These parameters are based on physical properties of the fluid, such as the buoyancy frequency N and the background wind U_0, as well as properties of the topography, such as the vertical scale h and horizontal scale a. In the case of atmospheric flows, the buoyancy frequency is defined in terms of the background potential temperature and is given in Equation 4.2.

The main parameter of interest in this study governs nonlinear effects and is given by

$$F_r = \frac{U_0}{Nh}.$$

This parameter compares the vertical length scale of the flow, that is, a measure of the vertical wavelength of vertically propagating waves (U_0/N) to the vertical length scale of the topography, h. It is often called a Froude number or the non-dimensional mountain height in the case of elevated topography. Nonlinear effects such as upstream blocking and flow splitting are favoured when F_r is small, i.e. the topography scale is large compared with the vertical scale of the flow. In the case of the crater topography, the vertical scale h is chosen to be the crater depth so that $h = 2$ km. With the other atmospheric properties, $U_0 = 10$ m s^{-1} and $N = 0.01$ s^{-1}, the base case is characterized by $F_r = 0.5$ which indicates that nonlinear effects will likely be observed in the base case.

The parameter F_r is used in many mountain wave studies to characterize the onset of gravity wave breaking, flow splitting, and upstream blocking (Baines, 1987; Smith, 2003). Flow splitting describes the tendency for fluid to pass around an obstacle rather than over it in the presence of high obstacles or strong stratification (hence small F_r) (Smith, 1989). Similarly, in two dimensions or for nearly two-dimensional topography,

upstream blocking is a phenomenon in which near-surface fluid is blocked by the obstacle and cannot pass over (Baines, 1987). Again, this can occur when F_r is small. In the context of depression topography such as craters, this parameter may not characterize these phenomena when h is chosen as the crater depth since the topography is not elevated. However, F_r can characterize situations better suited to depression topography, such as sweeping and stagnant flows. Previous numerical simulations and laboratory experiments examine the influence of F_r on flow over valley topography (Bell and Thompson, 1980). The authors found that a thermal stratification could be swept out of a valley for large values of F_r (i.e. $F_r > 1.3$). Although the scales are much different in the crater experiments, this aspect of sweeping flows is considered in the results.

The next non-dimensional parameter governs non-hydrostatic effects,

$$F_a = \frac{U_0}{Na},$$

where a is the horizontal scale of the topography. Similar to F_r, this parameter encompasses a comparison of length scales, i.e. the vertical scale of the flow to the horizontal scale of the topography. The flow is said to be hydrostatic if F_a is small, i.e. the horizontal length scale is much larger than the vertical. Selecting a as the crater diameter, $a = 100$ km, results in $F_a = 0.01$ indicating that the flow is mainly hydrostatic. This is tested by performing simulations with the hydrostatic option in WRF and comparing with the fully non-hydrostatic results.

A final parameter of interest is commonly used in the analysis of geophysical flows and can be important for topographic flows depending on the scale of the topography. The Rossby number,

$$R_o = \frac{U_0}{fa},$$

describes the importance of rotational effects by comparing the magnitude of the inertial force to the Coriolis force. Rotational effects become important when R_o is small. Taking $f = 10^{-4}$ s^{-1}, a value typical of midlatitudes on Earth and Mars (Read and Lewis, 2004), results in $R_o = 1$. This value indicates that rotation may be important, hence, several simulations including the effects of rotation are considered.

4.2.4 Description of Experiments

This section describes the numerical experiments that have been performed with the WRF model software. The first set of experiments are based on Earth-like atmospheric parameters and are variations on the base case as described below. The second set of simulations

examine seiche behaviour within the crater. A third set of simulations examine the role of surface friction and planetary boundary layer (PBL) parametrizations. The PBL schemes are described below. Finally, the adaptations that are required to perform simulations with a Martian-like atmosphere are described.

Variations on the Base Case

Several variations on the atmospheric and topographic properties are applied to the base case. As described above, the base case consists of an atmosphere with constant background wind $U_0 = 10$ m s^{-1}, constant buoyancy frequency $N = 0.01$ s^{-1}, and crater topography with 2-km depth, 100-km diameter, and rims that are 100 m high and 10 km wide. This sets the nonlinearity parameter as $F_r = 0.5$ and the non-hydrostatic parameter as $F_a = 0.01$. Rotation is neglected in the base case, hence the Rossby number is not applicable. Many of the variations on the base case have been published by Soontiens et al. (2013a) and will be reproduced here.

One of the atmospheric modifications consists of an atmosphere with reduced buoyancy frequency, $N = 0.005$ s^{-1}, giving $F_r = 1$. This value of N is closer to the value in the Martian atmosphere, which is often cited as $N = 0.006$ s^{-1} (Read and Lewis, 2004). Another atmospheric modification considers an atmosphere stratified in two layers, with constant potential temperature below $z = 0$ km within the crater and $N = 0.01$ s^{-1} above. In addition, a case with a spanwise shear in the background wind is also considered. The topographic modifications include a crater with no rims and a crater with reduced diameter (increased curvature). Finally, rotation is applied to the base case and the two-layer atmosphere using a Coriolis parameter of $f = 10^{-4}$ s^{-1}. The important parameters in these simulations are outline in Table 4.1.

In addition, several of these simulations have also been performed in two dimensions. The two-dimensional version of the topography is taken as a cross-section through $y = 0$ km. This cross-section is the most useful for comparison since the spanwise velocity is zero along $y = 0$ km due to symmetry. Additional cross-sections were considered as well, but the comparisons are less useful due to spanwise motions in three dimensions.

Table 4.1: Summary of simulation parameters for variations on the base case.

Description	N (s^{-1})	a (km)	F_r	F_a	R_o
Base case	0.01	100	0.5	0.01	N/A
Reduced stratification	0.005	100	1	0.01	N/A
Two-layer	0.01 for $z > 0$, 0 below	100	0.5, $z > 0$	0.01	N/A
Spanwise shear	0.01	100	0.5	0.01	N/A
No rims	0.01	100	0.5	0.01	N/A
Increased curvature	0.01	40	0.5	0.025	N/A
Rotation, base case	0.01	100	0.5	0.01	1
Rotation, two-layer	0.01 for $z > 0$, 0 below	100	0.5, $z > 0$	0.01	1

Seiches

Another set of numerical experiments investigates seiche behaviour within the crater. These experiments are initialized with no background wind, hence $U_0 = 0$ m s^{-1}, and tilted potential temperature contours within the crater. The initial potential temperature profile is visualized in Figure 4.2. Several variations on this set up include simulations with and without rotation, as well as explorations with higher resolution. The simulations are outlined in Table 4.2. These seiche experiments are meant to investigate any seiche motion within the crater in the absence of a background wind in order to study the seiche behaviour independently from the background forcing.

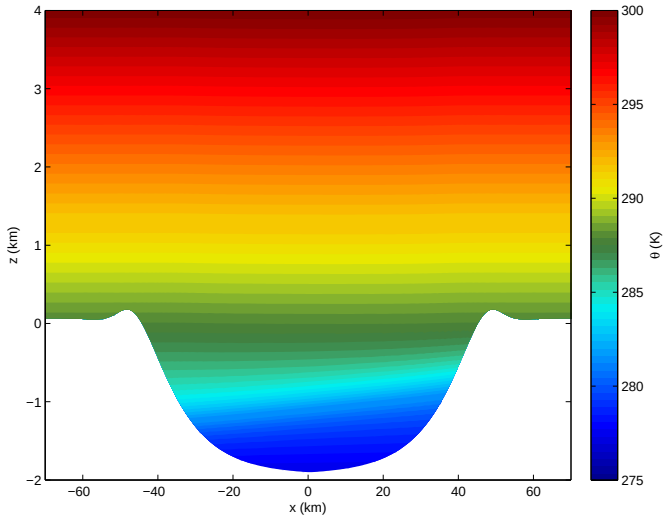

Figure 4.2: The initial potential temperature profiles for the seiche simulations.

The seiche experiments are motivated by work by Fritts et al. (2010) where time-dependent forcing was used to reproduce seiche behaviour in a small crater of 1.2-km diameter in Arizona. Fritts et al. (2010) chose periodic forcing based on the calculation of a fundamental seiche period, T_0. This calculation can be repeated for the large craters as a test to determine if seiching behaviour is expected in our basic simulations and in order to justify considering these seiche study extensions. The calculation is based on shallow water theory from Csanady (1967), defining

$$T_0 = \frac{\lambda_h}{c},$$

where $\lambda_h = 2D$, D is the diameter of the crater, and c is an equivalent shallow water phase

Table 4.2: Summary of parameters in seiche simulations. The Coriolis parameter is denoted by f and N_x, N_y, and N_z are the number of grid points in x, y, and z respectively. $\Delta x$and Δy are the horizontal grid spacings and $Delta_z$ is the approximate vertical grid spacing near the surface.

Description	f (s^{-1})	$N_x \times N_y \times N_z$	$\Delta x \times \Delta y \times \Delta z$ (m)
Low-resolution, no rotation	0	$400 \times 400 \times 250$	$500 \times 500 \times 70$
Low-resolution, rotation	10^{-4}	$400 \times 400 \times 250$	$500 \times 500 \times 70$
High-resolution, rotation	10^{-4}	$800 \times 800 \times 250$	$250 \times 250 \times 70$

speed for the crater. That is

$$c = (g_r H)^{1/2},$$

where H is the depth of the crater and g_r is the reduced gravity expressed as,

$$g_r = g \frac{H}{\bar{\theta}} \frac{\partial \bar{\theta}}{\partial z}.$$

In this expression, g is the acceleration due to gravity and $\bar{\theta}$ is the background temperature. Using parameter values from the base case yields $\lambda_h = 200$ km, $c = 10$ m s^{-1}, and hence $T_0 \approx 2.7$ hr. So, we might expect seiche behaviour in the base case simulations.

Planetary Boundary Layer and Surface Friction

A planetary boundary layer (PBL) scheme is employed in order to study the development of the topographic flow when boundary layer effects on momentum are modelled. Vertical subgrid-scale fluxes are treated by the WRF implementation of the Yonsei University (YSU) PBL in Subsection 4.3.6. The YSU PBL scheme uses counter-gradient fluxes for heat and moisture, which allows for treatment under well-mixed conditions, and an explicit treatment of entrainment at the top of the PBL (Hong et al., 2006). Surface layer friction velocities are calculated using the MM5 surface layer model (Skamarock et al., 2008), which takes wind and temperature gradients as a function of a stability parameter based on Monin-Obukhov similarity theory (Paulson, 1970).

The use of a PBL scheme is valid when there is a scale separation between resolved and unresolved eddies, an assumption which may be broken when the resolution approaches a few hundred metres (Skamarock et al., 2008). Hence, our grid spacing $\Delta x = \Delta y = 500$

m is at the small-scale end of the applicability of a PBL parametrization (e.g. Skamarock et al., 2008). As a result, an additional test with a turbulent kinetic energy (TKE) diffusion scheme for sub-grid turbulence is performed. Diffusion is parametrized using horizontal and vertical eddy viscosities, which are calculated through a prognostic equation for the TKE (Skamarock et al., 2008). The surface layer friction velocities are calculated with the same parametrization as the PBL simulation.

Martian Atmospheric Parameters

Several changes to physical constants in the WRF model enabled us to perform simulations in a Martian-like atmosphere. The new physical constants are outlined in Table 4.3 and are in line with the parameters used in the Mars version of the planetWRF model (Richardson et al., 2007).

Table 4.3: Summary of parameters in Martian atmosphere simulations.

Parameter	Earth	Mars
Acceleration due to gravity, g (m s $^{-1}$)	9.81	3.727
Gas constant, R (m^2 s^{-2} K^{-1})	287	192
Specific heat, c_p (m^2 s^{-2} K^{-1})	1004.6	768
Surface pressure, p_0 (mb)	100000	610
Air density at surface, ρ_{air} (kg m^{-3})	1.28	0.0117
Radius, r_e (m)	6370	3389.92
Buoyancy frequency, N (s^{-1})	0.01	0.006
Rotation rate, $10^{-5}s^{-1}$	7.294	7.088

Two types of scenarios are examined under Martian conditions. The first set of experiments investigates the propagation of internal gravity waves into the upper atmosphere. The temperature and wind profiles for these simulations are displayed in Figure 4.3 and are chosen from the initial conditions of planetWRF model (Richardson et al., 2007) at longitude/latitude coordinates (118 E,33 N). This profile was chosen so that the surface wind speed is approximately 10 m s^{-1} and so that the temperature profile is stable. In these simulations, the vertical extent of the atmosphere is 85 km and a Rayleigh damping layer is imposed above $z = 65$ km. Since the atmosphere is significantly higher than base case simulations in order to examine higher atmosphere dynamics, the grid size has been increased to $800 \times 800 \times 800$ with approximately the same grid spacing.

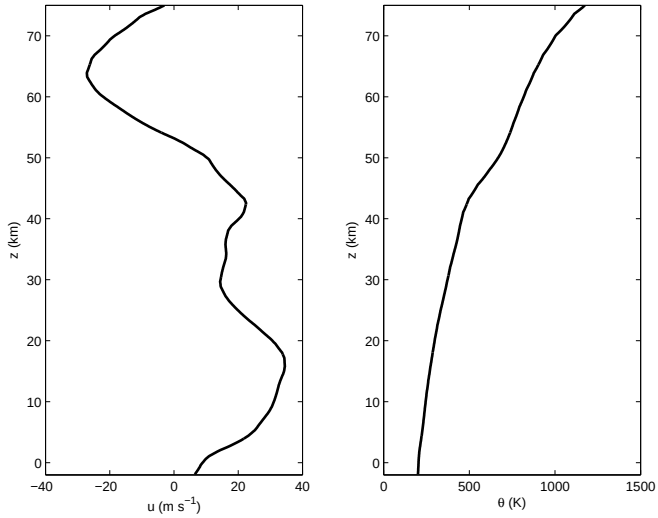

Figure 4.3: The initial streamwise velocity (left) and potential temperature (right) profiles for the simulations under Martian atmospheric conditions.

An additional set of experiments examines the effect of a near-surface temperature inversion combined with a constant background wind forcing of $U_0 = 10$ m s^{-1}. Past studies have indicated that wind-reversal levels associated with near-surface temperature inversions may lead to the development of downslope wind storms in the lee of topography (Klemp and Lilly, 1975; Vosper, 2004). Magalhães and Young (1995) have examined downslope wind storm conditions on Mars using a steady-state model for flow over bell-shaped topography based on the hydraulic flow analogy for downslope wind storms (Smith, 1985). They conclude that conditions typical of night-time temperature inversions on Mars may lead to surface wind speeds strong enough to induce dust lifting. The purpose of the next set of simulations is to evaluate the potential for dust transportation from a fully nonlinear, three-dimensional, dynamical perspective under conditions associated with temperature inversions.

In these experiments, the initial potential temperature profile is chosen to represent a night-time inversion structure based on results from a general circulation model by Rafkin et al. (2001) at the Mars Pathfinder Lander site. A potential temperature profile is constructed from these results with buoyancy frequency $N = 0.03$ s^{-1} for $z < 600$ m and $N = 0.006$ s^{-1} above, which approximately matches with the results from Rafkin et al. (2001). Stratification characteristics within crater depths are not well-known for Mars, hence, two extreme cases a considered: 1) a stratified interior with $N = 0.03$ s^{-1} throughout the entire depth of the crater up to $z = 600$ m, and 2) an unstratified interior with

$N = 0$ within the crater topped by a so-called capping inversion, with $N = 0.03$ s^{-1} for $0 < z < 600$ m and $N = 0.006$ s^{-1} above. The background wind is constant with $U_0 = 10$ m s^{-1}. The goal is to examine the wave characteristics and structures for dust lifting in each of these cases. Since near-surface features are more important than in the previous Martian investigation, the height of the numerical domain is set to 30 km as in the base case.

4.3 Results

This section includes a presentation of results from the numerical simulations. First, the base case is presented, along with the atmospheric modifications, topographic modifications, and cases with rotation. Most of those results have been presented by Soontiens et al. (2013a) and will be reproduced here with extra discussion and some expansion. Next, the seiche experiments are analyzed followed by the simulations with planetary boundary layer parametrizations and the simulations with Martian parameters.

4.3.1 Base Case, $F_r = 0.5$

The base case provides an initial picture of the flow evolution and generates a framework for understanding the physical characteristics of the flow. The additional cases explore variations in the topographic and atmospheric structure and confirm ideas about the physical processes involved with this flow set up. Several interesting features from the base case include primary waves over the leading and trailing crater edges, secondary waves over the crater centre, and the formation of a retreating gravity current which eventually behaves as a hydraulic jump-like structure. All of these features are prominent in Figure 4.4 and are detailed further below.

The most noticeable and expected features of this flow are the primary waves over the leading and trailing crater edges. These waves are formed as a response to buoyancy as air passes into the crater depths and over the trailing crater slope. These waves have vertical wavelength $\lambda_z \approx 6$ km, which matches the wavelength expected in the hydrostatic limit $\lambda_z = 2\pi U_0/N$ (Smith, 1979). Notice that the waves over the trailing crater edge are smaller in amplitude and have lower wave-induced velocities. This can be explained by the near stagnant fluid within the crater depths which effectively masks the influence of the trailing crater slope through a reduction in the effective topographic height. In addition, the characteristic horizontal length scale has increased since much of the topography's shape and slope is masked by the stagnant fluid. The result is a weaker beam of waves over the trailing edge; however, the wavelength remains the same since N and U_0 are unchanged

Another prominent feature of this flow is the low-level jet along the leading crater slope and its interaction with the cooler air within the crater depression. The low-level jet is similar to the chinook front noted in many studies on mountain waves (e.g. Kerr, 1986; Afanasyev and Peltier, 1998). Occasionally, these chinook fronts can develop into severe downslope wind storms which are associated with intensified lee slope winds and increased topographic drag (Peltier and Scinocca, 1990). During the 1970s and 1980s the

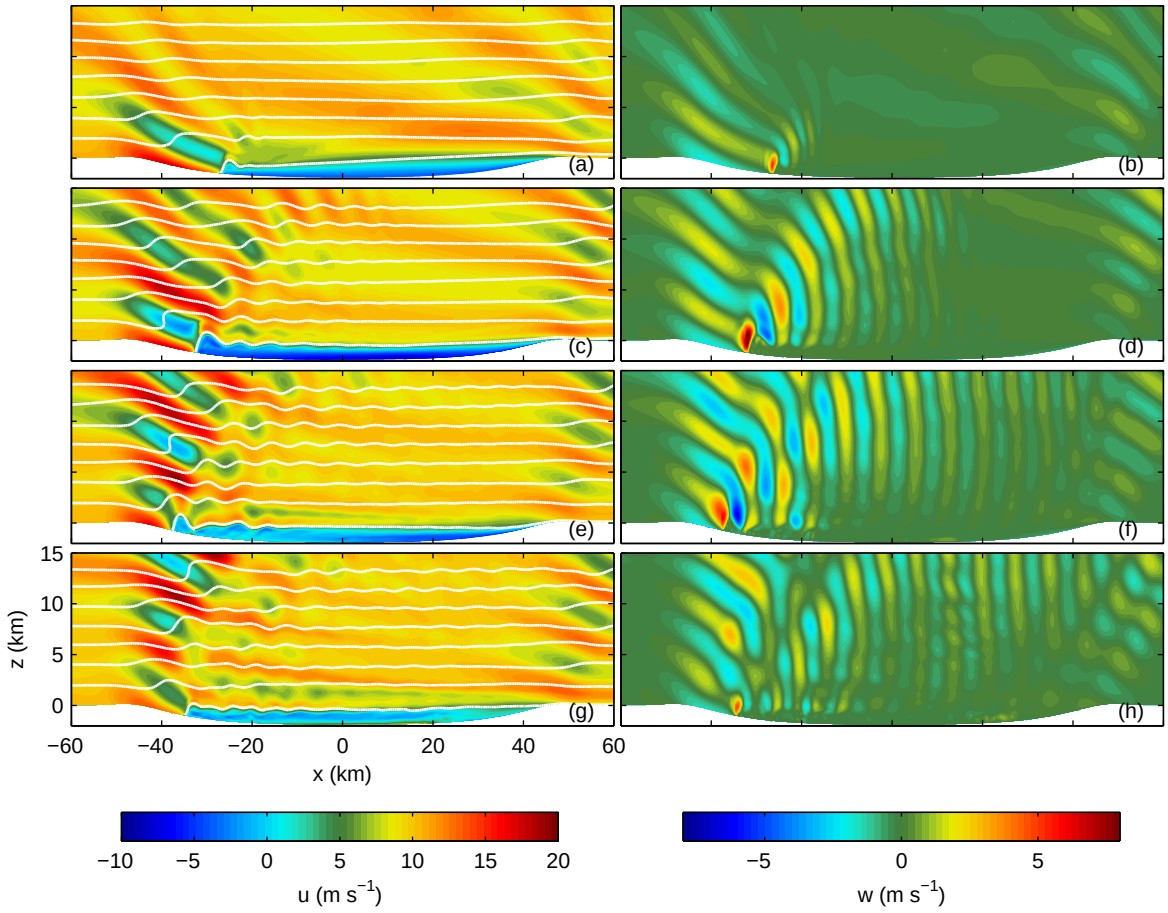

Figure 4.4: Flow evolution for the three-dimensional base case $F_r = 0.5$ simulation. Streamwise velocity with white potential temperature contours (left) and vertical velocity (right) through the crater centre, $y = 0$ km. The potential temperature contours are $\theta = [288, 294, 300, 306, 312, 318, 324, 330]$ K. The output times are $t = 1$ hr (a,b), 2 hr (c,d), 3 hr (e,f) and 4 hr (g,h). This figure has been adapted from Soontiens, N., M. Stastna, M. L. Waite (2013). Numerical simulations of waves over large crater topography in the atmosphere. *J. Atmos. Sci. 70*, 1216. ©American Meteorological Society. Used with permission.

downslope wind storm was a widely investigated topic in the study of mountain waves due to a devastating occurrence near Boulder, CO (Klemp and Lilly, 1975; Peltier and Clark, 1979). In the crater simulations, the near-surface streamwise velocities reach upwards of

17 m s^{-1} but do not exhibit the strong pulsations or gusts of a downslope wind storm.

The low-level jet more closely resembles a chinook front as described by Afanasyev and Peltier (1998). Their simulations present a chinook front which propagates downstream and away from the topography. In the case of the crater, the low-level jet interacts with the cooler crater air to cause tilting of potential temperature contours towards the trailing edge (Figure 4.4 (a)). The chinook front cannot propagate further due to the potential energy constraints of the cooler, denser crater air. After the initial tilting, the fluid readjusts to form a retreating gravity current as demonstrated by the negative streamwise velocities within the crater. The gravity current is clearly displayed by the lowest potential temperature contours in the streamwise velocity plots. This feature is similar to the seiche behaviour reported by Fritts et al. (2010) in a small crater of diameter 1.2 km, two orders of magnitude smaller than the large crater discussed here. The seiche period calculated in Subsection 4.2.4, $T_0 = 2.7$ hr, indicates that seiche behaviour should be observed in the time frame of these simulations (4 hr in Figure 4.4 and 10 hr total simulation time). However, in the large crater the potential temperature contours remain relatively flat after the initial tilting and no obvious seiche behaviour persists beyond the times in Figure 4.4. In addition, at $t = 4$ hr, the position of the gravity current head is $x \approx -35$ km where it remains relatively stationary, with adjustments of one or two kilometres. At early times, the gravity current head can be seen forming as far into the crater as $x \approx -27$ km.

Some characteristics of the gravity current resemble those of a hydraulic jump, a feature observed in several types of topographic flow (e.g. Durran, 1990; Smith, 2003; Armi and Mayr, 2011). The hydraulic jump is most often considered to be a layered fluid phenomenon, such as in the flow of a stream over a rock or in the descending flow of water along the walls of a dam. Its main features include fast moving fluid halted abruptly by slower moving or stationary fluid, an interaction which often causes severe turbulence. The term hydraulic jump has also been used in the context of continuously stratified flows. For example, the downslope wind storm is often associated with a hydraulic jump-like feature in the lee of the topography, as well as a sharp rising of potential temperature contours (Smith, 2003). In this context, the gravity current does indeed resemble a hydraulic jump since the gravity current head contains steepened potential temperature contours created when the low-level jet interacts with slower moving fluid within the crater depression. The terms gravity current and hydraulic jump are used interchangeably in the sections to follow.

The hydraulic jump has interesting implications for this flow environment because of its structure and scale. As displayed in the plots of vertical velocity, a set of waves originates from the position of the hydraulic jump. This suggests that the hydraulic jump is acting as a modified topography, forcing additional gravity waves. The concept of modified topography has been considered previously in the study of cold pools and mountain topography. Lee

et al. (1989) argued that cold pools trapped against the leeside of an elevated topography can produce a similar wave structure to a modified topography which takes into account the shape of the cold pool. In addition, there is other evidence that hydraulic jumps can act as modified topography as outlined in a review by Smith (2003). The hydraulic jump formed in these simulations is of particular interest because its height (about 1 km at $t = 4$ hr) is greater than the height of the crater rims. In fact, the hydraulic jump height is comparable to the depth of the crater. Constructing F_r based on the hydraulic jump height gives $F_r = 1$, indicating that the hydraulic jump can have a significant topographic influence which is likely more important than the crater rims which have $F_r = 10$. This suggests that the hydraulic jump can cause additional vertical displacements or even lateral deflections that are associated with other three-dimensional topographies.

The hydraulic jump is responsible for the secondary beam of waves over the crater centre. These waves are most clearly visualized in the plots of vertical velocity and are noticeable at all times in Figure 4.4. At the earliest time $t = 1$ hr in Figure 4.4 (a-b) the waves originate from $x \approx -28$ km, but later at $t = 4$ hr in Figure 4.4 (g-h) they are emanating from $x \approx -35$ km. The origin of the waves is moving with the head of the gravity current, resulting in some interesting wave structures.

The three-dimensional structure of the flow is presented in the low-level streamwise and spanwise velocities of Figure 4.5. First, the position of the gravity current head is clearly visible in the streamwise velocity plots. It is clear that the low-level jet along the leading crater slope is abruptly halted by the reversed flow of the gravity current. The gravity current front resembles the shape of the leading edge of the crater topography. This is apparent at both early and late times, although the later times show some additional small-scale motions and the gravity current front has moved closer to the leading crater edge.

The spanwise velocities provide insight into some of the three-dimensionality of the flow. Along the leading crater slope, the flow converges towards the centreline, $y = 0$ km, as it descends into the crater. However, directly behind the gravity current front a diverging pattern is noted. This is partially due to the reversed flow travelling up the crater slope, expanding outwards as it climbs. In addition, at the front of the gravity current, outwards spanwise deflections could be caused by the gravity current head itself acting as a topography. Previous work on flow splitting and lateral deflections discuss the tendency for air to pass around an obstacle, rather than over it for certain regimes of F_r and the aspect ratio of the topography (e.g. Smith, 1989; Epifanio and Durran, 2001). The hydraulic jump, with $F_r = 1$ is likely responsible for some of the lateral deflections. Interestingly, the crater rims do not appear to cause any lateral deflections even though they represent elevated topography. With $F_r = 10$, the topographic influence of the crater rims is masked

by the downward sloping crater walls. This is in line with the results of Smolarkiewicz and Rotunno (1989) who found that lateral deflections are small when $F_r \gg 1$. The gravity current head is expected to cause more spanwise motion since it has a much lower F_r. At a later time in Figure 4.5 (d), the outwards deflections near the gravity current front are more apparent in addition to further small-scale motions.

A useful diagnostic for examining the three-dimensional structure of the waves is the perturbation kinetic energy per unit mass, defined by

$$KE = 1/2\left(u^2 + v^2 + w^2\right) - 1/2\left(u_0^2 + v_0^2 + w_0^2\right), \tag{4.4}$$

where u_0, v_0, and w_0 are the initial streamwise, spanwise, and vertical velocities. This diagnostic is presented in Figure 4.6 where isosurfaces of 15% of the maximum perturbation kinetic energy at time $t = 5$ hr are plotted. The three-dimensional structure of the waves resembles a horse-shoe pattern, spreading laterally as the waves propagate upwards. Particularly in the upper part of the domain, a large proportion of the wave energy expands beyond the horizontal extent of the topography (indicated by the blue cylinder). The waves generated over the trailing crater edge are much weaker and are mainly found directly over the topography.

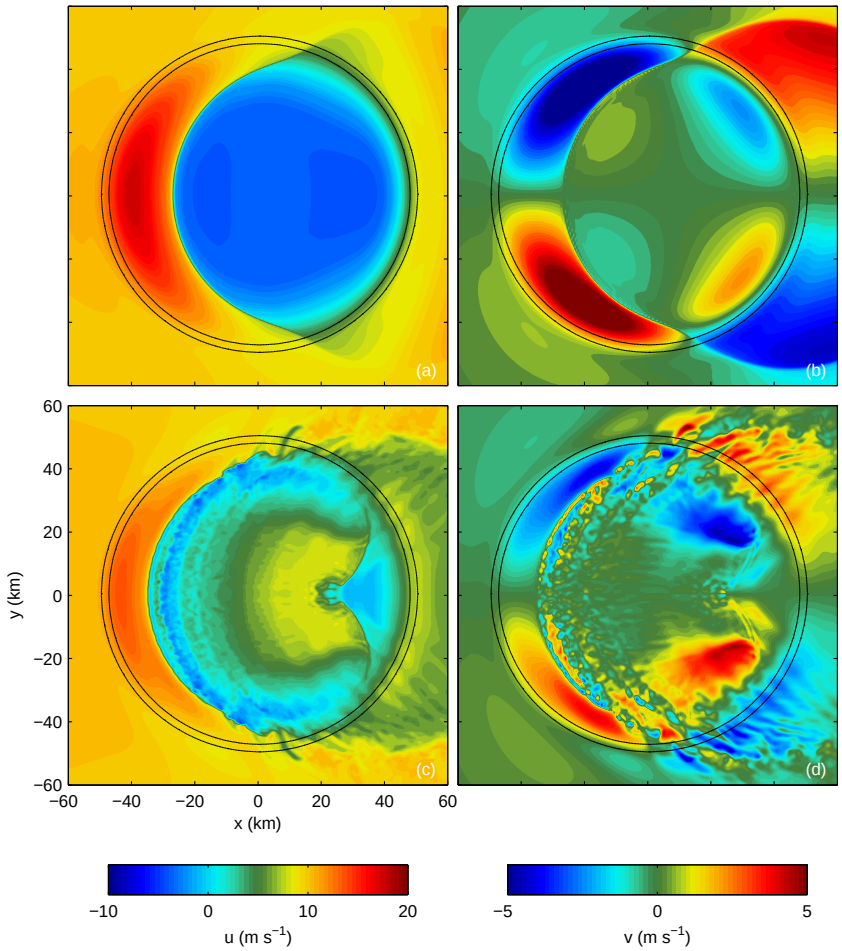

Figure 4.5: Low-level streamwise (left) and spanwise (right) velocities at two times: (a,b) $t = 1$ hr and (c,d) $t = 4$ hr. The velocities are taken from the first vertical grid point in the terrain-following coordinate system (about 60 m from the surface). The black circular contours indicate the position of the crater rims. This figure has been reprinted from Soontiens, N., M. Stastna, M. L. Waite (2013). Numerical simulations of waves over large crater topography in the atmosphere. *J. Atmos. Sci. 70*, 1216. ©American Meteorological Society. Used with permission.

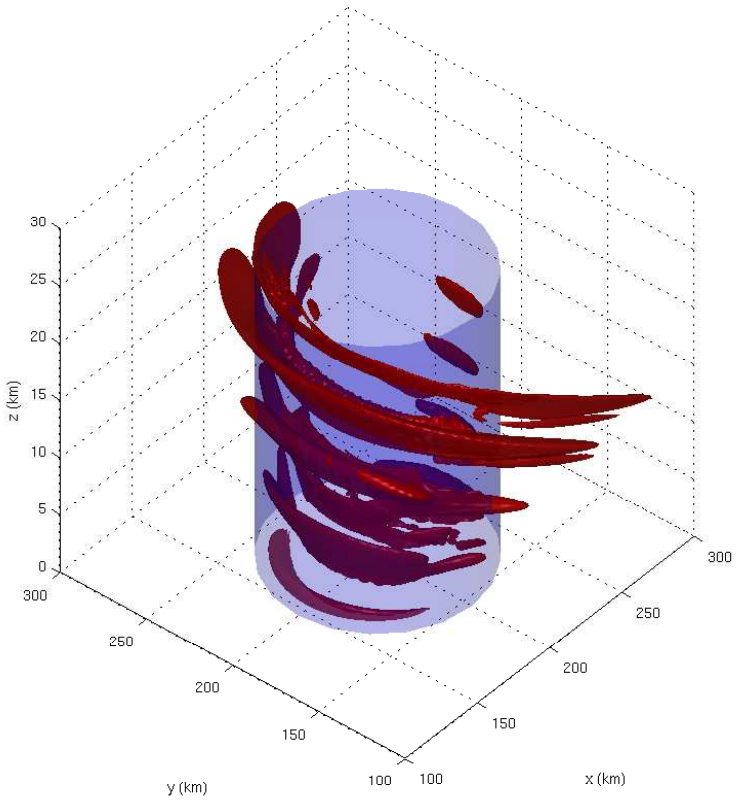

Figure 4.6: Isosurfaces of 15% of the maximum perturbation kinetic energy at time $t = 5$ hr. The blue cylinder indicates the extent of the crater rims.

Two-Dimensional Comparisons

Next, analogous two-dimensional simulations are used to highlight the aspects of the flow that are fundamentally three-dimensional through careful comparison of the two- and three-dimensional results. The two-dimensional version of the crater topography is taken as a slice through $y = 0$ km as depicted in Figure 4.1. The first two-dimensional simulation is performed with the same resolution as the three-dimensional analogue to highlight differences that can be attributed to access to the spanwise direction. A second two-dimensional simulation is performed with higher resolution, $\Delta x = 125$ m and 200 vertical grid points ($\Delta z \approx 120m$ near surface), to assess the robustness of these results under changes in resolution. The base case employed a horizontal grid spacing of $\Delta x = 500$ m, and 200 vertical points. The highest resolution simulations could not be carried out in three dimensions due to computational expense.

Although the crater topography is inherently three-dimensional, there are some similarities between the two- and three-dimensional simulations. In particular, for the low-resolution two-dimensional simulation the streamwise and vertical velocity plots (Figure 4.7) both display the primary waves over the leading and trailing crater edges, with wavelength $\lambda_z \approx 6$ km. In addition, the secondary waves over the crater centre are also present, as well as the development of the retreating gravity current/hydraulic jump. These aspects of the flow are very similar in both two and three dimensions.

However, there are some major differences that should be emphasized. Most noticeable is the degree of overturning of the potential temperature contours, which is much greater in two dimensions. This is not due to numerical damping since both simulations are performed with the same resolution. In the two-dimensional case, overturning is first noticeable at $t = 2$ hr in Figure 4.7 (c) above the leading crater slope near $z = 2.5$ km. The three-dimensional version also displays steepening at this point; however, the potential temperature contours are not as steep as in the two-dimensional analogue. At later times, overturning in the two-dimensional case occurs at higher altitudes, $z \approx 7$ km and $z \approx 14$ km. Peltier and Clark (1979) calculated the critical height for wave breaking in the case of flow over bell-shaped topography in the hydrostatic limit. They found that the critical height for wave breaking is related to the vertical wavelength by $z_c = 3/4\lambda_z$, which is 4.5 km here. Complex interactions between the flow and hydraulic jump, as well as changes in the topography shape results in a different breaking height here.

Comparing to the three-dimensional results of Figure 4.4, it is clear that steepening of potential temperature contours occurs at the same heights. However, this steepening does not lead to the small-scale motions associated with overturning in the two-dimensional plots. In addition, the wave-induced velocities are typically larger in the two-dimensional

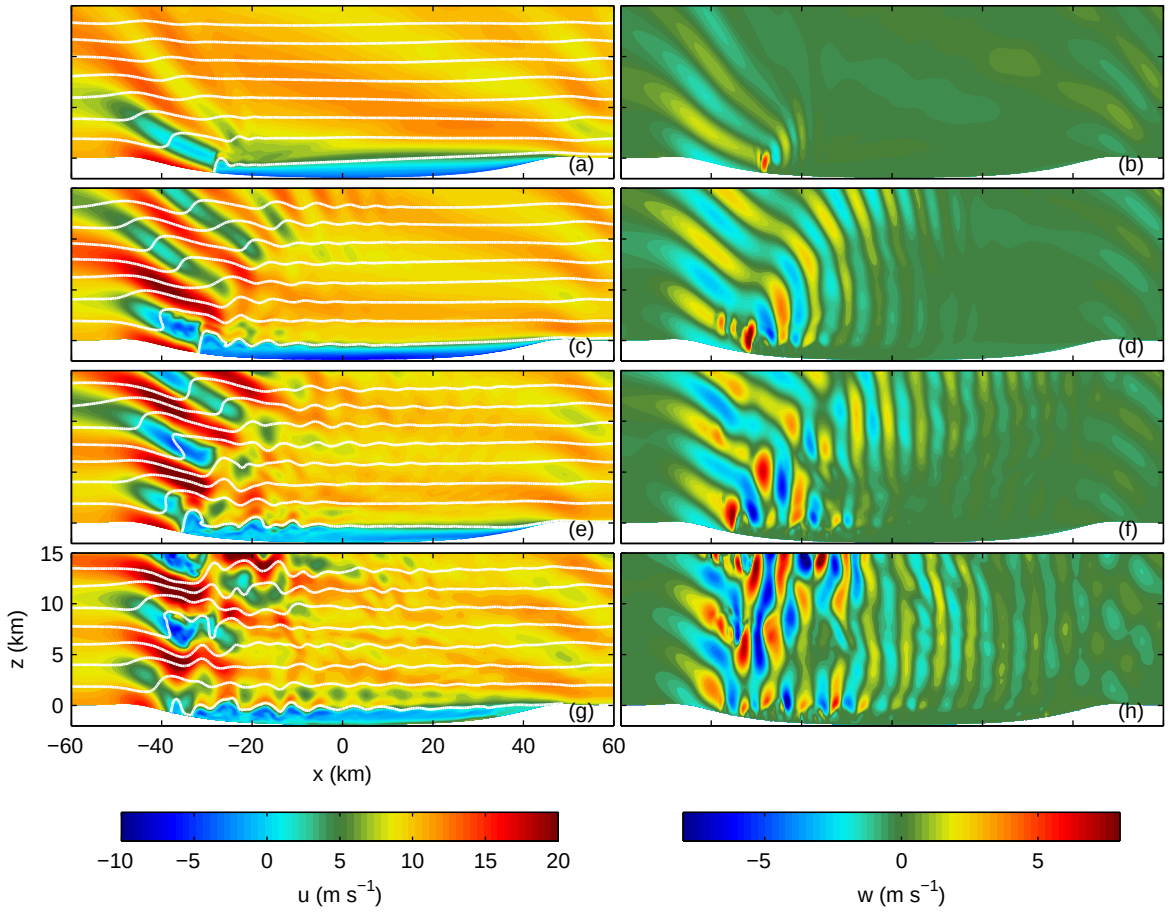

Figure 4.7: As in Figure 4.4 but for the corresponding two-dimensional simulation. This figure has been adapted from Soontiens, N., M. Stastna, M. L. Waite (2013). Numerical simulations of waves over large crater topography in the atmosphere. *J. Atmos. Sci. 70*, 1216. ©American Meteorological Society. Used with permission.

case. Several studies have observed differences in gravity wave breaking in two and three dimensions (e.g Andreassen et al., 1994; Afanasyev and Peltier, 2001; Epifanio and Durran, 2001). Andreassen et al. (1994) and Afanasyev and Peltier (2001) note that complex three-dimensional instabilities can influence the evolution of wave breaking in three dimensions. Epifanio and Durran (2001) observed that lateral deflections near the surface can effectively reduce vertical displacements and lower wave amplitudes resulting in less overturning in three dimensions, in the case of ridge-like topography. In the crater simulations,

outward deflections do not occur at the crater rims and the rims do not appear to greatly influence the wave generation. However, with access to the third dimension wave energy can be dispersed laterally at higher levels which can result in lower wave amplitudes, requiring higher topography for the onset of wave breaking as discussed by Smith and Gronas (1993) and Smith (2003) for mountainous topography. Indeed, the wave amplitudes in two dimensions are up 50% greater than in the three-dimensional simulations, explaining the reduced overturning and wave breaking in three dimensions.

Another aspect that is different between the two- and three-dimensional cases is the formation of an upstream propagating disturbance in Figure 4.7 (g), just above the surface at $x = -35$ km. This structure is not visible in the three-dimensional case of Figure 4.4. An additional comparison is made in Figure 4.8 by examining the streamwise velocities for both the two- and three-dimensional cases at later times. In the two-dimensional case, a disturbance is observed propagating upstream, most noticeable at $t = 7$ hr above $x \approx -60$ km and $t = 8$ hr above $x \approx -75$ km. This disturbance is not observed at any of the output times in the three-dimensional simulation. Epifanio and Durran (2001) also observe a similar discrepancy between two-dimensional and three-dimensional flows. In three dimensions the upstream disturbance disperses laterally and only extends a finite distance ahead of the topography. In the crater simulations, the disturbance originates from the hydraulic jump, providing further evidence that it behaves as a modified topography.

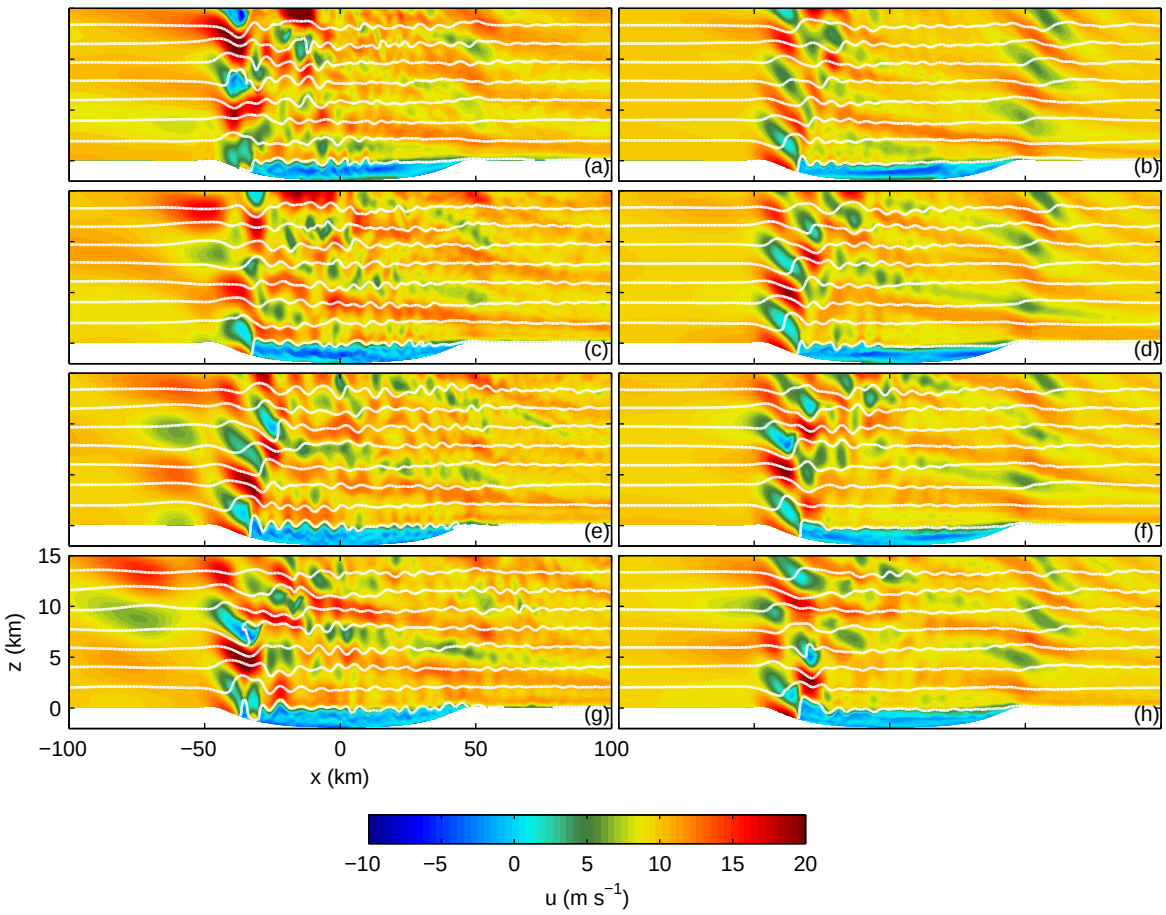

Figure 4.8: Comparison of two-dimensional (left) and three-dimensional (right) base case at later times. Streamwise velocity overlaid with white potential temperature contours at times $t = 5$ hr (a,b), $t = 6$ hr (c,d), $t = 7$ hr (e,f), and $t = 8$ hr (g,h). The potential temperature contours are $\theta = [288, 294, 300, 306, 312, 318, 324, 330]$ K.

Resolution Studies

Several simulations at various resolutions have provided insights into the robustness of these results. The resolution experiments have been performed in two dimensions to establish an efficient means of analysing dependence on resolution. In the three-dimensional simulations the finest resolution considered was from the base case which employed $\Delta x = \Delta y = 500$ m with 200 vertical grid points.

First, a re-examination of the two-dimensional base case is presented with improved horizontal resolution, $\Delta x = 125$ m and 200 vertical grid points (Figure 4.9). The main features of the flow remain robust: the retreating gravity current, primary and secondary beam of waves, and overturning heights. This robustness gives confidence that the base case is sufficiently well resolved for these processes. The most notable difference is the degree of small-scale motions near the shear layer and the more violent overturning in the high-resolution case. As mentioned previously, the intense overturning is not present in the three-dimensional simulation due to lateral dispersion of wave energy. However, it is less clear how the three-dimensionalization of the instabilities in the shear layer would proceed with adequate resolution in three dimensions. Comparing the high- and low-resolution two-dimensional cases, these instabilities may not be properly resolved in the low-resolution case. However, they do not seem to affect the large-scale features of the flow such as the gravity current formation and primary waves. These instabilities do seem to have an effect on the secondary waves at later times (Figure 4.9 (h)), by a complex interaction which may induce small-scale motions within the secondary waves. It is unclear how this interaction would evolve in three dimensions.

The next resolution studies compare the importance of adequate vertical and horizontal resolution. These tests have helped to determine an appropriate resolution for the three-dimensional simulations. Since the two-dimensional simulations are relatively inexpensive they provide an efficient means for testing for adequate resolution. The simulation results are presented in Figure 4.10 and the simulation parameters are given in Table 4.4.

In each of the cases displayed in Figure 4.10 the large-scale structure within the crater is identical. There is a large hydraulic feature along the leading crater edge followed by some wave-like features in its lee. The main differences lie in the fine details of the overturning within the crater, which is best resolved in Figure 4.10 (b). The importance of adequate vertical resolution in demonstrated by comparing Figure 4.10 (c) and Figure 4.10 (d) which are almost identical in spite of a factor of two difference in horizontal resolution. Hence, without adequate vertical resolution improvements in the horizontal resolution may not increase the accuracy of the simulations. These results indicate that the resolution in Figure 4.10 (a) is adequate for studying the large-scale features of this flow environment

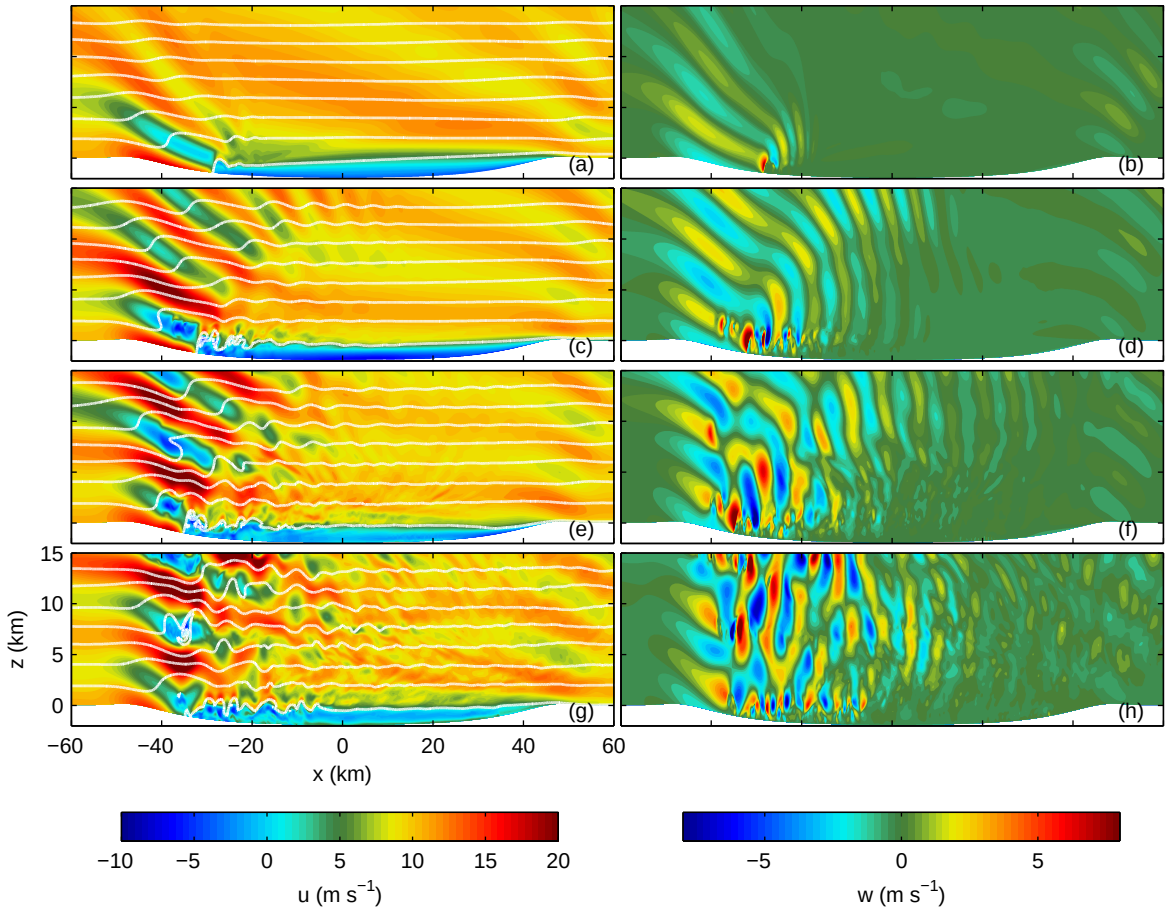

Figure 4.9: As in Figure 4.4 but for the corresponding two-dimensional simulation with high resolution ($\Delta x = 125$ m).

and is appropriate for the three-dimensional simulations presented here.

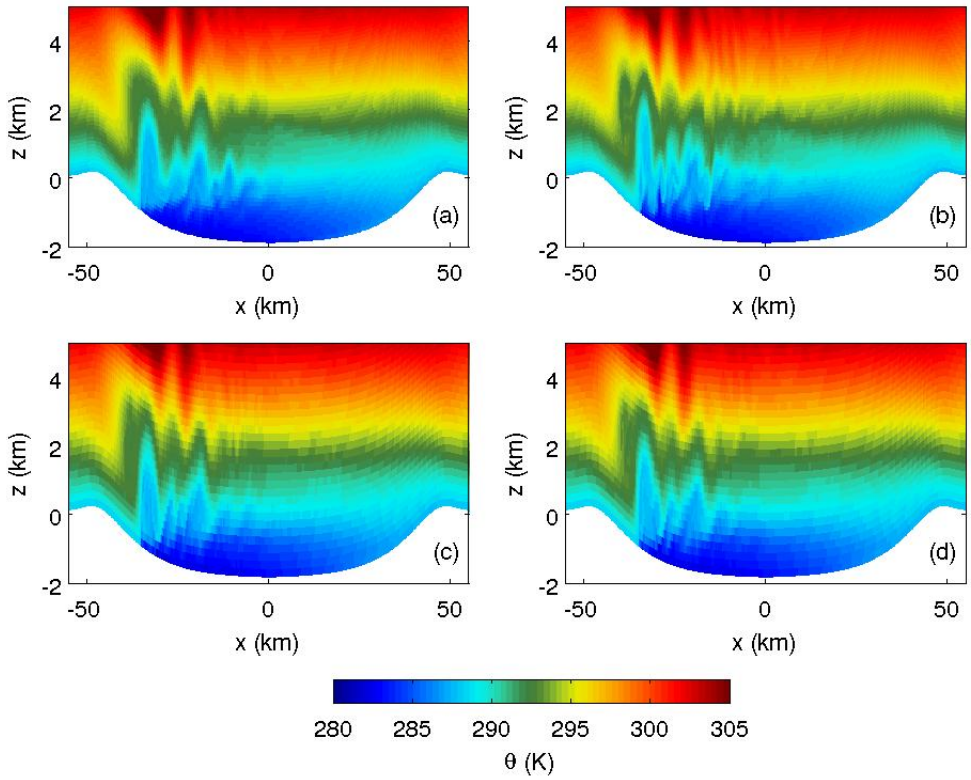

Figure 4.10: Plots of the potential temperature contours for several two-dimensional simulations under different resolution $N_x \times N_z$ where N_x is the number of horizontal grid points and N_z is the number of points in the vertical. (a) 800×200 (b) 1600×200 (c) 3200×100 (d) 1600×100

Table 4.4: Summary of simulation parameters for resolution studies.

Figure 4.10 panel	$N_x \times N_z$	Δx (m)	Near-surface Δz (m)
(a)	800×200	500	115
(b)	1600×200	250	115
(c)	3200×100	125	230
(d)	1600×100	250	230

Hydrostatic vs. Non-Hydrostatic

In addition to explaining the origin of the secondary waves, the hydraulic jump can be used to explain the failure of F_a to predict the non-hydrostatic nature of this flow. Based on the definition in Subsection 4.2.3, $F_a = 0.01$ for this flow environment, indicating that the flow should display mainly hydrostatic phenomena. However, the hydraulic jump is a non-hydrostatic process which is not accounted for in this simple calculation.

As a demonstration of the non-hydrostatic nature of this flow, Figure 4.11 displays the horizontal and vertical velocity fields for a simulation with the hydrostatic option from WRF employed. Numerical errors begin to develop early on in the simulation since the hydrostatic assumption is not valid in this flow environment (Figure 4.11 (a-b)). At a later time in Figure 4.11 (c-d) the vertical velocity is dominated by numerical error. Perhaps an alternative definition of F_a could be formulated using the distance from the crater rims to the hydraulic jump ($a \approx 15$ km) or the length of the jump head ($a \approx 5$ km), which may more accurately represent the non-hydrostatic nature of the flow. Respectively, these choices give $F_a = 0.067$ and $F_a = 0.2$, which are relatively large compared to the original choice of F_a using the crater diameter. This suggests that the crater diameter is not a particularly good choice of length scale for determining the hydrostatic nature of the flow. Perhaps a more appropriate choice is the radius of the crater which gives $F_a = 0.02$, but this again is not very insightful. However, since we have determined through F_r that nonlinear effects are important, we could examine other characteristics of the topography, such as the slope, in order to gain insights into the nature of the flow. In this case, the average slope is 0.04, which is fairly gradual but the expected nonlinear effects could play an important role here. Note that the waves over the leading crater edge match the vertical wavelength expected in the hydrostatic limit (6 km). The non-hydrostatic effects are observed within the depths of the crater and are an interesting contrast to the hydrostatic waves over the leading crater edge. The large scale of the crater basin allows for the retreating gravity current to form leading to the non-hydrostatic effects observed within the crater.

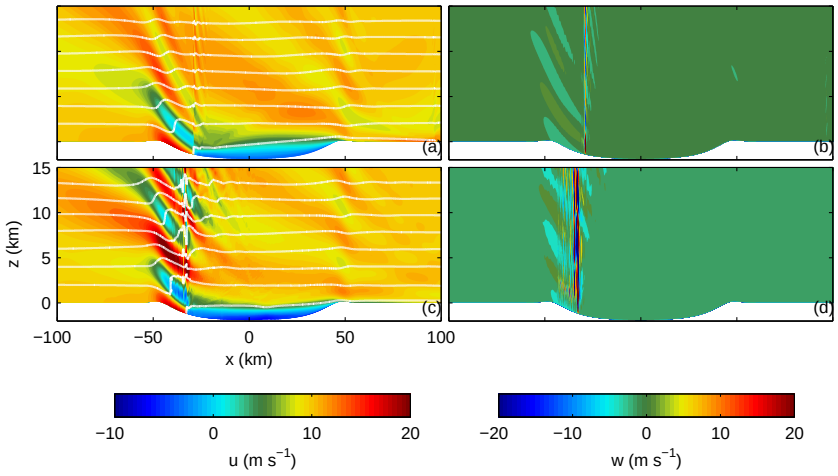

Figure 4.11: Shaded horizontal velocity contours (left) and vertical velocity contours (right) for a base case simulation with the hydrostatic option turned on. Two times are plotted: $t = 1$ hr in (a) and (c), $t = 2$ hr in (b) and (d). The white contours on the left are potential temperature contours.

4.3.2 Atmospheric Modifications

Several modifications to the initial profiles have been considered for further examination of the flow characteristics. The modifications include an atmosphere stratified with reduced buoyancy frequency, an atmosphere stratified in two layers, and an atmosphere with an additional shear background wind in the spanwise direction. These simulations illustrate relationships between atmospheric properties and the shape and size of the hydraulic jump, as well as provide further insights into the three-dimensional properties of the flow.

Reduced Stratification, $F_r = 1$

A simulation with reduced buoyancy frequency is used to further examine the flow evolution under different atmospheric conditions. In this simulation the buoyancy frequency is $N = 0.005$ s^{-1} which yields $F_r = 1$. This buoyancy frequency is more typical of the Martian atmosphere as outlined in Table 4.3. Flow over crater topography in the Martian atmosphere has been considered by Pirraglia (1976) and Pickersgill and Hunt (1979) in the context of steady theory and layered wind profiles. The present study will add to these results by considering time-dependent simulations for Martian wind and stratification profiles in Subsection 4.3.7.

This case evolves in a similar fashion as the base case. Features such as the retreating gravity current, and primary and secondary beams of waves are observed in Figure 4.12. A strong low-level jet enters the crater depths along the leading crater slope and interacts with the cooler air within the crater to form the hydraulic jump. At $t = 2$ hr in Figure 4.12 (c), the low-level jet enters further into the crater before the flow reverses to form the retreating gravity current. Since the stratification is reduced the potential energy constraints are lessened, allowing further advancement of the low-level jet into the crater. The upstream propagation of the retreating gravity current is very clear in Figure 4.12 (c, e, g). Its position at $t = 4$ hr is $x \approx -15$ km. After this time the gravity current head ranges between $x = -20$ km and $x = -8$ km. Examining the vertical velocity plots, it is clear that the gravity current is forcing the secondary waves which form over the crater centre.

Several differences between this case and the base case should be noted. First, the vertical wavelength of the primary beam of waves has increased to $\lambda_z \approx 12$ km. This once again matches the wavelength calculated in the hydrostatic limit $\lambda_z = 2\pi U_0/N$. Another difference is that the height of the gravity current is larger than in the base case. At $t = 4$ hr, the gravity current height is around 2 km, compared to about 1 km in the base case. The reduced stratification allows for larger displacements in the potential temperature contours. Also, in an analogous two-dimensional simulation, overturning occurs higher

in the atmosphere at $z \approx 2.5$ km and $z \approx 14$ km (not shown). This coincides with the prediction that overturning heights depend on vertical wavelength (Peltier and Clark, 1979).

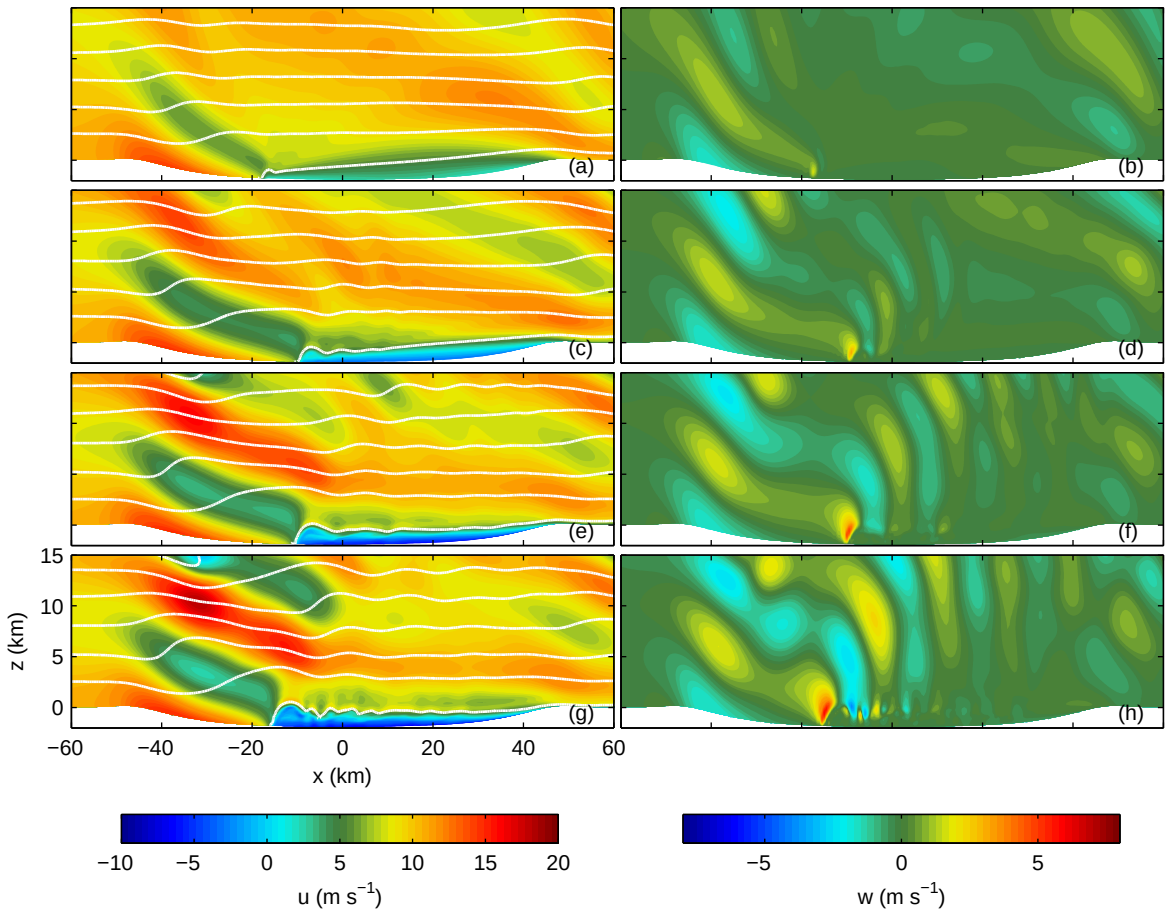

Figure 4.12: As in Figure 4.4 but for reduced stratification with $F_r = 1$. The potential temperature contours are $\theta = [288, 290, 292, 294, 296, 298, 300]$ K. This figure has been adapted from Soontiens, N., M. Stastna, M. L. Waite (2013). Numerical simulations of waves over large crater topography in the atmosphere. *J. Atmos. Sci. 70*, 1216. ©American Meteorological Society. Used with permission.

Two-Layer Atmosphere

Next, an atmosphere stratified in two layers is used to further examine the features of this flow. In this case, the atmosphere is stratified with constant potential temperature within the crater (below $z = 0$ km) and with constant buoyancy frequency, $N = 0.01$ s^{-1}, above this height. With this stratification, a gravity current should not be able to form since the potential temperature is constant within the crater. This case also serves as a test that the gravity current acts as a modified topography; if no secondary waves form then the absence of the gravity current is a likely explanation.

In the streamwise velocity plots of Figure 4.13, a low-level jet descends along the leading crater slope, similar to jet in the base case. This forces the primary beam of waves with $\lambda_z \approx 6$ km over the leading crater edge. These features are all similar to the base case. The main differences occur within the crater depths. First, it is clear that the retreating gravity current does not form in the two-layer atmosphere. The low-level jet enters the crater and is not obstructed by a hydraulic jump or gravity current. The potential energy constraints are diminished since the air is not stratified, allowing the jet to travel far into the crater depths. In the base case, the fluid passes over the gravity current, forming a shear layer between the background flow and the near stagnant fluid within the crater. In the two-layer atmosphere, the low-level jet passes under the stagnant fluid within the crater causing small-scale motions along the way. This is one of the major contrasts between the base case and the two-layer atmosphere. Another important point is that the secondary beam of waves over the crater centre is not present, providing further evidence that the gravity current acts as a modified topography. Note that some vertical motion exists over the crater centre, but not in the form of the clear beam of waves observed in the base case.

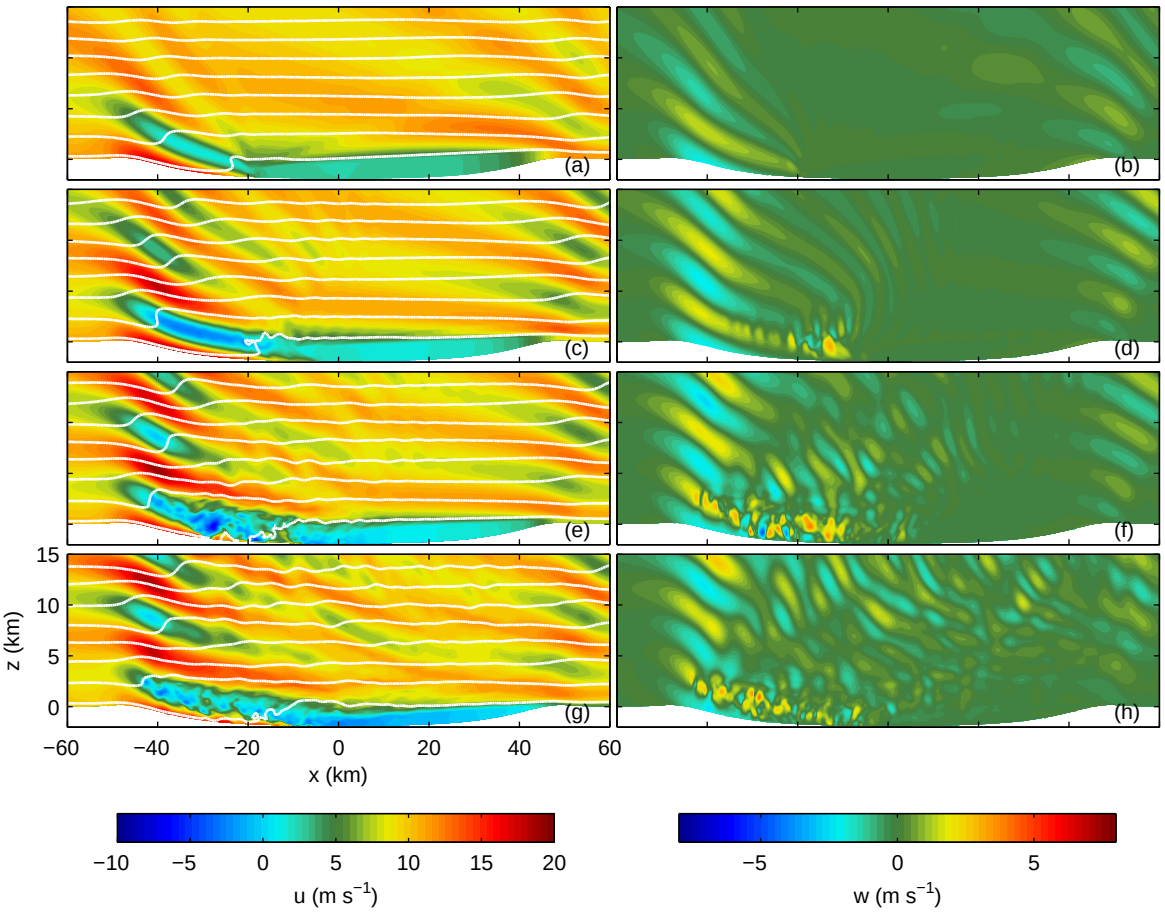

Figure 4.13: As in Figure 4.4 but for the two-layer atmosphere. The potential temperature contours are $\theta = [289, 295, 301, 307, 313, 319, 325, 331]$ K. This figure has been adapted from Soontiens, N., M. Stastna, M. L. Waite (2013). Numerical simulations of waves over large crater topography in the atmosphere. *J. Atmos. Sci. 70*, 1216. ©American Meteorological Society. Used with permission.

Spanwise Shear

A simulation with a spanwise shear background wind in addition to the streamwise wind $U_0 = 10$ m s^{-1} is presented next. The shear wind is added to the spanwise velocity and is given by

$$V(z) = \frac{v_*}{2}\left(1 + \tanh\left(\frac{z - z_0}{\delta_z}\right)\right),$$

with $v_* = 8$ m s^{-1}, $z_0 = 10$ km, and $\delta_z = 1$ km. The shear current is designed so that below the shear layer (about $z = 8$ km) the current is 0 m s^{-1} and above the shear layer (about $z = 12$ km) the current takes a value of v_*. The shear wind profile allows us to examine the three-dimensional propagation characteristics of the waves.

With the presence of the shear wind, there is now a north-south asymmetry in the wave response. In Figure 4.14, we display the vertical velocity through several vertical cross-sections at time $t = 3$ hr. The asymmetry between the southern (Figure 4.14 (a)) and northern (Figure 4.14 (c)) crater edges is due to the shear background wind; in the base case these plots are identical. Comparing the two plots, it is apparent that the waves over the southern edge have a larger amplitude than those over the northern edge, particularly above $z = 10$ km where the shear current becomes strong. Because of the horseshoe structure of the waves, as described in the base case, the shear current acts to amplify the waves over the southern edge. Also, the signature of the secondary waves is more apparent at the northern crater edge, especially above $z = 12$ km, again due to an interaction with the shear current. Through the crater centre, in Figure 4.14 (b), the amplitude of the wave-induced vertical velocity is greatest since the topography is largest. The wave structure at the centre is similar to the base case in Figure 4.4.

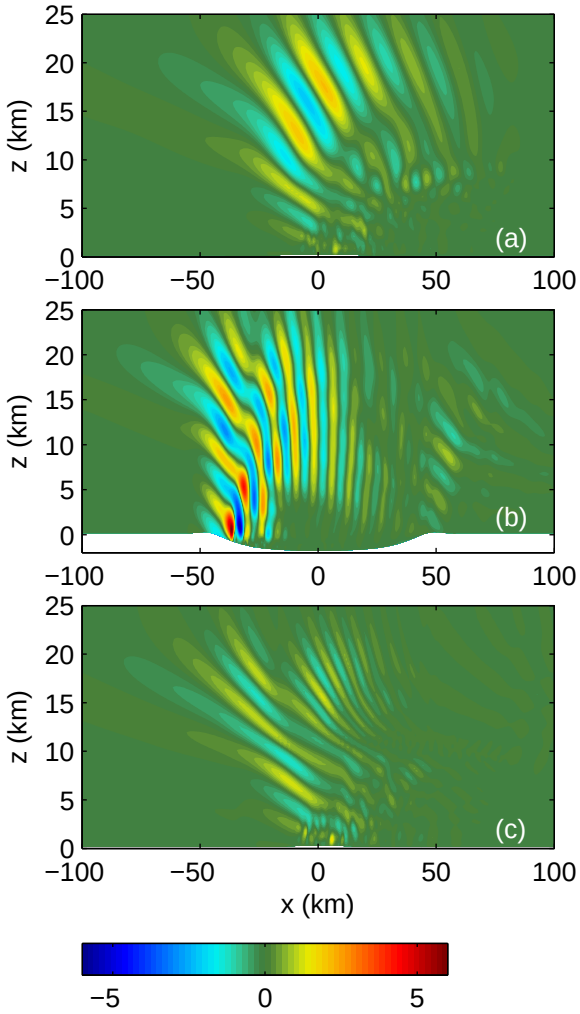

Figure 4.14: Comparison of the vertical velocity, w (m s^{-1}) for several vertical cross-sections in the shear background current simulation from time $t = 3$ hr: (a) The southern crater edge, $y = -50$ km, (b) the crater centre, $y = 0$ km, and (c) the northern crater edge, $y = 50$ km.

4.3.3 Topographic Modifications

Several topographic modifications establish the importance of the topography shape on the flow evolution. An important factor in this work is that it addresses crater shapes that are not considered previously in the literature. The 100-km diameter crater considered by Pirraglia (1976) and Pickersgill and Hunt (1979) only represents the crater rims. A simulation presented below models a crater with the rims removed in order to assess the influence of the rims on the flow evolution. In addition, work by Fritts et al. (2010) examines a crater with rims and depression and a diameter of 1.2 km. Hence, large-scale crater topography has not been fully considered in previous studies. A second topographic modification with reduced crater diameter compares the flow under larger and smaller scales.

No Rims

We next consider the influence of the crater rims on the development of the waves and retreating gravity current. The work by Pirraglia (1976) and Pickersgill and Hunt (1979) would seem to indicate that the rim structures are most important since their topography profile only considered rim structures without the crater depression. This simulation will assess the importance of the crater rims by comparing the results of a crater with no rims to the base case. The profile of the topography without crater rims is displayed in Figure 4.15.

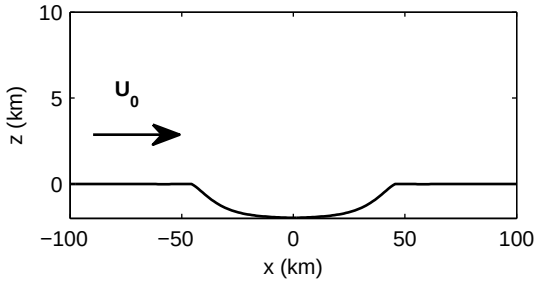

Figure 4.15: Visualization of the crater topography with no rims.

As described previously, the primary beam of waves over the leading crater edge is generated by the descent of air into the crater depths. This is replicated in the simulation with no crater rims (Figure 4.16). In fact, upon comparison with Figure 4.4, only very minor differences are observed between the base case and this simulation. The formation of

the retreating gravity current, the secondary and primary waves are all present and almost identical in both cases. The most substantial difference is the beam of waves over the trailing crater edge; the waves are stronger in the base case than in the present simulation. This implies that the crater rims are not very important in the generation of waves over the leading edge and interior, however, they have a greater influence on the waves over the trailing edge.

This interpretation is reinforced under further examination of F_r. Constructing F_r based on the height of the crater rims, $h = 100$ m, gives $F_r = 10$. Comparing to $F_r = 0.5$ based on the crater depth, it is clear that the crater depth will have a bigger impact on the wave motion than the crater rims. In addition, the gravity current with $F_r = 1$ is also expected to have a larger topographic influence. In conclusion, some useful insights into flow over large-scale crater topography can be revealed by this study, by considering a full crater profile which has not been considered in the past.

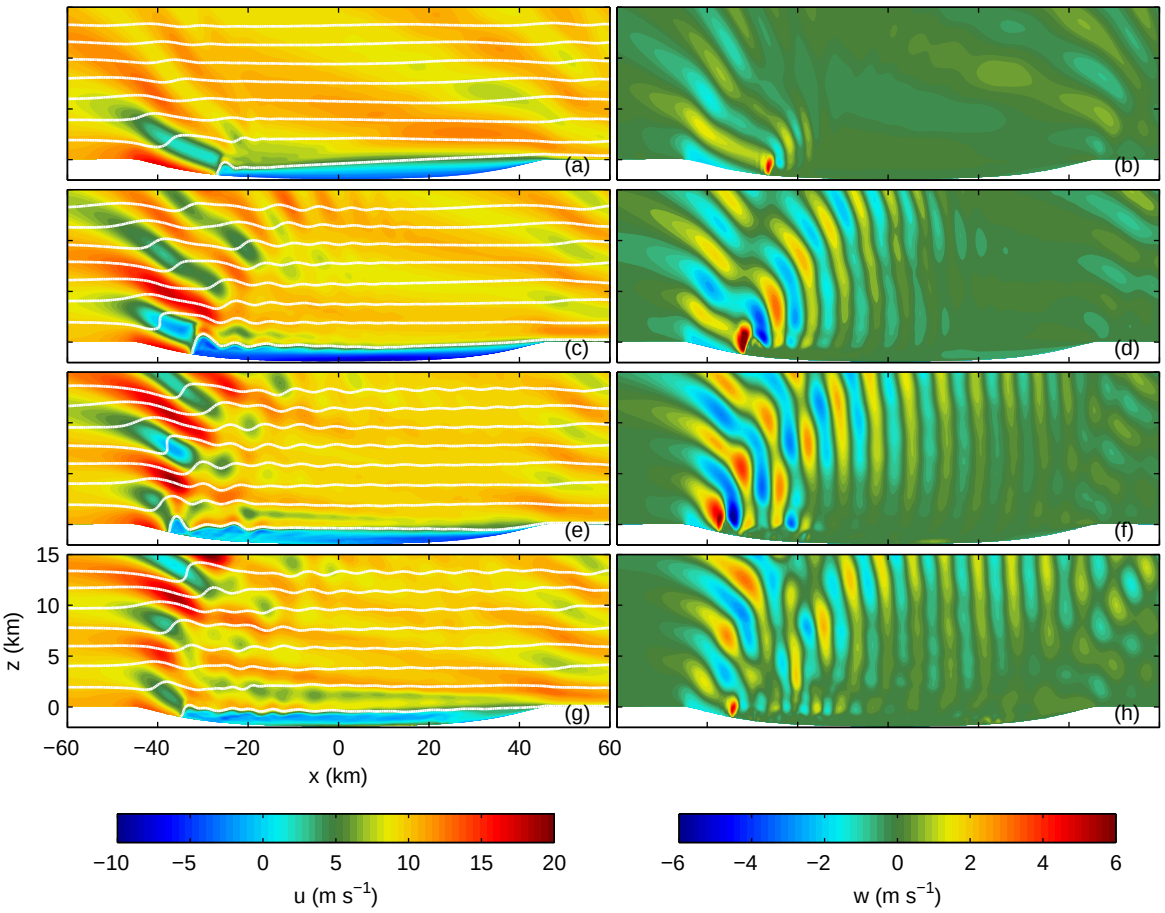

Figure 4.16: As in Figure 4.4 but for the simulation with no rims. This figure has been adapted from Soontiens, N., M. Stastna, M. L. Waite (2013). Numerical simulations of waves over large crater topography in the atmosphere. *J. Atmos. Sci. 70*, 1216. ©American Meteorological Society. Used with permission.

Increased Curvature

Next, the crater diameter has been reduced in order to assess the effect of curvature on the three-dimensionalization of the flow. In this simulation, the diameter has been reduced to $a = 40$ km giving $F_a = 0.025$, which in turn increases the crater curvature and the slope of the crater walls. The nonlinearity parameter F_r remains unchanged. The crater curvature should have an effect on the spanwise deflection, similar to the impact that elongated ridges has on lateral deflections (Olafsson and Bougeault, 1996; Epifanio and Durran, 2001). Since the crater is smaller, the domain has been decreased to 200 km $\times$ 200 km $\times$ 30 km. As a consequence, better resolution is afforded, with $\Delta x = \Delta y = 250$ m. The vertical resolution is unchanged. This case examines an intermediate scale between the large-scale topography discussed above and by Pirraglia (1976) and Pickersgill and Hunt (1979) and the small crater with 1.2-km diameter considered by Fritts et al. (2010).

The flow evolution with increased curvature through the crater centre is similar to the base case, with some differences due to the change in the topography slope (Figure 4.17). Note that the output times are different from in the base case. The main similarities include the primary waves over the leading and trailing crater edges and, at early times, the tilted potential temperature contours and reversed flow within the crater depression. The reversed flow leads to the formation of a hydraulic jump, although its shape and proximity to the crater edges are much different in this case. At early times, the hydraulic jump is forming at $x \approx -15$ km, where it remains relatively stationary for later times.

In addition, secondary waves appear to be forming near the hydraulic jump, most apparent in the vertical velocity plots at $t = 0.5$ hr in Figure 4.17 (b). At later times, these waves appear to interact with the primary waves since they are so close to the leading crater edge. Additionally, the primary beam of waves propagate at a larger angle to the vertical than in the base case, resulting in more interaction between the primary and secondary waves. There also appear to be some instabilities forming along the shear layer between the background flow and the fluid within the crater depression. These instabilities are better resolved in the increased curvature run, and also appear in the high-resolution two-dimensional simulation. They are not observed in the three-dimensional base case.

One other difference between the increased curvature simulation and the base case is the degree of overturning in the potential temperature contours. In the present simulation, there is less steepening and overturning of potential temperature contours, which can be explained by lateral deflections and spanwise motion. Due to the increase in curvature, it is expected that the smaller crater will induce more spanwise deflections. Hence, wave energy is more likely to be dispersed laterally, yielding lower amplitude waves that do not overturn. Spanwise motions and the three-dimensional aspects of the flow are examined

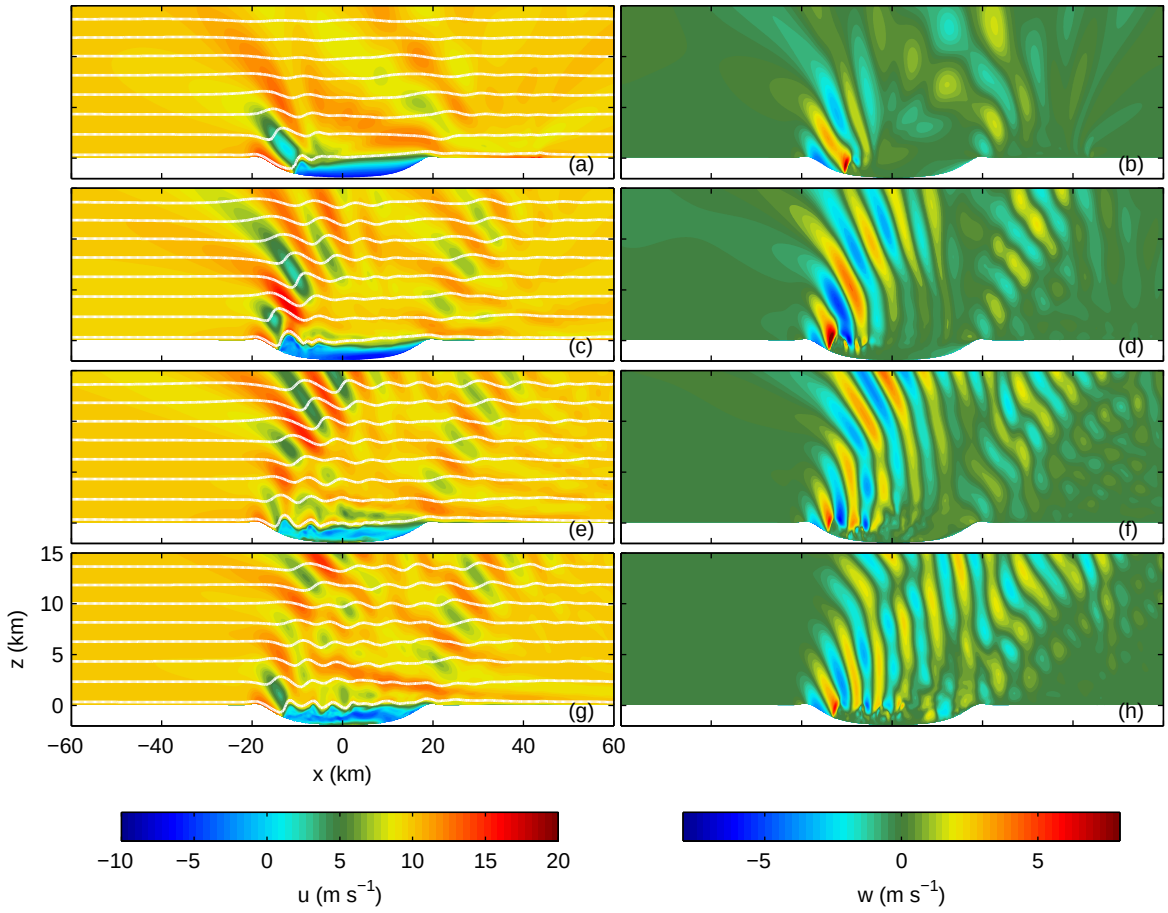

Figure 4.17: As in Figure 4.4 but for the crater with reduced diameter, $a = 40$ km. This figure has been adapted from Soontiens, N., M. Stastna, M. L. Waite (2013). Numerical simulations of waves over large crater topography in the atmosphere. *J. Atmos. Sci. 70*, 1216. ©American Meteorological Society. Used with permission.

further in Figure 4.18.

Examination of the spanwise velocities will help determine the reason for less steepening of potential temperature contours in the crater with increased curvature. In Figure 4.18, the spanwise velocity at two levels, 1 km above the surface and 10 km above the surface, are compared for the base and increased curvature cases. The structure of the spanwise velocity differs slightly between these two cases, although there are many similarities. First, both cases exhibit the convergence of air towards the crater centre at low levels

upstream of the hydraulic jump feature. The position of the hydraulic jump is apparent, indicated by an abrupt deflection towards the outer crater edges. The most noticeable difference between these two cases at low levels is the distribution of small-scale motion. In the increased curvature run, small-scale motions are distributed throughout the crater interior. However, in the base case, small-scale motions are found directly in the lee of the hydraulic jump and can extend outside of the crater limits.

Higher in the atmosphere, both simulations show outward stretching bands of positive and negative spanwise velocity in a wedge-like pattern, similar to the ship-wake pattern observed by Pirraglia (1976). In addition, both cases exhibit vortical structures in the lee of the crater, although they are much larger in the base case. The main difference at high levels is the location of maximum spanwise velocities. In the base case, the maximum spanwise velocities occur close to the leading crater edge, whereas the small crater exhibits large spanwise velocities in the lee-half of the crater.

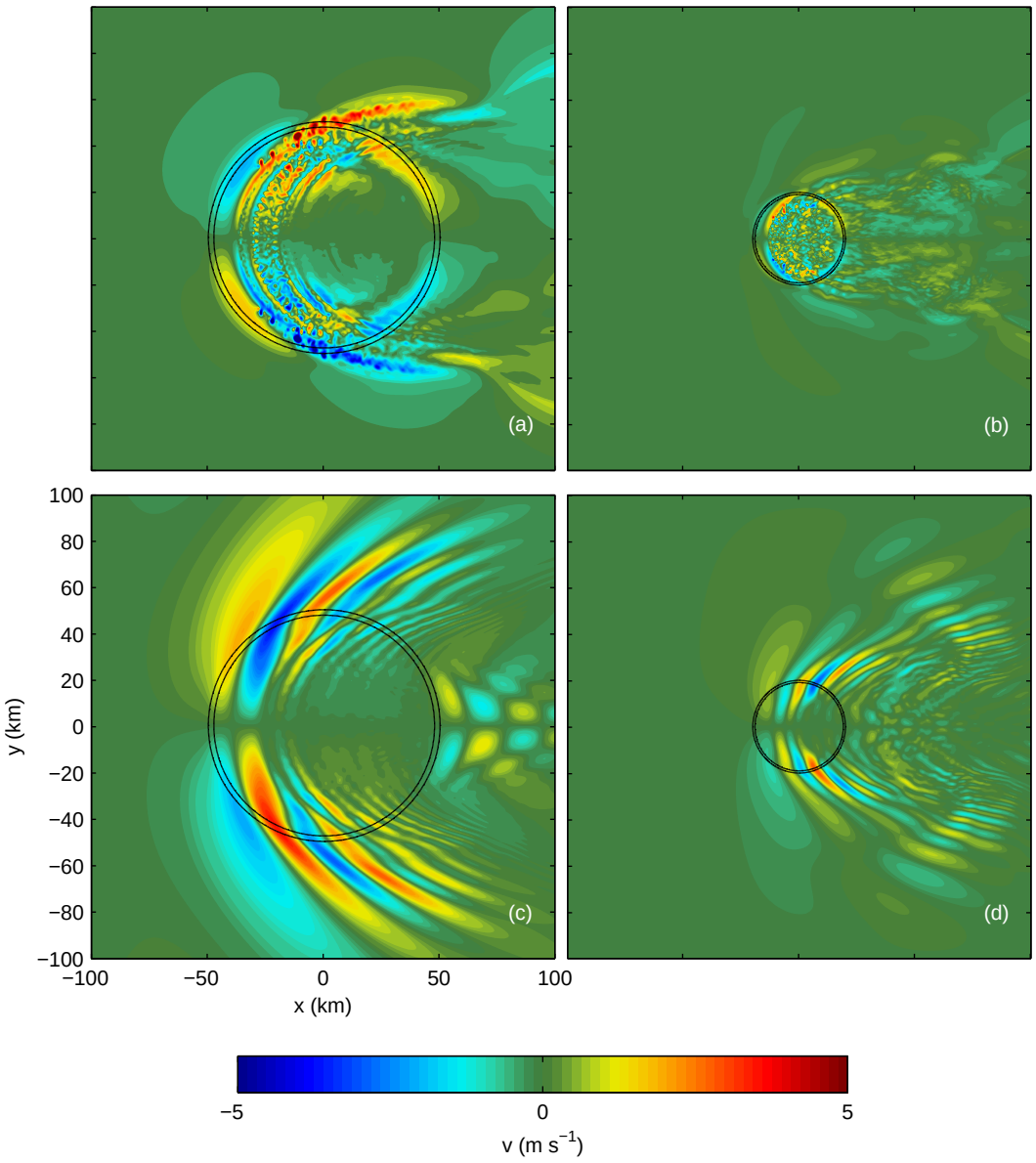

Figure 4.18: Spanwise velocity from the base case (left) and the simulation with smaller crater (right). The contours are from 1 km above the surface in (a), (b) and 10 km above the surface in (c), (d). The output time is $t = 3$ hr. This figure has been reprinted from Soontiens, N., M. Stastna, M. L. Waite (2013). Numerical simulations of waves over large crater topography in the atmosphere. *J. Atmos. Sci. 70*, 1216. ©American Meteorological Society. Used with permission.

4.3.4 Rotation

The influence of rotation is investigated next by considering two additional simulations. As mentioned in Subsection 4.2.3, the Rossby number is chosen to be order one. This indicates that rotation may be an important consideration for flow on this scale. Two simulations with the effects of rotation are examined: 1) the base case with rotation and 2) the two-layer atmosphere with rotation. These two cases represent very different thermal stratifications. The Coriolis parameter in both cases is $f = 10^{-4}$ s^{-1}. The perturbation kinetic energy, defined by Equation 4.4 is a useful diagnostic for analysing these two cases. This diagnostic is presented in Figure 4.19 at time $t = 4$ hr, just above the surface at 60 m for both cases, with and without rotation.

First, the base case is presented in the left panels of Figure 4.19. The high velocities associated with the low-level jet are very clear, along with the abrupt decrease of velocities in the crater centre and the front of the gravity current. This is apparent in both simulations with and without rotation. In addition, instances of small-scale motions are observed near the north and south crater edges, $y = \pm 50$ km. However, in the rotation case, the symmetry is broken and more small-scale structure is observed in the southern half of the crater (below $y = 0$ km). This indicates that rotation can induce a preference for small-scale activity over one half of the crater. While there is still activity above $y = 0$ km, there is more towards the southern crater edge. In the northern hemisphere, the rotation of the planet causes motion to be deflected to the right, hence, the increase of activity in the southern crater half. This is realized in the location of the maximum kinetic energy from the base cases with and without rotation. In the non-rotating cases, the maximum perturbation kinetic energy occurs along $y = 0$ km, whereas the maximum has shifted to the southern crater half in the rotating case. Hence, with high velocities focused in the southern half, one would expect increased episodes of small-scale motions.

The same result is confirmed in the two-layer atmosphere but in a much more dramatic fashion. In this case, a gravity current cannot form and does not interrupt the advancement of the low-level jet. As described in the case without rotation, the low-level jet induces many small-scale motions as it descends the leading crater slope. The inclusion of rotation does not change this aspect of the flow, however, the small-scale motions are focused in the southern crater half at this time.

The shift of small-scale motions to the southern half of the crater under the influence of rotation is common to both the constant N atmosphere and the two-layer atmosphere. The explanation is the tendency for motion to be deflected to the right in the northern hemisphere (positive f) due to the Coriolis force. In the two-layer atmosphere, the rotation case indicates that the low-level jet is deflected to the right as it descends into the crater.

Since the low-level jet is the main cause for the small-scale motion, it follows that the turbulence and small-scale structures are shifted as will. Similarly, in the constant N atmosphere the maximum velocities in the low-level jet are also deflected to the right, rather than along $y = 0$ km as in the base case. In turn, the southern half of the crater experiences more instances of small-scale motion.

This observation could have an interesting implication for dust-lifting in the Martian atmosphere. Typically, dust lifting can occur because of large near-surface wind velocities. The kinetic energy plots can indicate locations of large velocities and potential dust lifting hotspots. From these results, we could expect that dust lifting near crater topography is more likely to occur in an atmosphere with a nearly constant potential temperature profile within the crater depression. This is supported by the observations of Veverka et al. (1981) who conclude that erosional streaks around crater topography are more likely after an event which reduces the atmospheric stability, such as the uniform heating of a dust storm. The authors argue that atmospheric stability is more important than crater shape when considering dust erosion and deposition. In addition, the effects of rotation could indicate a preference for dust lifting in one half of the crater, depending on the hemisphere in which the crater is located. More comprehensive simulations with more accurate boundary layer dynamics, surface physics, flow separation, and dust lifting parametrizations are required to examine this topic further. Asymmetric patterns of dust streaks have been observed within Gusev Crater on Mars, although this has been attributed to a channel flow system caused by other topographic features (Greeley et al., 2003). Other asymmetric features include craters which under certain conditions can produce both light and dark streaks (Veverka et al., 1981).

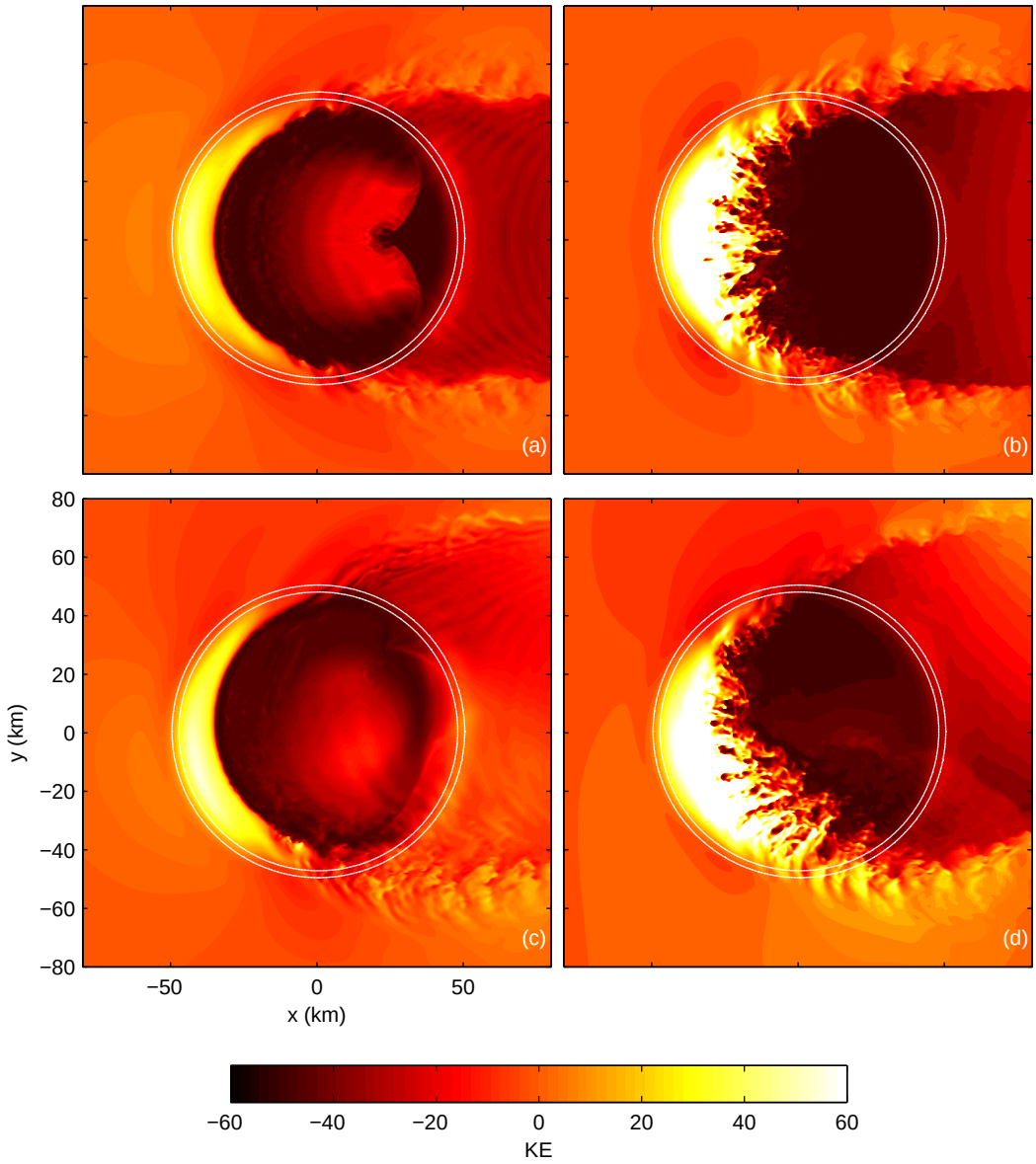

Figure 4.19: Perturbation kinetic energy density at time $t = 4$ hr at the first grid level for several simulations: (a) base case, (b) two-layer atmosphere, (c) base case with rotation, (d) two-layer atmosphere with rotation. This figure has been adapted from Soontiens, N., M. Stastna, M. L. Waite (2013). Numerical simulations of waves over large crater topography in the atmosphere. *J. Atmos. Sci. 70*, 1216. ©American Meteorological Society. Used with permission.

4.3.5 Seiches

Next, several simulations examine seiche behaviour within the crater by considering an initial potential temperature profile with tilted isentropes within the crater as depicted in Figure 4.2. The purpose is to examine other types of motion that could exist within the crater, in the absence of a background wind. As was demonstrated in the base case a background wind can act to tilt potential temperature contours leading to a retreating gravity current response. By removing the background wind and beginning with initially tilted isentropes we can differentiate between the seiche-like motion and the waves forced by the background wind. As seen in previous results, wind forcing may induce tilted potential temperature contours, and so, we begin the simulation with the initially tilted thermal stratification within the crater shown in Figure 4.2. The initial tilt of the potential temperature was chosen somewhat arbitrarily, but is less steep than the tilt produced by the background wind. In this section, we examine the seiche behaviour in rotating and non-rotating cases and we also consider one high-resolution simulation.

The seiche behaviour is observed in Figure 4.20 where the kinetic energy density through $y = 0$ km and the vertical velocity near the surface ($z = 330$ m, following the terrain) are plotted. This figure demonstrates the motion within the crater through approximately one half period. An interesting feature is the small-scale wave-like motion near the crater edges at $x = \pm 50$ km at time $t = 2$ hr in Figure 4.20 (d). At this time, the response is somewhat stronger over the $x = 50$ km edge. This feature will be investigated further at higher resolution and with rotation. In this experiment, the motion is mostly constrained to within the crater depths, although one might expect fluid to be ejected outside of the crater with a strong enough initial tilt or forcing. The wave response over the crater edges is of much smaller amplitude than the waves forced by the background flow in the base case.

Once again, since the diameter of the crater is quite large, the effects of rotation are important to consider and are examined in Figure 4.21 through a simulation with Coriolis parameter $f = 10^{-4}$ s^{-1}. For simple comparison, the same diagnostics as in the non-rotating case are considered. First, the vertical cross-sections of the kinetic energy are very similar to the base case. Additionally, the horizontal cross-sections of the vertical velocity are a useful tool for this case and are displayed in the lower panels of Figure 4.21. It can be seen that the rotation acts to deflect the plane of oscillating motion, similar to the action of a Foucault pendulum. By time $t = 2$ hr in Figure 4.21 (h) the oscillating motion is deflected by about 30° from its original plane, which was parallel to the x-axis. Beyond the deflection of the oscillations, many of the features are the same as in the non-rotating case.

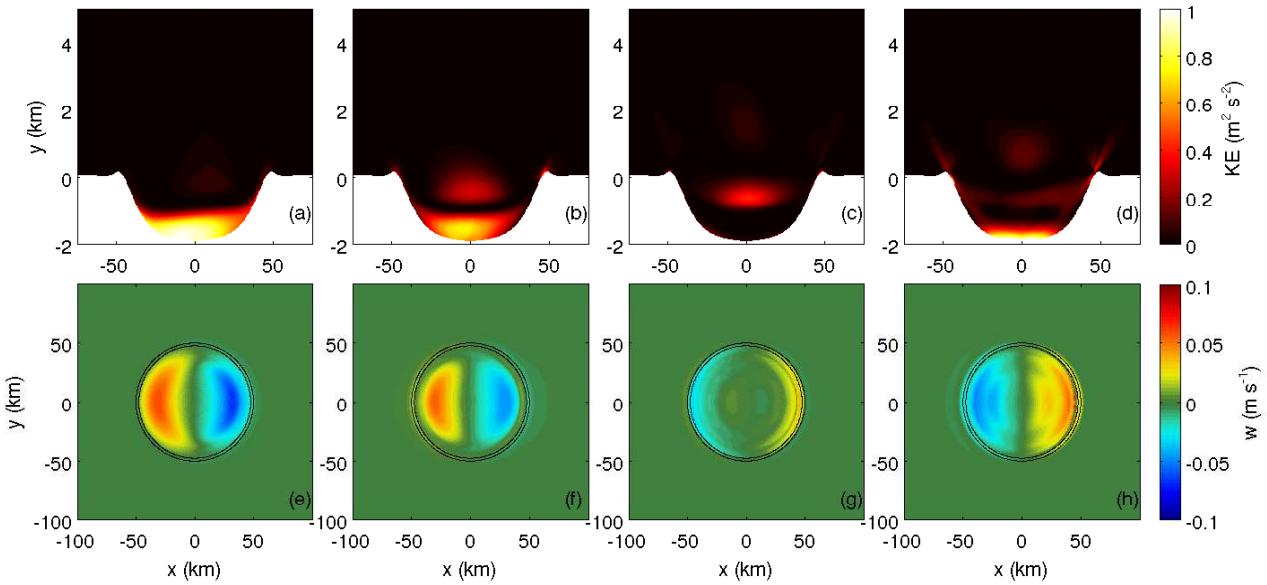

Figure 4.20: Plots of the kinetic energy density through $y = 0$ km (upper) and vertical velocity at $z = 330$ m above the surface following the terrain (lower) in the seiche simulation without rotation. The times displayed are (a),(e) $t = 0.5$hr, (b),(f), $t = 1$ hr,(c),(g) $t = 1.5$ hr, and (d),(h) $t = 2$ hr.

Finally, a closer examination of the wave features observed at the crater edges is presented in Figure 4.22. A higher resolution, rotating case is compared alongside the original rotating case. The higher resolution case uses twice as many grid points in the x and y direction with $\Delta x = \Delta y = 250$ m. The same number of vertical grid points is used in both simulations. First, the vertical velocity of the lower resolution case in Figure 4.22 (a) presents a detailed view of the waves at $t = 2.5$ hr. It is unclear whether or not the resolution is adequate, hence comparisons with a higher resolution case are shown in Figure 4.22 (b). Minor differences between the two cases are apparent. For example, the three major beams of waves extend at slightly different angles in these two plots and there are two additional minor beams in the higher resolution case. However, the velocities in these cases are quite small (less than 0.1 m s^{-1}) and may not be important in the large-scale picture.

The seiche simulations lead to an interesting point concerning flow over crater topography. The possibility of seiche behaviour as a result of wind forcing, similar to that observed in other lakes and basins, could be an interesting area of research for future

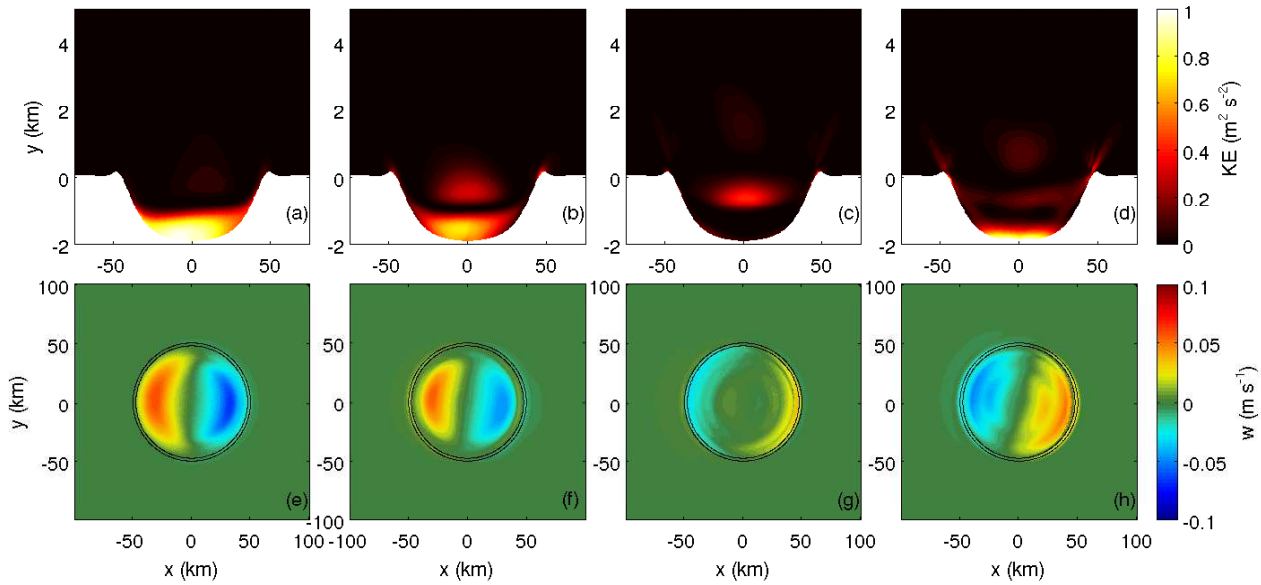

Figure 4.21: As in Figure 4.20 but for a rotating case.

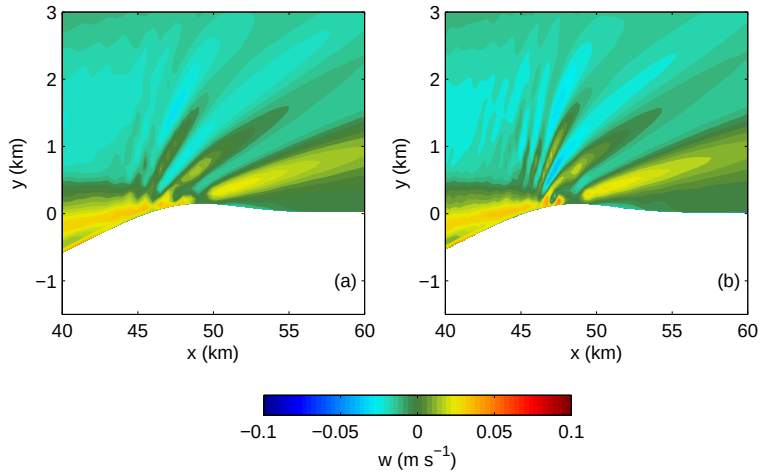

Figure 4.22: Vertical velocity contours through $y = 0$ km at $t = 2.5$ hr in the cases with (a) lower resolution case and (b) higher resolution.

studies in crater topographic flows due to the implications for sloshing and mixing (Fritts et al., 2010). The behaviour is not discussed in great detail here, but these cases offer a

preliminary investigation on the topic and could lead to a more thorough discussion in the future.

4.3.6 Planetary Boundary Layer

A simulation that includes the effects of surface friction through a planetary boundary layer parametrization is examined next. The effect of the PBL is to dampen the gravity current and to reduce the amplitude of the vertically propagating waves as shown in Figure 4.23. At an early time, $t = 1$ hr in Figure 4.23 (a-b), warm air enters the crater bowl and interacts with the cooler air, causing the temperature contours to tilt and readjust as a gravity current similar to the base case. A small beam of secondary waves is observed in the vertical velocity contours in Figure 4.23 (b) at $x \approx -35$ km. However, for later times in Figure 4.23 (c-h), after the tilted potential temperature contours have readjusted, there is no evidence of a gravity current at all. Yet, remnants of the secondary beam of waves, generated at an earlier time, remain. Notice that the waves, even those over the leading crater edge, have much smaller amplitudes than those in the base case shown in Figure 4.4. A point of separation occurs along the leading crater edge at $x \approx -40$ km at the latest times and the fluid within the crater is relatively stationary. The reduction in wave amplitude when compared to the base case is caused by the slower surface wind speeds due to the effects of surface friction as parametrized by the boundary layer scheme.

A similar situation unfolds with the TKE parametrization of boundary layer turbulence shown in Figure 4.24, where once again, the amplitude of the vertically propagating gravity waves are reduced due to smaller surface wind speeds. In fact, the TKE and PBL approaches both demonstrate very similar outcomes, as shown in Figure 4.25 where vertical profiles of the streamwise velocity are compared at $t = 3$ hr. Near the surface, the profiles match very well both at the crater centre and the leading crater edge. However, in the upper atmosphere the profiles do not match well, likely due to a difference in the initial response to the constant wind forcing at earlier times.

The results from the parametrized boundary layer turbulence simulations raise the question of the appropriateness of using planetary boundary layer schemes in mesoscale simulations where small-scale, non-hydrostatic features are important. Generally, the PBL parametrizations are applicable to large-scale flows with grid spacing greater than a few hundred metres (Skamarock et al., 2008), which is close to the grid spacing employed in these results ($\Delta x = 500$ m). The planetWRF modellers argue that boundary layer schemes should be transferable from planet to planet, so these length scales are believed to be appropriate for the Martian atmosphere as well (Richardson et al., 2007). These

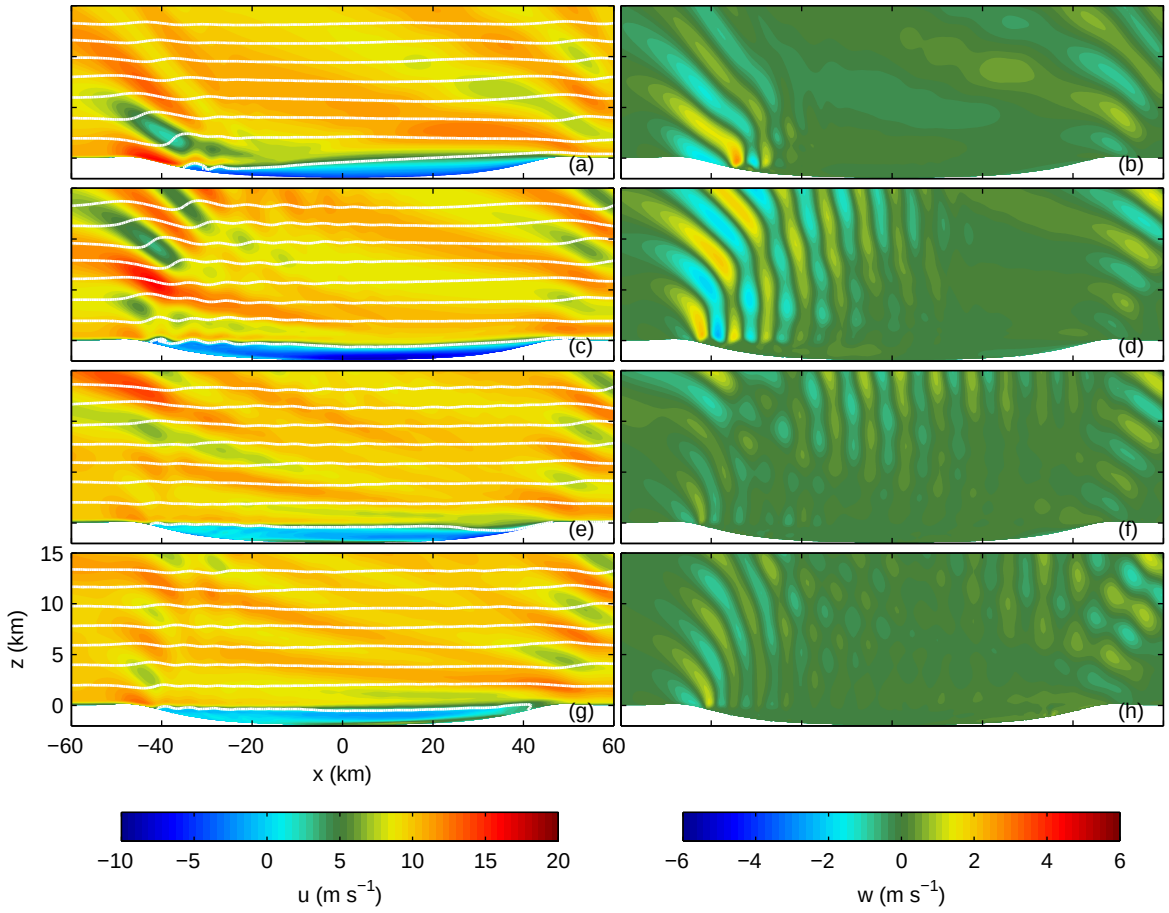

Figure 4.23: As in Figure 4.4 but for the simulation with a PBL scheme.

results indicate that with the inclusion of parametrized boundary layer turbulence the amplitude of topographically forced waves are reduced which may modify behaviour such as wave breaking. Additionally, the retreating gravity current is dampened which reduces the likelihood that the gravity current would act as a modified topography, however some evidence of secondary waves exists in these simulations, especially at early times. These differences also point to the possibility that the PBL schemes are excessively dissipative and may damp interesting flow features.

When the effects of friction are included flow separation is a possibility that may play a more important role than the gravity current in these simulations. However, there is a long list of literature on inviscid mountain wave studies, justifying the exclusion of surface

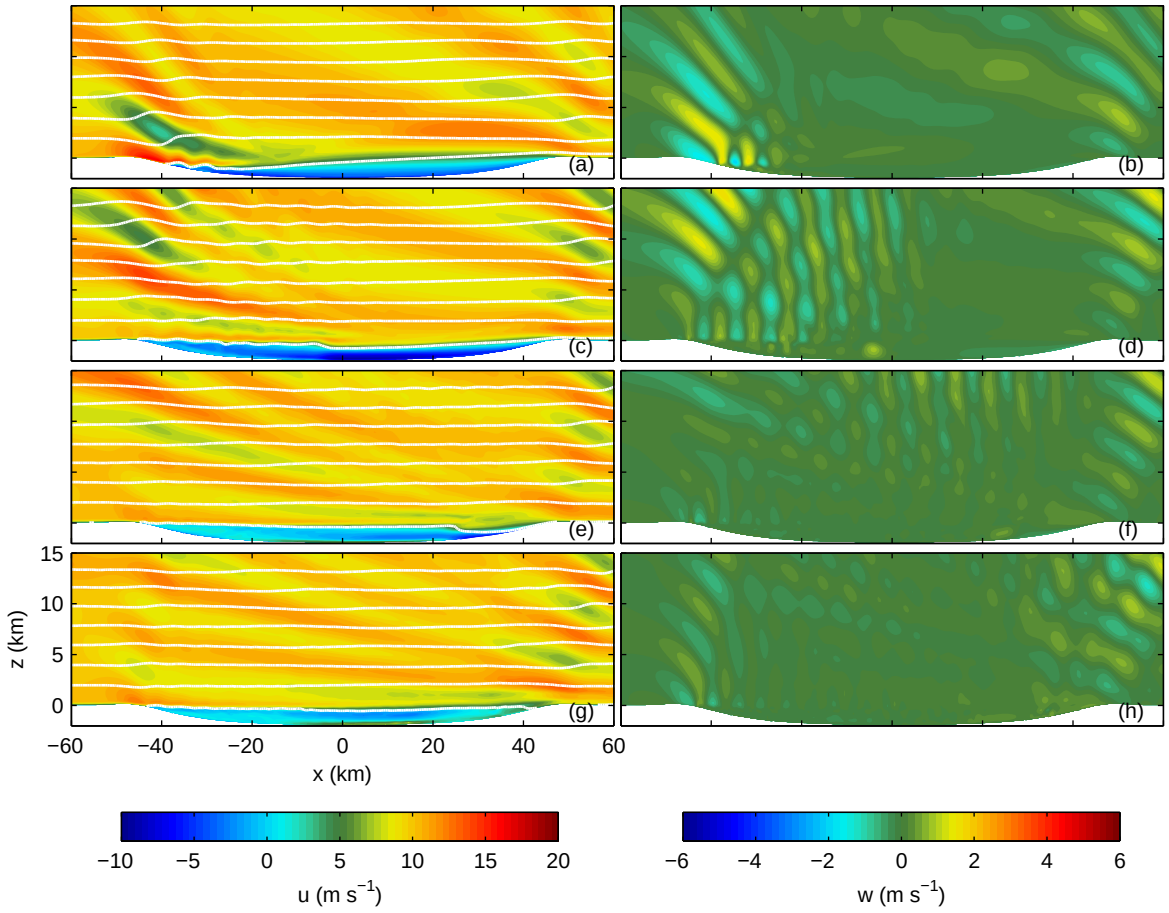

Figure 4.24: As in Figure 4.4 but for the simulation with a TKE scheme for boundary layer turbulence.

friction as an appropriate starting point in studies of flow over crater topography. The overall picture remains the same, with a primary beam of waves over the leading crater edge and a response to the initial tilting of the potential temperature contours. Finally, the WRF numerical model has many different parametrizations of boundary layer turbulence and surface friction, not all of which could be tested or examined thoroughly. The question of which parametrization to use remains open, although both the TKE and PBL schemes with the specified surface friction option performed similarly.

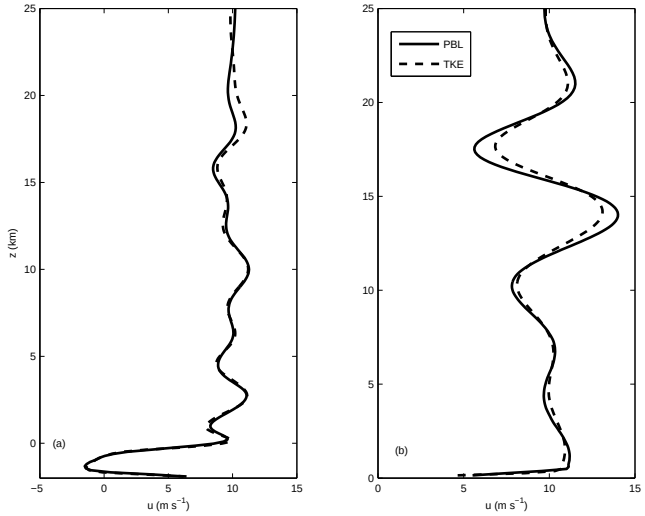

Figure 4.25: Comparison of streamwise velocity between the PBL (solid) and TKE (dashed) simulations at $t = 3$ hr. (a) At the centre of the crater $(x, y) = (0, 0)$ km. (b) At the leading crater edge $(x, y) = (-50, 0)$ km.

4.3.7 Martian Atmospheric Results

Two types of experiments under Martian atmospheric conditions are presented next. The modifications to the physical constants that are required to represent Martian conditions are outlined in Table 4.3. First, upper atmosphere internal wave propagation is examined under conditions associated with Martian temperature and wind profiles. Second, several simulations involving a low-level temperature inversion are considered. Both of these experiments still involve flow over crater topography and the crater described in Section 4.2 is used.

Upper Atmosphere Internal Wave Propagation

In the atmosphere, where the density decreases significantly with altitude, vertically propagating internal gravity waves are known to grow in amplitude as they ascend. As they grow in amplitude, nonlinear effects become important which may lead to overturning and breaking (Dosser and Sutherland, 2011). Recently, Spiga et al. (2012) found that internal gravity waves may be responsible for pockets of cold air and CO_2 clouds high in the Martian atmosphere. Using numerical simulations of flow over mountain topography with amplitude 4 km under Martian conditions with a uniform background wind of 30 m s^{-1} the authors found that internal waves could induce cold air pockets at an altitude around 80 km with temperature colder than the CO_2 condensation temperature at this altitude. These results matched with observations that show CO_2 clouds in an altitude range of 70-90 km (Clancy and Sandor, 1998).

This set of simulations examines gravity wave propagation as a result of flow over crater topography. The initial conditions are chosen as described in Subsection 4.2.4 and are displayed in Figure 4.3. Two simulations are presented. First, a simulations with a background wind profile given by a Mars general circulation model. Second, a simulation with a constant background wind of $U_0 = 10$ m s^{-1} is discussed.

The results from the first simulation are presented in Figure 4.26 and Figure 4.27. In this case the background wind exhibits a shear behaviour which resembles the zonal mean wind structure at this latitude (Read and Lewis, 2004). Wave characteristics are presented in the contours of the streamwise velocity through $y = 0$ km in Figure 4.26 (a). Similar to the results of the base case with Earth parameters, waves are generated over the leading and trailing crater edges, and a hydraulic feature forms within the crater interior. The internal waves grow with amplitude, particularly the waves over the leading crater edge. The wind-reversal level at $z \approx 55$ km acts as a barrier through which the internal waves do not seem to propagate (a gradual damping layer begins above $z = 65$ km). The

temperature contours in Figure 4.26 (b) exhibit pockets of air that, due to the presence of the internal gravity waves, are colder than their surroundings. However, these pockets do not approach the temperature required for CO_2 condensation at these altitudes. Spiga et al. (2012) found that relatively high background speeds of 30 m s^{-1} and topographic amplitudes of 4 km are required to induce such temperatures at high altitudes.

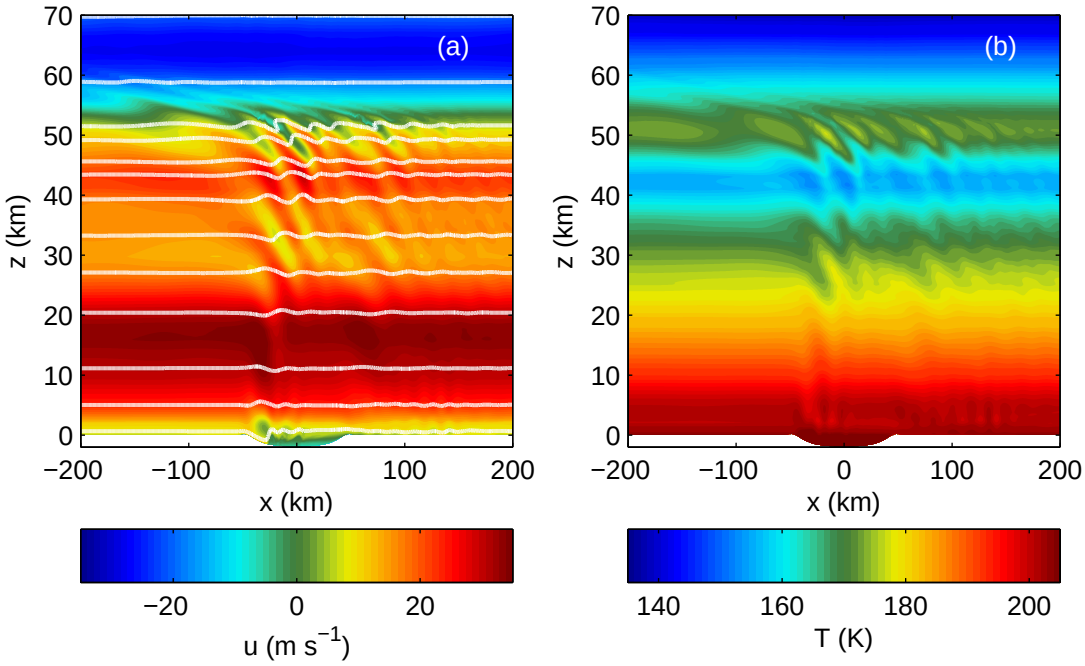

Figure 4.26: (a) Shaded contours of streamwise velocity overlaid with white potential temperature contours through $y = 0$ km for the crater with a shear background wind at $t = 3$ hr. (b) Shaded contours of the temperature at the same time.

Further examination of the waves characteristics is presented in Figure 4.27 where we have plotted the perturbation kinetic energy per unit mass as defined in Equation 4.4. This plot displays the horizontal structure of the waves, but also reflects the wave growth with altitude as the maximum kinetic energy increases with each successive plot. First, a horseshoe pattern of waves is observed in each plot with wave energy extending beyond the horizontal extent of the crater as occurred in the base case. Additionally, there appears to be some westward propagating motion that grows in amplitude at higher altitude. There also appears to be a focusing behaviour in the lee of the topography between a band centred at $y = 0$ km.

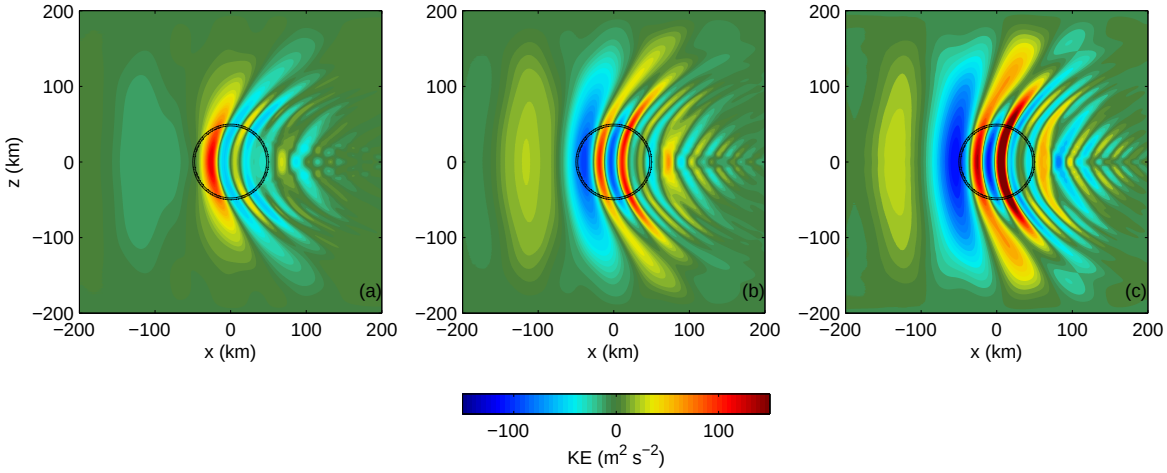

Figure 4.27: Perturbation kinetic energy at time $t = 3$ hr for the atmosphere with a zonal background wind. Three heights are shown (a) $z = 30$ km, (b) $z = 40$ km, and (c) $z = 43$ km.

The wind-reversal level appears to have a major impact on the upper atmosphere wave structure, hence we have performed an additional simulation with constant background wind $U_0 = 10$ m s^{-1}. This value of U_0 is chosen because it is close the the near-surface wind speed in the previous case. In Figure 4.28 we can see that the waves continue to grow in amplitude above $z = 55$ km in the absence of the wind-reversal level. Hence, the presence of a representative wind structure with wind-reversals at moderate altitudes may alter the wave structure in the highest part of the atmosphere. The hypothesis that internal gravity waves may induce cold pockets associated with CO_2 clouds should take into account the role of the background wind structure. This is considered by Spiga et al. (2012) by calculating a saturation index (Hauchecorne et al., 1987) to determine the likelihood that gravity waves break in the lower atmosphere before reaching high altitudes. They observe that in several locations where CO_2 clouds have been observed the saturation is suggestive of wave propagation to high altitudes.

A final comparison of the horizontal structure of the upper atmospheric waves is presented in Figure 4.29. First, it is evident that the waves in this case are much weaker than the waves in previous case, perhaps due to the effect of the wind-reversal level. The result is a strikingly different horizontal structure, with a stronger upstream response compared to the response in the downstream. However, the horseshoe-like structure of the waves remains, and has been documented in other three-dimensional flows over topography (Smith, 1979).

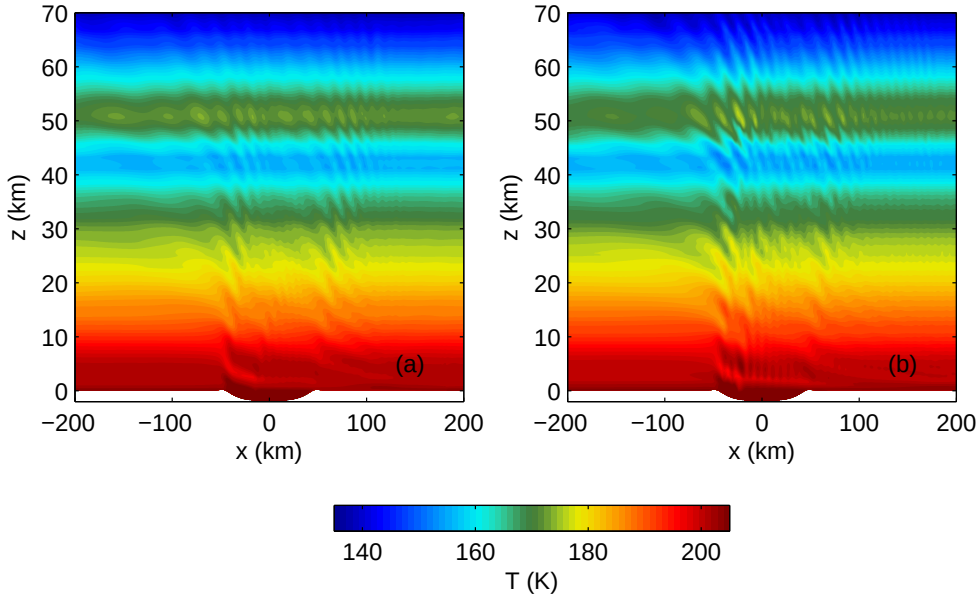

Figure 4.28: Shaded contours of the temperature for the atmosphere with a constant background wind. Two times are shown: (a) $t = 3$ hr and (b) $t = 5$ hr.

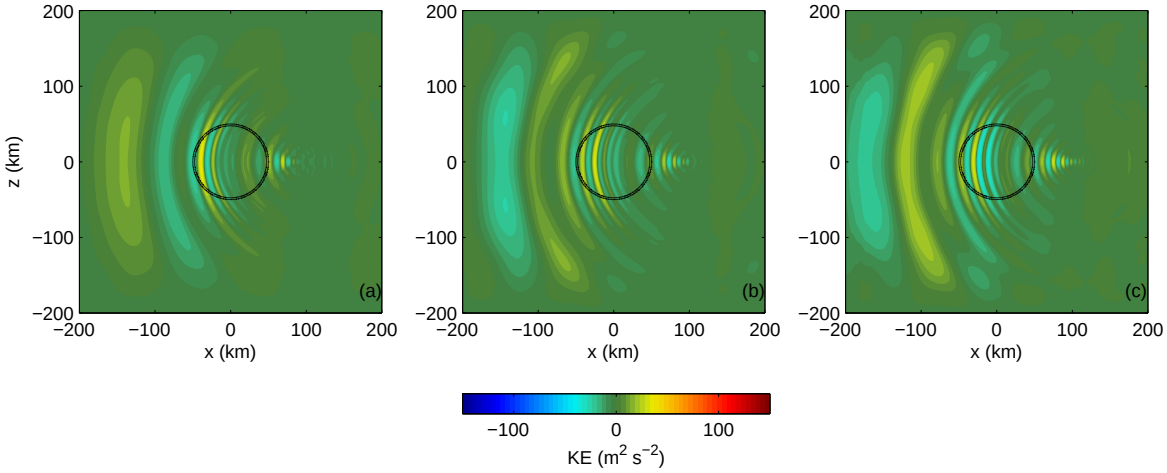

Figure 4.29: As in Figure 4.27 but for the atmosphere with a constant background wind.

In summary, the investigation of upper atmosphere waves in the Martian atmosphere remains an interesting avenue for further research. The suggestion by Spiga et al. (2012)

that internal gravity wave propagation could induce temperatures cold enough for the formation of CO_2 clouds is interesting but requires further investigation, particularly regarding the role of a realistic wind profile. The exploration of this topic could be simplified by considering bell-shaped topography since it is not likely that the horizontal shape of the topography would affect the high-altitude waves.

Low-Level Temperature Inversions

As outlined in Section 4.1, several studies have pointed to a connection between topographic flows and dust lifting/resuspension in the Martian atmosphere (Veverka et al., 1978, 1981; Lee, 1984; Magalhães and Young, 1995; Fenton et al., 2003) but these studies have not considered this issue from a full three-dimensional nonlinear dynamical perspective. In this section, we investigate numerical simulations of flow over crater topography in a Mars-like atmosphere with a near-surface temperature inversion. The purpose is to confirm whether or not flow structures associated with dust lifting, as suggested in other studies, do indeed form in a dynamical framework. The intent is to provide further insights into the mechanisms associated with topographic flows and potential for dust lifting, and in particular, to assess the role of a low-level temperature inversion on this process. As such, the focus of this section is on the mechanical processes of flow over crater topography and dust lifting parametrizations are left to be considered in a future study.

Since the stability characteristics within Martian crater interiors are not well-known, two cases involving low-level temperature inversions have been considered: 1) a crater with a stratified interior with $N = 0.03$ s^{-1} below $z = 600$ m and $N = 0.006$ s^{-1} above, and 2) a crater with an unstratified interior with $N = 0$ for $z < 0$, a capping inversion $N = 0.03$ s^{-1} for $0 < z < 600$ m, and $N = 0.006$ s^{-1} above this height. These are two extreme cases, either strongly stratified or not stratified, and will serve to demonstrate the role of the interior crater stratification on such a flow environment. They are loosely motivated by the difference between night and day near-surface stratifications: afternoon convection may cause a surface mixed layer with $N = 0$ and night-time cooling could result in a $N > 0$ stratification. This study is similar to the comparison between the base case and the two-layer atmosphere presented earlier; however, the presence of the capping inversion will affect the results. Additionally, since the crater is of a large size, the influence of rotation is also examined in both of these cases.

First, the crater with a strongly stratified interior is presented. A major consequence of the inversion is the nature of the large hydraulic response observed in Figure 4.30 (a) at time $t = 2$ hr near $x = -40$ km in the case with a stratified interior. This structure is similar to the retreating gravity current in the constant N, $F_r = 0.5$ base case noted above. The

retreating gravity current formed in response to the tilted potential temperature contours when warm fluid enters the cold crater interior, though it differs in a few key respects. First, the strongly stratified interior does not allow the fluid to penetrate far into the crater interior and, as such, the tilted potential temperature contours respond quickly by forcing a seiche-like behaviour in the crater interior. This is observed in Figure 4.30 (b)-(e) where the magnitude of the hydraulic response is found to grow and decay over time in an oscillatory fashion. Seiche behaviour for topographic crater flow has been noted previously in Subsection 4.3.5 and by Fritts et al. (2010) for a small crater with diameter 1.2 km in the Arizona desert which may lead to sloshing or ejection of the cold air from the crater interior, and the eventual break up of the cold pool within the crater interior. Some evidence of this is apparent in Figure 4.30 (a) at $x \approx 70$ km where pockets of fluid have been ejected from the crater interior. This seiche and sloshing behaviour was not observed in the constant N stratification discussed above. In those results, a retreating gravity current formed in response to the tilted potential temperature contours but it remained relatively stationary once it reached the leading crater edge.

A few features are similar to the results from the base case. First, vertically propagating gravity waves are present over both the leading and trailing crater edges with a three-dimensional structure similar to the base case. Additionally, the fluid is forced up and over the hydraulic feature in a similar manner to the effect of a modified topography, which shortens the effective topographic length scale of this flow environment. For instance, the entire 2 km depth of the crater is effectively not observed by the intruding air but rather a vertical length scale of approximately 1.5 km in Figure 4.30 (b) associated with the hydraulic feature is predominant. This vertical length scale changes over time due to the time-dependent nature of the flow and is approximately 1.5 km at $t = 2$ hr in Figure 4.30 (b). Similarly, the effective horizontal topographic length scale has been reduced to 7-10 km in Figure 4.30 due to the presence of the hydraulic feature. Another similar feature is the increase in surface velocities along the leading crater edge up to the location of the hydraulic feature. The streamwise velocity along this surface is up to 1.6 times greater than the background wind. Magalhães and Young (1995) suggest that downslope wind storms with wind speeds up to 4 times greater than the background wind are capable of initiating dust lifting. The factor increase observed here is significantly smaller than four. Magalhães and Young (1995) considered cases with the background wind ranging between 1-10 m s^{-1} hence many of their cases consider smaller wind speeds than those discussed in these results.

A visualization of the motion within the crater interior in a two-dimensional simulation is displayed in Figure 4.31 where we plot the streamwise velocity through the crater centre point $(x, y) = (0, 0)$ km at several different times. The behaviour of the streamwise velocity

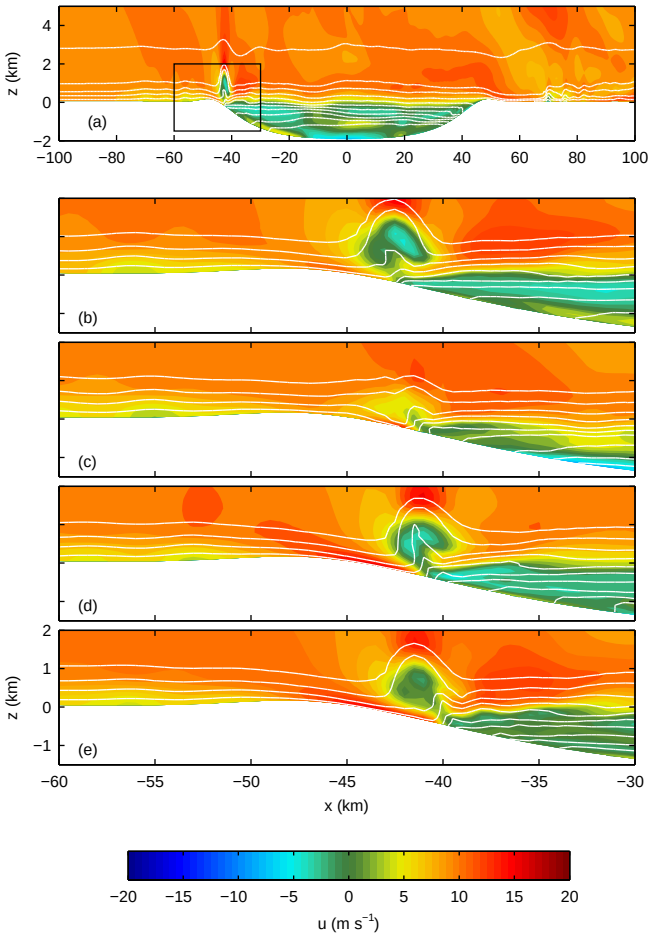

Figure 4.30: Shaded contours of streamwise velocity overlaid with white potential temperature contours for the crater with a stratified interior through $y = 0$ km. (a) A general view at $t = 2$ hr and detailed views within the black rectangle at (b) $t = 2$hr, (c) $t = 2.5$ hr, (d) $t = 3$ hr, (e) $t = 3.5$ hr.

within the crater interior is quite complicated but appears to be oscillatory in nature. Additionally, the dashed lines indicate a reasonable agreement between two-dimensional and three-dimensional simulations.

In Figure 4.32, a second profile through $(x, y) = (-40, 0)$ km is considered, which corresponds approximately to the location of hydraulic feature in Figure 4.30. Departures between two- and three-dimensional results are quite large in this region, where the hydraulic feature is the dominant effect. Hence, the dynamics of the hydraulic response are

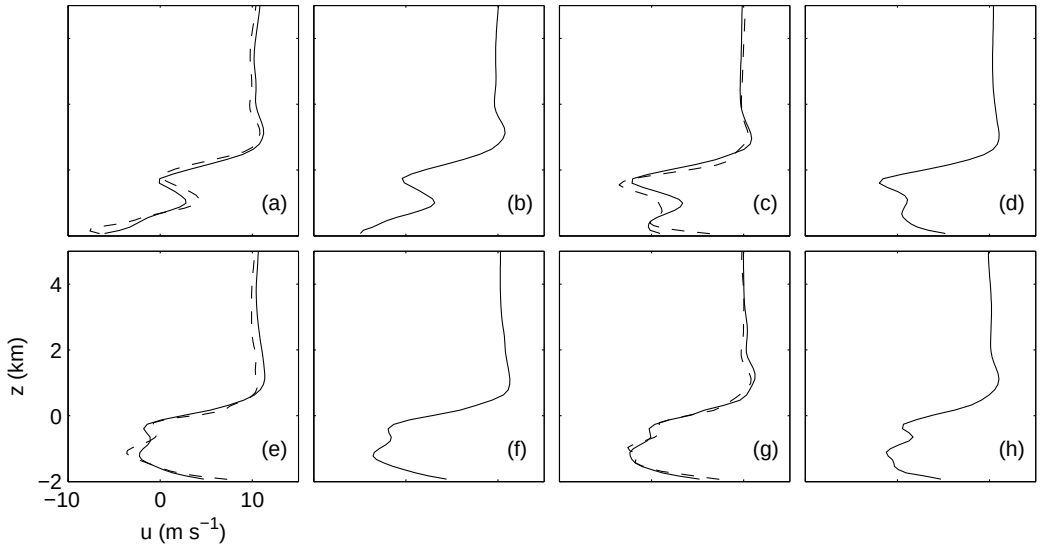

Figure 4.31: Streamwise velocity profile at the crater centre $(x, y) = (0, 0)$ km for the crater with a stratified interior. Panel (a) displays the profile at $t = 3$ hr and the time increasing by 15 minutes in each subsequent panel. The solid line displays the two-dimensional results and the dashed line displays the three-dimensional results.

believed to be primarily three-dimensional. Additionally, oscillatory motion with period approximately 1 hr is observed in this plot.

Since the diameter of the crater is relatively large the dynamics of this flow environment could be altered by the effects of rotation. As such, a simulation with a Coriolis frequency $f = 10^{-4}$ s^{-1}, consistent with a midlatitude value on Mars (Read and Lewis, 2004), is included for comparison in Figure 4.33 at time $t = 3$ hr. The near-surface kinetic energy density for the non-rotating case in Figure 4.33 (a), calculated at the first grid level at approximately 50 m above the surface, displays the horizontal structure of the flow near the surface. Higher velocities are evident along the leading crater edge between $x = -45$ km and $x = -40$ km. The lower kinetic energy within the crater reflects the fact that the fluid here moves relatively slowly when compared with other areas in the computational domain. The effect of rotation is displayed in Figure 4.33 (b) where, once again, the highest velocities are observed along the leading crater edge. However, here they are deflected to the right and focused below $y = 0$ km due to the rotation. Additionally, the rotating case exhibits a larger maximum kinetic energy and a more expansive region of greater kinetic energy density than in the non-rotating case. An area swept out from $x = -40$ km to $x = -35$ km up to about $y = 0$ km contains kinetic energy values greater than the

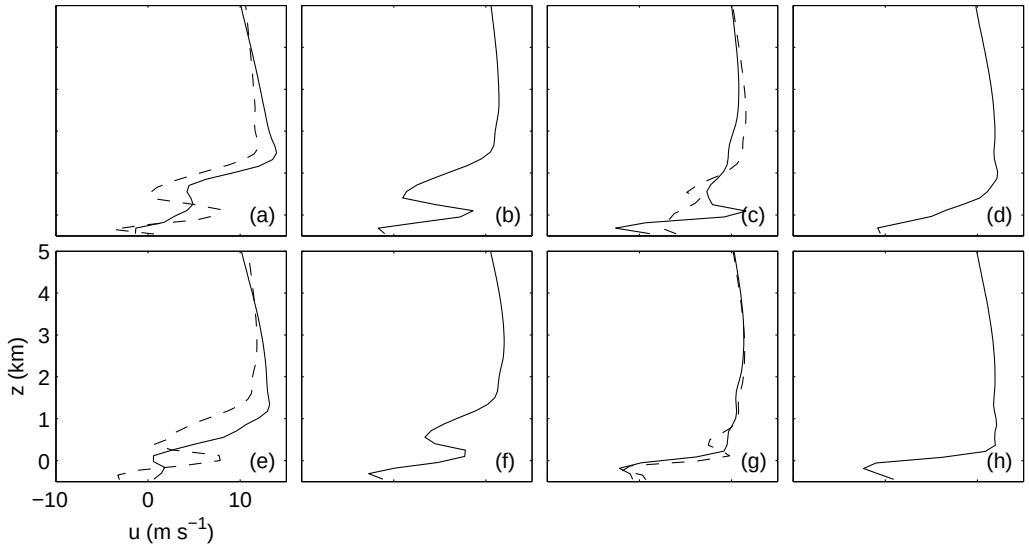

Figure 4.32: As in Figure 4.31 but through $(x, y) = (-40, 0)$ km.

maximum kinetic energy observed in Figure 4.33 (a). The area of increased kinetic energy follows the shape of the leading half of the crater in both cases, although the area in the rotating case is slightly wider in the region $y < 0$ km.

A quick overview of the streamwise velocity through the same profiles displayed in the non-rotating case are shown in Figure 4.34. Due to the high memory requirements for storing three-dimensional simulation results, we did not save outputs as often as in the two-dimensional and non-rotating cases. Hence, the times displayed in this figure range from $t = 2$ hr to $t = 5$ hr for profiles through $(x, y) = (0, 0)$ km in the upper panels (a-d) and $(x, y) = (-40, 0)$ km in the lower panels (e-h). The results are quite similar to the non-rotating case.

Since the temperature stratification within crater interiors on Mars is not generally well-known, we have performed an additional simulation in order to test whether the interior stratification plays an important role in the dynamics of the flow. A crater with an unstratified interior is considered in the next simulation, where $N = 0$ below $z = 0$ km in the crater interior above which a capping inversion is placed, with $N = 0.03$ s^{-1} for $0 < z < 600$ m and $N = 0.006$ s^{-1} above. The results are plotted in Figure 4.35 where potential temperature contours and the streamwise velocity are displayed for several times, similar to that shown in Figure 4.30. First, the wave response is very similar to the previous case, with vertically propagating gravity waves over the leading and trailing crater edges.

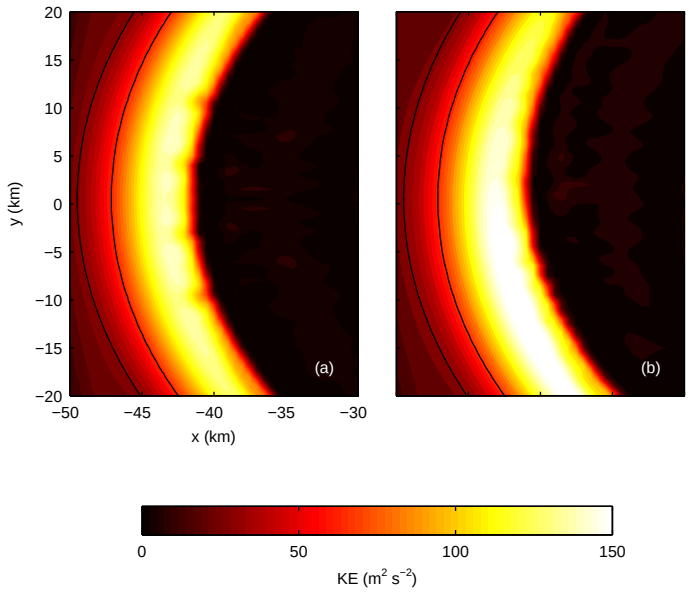

Figure 4.33: Kinetic energy per unit mass near the surface at $t = 3$ hr for the crater with a stratified interior. The black contours indicate the crater rims. (a) no rotation, (b) rotation.

This is expected since parameters governing the wave dynamics in the atmosphere outside of the crater are unchanged. Within the crater, the fluid is almost stationary throughout the entire depth. This is quite different from the stratified case where oscillatory motions with a period approximately $T_0 = 1$ hr were observed (Figure 4.30). This, in turn, leads to a different behaviour near the leading crater edge in Figure 4.35 (b)-(e). Previously, the hydraulic feature at the leading crater edge exhibited quasi-periodic growth and decay as the stratified interior responded to the initial disturbance. In this case no oscillatory motion is observed but the hydraulic feature grows over time leading to some overturning at the leading crater edge and nearly vertical potential temperature contours. A low-level jet enters further into the crater depth than in the stratified case, similar to that observed in the two-layer atmosphere case presented above. However, the presence of a capping inversion causes the formation of a hydraulic structure near the leading crater edge, which may have important implications for dust resuspension. Once again, the effective horizontal and vertical length scales of the topography have been reduced due to non-hydrostatic features such as the hydraulic response.

The behaviour within the crater interior is much different than that observed in the

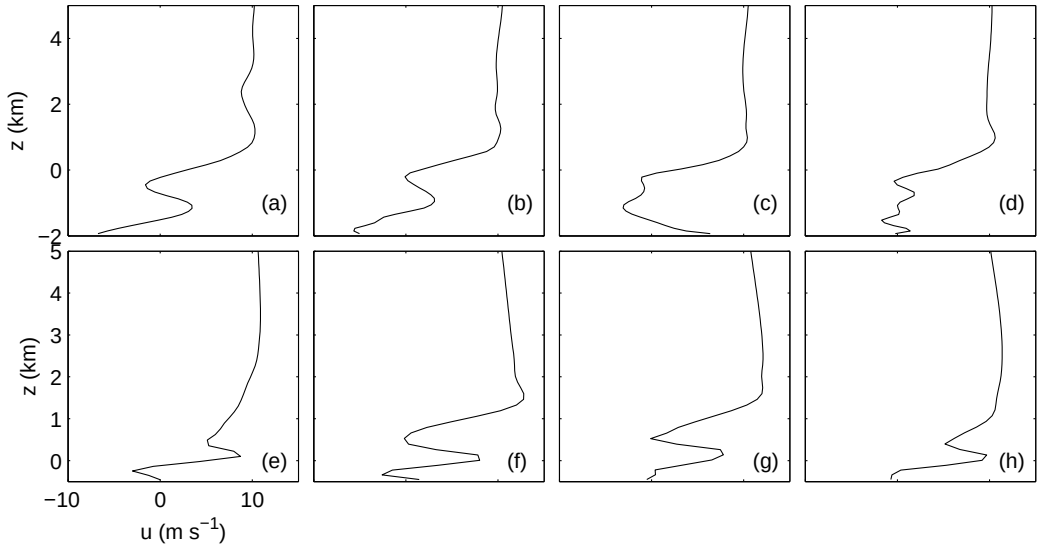

Figure 4.34: Plots of the streamwise velocity for the stratified rotating case through: $(x, y) = (0, 0)$ km in the upper panels (a-d) and $(x, y) = (-40, 0)$ km in the lower panels (e-h). The times displayed are: $t = 2$ hr (a and e), $t = 3$ hr (b and f), $t = 4$ hr (c and g), and $t = 5$ hr (d and h).

stratified case, as demonstrated in Figure 4.36 where the streamwise velocity through $(x, y) = (0, 0)$ km is plotted for a two-dimensional simulation. Here, it is very clear that the crater interior is relatively motionless, and no seiche or oscillatory behaviour is observed. Once again, the two- and three-dimensional simulations match nicely through this profile.

A different profile is considered through $(x, y) = (-40, 0)$ km in Figure 4.37 where the hydraulic response is the dominant feature. No oscillatory motion is observed in this case, but the jet of air descending into the crater depths is clearly captured in the streamwise velocity profile. Differences between the two- and three-dimensional results are more substantial than the profile through $(x, y) = (0, 0)$ km, likely since the hydraulic feature is inherently three-dimensional.

The effect of rotation for this case is displayed in Figure 4.38 in the near-surface kinetic energy density at time $t = 3$ hr in both a non-rotating and rotating case. High near-surface velocities extend further into the crater than in the stratified case, however, the kinetic energy density is of a smaller magnitude in most locations. Similar to the previous case, the kinetic energy density is lowest throughout the crater interior where the fluid is nearly stationary. This case also displays some three-dimensional structure which extends beyond

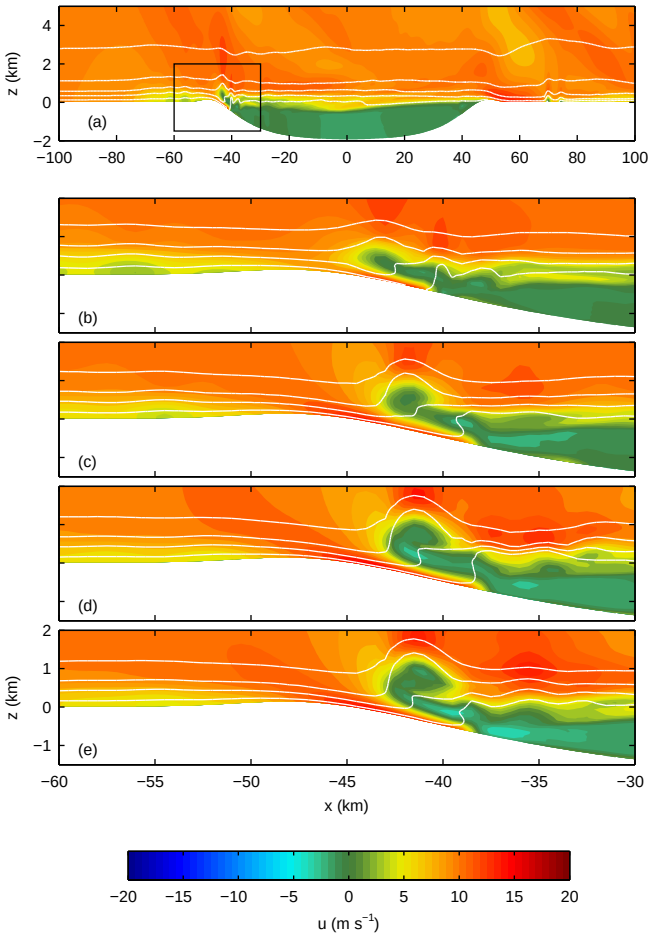

Figure 4.35: As in Figure 4.30 but for the crater with an unstratified interior.

the high kinetic energy density region over the leading crater edge. Small protrusions along the front are clearly visible, and are likely associated with overturning or breaking events (Afanasyev and Peltier, 1998). These protrusions may be important for dust distribution along the surface and could lead to light and dark dust streaking behaviour. The areas of high kinetic energy could lead to a scouring of the surface resulting in dust erosion and dark streaks. The areas of low kinetic energy may be associated with deposition and light streaks. This feature should be examined more closely and should be compared with observations. The rotating case displays a similar scenario but the low-level jet exhibits higher velocities below $y = 0$ km due the effects of rotation. The result is a focusing of velocities along the jet in the southern crater half, similar to that observed in the stratified

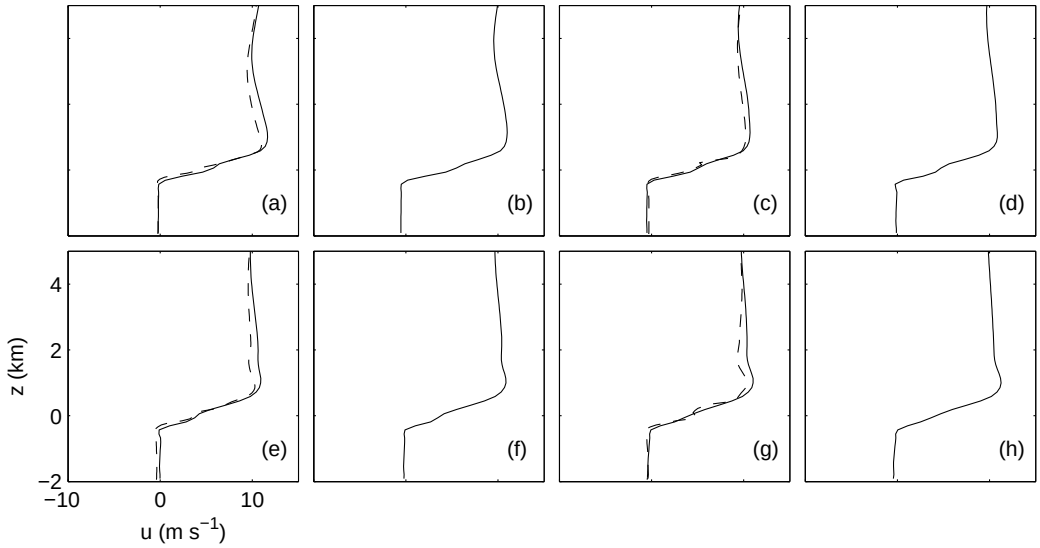

Figure 4.36: As in Figure 4.31 but for the crater with an unstratified interior.

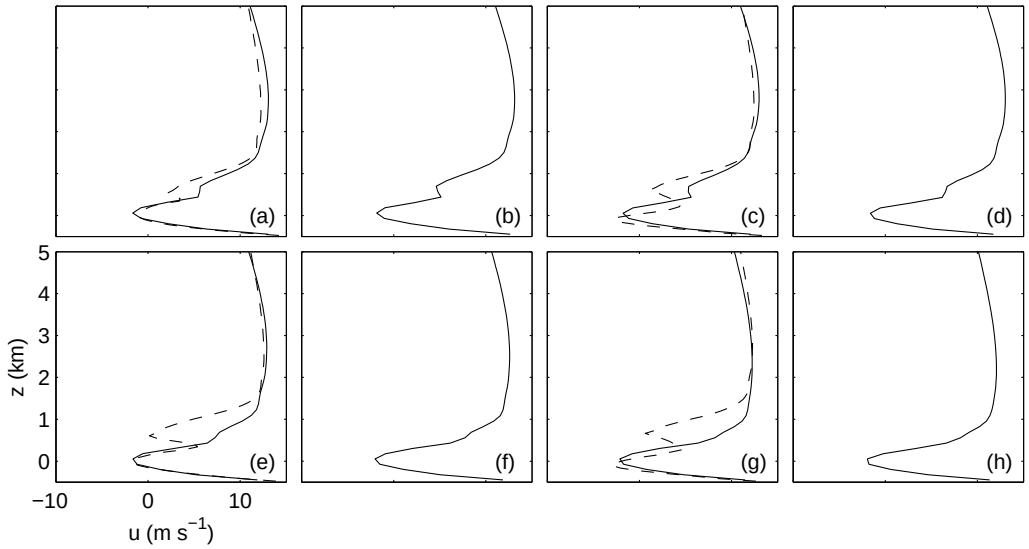

Figure 4.37: As in Figure 4.36 but through $(x, y) = (-40, 0)$ km.

case.

Profiles of the streamwise velocity through $(x, y) = (0, 0)$ km and $(x, y) = (-40, 0)$ km with rotation are shown in Figure 4.39 similar to Figure 4.34 for the stratified case.

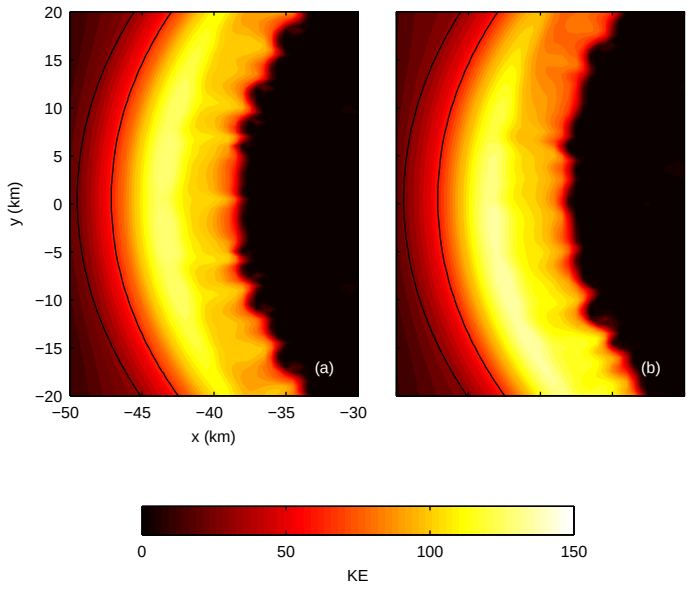

Figure 4.38: As in Figure 4.33 but for the crater with an unstratified interior. (a) no rotation, (b) rotation.

Here, it is a apparent that a very different type of behaviour occurs through the crater centre where the fluid is almost stationary, and between at the leading crater edge where the hydraulic response is the dominant feature. The profiles appear to be similar to those shown in the non-rotating unstratified case.

The presence of a near-surface temperature inversion in flow over crater topography may have implications for dust resuspension in the Martian atmosphere. The hydraulic response formed along the leading crater edge may provide a mechanism for transporting dust away from the surface, higher into the atmosphere. This hydraulic response was present in both of the cases presented here, and a similar structure was formed in the base case with constant N stratification. Hence, this structure appears to be robust under stratified conditions. Whether near-surface wind speeds along the leading crater edge reach sufficiently high values to initiate dust lifting in such flow environments remains an open question but is addressed to some degree by Magalhães and Young (1995) for bell-shaped topography. The authors found, using a steady-state model, that night-time temperature inversions and wind-reversal levels combined with wind speeds typical of the Martian atmosphere could lead to surface velocities up to four times greater than the background state. Work by Greeley et al. (1980) predicts surface friction velocities required

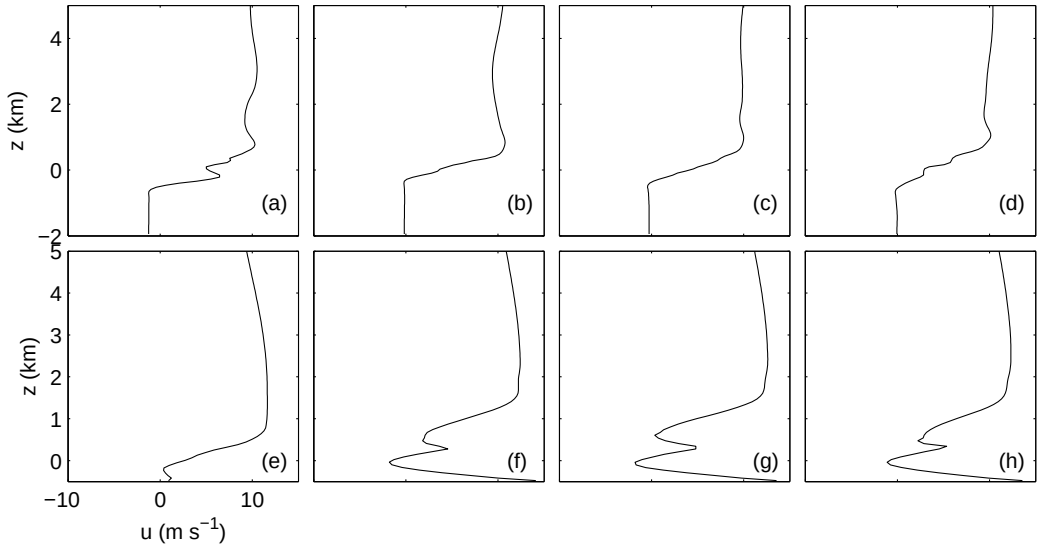

Figure 4.39: As in Figure 4.34 but for the case with an unstratified crater interior.

for dust lifting on Mars to be $u_*^t = 1-2$ m s^{-1}, a value far greater than the friction velocities calculated by Martian general circulation models. Magalhães and Young (1995) suggest that the factor of 4 increase in wind speeds due to downslope wind storms could account for the discrepancy between the threshold friction velocity and general circulation model results. Thus, topographic effects such as downslope wind storms, which are unresolved in general circulation models, could provide an explanation for the dust lifting and wind streaks observed on the Martian surface.

In the results presented here, the highest velocities occur along the leading crater slope as air begins to enter the crater interior, which indicates that there may be potential for dust lifting in this area. The highest velocities attained were around $u \approx 16$ m s^{-1} at a height of $z \approx 60$ m. Close to the surface, air velocities are known to follow an approximately logarithmic profile with height (Read and Lewis, 2004):

$$u(z) = \frac{u_*}{k} \ln\left(\frac{z}{z_0}\right),$$

where z_0 is the roughness length, and $k \approx 0.4$ is the von Karman constant. On Mars, the roughness length is $z_0 \approx 1$ cm (Read and Lewis, 2004). These values can be used to produce a very rough calculation of the friction velocity $u_* \approx 0.7357$ m s^{-1}, which is slightly less than the threshold expected for lifting $u_*^t = 1-2$ m s^{-1} but higher than values predicted by Martian general circulation models (Magalhães and Young, 1995). However,

this is a very rough calculation and a study with the inclusion of boundary layer turbulence and surface friction would more accurately diagnose the near-surface friction velocities in this flow environment.

Another factor which could cause higher near-surface wind speeds along the leading crater edge is rotation. In the cases presented here, rotation acted to increase near-surface velocities throughout a region along the leading crater edge. This focusing effect provides a clue as to where dust lifting is most likely to occur in large craters, with respect to the direction of the background wind. In the cases presented here, an eastward wind induces highest near-surface velocities in the southern half of a crater that is located in the northern hemisphere.

4.4 Discussion and Future Work

This chapter has outlined many aspects of flow over crater topography ranging from variations in atmospheric parameters, topographic shapes, and forcing conditions. The main results, which include the base case, reduced stratification, two-layer atmosphere, the crater with no rims, increased curvature, and the section on rotation have all been discussed thoroughly by Soontiens et al. (2013a). The remaining results, including the spanwise shear, seiche simulations, planetary boundary layer, and Martian atmospheric parameters, serve as an extension to the discussion by Soontiens et al. (2013a) and provide a more complete picture of the flow environment. This investigation of flow over crater topography was motivated by the connection between crater topography and dust streaks in the Martian atmosphere (Veverka et al., 1978, 1981; Lee, 1984; Fenton et al., 2003). Although dust lifting parametrizations were not considered in this work, the dynamical perspective presented in this chapter is a necessary beginning for studying this connection, since flow over crater topography has not been investigated thoroughly in a dynamical framework. Thus, this chapter outlines a foundation for studying the influence of crater topographic flows on dust listing. An extensive array of literature on topographic flows and mountain waves was essential for researching this topic.

An important extension for this work is the inclusion of dust lifting parametrizations in this flow environment. The purpose of studying flow over crater topography was to investigate the mechanics associated with dust lifting around craters in the Martian atmosphere. Without the inclusion of dust tracers and lifting parametrizations, only hypotheses can be made about the role of topographic flows on dust resuspension. In many of the cases presented here, including the base case and cases with temperature inversions, a hydraulic structure of large amplitude formed along the leading crater edge, which acted as a modified topography forcing additional vertical displacements. This modified topography has the potential to induce the transport of dust away from the surface and high into the atmosphere, provided that wind speeds along the leading crater edge are high enough to induce dust lifting. Accurate dust lifting and surface friction parametrizations are needed to confirm this idea, but these preliminary results have indicated that this topic is worthwhile for future investigations, particularly under Martian atmospheric conditions.

Some typical mountain wave properties have been examined, including three-dimensional properties of the waves and comparisons with two-dimensional results. Some aspects, such as the absence of an upstream propagating disturbance in three dimensions, a reduced likelihood for wave breaking in three dimensions, and the lateral dispersion of wave energy aloft, that have been outlined in mountain wave studies have been shown here to also occur for crater topography. An important result is the reduction of topographic length scales

due to the hydraulic response within the crater. This reduction of length scales makes properties such as the hydrostatic nature of the flow difficult to determine *a priori*. Additionally, it was discovered that, for the crater profile considered here with 100 m rims and a 2 km depth, the rims have little impact on the wave structure and the topographic depth and hydraulic response produce more significant wave signatures. Early studies regarding flow over crater topography considered only the rim structure of the crater and neglected to include the effects of the depression (Pirraglia, 1976; Pickersgill and Hunt, 1979). Finally, the importance of adequate vertical resolution was discussed by considering several simulations under a variety of resolutions. It was found that increasing the horizontal resolution in cases where the vertical scale was moderately resolved made little difference in the simulation results. The vertical grid spacing should be at least on the same scale as the horizontal grid spacing, if not smaller.

This chapter has also shown the potential importance of boundary layer parametrizations and seiche behaviour, both of which require further investigation. The planetary boundary layer simulations are important to consider if dust lifting is to be examined in this flow environment since surface friction and accurate surface physics will undoubtedly impact the process of dust lifting and resuspension. These results show that surface friction acts to reduce amplitudes, both of the vertically propagating waves and of the hydraulic response, although this may be the result of excessively dissipative surface friction and PBL schemes. Further work involving PBL parametrizations appropriate for mesoscale dynamics is warranted. Additionally, the seiche behaviour should be investigated further since it may have important implications for ejection of fluid outside of the crater basin and mixing within the crater interior (Fritts et al., 2010). The seiche behaviour was discussed in this chapter, to differentiate any wave motion caused by the background wind and that caused by any seiche oscillations within the crater. This is an interesting topic that could be expanded upon in future work.

Martian atmospheric conditions were also considered and extend upon previous work on topographic flows on Mars. First, predictions by Spiga et al. (2012) that gravity waves could be responsible for cold pockets that cause CO_2 clouds high in the Martian atmosphere were tested with a zonal wind structure rather than the constant background wind. We found that the wind-reversal level in the wind may hinder the propagation of gravity waves high into the atmosphere. Additionally, the work by Magalhães and Young (1995) suggested that downslope wind storms may be responsible for dust lifting events in the Martin atmosphere. Since downslope winds storms are often associated with low-level temperature inversion or wind-reversal levels, we have considered this idea from a dynamical perspective over crater topography. We found that this environment may lead to fluid structures associated with dust resuspension, but dust lifting parametrizations and surface friction should be

included to examine this topic more completely. Two stratifications with a temperature inversion were considered: one with a strongly stratified crater interior and one with an unstratified crater interior. These two stratifications were motivated by the possibility of afternoon convection causing a well-mixed, unstratified surface layer or night-time cooling which could result in $N > 0$ near the surface. In the case of an unstratified crater interior, areas of high and low kinetic energy along the leading crater edge may lead to a streaking pattern in dust distribution along the surface. The studies which included the effect of rotation found a focusing of velocities along the leading crater which may lead to clues about locations of dust lifting in large-scale crater topography.

The study of flow over crater topography serves as an interesting and natural extension to previous mountain wave studies. It is an important topic to consider for understanding topographic effects in the atmospheric circulation of Mars since crater topography is abundant on the Martian surface. Additionally, some findings can be carried over to studies of topographic flows on Earth where crater topography does exist (Fritts et al., 2010) although usually on a smaller scale. Finally, the three-dimensional nature of the flow can now be carefully studied with numerical simulations and increased computing power.

Chapter 5

Concluding Remarks

This chapter builds on the conclusions given at the end of Chapters 2-4 by highlighting the connections between the parts of this thesis and discussing relationships between the results. First, comparisons between the inviscid and viscous results of chapters 2 and 3 serve to outline the effects of the viscous boundary layer. One important question is whether or not steady trapped waves exist when the effects of the viscous boundary layer are taken into account. Clearly, for the parameters considered here the boundary layer is not steady and is subject to eventual turbulent breakdown away from the topography. Moreover, the steadiness of the trapped wave of elevation in each of the viscous simulations remains uncertain. For instance, over elevation topography, one might expect the boundary layer to act as an extension of the topography, and thus would have little effect on the trapped wave. However, we saw that after long simulation times, instabilities could form on the upstream slope. There is potential for these upstream instabilities to shed vortices into the water column and interact with the pycnocline to alter the properties of the steady trapped waves. Whether the overall structure of the trapped wave is maintained in some sort of quasi-steady state is a subject for future exploration. The interaction between the trapped wave and the boundary layer instabilities should be investigated further by considering different stratifications, background speeds, and topographic profiles.

Taken at face value, the largest trapped waves observed in the steady inviscid results should have the biggest effect on the boundary layer due to their large wave-induced velocities. However, the formation of the boundary layer and separation region found with depression topography could alter the amplitude of the trapped internal waves of depression to fundamentally alter this conclusion. The results with depression topography in the viscous simulations suggest that this scenario is likely at least for experimental-scale domains. Further study is required to determine how these findings carry over for large-

scale dynamics over topography (Fritts et al., 2010). However, it is interesting to note that over the lee (or downslope) side of the elevated topography we did not observe a separation region, even though the shape of the topography and slope is similar to the depression case. The absence of separation is likely due to the very large velocities induced by the waves generated by the topographic flow (or equivalently the large-scale pressure distribution). Perhaps the downslope wind storms discussed in the craters chapter could have a similar effect in producing velocities large enough to overcome local separation along downward topographic slopes. As discussed previously, a near-surface temperature inversion could act to enhance downslope winds. The temperature inversion acts in a similar manner to the pycnocline since they both contain an area of increased buoyancy frequency.

The downstream instabilities observed in the viscous simulations of flow over elevation topography are likely to induce sediment pickup and resuspension in the topographic lee. This result may have a connection with the downstream behaviour in the flow over crater topography. Although viscous dynamics were not considered in the crater topography, interesting dynamics were observed in the crater's lee. The viscous simulations indicate that the instabilities in the topographic lee could lead to sediment resuspension and vortex shedding. On a larger scale, under viscous conditions, this may explain the the dust streaking behaviour observed in the lee of many Martian craters. This behaviour motivates future studies on flow over crater topography with the inclusion of surface friction and dust lifting parametrizations, or even more complete turbulence models.

Finally, the viscous boundary layer simulations were performed at scales more typical of laboratory experiments than geophysical flows (a depth of approximately 1 m). Questions as to whether or not the results and instabilities would carry over to a scaled-up environment more appropriate to lake or coastal ocean scales remain open. However, preliminary simulation results in a 10 m deep channel indicate that these instabilities are present for large enough waves. As in the lab-scale simulations, small separation bubbles form in a convergence zone downstream of the topography. Additionally, the fact that overdamping (i.e. high eddy viscosity) in the lab-scale boundary layer simulations led to a drastic change in the energetics of the boundary layer instabilities suggests that planetary boundary layer and surface friction schemes in modelling atmospheric flows may not represent the mechanisms that are most important for dust lifting. It is unlikely that large-scale, or even mesoscale, simulations could resolve the mechanisms for dust lifting entirely, hence PBL and dust lifting parametrizations remain necessary. Perhaps topographic effects should be accounted for in the dust lifting parametrizations through increased lifting tendencies in the topographic lee. Typically, dust lifting parametrizations are framed in terms of a threshold friction velocity that determines the onset of dust lifting (Read and Lewis, 2004). If topography is left unresolved in general circulation models then any increased velocities

caused by some topographic flows, such as downslope wind storms, are not accounted for and cannot contribute to dust lifting. Other dust lifting parametrizations which account for gustiness by using a Weibull distribution and also dust devils have been developed (Newman et al., 2002). Certainly, the study of dust lifting parametrizations is advancing and more work can be completed to investigate modified parametrizations that account for topographic effects.

Although the topics discussed in this thesis span a range of length scales and flow environments, each of the chapters have inspired ideas for future work in all areas. Combined, they have all contributed to a general advancement of the study of stratified flow over topography by comparing viscous and inviscid results, and comparing flows over small and large scales. The topics discussed in this work have addressed questions that have not been investigated in the current literature. For instance, this thesis has provided an in-depth analysis of steady inviscid flow over topography by examining large-amplitude waves under Boussinesq and non-Boussinesq conditions, as well as constant and sheared background currents. The analysis of the DJL equation has allowed for an efficient exploration of parameter space in a fully nonlinear, steady framework. Additionally, these results have been extended with the addition of a viscous boundary layer under similar flow conditions. The boundary layer instabilities caused by the passage of topographically generated internal waves have been studied in three dimensions, a computationally expensive problem, even at laboratory scales. Finally, the flow over crater topography has not been thoroughly examined from a dynamical perspective in the past. As such, this topic serves as a natural extension to the current literature on mountain waves. In addition, the results may lead to insights into the connection between crater topography and dust streaks on the Martian surface.

Copyright Letters

Copyright permission letters have been attached here.

AIP PUBLISHING LLC LICENSE TERMS AND CONDITIONS

Sep 11, 2013

All payments must be made in full to CCC. For payment instructions, please see information listed at the bottom of this form.

License Number	
Order Date	Sep 11, 2013
Publisher	AIP Publishing LLC
Publication	Physics of Fluids
Article Title	Numerical simulation of supercritical trapped internal waves over topography
Author	Nancy Soontiens, Christopher Subich, Marek Stastna
Online Publication Date	Nov 24, 2010
Volume number	22
Issue number	11
Type of Use	Thesis/Dissertation
Requestor type	Author (original article)
Format	Print and electronic
Portion	Excerpt (> 800 words)
Will you be translating?	No
Title of your thesis / dissertation	Stratified flow over topography: steady nonlinear waves, boundary layer instabilities, and crater topography
Expected completion date	Nov 2013
Estimated size (number of pages)	200
Total	0.00 USD
Terms and Conditions	

AIP Publishing LLC -- Terms and Conditions: Permissions Uses

AIP Publishing LLC ("AIPP"") hereby grants to you the non-exclusive right and license to use and/or distribute the Material according to the use specified in your order, on a one-time basis, for the specified term, with a maximum distribution equal to the number that you have ordered. Any links or other content accompanying the Material are not the subject of this license.

1. You agree to include the following copyright and permission notice with the reproduction of the Material:"Reprinted with permission from [FULL CITATION]. Copyright [PUBLICATION YEAR], AIP Publishing LLC." For an article, the copyright and permission notice must be printed on the first page of the article or book chapter. For photographs, covers, or tables, the copyright and permission notice may appear with the Material, in a footnote, or in the reference list.
2. If you have licensed reuse of a figure, photograph, cover, or table, it is your responsibility to ensure that the material is original to AIPP and does not contain the copyright of another entity, and that the copyright notice of the figure, photograph, cover, or table does not indicate that it was reprinted by AIPP, with permission, from another source. Under no circumstances does AIPP, purport or intend to grant permission to reuse material to which it

does not hold copyright.

3. You may not alter or modify the Material in any manner. You may translate the Material into another language only if you have licensed translation rights. You may not use the Material for promotional purposes. AIPP reserves all rights not specifically granted herein.
4. The foregoing license shall not take effect unless and until AIPP or its agent, Copyright Clearance Center, receives the Payment in accordance with Copyright Clearance Center Billing and Payment Terms and Conditions, which are incorporated herein by reference.
5. AIPP or the Copyright Clearance Center may, within two business days of granting this license, revoke the license for any reason whatsoever, with a full refund payable to you. Should you violate the terms of this license at any time, AIPP, AIP Publishing LLC, or Copyright Clearance Center may revoke the license with no refund to you. Notice of such revocation will be made using the contact information provided by you. Failure to receive such notice will not nullify the revocation.
6. AIPP makes no representations or warranties with respect to the Material. You agree to indemnify and hold harmless AIPP, AIP Publishing LLC, and their officers, directors, employees or agents from and against any and all claims arising out of your use of the Material other than as specifically authorized herein.
7. The permission granted herein is personal to you and is not transferable or assignable without the prior written permission of AIPP. This license may not be amended except in a writing signed by the party to be charged.
8. If purchase orders, acknowledgments or check endorsements are issued on any forms containing terms and conditions which are inconsistent with these provisions, such inconsistent terms and conditions shall be of no force and effect. This document, including the CCC Billing and Payment Terms and Conditions, shall be the entire agreement between the parties relating to the subject matter hereof.

This Agreement shall be governed by and construed in accordance with the laws of the State of New York. Both parties hereby submit to the jurisdiction of the courts of New York County for purposes of resolving any disputes that may arise hereunder.

If you would like to pay for this license now, please remit this license along with your payment made payable to "COPYRIGHT CLEARANCE CENTER" otherwise you will be invoiced within 48 hours of the license date. Payment should be in the form of a check or money order referencing your account number and this invoice number RLNK501110627. Once you receive your invoice for this order, you may pay your invoice by credit card. Please follow instructions provided at that time.

Make Payment To:
Copyright Clearance Center
Dept 001
P.O. Box 843006
Boston, MA 02284-3006

For suggestions or comments regarding this order, contact RightsLink Customer Support: customercare@copyright.com or +1-877-622-5543 (toll free in the US) or +1-978-646-2777.

Gratis licenses (referencing $0 in the Total field) are free. Please retain this printable license for your reference. No payment is required.

AIP PUBLISHING LLC LICENSE TERMS AND CONDITIONS

Sep 11, 2013

All payments must be made in full to CCC. For payment instructions, please see information listed at the bottom of this form.

License Number	
Order Date	Sep 11, 2013
Publisher	AIP Publishing LLC
Publication	Physics of Fluids
Article Title	Numerical simulation of supercritical trapped internal waves over topography
Author	Nancy Soontiens, Christopher Subich, Marek Stastna
Online Publication Date	Nov 24, 2010
Volume number	22
Issue number	11
Type of Use	Thesis/Dissertation
Requestor type	Author (original article)
Format	Print and electronic
Portion	Figure/Table
Number of figures/tables	11
Title of your thesis / dissertation	Stratified flow over topography: steady nonlinear waves, boundary layer instabilities, and crater topography
Expected completion date	Nov 2013
Estimated size (number of pages)	200
Total	0.00 USD
Terms and Conditions	

AIP Publishing LLC -- Terms and Conditions: Permissions Uses

AIP Publishing LLC ("AIPP"") hereby grants to you the non-exclusive right and license to use and/or distribute the Material according to the use specified in your order, on a one-time basis, for the specified term, with a maximum distribution equal to the number that you have ordered. Any links or other content accompanying the Material are not the subject of this license.

1. You agree to include the following copyright and permission notice with the reproduction of the Material:"Reprinted with permission from [FULL CITATION]. Copyright [PUBLICATION YEAR], AIP Publishing LLC." For an article, the copyright and permission notice must be printed on the first page of the article or book chapter. For photographs, covers, or tables, the copyright and permission notice may appear with the Material, in a footnote, or in the reference list.
2. If you have licensed reuse of a figure, photograph, cover, or table, it is your responsibility to ensure that the material is original to AIPP and does not contain the copyright of another entity, and that the copyright notice of the figure, photograph, cover, or table does not indicate that it was reprinted by AIPP, with permission, from another source. Under no circumstances does AIPP, purport or intend to grant permission to reuse material to which it

does not hold copyright.

3. You may not alter or modify the Material in any manner. You may translate the Material into another language only if you have licensed translation rights. You may not use the Material for promotional purposes. AIPP reserves all rights not specifically granted herein.
4. The foregoing license shall not take effect unless and until AIPP or its agent, Copyright Clearance Center, receives the Payment in accordance with Copyright Clearance Center Billing and Payment Terms and Conditions, which are incorporated herein by reference.
5. AIPP or the Copyright Clearance Center may, within two business days of granting this license, revoke the license for any reason whatsoever, with a full refund payable to you. Should you violate the terms of this license at any time, AIPP, AIP Publishing LLC, or Copyright Clearance Center may revoke the license with no refund to you. Notice of such revocation will be made using the contact information provided by you. Failure to receive such notice will not nullify the revocation.
6. AIPP makes no representations or warranties with respect to the Material. You agree to indemnify and hold harmless AIPP, AIP Publishing LLC, and their officers, directors, employees or agents from and against any and all claims arising out of your use of the Material other than as specifically authorized herein.
7. The permission granted herein is personal to you and is not transferable or assignable without the prior written permission of AIPP. This license may not be amended except in a writing signed by the party to be charged.
8. If purchase orders, acknowledgments or check endorsements are issued on any forms containing terms and conditions which are inconsistent with these provisions, such inconsistent terms and conditions shall be of no force and effect. This document, including the CCC Billing and Payment Terms and Conditions, shall be the entire agreement between the parties relating to the subject matter hereof.

This Agreement shall be governed by and construed in accordance with the laws of the State of New York. Both parties hereby submit to the jurisdiction of the courts of New York County for purposes of resolving any disputes that may arise hereunder.

If you would like to pay for this license now, please remit this license along with your payment made payable to "COPYRIGHT CLEARANCE CENTER" otherwise you will be invoiced within 48 hours of the license date. Payment should be in the form of a check or money order referencing your account number and this invoice number RLNK501110630. Once you receive your invoice for this order, you may pay your invoice by credit card. Please follow instructions provided at that time.

Make Payment To:
Copyright Clearance Center
Dept 001
P.O. Box 843006
Boston, MA 02284-3006

For suggestions or comments regarding this order, contact RightsLink Customer Support: customercare@copyright.com or +1-877-622-5543 (toll free in the US) or +1-978-646-2777.

Gratis licenses (referencing $0 in the Total field) are free. Please retain this printable license for your reference. No payment is required.

AIP PUBLISHING LLC LICENSE TERMS AND CONDITIONS

Sep 11, 2013

All payments must be made in full to CCC. For payment instructions, please see information listed at the bottom of this form.

License Number	
Order Date	Sep 11, 2013
Publisher	AIP Publishing LLC
Publication	Physics of Fluids
Article Title	Trapped internal waves over topography: Non-Boussinesq effects, symmetry breaking and downstream recovery jumps
Author	Nancy Soontiens, Marek Stastna, Michael L. Waite
Online Publication Date	Jun 24, 2013
Volume number	25
Issue number	6
Type of Use	Thesis/Dissertation
Requestor type	Author (original article)
Format	Print and electronic
Portion	Excerpt (> 800 words)
Will you be translating?	No
Title of your thesis / dissertation	Stratified flow over topography: steady nonlinear waves, boundary layer instabilities, and crater topography
Expected completion date	Nov 2013
Estimated size (number of pages)	200
Total	0.00 USD
Terms and Conditions	

AIP Publishing LLC -- Terms and Conditions: Permissions Uses

AIP Publishing LLC ("AIPP"") hereby grants to you the non-exclusive right and license to use and/or distribute the Material according to the use specified in your order, on a one-time basis, for the specified term, with a maximum distribution equal to the number that you have ordered. Any links or other content accompanying the Material are not the subject of this license.

1. You agree to include the following copyright and permission notice with the reproduction of the Material:"Reprinted with permission from [FULL CITATION]. Copyright [PUBLICATION YEAR], AIP Publishing LLC." For an article, the copyright and permission notice must be printed on the first page of the article or book chapter. For photographs, covers, or tables, the copyright and permission notice may appear with the Material, in a footnote, or in the reference list.
2. If you have licensed reuse of a figure, photograph, cover, or table, it is your responsibility to ensure that the material is original to AIPP and does not contain the copyright of another entity, and that the copyright notice of the figure, photograph, cover, or table does not indicate that it was reprinted by AIPP, with permission, from another source. Under no circumstances does AIPP, purport or intend to grant permission to reuse material to which it

does not hold copyright.

3. You may not alter or modify the Material in any manner. You may translate the Material into another language only if you have licensed translation rights. You may not use the Material for promotional purposes. AIPP reserves all rights not specifically granted herein.
4. The foregoing license shall not take effect unless and until AIPP or its agent, Copyright Clearance Center, receives the Payment in accordance with Copyright Clearance Center Billing and Payment Terms and Conditions, which are incorporated herein by reference.
5. AIPP or the Copyright Clearance Center may, within two business days of granting this license, revoke the license for any reason whatsoever, with a full refund payable to you. Should you violate the terms of this license at any time, AIPP, AIP Publishing LLC, or Copyright Clearance Center may revoke the license with no refund to you. Notice of such revocation will be made using the contact information provided by you. Failure to receive such notice will not nullify the revocation.
6. AIPP makes no representations or warranties with respect to the Material. You agree to indemnify and hold harmless AIPP, AIP Publishing LLC, and their officers, directors, employees or agents from and against any and all claims arising out of your use of the Material other than as specifically authorized herein.
7. The permission granted herein is personal to you and is not transferable or assignable without the prior written permission of AIPP. This license may not be amended except in a writing signed by the party to be charged.
8. If purchase orders, acknowledgments or check endorsements are issued on any forms containing terms and conditions which are inconsistent with these provisions, such inconsistent terms and conditions shall be of no force and effect. This document, including the CCC Billing and Payment Terms and Conditions, shall be the entire agreement between the parties relating to the subject matter hereof.

This Agreement shall be governed by and construed in accordance with the laws of the State of New York. Both parties hereby submit to the jurisdiction of the courts of New York County for purposes of resolving any disputes that may arise hereunder.

If you would like to pay for this license now, please remit this license along with your payment made payable to "COPYRIGHT CLEARANCE CENTER" otherwise you will be invoiced within 48 hours of the license date. Payment should be in the form of a check or money order referencing your account number and this invoice number RLNK501110632. Once you receive your invoice for this order, you may pay your invoice by credit card. Please follow instructions provided at that time.

Make Payment To:
Copyright Clearance Center
Dept 001
P.O. Box 843006
Boston, MA 02284-3006

For suggestions or comments regarding this order, contact RightsLink Customer Support: customercare@copyright.com or +1-877-622-5543 (toll free in the US) or +1-978-646-2777.

Gratis licenses (referencing $0 in the Total field) are free. Please retain this printable license for your reference. No payment is required.

AIP PUBLISHING LLC LICENSE TERMS AND CONDITIONS

Sep 11, 2013

All payments must be made in full to CCC. For payment instructions, please see information listed at the bottom of this form.

License Number	
Order Date	Sep 11, 2013
Publisher	AIP Publishing LLC
Publication	Physics of Fluids
Article Title	Trapped internal waves over topography: Non-Boussinesq effects, symmetry breaking and downstream recovery jumps
Author	Nancy Soontiens, Marek Stastna, Michael L. Waite
Online Publication Date	Jun 24, 2013
Volume number	25
Issue number	6
Type of Use	Thesis/Dissertation
Requestor type	Author (original article)
Format	Print and electronic
Portion	Figure/Table
Number of figures/tables	11
Title of your thesis / dissertation	Stratified flow over topography: steady nonlinear waves, boundary layer instabilities, and crater topography
Expected completion date	Nov 2013
Estimated size (number of pages)	200
Total	0.00 USD
Terms and Conditions	

AIP Publishing LLC -- Terms and Conditions: Permissions Uses

AIP Publishing LLC ("AIPP"") hereby grants to you the non-exclusive right and license to use and/or distribute the Material according to the use specified in your order, on a one-time basis, for the specified term, with a maximum distribution equal to the number that you have ordered. Any links or other content accompanying the Material are not the subject of this license.

1. You agree to include the following copyright and permission notice with the reproduction of the Material:"Reprinted with permission from [FULL CITATION]. Copyright [PUBLICATION YEAR], AIP Publishing LLC." For an article, the copyright and permission notice must be printed on the first page of the article or book chapter. For photographs, covers, or tables, the copyright and permission notice may appear with the Material, in a footnote, or in the reference list.
2. If you have licensed reuse of a figure, photograph, cover, or table, it is your responsibility to ensure that the material is original to AIPP and does not contain the copyright of another entity, and that the copyright notice of the figure, photograph, cover, or table does not indicate that it was reprinted by AIPP, with permission, from another source. Under no circumstances does AIPP, purport or intend to grant permission to reuse material to which it

does not hold copyright.

3. You may not alter or modify the Material in any manner. You may translate the Material into another language only if you have licensed translation rights. You may not use the Material for promotional purposes. AIPP reserves all rights not specifically granted herein.
4. The foregoing license shall not take effect unless and until AIPP or its agent, Copyright Clearance Center, receives the Payment in accordance with Copyright Clearance Center Billing and Payment Terms and Conditions, which are incorporated herein by reference.
5. AIPP or the Copyright Clearance Center may, within two business days of granting this license, revoke the license for any reason whatsoever, with a full refund payable to you. Should you violate the terms of this license at any time, AIPP, AIP Publishing LLC, or Copyright Clearance Center may revoke the license with no refund to you. Notice of such revocation will be made using the contact information provided by you. Failure to receive such notice will not nullify the revocation.
6. AIPP makes no representations or warranties with respect to the Material. You agree to indemnify and hold harmless AIPP, AIP Publishing LLC, and their officers, directors, employees or agents from and against any and all claims arising out of your use of the Material other than as specifically authorized herein.
7. The permission granted herein is personal to you and is not transferable or assignable without the prior written permission of AIPP. This license may not be amended except in a writing signed by the party to be charged.
8. If purchase orders, acknowledgments or check endorsements are issued on any forms containing terms and conditions which are inconsistent with these provisions, such inconsistent terms and conditions shall be of no force and effect. This document, including the CCC Billing and Payment Terms and Conditions, shall be the entire agreement between the parties relating to the subject matter hereof.

This Agreement shall be governed by and construed in accordance with the laws of the State of New York. Both parties hereby submit to the jurisdiction of the courts of New York County for purposes of resolving any disputes that may arise hereunder.

If you would like to pay for this license now, please remit this license along with your payment made payable to "COPYRIGHT CLEARANCE CENTER" otherwise you will be invoiced within 48 hours of the license date. Payment should be in the form of a check or money order referencing your account number and this invoice number RLNK501110633. Once you receive your invoice for this order, you may pay your invoice by credit card. Please follow instructions provided at that time.

Make Payment To:
Copyright Clearance Center
Dept 001
P.O. Box 843006
Boston, MA 02284-3006

For suggestions or comments regarding this order, contact RightsLink Customer Support: customercare@copyright.com or +1-877-622-5543 (toll free in the US) or +1-978-646-2777.

Gratis licenses (referencing $0 in the Total field) are free. Please retain this printable license for your reference. No payment is required.

References

Afanasyev, Y. and W. Peltier (1998). The three-dimensionalization of stratified flow over two-dimensional topography. *J. Atmos. Sci. 55*, 19–39.

Afanasyev, Y. and W. Peltier (2001). Numerical simulations of internal gravity wave breaking in the middle atmosphere: the influence of dispersion and three-dimensionalization. *J. Atmos. Sci. 58*, 132–153.

Aghsaee, P., L. Boegman, P. J. Diamessis, and K. G. Lamb (2012). Boundary-layer-separation-driven vortex shedding beneath internal solitary waves of depression. *J. Fluid Mech. 690*, 321–344.

Alam, M. and N. Sandham (2000). Direct numerical simulation of short laminar separation bubbles with turbulent reattachment. *J. Fluid Mech. 410*(1), 1–28.

Andreassen, Ø., C. Wasberg, D. Fritts, and J. Isler (1994). Gravity wave breaking in two and three dimensions 1. Model description and comparison of two-dimensional evolutions. *J. Geophys. Res. 99*, 8095–8108.

Armi, L. and G. Mayr (2011). The descending stratified flow and internal hydraulic jump in the lee of the Sierras. *J. Appl. Meteor. Climatol. 50*, 1995–2011.

Baines, P. (1987). Upstream blocking and airflow over mountains. *Annu. Rev. Fluid Mech. 19*, 75–95.

Baines, P. (1995). *Topographic effects in stratified flows*. Cambridge Univ. Press.

Bell, J. B. and D. L. Marcus (1992). A second-order projection method for variable-density flows. *J. Comput. Phys. 101*(2), 334–348.

Bell, R. and R. Thompson (1980). Valley ventilation by cross winds. *J. Fluid Mech. 96*, 757–767.

Benjamin, T. B. (1966). Internal waves of finite amplitude and permanent form. *J. Fluid Mech. 25*, 241.

Benney, D. (1966). Long non-linear waves in fluid flows. *J. Math. Phys. 45*, 52.

Bogucki, D., T. Dickey, and L. Redekopp (1997). Sediment resuspension and mixing by resonantly generated internal solitary waves. *J. Phys. Oceanogr. 27*(7), 1181–1196.

Bogucki, D. J. and L. G. Redekopp (1999). A mechanism for sediment resuspension by internal solitary waves. *Geophys. Res. Lett. 26*(9), 1317–1320.

Brown, D. and D. Christie (1998). Fully nonlinear solitary waves in continuously stratified incompressible Boussinesq fluids. *Phys. Fluids 10*, 2569.

Burt, J., J. Veverka, and K. Cook (1976). Depth-diameter relation for large Martian craters determined from Mariner 9 UVS altimetry. *Icarus 29*, 83–90.

Carr, M. and P. Davies (2010). Boundary layer flow beneath an internal solitary wave of elevation. *Phys. Fluids 22*, 026601.

Carr, M., P. Davies, and P. Shivaram (2008). Experimental evidence of internal solitary wave-induced global instability in shallow water benthic boundary layers. *Phys. Fluids 20*, 066603.

Carr, M., M. Stastna, and P. A. Davies (2010). Internal solitary wave-induced flow over a corrugated bed. *Ocean Dynamics 60*(4), 1007–1025.

Clancy, R. T. and B. J. Sandor (1998). CO_2 ice clouds in the upper atmosphere of Mars. *Geophys. Res. Lett. 25*(4), 489–492.

Csanady, G. (1967). Large-scale motion in the great lakes. *J. Geophys. Res 72*(16), 4151–4162.

Davies, P., D. Acheson, and C. Titman (1975). A note on the geostrophic flow past a crater in a rotating fluid. *Geophys. Fluid Dyn. 7*, 119–131.

Diamessis, P. J. and L. G. Redekopp (2006). Numerical investigation of solitary internal wave-induced global instability in shallow water benthic boundary layers. *J. Phys. Oceanogr. 36*(5), 784–812.

Djordjevic, V. D. and L. Redekopp (1978). The fission and disintegration of internal solitary waves moving over two-dimensional topography. *J. Phys. Oceanogr. 8*(6), 1016.

Dosser, H. V. and B. R. Sutherland (2011). Anelastic internal wave packet evolution and stability. *J. Atmos. Sci. 68*(12), 2844–2859.

Doyle, J., D. Durran, C. Chen, B. Colle, M. Georgelin, V. Grubisic, W. Hsu, C. Huang, D. Landau, Y. Lin, et al. (2000). An intercomparison of model-predicted wave breaking for the 11 January 1972 Boulder windstorm. *Mon. Wea. Rev. 128*(3), 901–914.

Dubreil-Jacotin, M. (1932). Sur les ondes de type permanent dans les liquides hétérogenes. *Atti Accad. Naz. Lincei Rend 6*, 814–819.

Duda, T., J. Lynch, J. Irish, R. Beardsley, S. Ramp, C. Chiu, T. Tang, and Y. Yang (2004). Internal tide and nonlinear internal wave behavior at the continental slope in the northern South China Sea. *IEEE J. Oceanic Eng. 29*(4), 1105.

Durran, D. (1986). Another look at downslope windstorms. Part I: The development of analogs to supercritical flow in an infinitely deep, continuously stratified fluid. *J. Atmos. Sci. 43*, 2527–2543.

Durran, D. R. (1990). Mountain waves and downslope winds. *Atmospheric Processes over Complex Terrain 23*, 59–81.

Epifanio, C. and D. Durran (2001). Three-dimensional effects in high-drag-state flows over long ridges. *J. Atmos. Sci. 58*, 1051–1065.

Esler, J., O. Rump, and E. Johnson (2005). Steady rotating flows over a ridge. *Phys. Fluids 17*(11), 116601.

Esler, J., O. Rump, and E. Johnson (2007). Transcritical rotating flow over topography. *J. Fluid Mech. 590*, 81.

Esler, J., O. Rump, and E. Johnson (2009). Supercritical rotating flow over topography. *Phys. Fluids 21*(6), 066601.

Fenton, L. K., J. L. Bandfield, and A. Ward (2003). Aeolian processes in proctor crater on mars: Sedimentary history as analyzed from multiple data sets. *J. Geophys. Res: Planets 108*(E12).

Fritts, D., D. Goldstein, and T. Lund (2010). High-resolution numerical studies of stable boundary layer flows in a closed basin: Evolution of steady and oscillatory flows in an axisymmetric Arizona Meteor Crater. *J. Geophys. Res. 115*, D18109.

Fructus, D., M. Carr, J. Grue, A. Jensen, and P. Davies (2009). Shear-induced breaking of large internal solitary waves. *J. Fluid Mech. 620*, 1.

García, M. H. (1999). Sedimentation and erosion hydraulics. *Hydraulic design handbook*, 6–1.

Garrett, C. and W. Munk (1979). Internal waves in the ocean. *Annu. Rev. Fluid Mech. 11*(1), 339–369.

Gill, A. (1982). *Atmosphere-ocean dynamics*. Academic Press.

Greeley, R., R. O. Kuzmin, S. C. Rafkin, T. I. Michaels, and R. Haberle (2003). Wind-related features in gusev crater, mars. *J. Geophys. Res. 108*(E12), 8077.

Greeley, R., R. Leach, B. White, J. Iversen, and J. Pollack (1980). Threshold windspeeds for sand on Mars: Wind tunnel simulations. *Geophys. Res. Lett. 7*(2), 121–124.

Grimshaw, R. and N. Smyth (1986). Resonant flow of a stratified fluid over topography. *J. Fluid Mech. 169*, 429.

Guo, C. and X. Chen (2013). A review of internal solitary wave dynamics in the northern South China Sea. *Prog. Oceanogr*.

Hauchecorne, A., M. L. Chanin, and R. Wilson (1987). Mesospheric temperature inversion and gravity wave breaking. *Geophys. Res. Lett. 14*(9), 933–936.

Helfrich, K. and W. Melville (2006). Long nonlinear internal waves. *Annu. Rev. Fluid Mech. 38*, 395.

Helfrich, K. R. and B. L. White (2010). A model for large-amplitude internal solitary waves with trapped cores. *Nonlin. Proc. Geophys. 17*, 303.

Hodges, B. R., J. Imberger, A. Saggio, and K. B. Winters (2000). Modeling basin-scale internal waves in a stratified lake. *Limnol. Oceanogr. 45*(7), 1603–1620.

Hong, S., Y. Noh, and J. Dudhia (2006). A new vertical diffusion package with an explicit treatment of entrainment processes. *Mon. Wea. Rev. 134*, 2318–2341.

Imberger, J. and J. C. Patterson (1989). Physical limnology. *Adv. Appl. Mech. 27*, 303–475.

Jankowski, D. and S. Squyres (1992). The topography of impact craters in 'softened' terrain on Mars. *Icarus 100*, 26–39.

Kakutani, T. and N. Yamasaki (1978). Solitary waves on a two-layer fluid. *J. Phys. Soc. Japan 45*(2), 674–679.

Kerr, R. (1986). Chinook winds resemble water flowing over a rock. *Science 231*, 1244–1245.

Kim, Y., S. Eckermann, and H. Chun (2003). An overview of the past, present and future of gravity-wave drag parametrization for numerical climate and weather prediction models. *Atmos.-Ocean 41*, 65–98.

King, S., M. Carr, and D. Dritschel (2011). The steady-state form of large-amplitude internal solitary waves. *J. Fluid Mech. 666*, 477.

Klemp, J. B. and D. K. Lilly (1975). Dynamics of wave-induced downslope winds. *J. Atmos. Sci. 32*(2), 320–339.

Kundu, P. and I. Cohen (2008). *Fluid Mechanics*. Elsevier Academic Press.

Lamb, K. G. (1994). Numerical simulations of stratified inviscid flow over a smooth obstacle. *J. Fluid Mech. 260*(1), 1–22.

Lamb, K. G. (1999). Theoretical descriptions of shallow-water solitary internal waves: Comparisons with fully nonlinear waves. In T. F. Duda and D. M. Farmer (Eds.), *The 1998 WHOI/IOSA/ONR Internal Solitary Wave Workshop: Contributed Papers, Tech. Rep. WHOI-99-07*, Woods Hole, Mass. Woods Hole Oceanogr. Inst.

Lamb, K. G. (2002). A numerical investigation of solitary internal waves with trapped cores formed via shoaling. *J. Fluid Mech. 451*, 109.

Lamb, K. G. (2003). Shoaling solitary internal waves: on a criterion for the formation of waves with trapped cores. *J. Fluid Mech. 478*, 81–100.

Lamb, K. G. and D. Farmer (2011). Instabilities in an internal solitary-like wave on the oregon shelf. *J. Phys. Oceanogr. 41*(1), 67.

Lamb, K. G. and B. Wan (1998). Conjugate flows and flat solitary waves for a continuously stratified fluid. *Phys. Fluids 10*(8), 2061.

Lamb, K. G. and L. Yan (1996). The evolution of internal wave undular bores: comparisons of a fully nonlinear numerical model with weakly nonlinear theory. *J. Phys. Oceanogr. 26*(12), 2712.

Laprise, R. and W. Peltier (1989). On the structural characteristics of steady finite-amplitude mountain waves over bell-shaped topography. *J. Atmos. Sci. 46*, 586–595.

Lawrence, G. (1987). Steady flow over an obstacle. *J. Hydraul. Eng. 113*, 981.

Lee, S. (1984). Mars: Wind streak production as related to obstacle type and size. *Icarus 58*, 339–357.

Lee, T., R. Pielke, R. Kessler, and J. Weaver (1989). Influence of cold pools downstream of mountain barriers on downslope winds and flushing. *Mon. Wea. Rev 117*, 2041–2058.

Lee, Y., D. Muraki, and D. Alexander (2006). A resonant instability of steady mountain waves. *J. Fluid Mech. 568*, 303–327.

Loken, C., D. Gruner, L. Groer, R. Peltier, N. Bunn, M. Craig, T. Henriques, J. Dempsey, C. Yu, J. Chen, et al. (2010). Scinet: Lessons learned from building a power-efficient top-20 system and data centre. In *J. Phys.: Conf. Ser.*, Volume 256, pp. 012026. IOP Publishing.

Long, R. (1953). Some aspects of the flow of stratified fluids: I. A theoretical investigation. *Tellus 5*, 42–58.

Magalhāes, J. and R. Young (1995). Downslope windstorms in the lee of ridges on Mars. *Icarus 113*(2), 277–294.

McLandress, C. (1998). On the importance of gravity waves in the middle atmosphere and their parameterization in general circulation models. *J. Atmos. Sol.-Terr. Phys. 60*, 1357–1383.

Melville, W. and K. R. Helfrich (1987). Transcritical two-layer flow over topography. *J. Fluid Mech. 178*, 31–52.

Muraki, D. J. (2011). Large-amplitude topographic waves in 2D stratified flow. *J. Fluid Mech. 681*, 173–192.

Newman, C. E., S. R. Lewis, P. L. Read, and F. Forget (2002). Modeling the Martian dust cycle 1. Representations of dust transport processes. *J. Geophys. Res. 107*.

Olafsson, H. and P. Bougeault (1996). Nonlinear flow past an elliptic mountain ridge. *J. Atmos. Sci. 53*, 2465–2489.

Paulson, C. A. (1970). The mathematical representation of wind speed and temperature profiles in the unstable atmospheric surface layer. *J. Appl. Meteorol. 9*(6), 857–861.

Peltier, W. and T. Clark (1979). The evolution and stability of finite-amplitude mountain waves. Part II: Surface wave drag and severe downslope windstorms. *J. Atmos. Sci. 36*, 1498–1529.

Peltier, W. and J. Scinocca (1990). The origin of severe downslope windstorm pulsations. *J. Atmos. Sci. 47*, 2853–2870.

Pickersgill, A. and G. Hunt (1979). The formation of Martian lee waves generated by a crater. *J. Geophys. Res. 84*, 8317–8331.

Pirraglia, J. (1976). Martian atmospheric lee waves. *Icarus 27*, 517–530.

Rafkin, S. C., R. M. Haberle, and T. I. Michaels (2001). The Mars Regional Atmospheric Modeling System: Model Description and Selected Simulations. *Icarus 151*(2), 228 – 256.

Read, P. and S. Lewis (2004). *The Martian climate revisited: atmosphere and environment of a desert planet*. Springer Verlag.

Richardson, M., A. Toigo, and C. Newman (2007). PlanetWRF: A general purpose, local to global numerical model for planetary atmospheric and climate dynamics. *J. Geophys. Res. 112*, E09001.

Rusås, P. and J. Grue (2002). Solitary waves and conjugate flows in a three-layer fluid. *Eur. J. Mech. B/Fluids 21*(2), 185.

Scinocca, J. and W. Peltier (1989). Pulsating downslope windstorm. *J. Atmos. Sci. 46*, 2885–2914.

Skamarock, W., J. Klemp, J. Dudhia, D. Gill, D. Barker, M. Duda, M. Huang, W. Wang, and J. Powers (2008). A Description of the Advanced Research WRF Version 3. NCAR Tech. Note NCAR/TN-475+ STR.

Smith, R. B. (1979). The influence of mountains on the atmosphere. *Adv. Geophys. 21*, 87–230.

Smith, R. B. (1980). Linear theory of stratified hydrostatic flow past an isolated mountain. *Tellus 32*, 348–364.

Smith, R. B. (1985). On severe downslope winds. *J. Atmos. Sci. 42*, 2597–2603.

Smith, R. B. (1989). Hydrostatic airflow over mountains. *Adv. Geophys. 31*, 1–41.

Smith, R. B. (2003). Stratified flow over topography. In R. Grimshaw (Ed.), *Environmental Stratified Flows*, pp. 119–159. Kluwer Academic Publishers.

Smith, R. B. and S. Gronas (1993). Stagnation points and bifurcation in 3-d mountain air-flow. *Tellus A 45A*(1), 28–43.

Smolarkiewicz, P. K. and R. Rotunno (1989). Low Froude-number flow past three-dimensional obstacles Part 1. Baroclinically generated lee vortices. *J. Atmos. Sci. 46*, 1154–1164.

Smyth, N. and P. Holloway (1988). Hydraulic jump and undular bore formation on a shelf break. *J. Phys. Oceanogr 18*(7), 947–962.

Soontiens, N., M. Stastna, and M. L. Waite (2013a). Numerical simulations of waves over large crater topography in the atmosphere. *J. Atmos. Sci. 70*, 1216.

Soontiens, N., M. Stastna, and M. L. Waite (2013b). Trapped internal waves over topography: Non-boussinesq effects, symmetry breaking and downstream recovery jumps. *Phys. Fluids 25*, 066602.

Soontiens, N., C. Subich, and M. Stastna (2010). Numerical simulation of supercritical trapped internal waves over topography. *Phys. Fluids 22*(11), 116605.

Spiga, A., F. González-Galindo, M.-Á. López-Valverde, and F. Forget (2012). Gravity waves, cold pockets and CO_2 clouds in the Martian mesosphere. *Geophys. Res. Lett. 39*(2).

Stastna, M. (2001). *Large fully nonlinear solitary and solitary-like internal waves in the oceans*. Ph. D. thesis, University of Waterloo.

Stastna, M. and K. G. Lamb (2002a). Large fully nonlinear internal solitary waves: The effect of background current. *Phys. Fluids 14*, 2987.

Stastna, M. and K. G. Lamb (2002b). Vortex shedding and sediment resuspension associated with the interaction of an internal solitary wave and the bottom boundary layer. *Geophys. Res. Lett. 29*(11).

Stastna, M. and K. G. Lamb (2008). Sediment resuspension mechanisms associated with internal waves in coastal waters. *J. Geophys. Res: Oceans 113*(C10).

Stastna, M. and W. Peltier (2005). On the resonant generation of large-amplitude internal solitary and solitary-like waves. *J. Fluid Mech. 543*(1), 267.

Stastna, M., C. Subich, and N. Soontiens (2012). Trapped disturbances and finite amplitude downstream wavetrains on the f-plane. *Phys. Fluids 24*, 106601.

Subich, C. (2011). *Simulation of the Navier-Stokes Equations in Three Dimensions with a Spectral Collocation Method*. Ph. D. thesis, University of Waterloo.

Subich, C. J., K. G. Lamb, and M. Stastna (2013). Simulation of the Navier-Stokes equations in three dimensions with a spectral collocation method. *Int. J. Numer. Meth. Fluids 73*, 103–129.

Trefethen, L. (2000). *Spectral methods in MATLAB*. Society for Industrial Mathematics.

Tung, K., T. Chan, and T. Kubota (1982). Large amplitude internal waves of permanent form. *Stud. Appl. Math. 66*, 1.

Veverka, J., K. Cook, and J. Goguen (1978). A statistical study of crater-associated wind streaks in the north equatorial zone of Mars. *Icarus 33*, 466–482.

Veverka, J., P. Gierasch, and P. Thomas (1981). Wind streaks on Mars: Meteorological control of occurence and mode of formation. *Icarus 45*, 154–166.

Vosper, S. (2004). Inversion effects on mountain lee waves. *Q. J. Roy. Meteor. Soc. 130*, 1723–1748.

Wurtele, M., R. Sharman, and A. Datta (1996). Atmospheric lee waves. *Annu. Rev. Fluid Mech. 28*, 429–476.

Wurtele, M. G. (1957). The three-dimensional lee wave. *Beitr. Phys. Atmos 29*, 242–252.